Protein Transport and Signaling Deficits at the Blood-Brain Barrier in Preclinical Models of Alzheimer's Disease and Metabolic Syndrome

A thesis submitted to the faculty of the University of Minnesota-Twin Cities

By:

Andrew Zhou

In partial fulfillment of the requirements for the degree of Doctor of Philosophy in Pharmaceutics

Advisor:

Karunya K. Kandimalla, Ph.D.

August 2023

Abstract

Several major risk factors have emerged for Alzheimer's disease (AD), including advanced age and metabolic syndromes like cardiovascular disease (CVD) and type 2 diabetes mellitus (T2DM). Blood-brain barrier (BBB) dysfunction is a shared feature among these disorders and precedes the emergence of histopathological hallmarks and cognitive decline in AD patients. Endogenous proteins like apolipoprotein A-I (ApoA-I), insulin, and amyloid-β (Aβ) peptides are heavily implicated in AD, and play key roles in CVD, T2DM and cerebral amyloid angiopathy, respectively. However, the mechanisms governing the BBB transport and function of these key proteins are poorly understood. Further, it is unclear how these mechanisms are altered by major AD risk factors.

My thesis seeks to identify key mechanisms governing the transport and function of ApoA-I, insulin and Aβ peptides at the BBB, under healthy conditions and in the presence of various AD risk factors that are associated with peripheral insulin resistance. This involved pharmacokinetic experiments using ^{125}I radiolabeled proteins in rodent models representing various AD risk factors, alongside in vitro transport and signaling studies performed using an in vitro BBB cell model. Findings from Chp. 2 showed that the BBB plays a major role in ApoA-I brain delivery in rats, refuting a recent claim that blood-CSF barrier is the major portal for ApoA-I brain delivery. Findings from Chp. 3 showed that aging is associated with reduced insulin brain delivery and increased brain Aβ accumulation, which is expected to contribute to AD progression. Findings from Chp. 4 showed that insulin brain delivery is reduced in T2DM or AD mouse models compared to the healthy controls, with the lowest insulin brain delivery observed in mice that manifest. Further, these reductions in brain insulin delivery were

associated with deficits in insulin signaling pathways at the BBB, based on western blots performed on brain microvessels harvested from the different mouse models.

Findings from Chp. 5 provided a functional validation of the importance of insulin signaling pathways in regulating insulin and Aβ peptide transport at the BBB. In healthy mice, treatment with an insulin signaling inhibitor reduced brain insulin delivery and increased brain Aβ accumulation, recapitulating the trends observed in the mouse models of AD risk factors. This was supported by in vitro studies performed in BBB cell monolayers. Further, insulin uptake was reduced upon direct inhibition of the insulin receptor, but not by inhibition of either or both downstream signaling arms, specifically the PI3K/AKT and MAPK/ERK pathways. Additionally, the inhibitory effects of Aβ peptides on insulin uptake in the BBB cell monolayers were characterized.

Finally, the mechanisms of action of two different potential approaches for reducing brain Aβ levels as a treatment for AD were explored. Findings from Chp. 6 showed the ApoA-I mimetic peptide 4F has substantially greater brain permeability compared to full-length ApoA-I in healthy mice. The 4F was further shown to beneficially modulate the transport of Aβ40 and Aβ42 peptides in healthy mice, which was confirmed using an in vitro BBB cell model. Findings from Chp. 7 showed that systemic treatment with an anti-Aβ monoclonal antibody led to sequestration of plasma Aβ and reduced brain Aβ accumulation in healthy mice. This offers mechanistic insight into the previously established “sink effect” of Aβ immunotherapies on brain Aβ clearance.

Together, these findings provide novel mechanistic insights into how AD risk factors contribute to BBB dysfunction, and how therapeutic agents like ApoA-I mimetic peptides and Aβ immunotherapies could potentially be used to restore BBB function.

Table of Contents

Chapter 1: Introduction

1.1. Synopsis

Numerous epidemiological studies have established strong connections between Alzheimer's disease (AD) and several of its major risk factors, including aging, cardiovascular disease (CVD) and type 2 diabetes mellitus (T2DM). It has also become clear that blood-brain barrier (BBB) dysfunction is a common feature among all of these disorders. Moreover, BBB dysfunction precedes the emergence of histopathological hallmarks and cognitive decline in AD patients. Peripheral abnormalities such as dyslipidemia in CVD and insulin resistance in T2DM are known to promote BBB dysfunction, which could offer a mechanistic link between specific risk factors and the onset of AD. However, the cellular and molecular mechanisms by which key proteins implicated in CVD, T2DM and AD (HDL, insulin and Aβ peptides, respectively) interact with one another and influence BBB function are poorly understood. Further, it remains unclear how these mechanisms are affected by different AD risk factors, such as aging, CVD, T2DM and CAA. An improved mechanistic understanding of how AD risk factors contribute to BBB insulin resistance and subsequent barrier dysfunction could help drive the discovery of novel diagnostic or therapeutic targets for the clinical management of AD. Several therapeutic strategies have emerged for elevating brain insulin levels or lowering brain Aβ levels, with the goal of mitigating cognitive decline in AD patients. However, these strategies have faced significant challenges in the clinic, and their mechanisms of action in altering BBB transport functions have not been fully established.

1.2. Epidemiological links between AD, metabolic syndrome, and BBB dysfunction

Over the last 30 years, a large number of epidemiological studies have established strong connections between Alzheimer's disease (AD) and several of its major risk factors, including aging, cardiovascular disease (CVD) and type 2 diabetes mellitus (T2DM). It has also become clear that blood-brain barrier (BBB) dysfunction is a common feature among all of these disorders. Moreover, BBB dysfunction precedes the emergence of histopathological hallmarks and cognitive decline in AD patients. The two histopathological hallmarks that define AD are the deposition of amyloid-beta (Aβ) peptides in both the brain parenchyma and at the BBB, and the formation of neurofibrillary tangles that consist of hyperphosphorylated tau protein.

Peripheral abnormalities such as dyslipidemia in CVD and insulin resistance in T2DM are known to promote BBB dysfunction, which could offer a mechanistic link between specific risk factors and the onset of AD. However, the cellular and molecular mechanisms by which key proteins implicated in CVD, T2DM and AD (HDL, insulin and Aβ peptides, respectively) interact with one another and influence BBB function are poorly understood. Further, it remains unclear how these mechanisms are affected by different AD risk factors, such as aging, CVD, T2DM, and cerebral amyloid angiopathy (CAA).

The BBB plays an essential role in maintaining the brain microenvironment by facilitating transport of endogenous solutes between the systemic circulation and brain interstitial fluid. The exquisite selectivity of the BBB endothelium is achieved by the presence of tight junctions and specialized receptors/transporters, along with their

associated regulatory networks. These properties enable highly selective uptake of essential nutrients to the brain, while greatly restricting uptake of toxic metabolites circulating in blood. The BBB also functions as a clearance portal to remove metabolic waste products from the brain, such as amyloid beta (Aβ) peptides. Impairments in BBB transport functions are among the earliest neuropathological changes documented in patients with Alzheimer's disease (AD) (Zlokovic, 2011).

1.3. Contribution of AD risk factors to BBB dysfunction

1.3.1. Advanced age. Normal aging is associated with gradual loss of BBB function and appearance of neuropathological changes (Montagne et al., 2015). These changes are accelerated in AD brain and trigger catastrophic neurocognitive changes (Popescu et al., 2009). It has been estimated that 20-30% of all cognitively normal older adults display significant Aβ deposition in brain (Rodrigue et al., 2009). In aged nonhuman primates, it was shown that systemically injected Aβ efficiently crossed the BBB and became incorporated into existing parenchymal plaques (Mackic et al., 2002). Further, increased brain Aβ deposition in aged rats was associated with increased BBB expression of the receptor for advanced glycation end products (RAGE), which handles Aβ influx to the brain (Silverberg et al., 2010b). A separate study confirmed an age-dependent increase in RAGE and decrease in low density lipoprotein 1 receptor (LRP1), which handles Aβ efflux from the brain, in AD transgenic mice (Do et al., 2016). Interestingly, these changes were counterbalanced by upregulation of cholesterol transporters at the BBB (ABCA1 and ABCG4), but only at younger ages, which helped to maintain the balance between Aβ influx and efflux at the BBB (Do et al., 2016).

Elevated serum Aβ levels are also known to increase the risk of AD in elderly patients (Okereke et al., 2009).

BBB dysfunction in aging and AD also manifests as decreased influx of essential nutrients to the brain, such as glucose and insulin (Sartorius et al., 2015). Insulin concentrations and insulin receptor (IR) density in postmortem brain were also shown to decrease with age in subjects with or without AD (Frolich et al., 1998). Further, aging was associated with a shift in transport from ligand specific receptor mediated to non-specific caveolar transcytosis in mice, which coincided with an increase in caveolin-1 expression and decrease in IR expression at the BBB (Yang et al., 2020). Further studies are needed to better understand how normal aging alters BBB transport functions, leading to AD pathogenesis in some elderly subjects but not others.

1.3.2. Cardiovascular disease. Cardiovascular diseases (CVDs) represent a diverse set of related disorders, which includes hypertension, atherosclerosis, heart failure and cerebrovascular disease (Leszek et al., 2021). The brain is highly vascularized and receives ~15% of the total cardiac output. As such, the brain is highly susceptible to disruptions to cerebral blood flow, which are common in heart failure (de la Torre, 2002). Reduced cerebral blood flow is commonly observed in AD patients and is suggested to promote the development of neurofibrillary tangles and Aβ peptide deposits in AD brain (Adelborg et al., 2017). Further, disruptions to cerebral blood flow may contribute to BBB dysfunction. In Sprague-Dawley rats, reduced cerebral blood flow led to decreased BBB transport of insulin from blood to brain (Hom et al., 2001).

Chronic hypertension is a significant risk factor for AD and is driven by the development of atherosclerotic plaques, which form on the luminal surface of blood vessels in both the periphery and the brain (Iadecola and Davisson, 2008). Cholesterol is a major component of the atherosclerotic plaques. Hypercholesterolemia is a major feature of dyslipidemia and represents a risk factor for AD, although statins have shown limited benefit in AD clinical trials (Torrandell-Haro et al., 2020). Apolipoprotein A-I (ApoA-I) serves as the major protein constituent of high-density lipoprotein (HDL) particles in plasma. HDL is involved in the reverse transport of cholesterol from peripheral tissues to liver and thereby plays a critical role in protecting against hypercholesterolemia, atherosclerosis, and CVD (Assmann and Gotto, 2004). In addition, emerging evidence suggests that ApoA-I/HDL impacts cerebrovascular accumulation of Aβ peptides in AD brain (Hottman et al., 2014; Stukas et al., 2014b).

Specific studies in APP/PS1 transgenic mice, which express excess Aβ, have revealed the potential role of ApoA-I in protecting against cerebrovascular Aβ deposition, cerebral amyloid angiopathy (CAA), and cognitive decline. Deletion of ApoA-I increased CAA and exacerbated cognitive impairment in APP/PS1 mice (Lefterov et al., 2010). Conversely, ApoA-I overexpression reduced CAA and preserved cognitive function in APP/PS1 mice (Lewis et al., 2010). It has also been reported that luminal ApoA-I can mobilize the abluminal efflux of Aβ across cerebrovascular endothelial cell monolayers (Merino-Zamorano et al., 2016). Thus, ApoA-I appears to be important in alleviating Aβ load in the cerebral vasculature and protecting against cognitive deficits associated with AD. As such, alterations in ApoA-I disposition and function are expected to have a significant impact on the cerebrovascular contributions to AD pathogenesis.

1.3.3. Type 2 diabetes mellitus. Numerous studies have indicated that T2DM is associated with BBB dysfunction, as evidenced by increased brain uptake of tracer molecules, along with altered BBB expression of tight junction proteins (Starr et al., 2003; Hawkins et al., 2007). Further, loss of BBB integrity was shown to precede the onset of cognitive decline and neurodegeneration in mice maintained on a high-fat diet (Takechi et al., 2017). The expression of specific receptors that handle the BBB transport of various peptides/proteins is also known to be altered by T2DM. Compared to nondiabetic db/+ mice, diabetic db/db mice demonstrated increased BBB expression of the Aβ receptor RAGE, alongside reduced expression of LRP-1 (Chen et al., 2016). Further, this was associated with enhanced brain Aβ deposition and cognitive decline (Chen et al., 2016). The effects of high fat diet on brain Aβ burden were confirmed in a separate study using AD transgenic mice (Julien et al., 2010). However, a more recent study concluded that high fat diet had no effect on Aβ42 levels in the cortex of AD transgenic mice and may actually improve cognitive function, suggesting that the effects of high fat diet on brain Aβ deposition and AD progression are still controversial (Elhaik Goldman et al., 2018).

Peripheral insulin resistance, which is a hallmark of T2DM, has also been shown to interfere with the BBB transport of insulin. Insulin delivery to the brain from systemic circulation is crucial for normal brain functions, such as energy metabolism and learning/memory. In healthy human subjects, the severity of insulin resistance was shown to correlate with reduced insulin ratios in brain/plasma (Heni et al., 2014). Elevated plasma insulin levels, known as hyperinsulinemia, is highly prevalent among T2DM patients and represents a major risk factor for AD (Luchsinger et al., 2004).

Elevated plasma levels could lead to overstimulation of IR expressed on the luminal side of BBB endothelial cells, resulting in negative feedback mechanisms that downregulate IR and trigger BBB insulin resistance. A recent study demonstrated that high fat diet led to increased IR expression in tandem with decreased IR signaling in brain microvessels harvested from the mice (Watson et al., 2022). Thus, T2DM and its associated pathologies are associated with various deleterious changes in BBB dysfunction, which have been linked to the etiology of AD.

1.4. HDL/ApoA-I trafficking at the BBB

ApoA-I is the second most abundant lipoprotein after ApoE in the cerebrospinal fluid (CSF) (Roheim et al., 1979; Koch et al., 2017), yet ApoA-I mRNA has not been detected in brain, at least in the murine models (Elliott et al., 2010). While ApoE is synthesized both in the brain and in the periphery, ApoA-I is produced primarily by the liver and intestine. Hence, the CNS pool of ApoA-I is thought to be delivered from the periphery through the blood-CSF barrier (BCSFB) and/or the BBB. Both barriers show exquisite selectivity in their permeability, and together represent the two major portals regulating flux of macromolecules between blood and brain (Strazielle and Ghersi-Egea, 2013). The BCSFB is lined by the choroid epithelium at the four ventricles, whereas the BBB is lined by the diffuse network of brain microvessels that comprise the cerebrovascular endothelium. Stukas et al. (2014) have previously demonstrated the localization of Alexa Fluor 647-labeled ApoA-I at the choroid plexus following intravenous injection in mice, thereby concluding preferential ApoA-I brain entry via the BCSFB. The investigators however noted that contribution of the BBB in ApoA-I brain

delivery remains unresolved. Due to the emerging role of ApoA-I in protecting the cerebral vasculature from Aβ deposition, there is a need to clarify the relevance of the BBB as a portal for ApoA-I brain delivery.

1.5. Insulin resistance is an emerging hallmark of AD

The term “type 3 diabetes” has gained traction over the last 10 years and was coined to describe the subset of AD patients who also have T2DM as a comorbidity. The term further reflects the AD field’s newfound understanding of the role of brain insulin resistance in cognitive impairment and AD pathogenesis (Kandimalla et al., 2017). Numerous studies have revealed common links between T2DM and AD, specifically with regard to the cellular and molecular mechanisms by which insulin resistance emerges in both peripheral tissues as well as in the brain. These mechanisms include but are not limited to alterations in IR/IGF1R signaling, inflammatory response, oxidative stress, Aβ peptide production/deposition, GSK3β signaling, and tau phosphorylation (Kandimalla et al., 2017).

The prevailing hypothesis is that in T2DM, peripheral insulin resistance translates into brain insulin resistance and plays a key role in triggering early neuropathological changes in the brain, eventually giving rise to catastrophic changes in BBB function, memory/cognition, and emergence of the major histopathological hallmarks that define AD. Previously, it was shown that patients with either T2DM or AD both exhibit reduced expression/activity of several components of the insulin/PI3K/AKT signaling pathway in the frontal cortex (Liu et al., 2011). Moreover, patients with both T2DM and AD had the most severe deficits in brain insulin signaling, which also correlated with increased tau

hyperphosphorylation (Liu et al., 2011). However, additional studies are required to elucidate the effects of T2DM and AD pathology on BBB insulin signaling pathways, and the deleterious effects this may have on BBB transport functions.

1.6. Insulin trafficking at the BBB

Insulin is produced almost exclusively in the pancreas, with little to no production occurring in the brain. After entering the systemic circulation, insulin must be trafficked across the BBB to enter the brain. Insulin in the brain is needed to drive crucial neurobiological functions that play key roles in brain glucose metabolism and learning/memory. These functions are severely compromised in the brains of patients with AD and/or T2DM.

Over the last 5 years, substantial controversy has arisen surrounding the molecular mechanisms and regulators of insulin transport at the BBB. Historically, the insulin receptor (IR) was believed to be responsible for mediating receptor mediated transcytosis of insulin at the BBB (Rhea and Banks, 2021). This belief was largely based on earlier studies that demonstrated insulin binding to IR in isolated brain microvessels (Frank and Pardridge, 1981; Yu et al., 2006), and subsequent studies that showed insulin uptake/transport in BBB cells is blocked by a selective IR inhibitor, S961 (Meijer et al., 2016; Gray et al., 2017). However, it was more recently reported that insulin uptake to the brain is maintained in endothelial specific IR knockout mice, as well as in wild type mice upon treatment with S961 (Rhea et al., 2018). A separate group further demonstrated that insulin transport across an in vitro BBB cell model was not inhibited by S961 (Hersom et al., 2018). This led the authors to conclude that IR is not

required for insulin transport at the BBB. An alternate explanation is that compensatory mechanisms may still enable insulin transport at the BBB, such as via the IGF-1 receptor (Yu et al., 2006).

In peripheral tissues, it has been shown that insulin transport across the vascular endothelium is mediated by insulin binding to IR (Hachiya et al., 1988; Wang et al., 2006; Jaldin-Fincati et al., 2018). The insulin-IR complex is then internalized, allowing for subsequent transcytosis across the cell (Fagerholm et al., 2009). While it is possible that insulin transport across BBB endothelium follows a different mechanism than insulin transport across vascular endothelium that lines peripheral tissues, further studies are needed to clarify the role of IR in insulin transport at the BBB. Additionally, there are conflicting reports on the role of clathrin vs. caveolin in mediating insulin endocytosis in vascular endothelial cells (Wang et al., 2011; Azizi et al., 2015; Wang et al., 2015), which further highlights the need for additional mechanistic studies.

1.7. Insulin signaling at the BBB

Insulin binding to IR triggers a diverse and complex cascade of intracellular mediators that comprise the insulin signaling pathway. Insulin signaling is critical for neurobiological functions such as energy metabolism (Jauch-Chara et al., 2012), neuronal growth/division (Gu et al., 2014), and learning/memory (Dou et al., 2005). Insulin signaling is mediated by the insulin receptor (IR) and insulin-like growth factor 1 receptor (IGF1R), which converge at several downstream signaling kinases. The two major signaling arms are the PI3K/Akt and MAPK/Erk pathways. These two pathways are canonically responsible for metabolic and mitogenic functions, respectively.

However, the functional role of insulin signaling at the BBB and its contribution to AD are poorly understood (Rhea and Banks, 2019).

Insulin signaling pathways have been implicated in the regulation of BBB tight junction integrity. This notion is supported by the observation that T2DM patients show loss of BBB tight junction integrity with increased brain uptake of tracer molecules. However, an early study reported that endothelial-specific IR knockout mice have a normal BBB, with no leakage of Evans blue dye (Kondo et al., 2004). It is possible this method could not detect minor changes in BBB integrity, as only catastrophic loss of BBB integrity is expected to allow for increased brain uptake of serum albumin, which binds Evans blue dye. In support of the role of insulin signaling in maintaining BBB integrity, it was later shown that insulin increased tight junction integrity using an in vitro BBB cell model, and this effect was blocked by pretreatment with an IGF1R/IR dual kinase inhibitor, AG1024 (Ito et al., 2017).

The role of insulin signaling pathways on insulin transport at the BBB have not been fully evaluated. It was previously reported that treatment with PI3K/AKT or MAPK/ERK inhibitors reduced insulin uptake into bovine aortic endothelial cells (Wang et al., 2008). However, it was later reported by the same group that the same insulin signaling inhibitors had no effect on insulin uptake in rat brain microvascular endothelial cells (Gray et al., 2017). This led the authors to conclude that insulin signaling is not required for insulin transport at the BBB. Some of the inhibitors used, such as wortmannin and PD98059, are reported to have numerous off-target and pleiotropic effects, which can confound the mechanistic interpretation of these findings (Tan et al., 2011; Wauson et al., 2013).

1.8. Amyloid-β peptide trafficking at the BBB

BBB dysfunction contributes to increased levels of toxic Aβ peptides in the brain, which represents one of the primary neuropathological hallmarks of AD. Two major Aβ isoforms accumulate in AD brain: Aβ42, which is regarded as the most neurotoxic and amyloidogenic isoform (Qiu et al., 2015), and Aβ40, which is less neurotoxic and was shown to be protective against Aβ42 aggregation and toxicity (Kim et al., 2007; Murray et al., 2009). While Aβ42 is the major isoform present in parenchymal plaques, Aβ40 is the major isoform present in cerebrovascular amyloid deposits and gives rise to cerebral amyloid angiopathy (CAA). The Aβ peptides are produced primarily in the brain and to a lesser extent in the periphery. Clearance of Aβ peptides from the brain is handled by receptor-mediated transcytosis at the BBB along with perivascular drainage. Although the Aβ concentrations in plasma are ~6 fold lower than the soluble Aβ concentrations in the brain, the absolute amount of Aβ in plasma is estimated to be ~10 fold greater than the amount of soluble Aβ in the brain (Deane et al., 2004). It was also reported that upon systemic injection, Aβ peptides were rapidly incorporated into existing Aβ plaques in the brains of aged monkeys (Mackic et al., 2002). Moreover, elevated plasma Aβ levels are associated with increased AD risk in elderly patients (Okereke et al., 2009). Thus, systemic Aβ is proposed to contribute to the brain Aβ load directly, by Aβ trafficking into the brain, and indirectly, by impairing the ability of the BBB to clear Aβ from the brain.

Transcytosis of Aβ at the BBB in the blood-to-brain direction is predominantly mediated by the receptor for advanced glycation end products (RAGE), and in the brain-to-blood direction by the low-density lipoprotein receptor related protein 1 (LRP1)

(Deane et al., 2004). These bidirectional transcytotic processes maintain a dynamic equilibrium between the soluble Aβ pools in brain and plasma (Xin et al., 2018). We previously reported that intravenous bolus injection of insulin altered the brain influx of Aβ peptides in mice, and that insulin treatment increased plasma membrane levels of RAGE and LRP-1 in BBB cells in vitro (Swaminathan et al., 2018a). These findings suggest that insulin signaling could be involved in the regulation of Aβ transcytosis at the BBB.

1.9. Therapeutic strategies to elevate brain insulin levels or lower brain Aβ levels as potential treatments for AD

1.9.1. Intranasal insulin delivery. Given the observations that insulin levels are reduced in the brains of AD patients, and that insulin in the brain is critical for learning/memory functions, insulin delivery to the brain via the intranasal route has emerged as a potential therapeutic strategy for AD (Hallschmid, 2021). The intranasal route bypasses the BBB, which could potentially allow for greater quantities of insulin to reach the brain, as compared to systemic delivery followed by transport across the BBB. In small-scale clinical trials, intranasal insulin was shown to induce memory improvements in healthy subjects without cognitive impairments (Benedict et al., 2004; Benedict et al., 2008). Similar cognitive benefits of intranasal insulin have been reported for patients with mild cognitive impairment or AD, although these trials enrolled only a small number of patients (Craft et al., 1999; Reger et al., 2006). The results of the first multicenter phase II/III clinical trial of intranasal insulin for patients with mild cognitive impairment or AD was recently reported (Craft et al., 2020). Importantly, no differences were observed

between the insulin and placebo groups on measures of cognitive function and key AD biomarkers. Thus, the potential utility of intranasal insulin as a treatment for AD has now come into question.

The intranasal route for insulin delivery is also complicated by variable absorption of insulin at the nasal mucosa, which could lead to variability in the amount of insulin delivered to the brain and therapeutic outcomes in different patients. Further, as a growth factor, insulin has potent mitogenic properties. Chronic exposure to high insulin doses at the nasal mucosa could potentially lead to adverse mitogenic side effects. Given these challenges, other strategies should be explored for increasing brain insulin delivery and alleviating brain insulin resistance as potential treatments for AD.

1.9.2. HDL mimetic peptides. Despite the well-documented cardio-and-neuro-vasoprotective effects of ApoA-I, therapeutic applications are limited by its poor oral bioavailability, high manufacturing costs, and low brain permeability. To address these limitations, small peptides that mimic ApoA-I/HDL function have been developed (Navab et al., 2010). The most notable of these HDL mimetics is the 18 amino acid peptide "4F", which contains 4 phenylalanine (F) residues (Ac-DWFKAFYDKVAEKFKEAF-NH_2) and was designed to mimic the amphipathic alpha helix motif present in ApoA-I, which is important for its biological activity (Anantharamaiah et al., 2007). Oral administration of 4F was shown to reduce atherosclerotic lesions and plaque inflammation in a diabetes mouse model (Morgantini et al., 2010). Treatment with 4F was also shown to decrease cerebrovascular inflammation and improve cognitive function in a mouse model of atherosclerosis (Buga et al., 2006). Moreover, oral administration of 4F

together with a statin drug reduced Aβ deposition in the brain parenchyma, ameliorated Aβ-associated neuroinflammation, and improved cognitive function in an AD transgenic mouse model (Handattu et al., 2009).

These literature reports suggest that 4F could potentially be employed as a therapeutic agent to mitigate sporadic CAA and AD related neurovascular pathologies. However, the brain penetrance of 4F has not been established, and the mechanisms by which 4F influences parenchymal and cerebrovascular Aβ deposition are poorly understood.

1.9.3. Passive Aβ immunotherapy. The passive immunotherapy approach using immunoglobulin G (IgG) antibodies engineered to bind and clear Aβ peptides from the brains of AD patients remains an attractive yet controversial area in AD drug development. This is largely due to the mixed success of several high-profile phase 3 clinical trials for various anti-Aβ monoclonal antibodies (mAbs) being developed by various pharmaceutical companies (Tolar et al., 2020). Aducanumab, the first Aβ immunotherapy to receive FDA approval in 2021, has been fraught with controversy regarding its efficacy in mitigating cognitive decline, and is broadly considered a commercial failure (Alexander et al., 2021). Furthermore, the serious side effect of cerebral microhemorrhages, referred to as amyloid-related imaging abnormalities (ARIA), is common for this class of drugs (Filippi et al., 2022; Foley and Wilcock, 2022). Despite these challenges, similar molecules such as lecanemab and several next-generation anti-Aβ antibodies have shown promise and are being actively pursued by several companies (Shi et al., 2022).

Conventional mAbs comprised of a full-length IgG backbone demonstrate extremely low permeability across the blood-brain barrier (BBB) after systemic administration (Poduslo et al., 1994), likely due to their large size (150 kDa). It is estimated that only 0.1% of a mAb dose given intravenously enters the brain (Bard et al., 2012). As such, the “sink hypothesis” has been proposed as a potential mechanism to explain the ability of systemically administered anti-Aβ mAbs to reduce brain Aβ burden in AD patients and mouse models (Zhang and Lee, 2011; Liu et al., 2015). This hypothesis proposes that anti-Aβ mAbs in plasma bind to and sequester circulating soluble Aβ species, resulting in a shift in the dynamic equilibrium between the Aβ pools in plasma and brain interstitial fluid. These two pools undergo reversible exchange via bidirectional receptor-mediated transcytosis processes at the BBB (Deane et al., 2004). By sequestering plasma Aβ, the mAb is believed to act as a sink that drives brain Aβ efflux to the plasma, where it may then be cleared by the liver and kidneys (Ghiso et al., 2004).

In support of the sink hypothesis, solanezumab and ponezumab, which target Aβ but do not bind to insoluble aggregates in the brain, were shown to decrease brain Aβ burden in AD patients (Doody et al., 2014; Salloway et al., 2014). Notably, cerebral microhemorrhages associated with ARIA have been rarely observed for anti-Aβ mAbs that do not bind to Aβ aggregates in the brain, such as solanezumab (Carlson et al., 2011). This is potentially due to Fc effector functions that trigger inflammation directly at the sites of antibody binding to Aβ plaques/deposits in the brain (Mader et al., 2017). These observations suggest that peripheral action of anti-Aβ mAbs may have an improved safety profile over central action as a treatment for AD. In AD transgenic mice,

systemic administration of an anti-Aβ mAb led to a rapid increase in endogenous plasma Aβ levels, which correlated with a decrease in brain Aβ burden (DeMattos et al., 2002). While this study and similar findings in the clinic have been broadly interpreted as evidence of the sink effect (Liu et al., 2015), the antibody effects on plasma Aβ could also be explained by antibody binding to Aβ in plasma, which is expected to alter the Aβ plasma pharmacokinetics.

1.10. Rationale

Several major risk factors have been established for AD, including advanced age, CVD and T2DM. It has also become clear that BBB dysfunction is a common feature among all of these disorders. Moreover, BBB dysfunction precedes the emergence of histopathological hallmarks and cognitive decline in AD patients. Peripheral abnormalities such as dyslipidemia in CVD and insulin resistance in T2DM are known to promote BBB dysfunction, which could offer a mechanistic link between specific risk factors and the onset of AD. However, the cellular and molecular mechanisms by which key proteins implicated in CVD, T2DM and AD (HDL, insulin and Aβ peptides, respectively) interact with one another and influence BBB function are poorly understood. Further, it remains unclear how these mechanisms are affected by different AD risk factors, such as aging, CVD, T2DM and CAA.

Several therapeutic strategies have emerged as a potential means for alleviating brain Aβ burden, with the goal of mitigating cognitive decline in AD patients. However, these strategies have faced significant challenges in the clinic, and their mechanisms of action in lowering brain Aβ levels have not been fully established.

1.11. Specific aims

My doctoral thesis seeks to identify key molecular mechanisms governing the transport and function of ApoA-I, insulin and Aβ peptides at the BBB. Further, my thesis explores how these mechanisms are perturbed by various AD risk factors. Finally, my thesis examines the mechanisms of action of two different potential therapeutic approaches for restoring Aβ peptide transport at the BBB. These objectives are detailed in the following specific aims:

Aim 1: Investigate role of the BBB in ApoA-I delivery to the brain

Aim 1a: Assess ^{125}I-ApoA-I distribution to various brain regions upon systemic injection in wild-type rats ***(Chp. 2)***.

Aim 1b: Identify molecular mechanisms responsible for ApoA-I uptake and transcytosis using an in vitro BBB cell model ***(Chp. 2)***.

Expected outcomes: The ^{125}I-ApoA-I distribution to various brain regions will provide insight into the relative contributions of the BBB and BCSFB in ApoA-I delivery to the brain. The in vitro studies are expected to support the in vivo findings and will help establish the mechanisms of ApoA-I endocytosis on the luminal side of the BBB.

Aim 2: Examine individual effects of AD risk factors (normal aging, peripheral insulin resistance or Aβ peptide exposure) on insulin and Aβ peptide transport at the BBB

Aim 2a: Assess the plasma pharmacokinetics and brain distribution of ^{125}I-insulin and ^{125}I-Aβ peptides in wild-type and/or APP/PS1 transgenic mice at different ages ***(Chp. 3)***.

Aim 2b: Assess the plasma pharmacokinetics and brain distribution of ^{125}I-insulin in diabetic db/db mice vs. non-diabetic db/+ control mice ***(Chp. 4)***.

Aim 2c: Assess the plasma pharmacokinetics and brain distribution of ^{125}I-insulin in wild-type vs. APP/PS1 transgenic mice maintained on a regular chow vs. high-fat diet. Further, to assess the activity of insulin signaling pathways in brain microvessels harvested from the mice ***(Chp. 4)***.

Expected outcomes: The in vivo studies performed in mouse models representing different AD risk factors will help to establish the individual role of each risk factor in altering insulin transport and signaling at the BBB. The studies in young vs. aged mice will also establish the effects of normal aging on Aβ peptide transport at the BBB.

Aim 3: Identify molecular mechanisms by which peripheral insulin resistance contributes to BBB dysfunction

Aim 3a: Assess the plasma pharmacokinetics and brain distribution of ^{125}I-insulin and ^{125}I-Aβ peptides in wild-type mice infused with AG1024, an inhibitor of IGF1R and IR kinase activity. Further, to assess the brain efflux of ^{125}I-Aβ42 upon intracerebral injection in wild-type mice infused with AG1024 ***(Chp. 5)***.

Aim 3b: Examine the effects of AG1024 and other insulin signaling inhibitors on insulin and Aβ peptide uptake, as well as luminal receptor expression, using an in vitro BBB

cell model. Further, to characterize the inhibitory effects of Aβ peptides and S961, a competitive IR inhibitor, on insulin uptake in BBB cells in vitro ***(Chp. 5)***.

Expected outcomes: The in vivo studies with AG1024 are expected to provide a functional validation of the role of IGF1R and IR signaling in regulating insulin and Aβ peptide transport at the BBB. The in vitro studies are expected to support the in vivo findings, and will offer additional mechanistic insight into the roles of Aβ peptides, IR and downstream signaling kinases in regulating insulin and Aβ peptide transport at the BBB.

Aim 4: Explore therapeutic utility of two different approaches for restoring Aβ peptide transport at the BBB

Aim 4a: Assess the brain distribution of the ApoA-I mimetic peptide 4F upon intravenous injection in wild-type mice. Further, to examine the effects of 4F on the plasma pharmacokinetics, brain influx and brain efflux of ^{125}I-Aβ peptides in wild-type mice. Results will be supported by in vitro studies performed using a BBB cell model ***(Chp. 6)***.

Aim 4b: Assess the plasma pharmacokinetics and brain distribution of ^{125}I-Aβ40 and ^{125}I-Aβ42 in wild-type mice upon intravenous injection with IgG4.1, an established human IgG against soluble Aβ species ***(Chp. 7)***.

Expected outcomes: The findings are expected to offer mechanistic insight to support previous reports on the potential therapeutic benefits of 4F and anti-Aβ monoclonal antibodies in alleviating brain Aβ burden in AD transgenic mice and/or patients.

1.12. Significance

Several different therapeutic strategies have emerged for elevating brain insulin levels or reducing brain Aβ levels as potential treatments for AD, and are currently in various stages of preclinical and clinical development. Brain insulin delivery via the intranasal route is limited by variable absorption at the nasal mucosa, along with potential mitogenic risks due to chronic exposure to high insulin doses administered to the nasal cavity. Efforts are also underway to repurpose existing T2DM drugs to treat brain insulin resistance in AD. However, the specific molecular targets that are most influential on BBB dysfunction, AD progression and cognitive decline have not been identified. Given the protective role of HDL/ApoA-I in preserving BBB function, ApoA-I mimetic peptides like 4F have been developed and are being explored for the treatment of AD. Treatment with 4F was shown to reduce brain Aβ burden and mitigate cognitive decline in AD transgenic mice, although the mechanisms are unclear. In addition, the passive Aβ immunotherapy approach remains a high-interest yet controversial area in AD drug development. Different anti-Aβ mAbs have shown mixed success in the clinic, along with the serious adverse event of ARIA. Further, it is unclear whether systemic mAb exposure, with limited brain uptake, is sufficient to induce a meaningful decline in brain Aβ burden.

An improved mechanistic understanding of how ApoA-I, insulin and Aβ peptides interact with one other and regulate BBB function could help drive the discovery of novel diagnostic and therapeutic targets for the clinical management of AD. These insights are expected to help establish the causal connections linking various risk factors to AD. Identifying the mechanisms by which HDL mimetic peptides and Aβ immunotherapies

alter BBB function and alleviate brain Aβ burden could have important ramifications for the design of future therapies against AD.

1.13. Approach

Wild-type Sprague Dawley rats were used for the ApoA-I distribution studies. To study the effects of normal aging, wild-type (B6SJLF1) mice in different age cohorts were used. To study the effects of T2DM, db/db mice were used, which are leptin receptor deficient and develop morbid obesity/T2DM. Nondiabetic db/+ mice were used as a control. As a second model of T2DM, wild-type mice were maintained on either a high-fat or regular chow diet. To study the effects of Aβ peptide exposure, APP/PS1 transgenic mice were used, which overexpress Aβ and recapitulate AD pathophysiology. To study the combined effects of T2DM and AD, a separate cohort of APP/PS1 transgenic mice were maintained on a high-fat diet. Various inhibitors and pharmacological agents were used for subsequent mechanistic studies on BBB function. This included an IGF1R/IR kinase inhibitor (AG1024), a competitive IR inhibitor (S961), an HDL mimetic peptide (4F), and a mAb against human Aβ42 (IgG4.1).

Various peptides/proteins were labeled with ^{125}I using the chloramine-T procedure, including ApoA-I, 4F, insulin, Aβ40 and Aβ42. For plasma pharmacokinetic and brain distribution studies, a single dose of the radioligand was injected to the femoral vein. Following which, serum samples were collected from the femoral artery at different time points in a serial fashion. After perfusion with excess PBS, the ^{125}I activity in various excised brain regions (cortex, caudate putamen, hippocampus, thalamus, brain stem and cerebellum) was measured using a gamma counter. This was used to

estimate the permeability-surface area (PS) products at various brain regions for each radioligand. In a separate study, upon femoral injection of each radioligand, the brain distribution was monitored by dynamic single-photon emission computed tomography/computed tomography (SPECT/CT) imaging. Multiple-time-regression analyses were performed to estimate the brain influx clearance and initial BBB binding of each radioligand. For brain efflux studies, ^{125}I-Aβ42 was injected directly into the hippocampus, and the decline in brain radioactivity over time was monitored by dynamic SPECT/CT imaging to estimate the brain efflux rate constant. For select studies, the mice were infused with various pharmacological agents (AG1024, 4F or IgG4.1) prior to injection of the radioligand.

To investigate insulin signaling at the BBB, brain microvessels were harvested from the T2DM and AD mouse models, along with the healthy control mice. Western blots were performed to assess the expression/activity of various insulin signaling kinases. To corroborate the in vivo findings and further establish the underlying mechanisms, a suite of in vitro studies were performed using a polarized human BBB endothelial cell model. This included cell uptake and transcytosis studies using fluorescent or radiolabeled ApoA-I, insulin or Aβ peptides, assessed by flow cytometry or gamma counting. Further, the expression/activity of various endocytotic receptors and insulin signaling kinases were assessed by western blots. For select studies, the cells were pretreated with various pharmacological agents, such as Aβ peptides, insulin, insulin signaling inhibitors or the HDL mimetic 4F.

Chapter 2: Role of the BBB in ApoA-I delivery to the brain

2.1. Synopsis

Recent studies suggest that apolipoprotein A-I (ApoA-I), the major protein constituent of high-density lipoprotein particles, plays a key role in preserving cerebrovascular integrity and reducing Alzheimer's risk. ApoA-I present in brain is thought to be primarily derived from the peripheral circulation. Although plasma-to-brain delivery of ApoA-I is claimed to be handled by the blood-cerebrospinal fluid barrier (BCSFB), contribution by the blood-brain barrier (BBB), which serves as a major portal for protein delivery to brain, cannot be ruled out. In this study, we assess the permeability-surface area (PS) product of radioiodinated ApoA-I (^{125}I-ApoA-I) in various brain regions of wild-type rats following an intravenous bolus injection. The PS values at the cortex, caudate putamen, hippocampus, thalamus, brain stem, and cerebellum are found to be 0.39, 0.28, 0.28, 0.36, 0.69, and 0.76 (mL/g/s x 10-6), respectively. Solutes delivered into brain via the BCSFB are expected to show greater accumulation in thalamus due to its periventricular location. The modest permeability for ^{125}I-ApoA-I into thalamus relative to other regions suggests that BCSFB transport accounts for only a portion of total brain uptake and therefore BBB transport cannot be neglected. In addition, we show that Alexa Fluor 647-labeled ApoA-I (AF647-ApoA-I) undergoes clathrin-independent and cholesterol-mediated endocytosis in transformed human cerebral microvascular endothelial cells (hCMEC/D3). Further, Z-series confocal images of the hCMEC/D3 monolayers and western blot detection of intact ApoA-I on the

abluminal side demonstrate AF647-ApoA-I transcytosis across the endothelium. These findings implicate the BBB as a significant portal for ApoA-I delivery to the brain.

2.2. Background

Apolipoprotein A-I (ApoA-I) serves as the major protein constituent of high-density lipoprotein (HDL) particles in plasma. HDL is involved in the reverse transport of cholesterol from peripheral tissues to liver and thereby plays a critical role in protecting against hypercholesterolemia, which causes atherosclerosis (Assmann and Gotto, 2004). In addition, emerging evidence suggests that ApoA-I/HDL impacts cerebrovascular accumulation of amyloid beta (Aβ) peptides in Alzheimer's disease brain (Hottman et al., 2014; Stukas et al., 2014b). This has implications for the effective treatment of Alzheimer's disease (AD), in which cerebrovascular Aβ deposition was shown to substantially augment cognitive decline and AD progression (Weller et al., 2009).

Specific studies in APP/PS1 transgenic mice, which express excess Aβ, have revealed the potential role of ApoA-I in protecting against cerebrovascular Aβ deposition, cerebral amyloid angiopathy (CAA), and cognitive decline. Deletion of ApoA-I increased CAA and exacerbated cognitive impairment in APP/PS1 mice (Lefterov et al., 2010). Conversely, ApoA-I overexpression reduced CAA and preserved cognitive function in APP/PS1 mice (Lewis et al., 2010). It has also been reported that luminal ApoA-I can mobilize the abluminal efflux of Aβ across cerebrovascular endothelial cell monolayers (Merino-Zamorano et al., 2016). Thus, ApoA-I appears to be important in alleviating Aβ load in the cerebral vasculature and protecting against cognitive deficits

associated with AD. As such, alterations in ApoA-I disposition and function are expected to have a significant impact on the cerebrovascular contributions to AD pathogenesis.

ApoA-I is the second most abundant lipoprotein after ApoE in the cerebrospinal fluid (CSF) (Roheim et al., 1979; Koch et al., 2017), yet ApoA-I mRNA has not been detected in brain, at least in the murine models (Elliott et al., 2010). While ApoE is synthesized both in the brain and in the periphery, ApoA-I is produced primarily by the liver and intestine. Hence, the CNS pool of ApoA-I is thought to be delivered from the periphery through the blood-CSF barrier (BCSFB) and/or the blood-brain barrier (BBB). Both barriers show exquisite selectivity in their permeability, and together represent the two major portals regulating flux of macromolecules between blood and brain (Strazielle and Ghersi-Egea, 2013). The BCSFB is lined by the choroid epithelium at the four ventricles, whereas the BBB is lined by the diffuse network of brain microvessels that comprise the cerebrovascular endothelium. Stukas et al. (2014) have previously demonstrated the localization of Alexa Fluor 647-labeled recombinant ApoA-I (AF647-rApoA-I) at the choroid plexus following intravenous injection in mice, thereby concluding preferential ApoA-I brain entry via the BCSFB. The investigators however noted that contribution of the BBB in ApoA-I brain delivery remains unresolved. Due to the emerging role of ApoA-I in protecting the cerebral vasculature from Aβ deposition, there is a need to clarify the relevance of the BBB as a portal for ApoA-I brain delivery.

2.3. Materials & Methods

2.3.1. Animals. Wild-type (WT) Sprague-Dawley male rats, 16-week-old, were obtained from Harlan Sprague-Dawley (Indianapolis, IN) and maintained in the animal facility at

Mayo Clinic. The animals were provided with food and water ad libitum. All procedures involving animals were carried out in accordance with the Guide for the Care and Use of Laboratory Animals outlined by the National Institute of Health and were approved by the Mayo Institutional Animal Care and Use Committee.

2.3.2. Radioiodination of ApoA-I. Human serum derived ApoA-I (EMD Millipore; Burlington, MA) was labeled with ^{125}I or ^{131}I radionuclides (PerkinElmer Life and Analytical Sciences; Boston, MA) using the chloramine-T procedure described previously (Poduslo et al., 1994; Kandimalla et al., 2005). After dialysis in 0.01 M Dulbecco's phosphate buffered saline (DPBS) to remove unconjugated radionuclide, the intact radiolabeled peptides (^{125}I-ApoA-I and ^{131}I-ApoA-I) were assayed by trichloroacetic acid (TCA) precipitation.

2.3.3. Blood-to-brain permeability of ^{125}I-ApoA-I. Each rat was anesthetized with 1.5% isoflurane in 4 L/min oxygen. The femoral vein and artery were catheterized. An intravenous (IV) bolus injection of ^{125}I-ApoA-I (50 µCi) was administered to the femoral vein at t= 0 min, and a 20 µL blood sample was collected from the femoral artery at 0.25, 1, 5, 10, 15, 30, 45, and 59 min post-injection. To measure the residual plasma volume (V_p), an IV bolus injection of ^{131}I-ApoA-I (50 µCi) was administered at t= 59 min. A final blood sample was collected at t= 60 min, and the animal was euthanized. Blood samples were diluted to 100 µL in saline and centrifuged. The supernatant was TCA precipitated and analyzed for intact ^{125}I-ApoA-I and ^{131}I-ApoA-I using a two-channel gamma counter (Cobra II; Amersham Biosciences Inc.; Piscataway, NJ). Activity counts were corrected for background and spillover between ^{125}I and ^{131}I channels. The brain

was removed at the end of the experiment, dissected into anatomical regions (cortex, caudate putamen, hippocampus, thalamus, brain stem, and cerebellum), then assayed for ^{125}I and ^{131}I activity. The entire experimental procedure is outlined in Fig. 2.1.

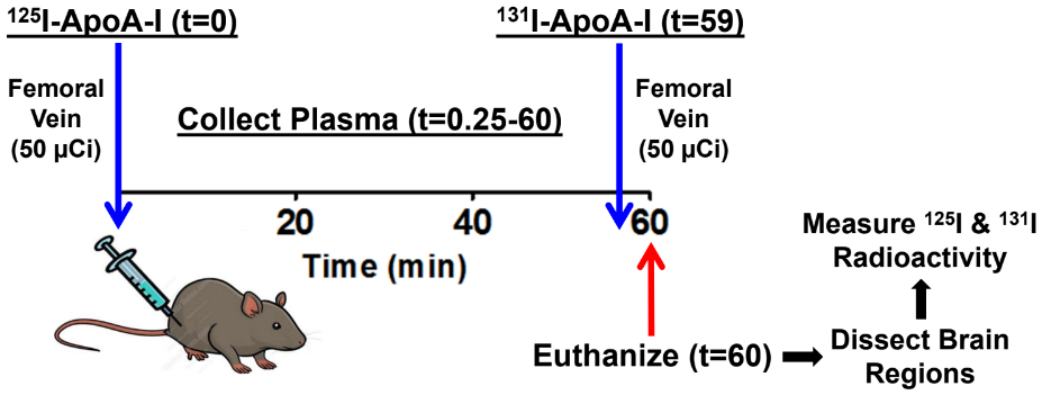

Figure 2.1. Layout of experiments to assess the plasma pharmacokinetics and brain permeability of ^{125}I-ApoA-I after a single IV dose in rats

2.3.4. Cell culture. The immortalized human cerebral microvascular endothelial cell line (hCMEC/D3) was a gift from P-O Couraud (Institut Cochin, France). The cells were cultured as described previously (Weksler et al., 2013) in endothelial basal medium-2 (EBM-2) (Lonza; Basel, Switzerland) prepared with the following additives: 1 % v/v penicillin-streptomycin (Sigma-Aldrich; St. Louis, MO), 1.4 µM hydrocortisone (Sigma-Aldrich; St. Louis, MO), 5 µg/mL ascorbic acid (Sigma-Aldrich; St. Louis, MO), 1 % v/v chemically defined lipid concentrate (ThermoFisher Scientific; Waltham, MA), 10 mM HEPES (Sigma-Aldrich; St. Louis, MO), and 1 ng/mL recombinant human fibroblast growth factor-basic (FGF) (PeproTech; Rocky Hill, NJ). The medium supplemented with these additives is hereinafter referred to as D3 medium. Cells were cultured in D3

medium containing 5 % v/v fetal bovine serum (FBS) (Atlanta Biologicals; Flowery Branch, GA).

2.3.5. Conjugation of ApoA-I with Alexa Fluor 647. Human serum derived ApoA-I was buffer exchanged into DPBS using an ultrafiltration unit with 10 kDa molecular weight cutoff (EMD Millipore; Burlington, MA). Alexa Fluor 647 (AF647) was conjugated to ApoA-I using the labeling kit with minor deviations from the manufacturer's protocol (Invitrogen; Carlsbad, CA). Briefly, 1 M sodium bicarbonate solution in distilled water was added to 2 mg/mL ApoA-I solution to increase the pH to ~8, reactive dye was added to the protein solution, and stirred at room temperature for 1 h. Then, fluorescently labeled ApoA-I was separated from the unconjugated dye using a dye removal column (ThermoFisher Scientific; Waltham, MA), and the concentration of labeled protein was determined as follows:

$$\text{Protein concentration (M)} = \frac{[\text{A}_{280} - (\text{A}_{600} \times 0.03)] \times \text{dilution factor}}{37410\ \text{M}^{-1}\text{cm}^{-1}}$$

where A_{280} is the absorbance of ApoA-I solution at 280 nm, A_{600} is the absorbance at 600 nm, 0.03 is a correction factor for dye absorption at 280 nm, and 37,410 M^{-1} cm^{-1} is the molar extinction coefficient of ApoA-I. Absorbance was measured using quartz cuvettes in a UV/Vis spectrophotometer (BioPhotometer 6131; Eppendorf; Hamburg, Germany), and the degree of labeling was determined as follows:

$$\text{Protein concentration (M)} = \frac{[\text{A}_{280} - (\text{A}_{600} \times 0.03)] \times \text{dilution factor}}{37410\ \text{M}^{-1}\text{cm}^{-1}}$$

where A_{280} is the absorbance of ApoA-I solution at 280 nm wavelength, A_{600} is the absorbance at 600 nm, 0.03 is a correction factor for dye absorption at 280 nm, and

37,410 M^{-1} cm^{-1} is the molar extinction coefficient of ApoA-I. Absorbance was measured using quartz cuvettes in a UV/Vis spectrophotometer (BioPhotometer 6131; Eppendorf; Hamburg, Germany), and the degree of labeling was determined as follows:

$$\text{Moles of dye per mole of protein} = \frac{A_{600} \times \text{dilution factor}}{239000\ M^{-1}cm^{-1} \times \text{protein concentration (M)}}$$

where 239,000 M^{-1} cm^{-1} is the molar absorptivity of AF647 dye.

2.3.6. Flow cytometry. The hCMEC/D3 cells were cultured in 6-well plates as described previously (Swaminathan et al., 2018a). Upon reaching confluency, cells were incubated for 1 h at 37 ^{o}C with 1 mL of D3 medium containing 1 % v/v FBS with or without 10 mM methyl-β-cyclodextrin (MβCD) (Acros Organics; Morris Plains, NJ) or 50 µM nystatin (Sigma-Aldrich; St. Louis, MO). The AF647-ApoA-I (0.4 µM) was added to the wells, and the plate was gently rocked to ensure even dispersion of the labeled protein. Following 1 h incubation at 37 ^{o}C, the cells were washed twice with DPBS, trypsinized, and resuspended in 250 µL of DPBS. A 250 µL aliquot of ice-cold 4 % v/v paraformaldehyde (PFA) was then added, and the cells were fixed on ice for 15 min. The fluorescence uptake was measured using a LSR-II Fortessa™ flow cytometer equipped with a 40 mW (640 nm) laser (BD Biosciences; San Jose, CA) and analyzed using FlowJo software (TreeStar Inc.; San Carlos, CA).

2.3.7. Confocal microscopy. The hCMEC/D3 cells were cultured on 35 mm coverslip bottom dishes as described previously (Swaminathan et al., 2018a). Upon reaching confluency, the cell monolayers were preincubated for 1 h at 37 ^{o}C in 500 µL of DMEM (0.1 % w/v BSA) with or without 10 mM MβCD. Then, AF647-ApoA-I (0.4 µM) was

added to the dish upon gentle rocking. After 1 h incubation at 37 ^{o}C, the cells were washed three times with DPBS and fixed in 1 mL of ice-cold 4 % v/v PFA on ice for 1 h. The fixed cells were washed three times with DPBS, mounted with ProLong™ Diamond Mounting medium containing DAPI (Invitrogen; Carlsbad, CA), and then imaged using a Zeiss LSM 780 laser confocal microscope equipped with a C-Apochromat 40X/1.2W objective.

For siRNA knockdown studies, hCMEC/D3 cells were grown to confluency on 35 mm coverslip bottom dishes and transfected with clathrin heavy chain siRNA (Dharmacon; Lafayette, CO), vehicle alone, or siGLO red transfection indicator (Dharmacon; Lafayette, CO) using a Lipofectamine RNAiMAX transfection kit (Invitrogen; 13778030). Following 48 h incubation at 37 ^{o}C with D3 medium, the transfected cells were incubated with 0.4 μM AF647-ApoA-I in 500 μL of DMEM containing 0.1 % w/v BSA for 30 min at 37 ^{o}C. Then, 20 μg of human serum transferrin (TRF) labeled with fluorescein isothiocyanate (FITC) (Invitrogen; Carlsbad, CA; T2871) was added to the dish, and the cell monolayer was incubated for an additional 30 min at 37 ^{o}C. The cells were washed, fixed, mounted, and imaged as described above. From the confocal micrographs, the intracellular fluorescence intensities of 25 cells for each treatment group (n=4) were quantified using ImageJ software. To verify siRNA knockdown of clathrin heavy chain, hCMEC/D3 cells were cultured on 6 well plates (Corning; Corning, NY) and transfected with clathrin heavy chain siRNA or vehicle alone. After 48 h, whole cell lysates were obtained and later assessed by western blot.

2.3.8. Transcytosis studies. The hCMEC/D3 cells were cultured on 12 mm Transwell® filters with 0.4 µm pores (Corning; Corning, NY) as described previously (Swaminathan et al., 2018a). Upon reaching confluency, the polarized monolayer of hCMEC/D3 cells was incubated with 0.4 µM AF647-ApoA-I in 500 µL of D3 media containing 1 % v/v FBS in the donor (luminal) compartment for 1 h at 37 ºC. The monolayer was washed with DPBS and fixed in ice-cold 4 % v/v PFA for 1 h. The fixed cells were washed with DPBS and mounted as described above.

Alternately, hCMEC/D3 cells were cultured on 24 mm Transwell® filters with 0.4 µm pores. Upon reaching confluency, the cells were treated with AF647-ApoA-I as described above. At the end of the experiment, whole cell lysates were obtained and the solution in the receiver (abluminal) compartment was collected for subsequent detection of ApoA-I by western blot.

2.3.9. Western blot. Total protein levels in the whole cell lysates were quantified by bicinchoninic acid (BCA) assay using a commercial kit (Pierce; Waltham, MA). Equal protein quantities of each lysate were loaded onto a 4-12 % Criterion™ XT precast gel (Bio-Rad; Hercules, CA). To detect ApoA-I protein in the abluminal solution obtained from the transcytosis studies, equal volumes of the abluminal solution collected at the end of the experiment were loaded onto the gel. The protein bands were electrotransferred onto a nitrocellulose membrane (Bio-Rad; Hercules, CA). The blot was blocked for 1.25 h with 5 % nonfat milk in Tris-buffered saline containing 0.1 % Tween 20 (TBST), followed by overnight incubation at 4 ºC with the appropriate primary antibody solutions: glyceraldehyde 3-phosphate dehydrogenase (GAPDH) (1:1000,

D16H11, Cell Signaling Technology; Danvers, MA), clathrin heavy chain (1:1000, D3C6, Cell Signaling Technology; Danvers, MA), or ApoA-I (1:1000, 5F4, Cell Signaling Technology; Danvers, MA). The next day, the blot was washed 4 times with TBST and then incubated for 1.25 h with the appropriate anti-rabbit or anti-mouse horseradish peroxidase (HRP)-conjugated secondary antibody (1:5000, Cell Signaling Technology; Danvers, MA). After washing 4 times with TBST, the blot was incubated with SuperSignal™ West Dura Extended Duration Substrate (ThermoFisher Scientific; Waltham, MA) and then analyzed by autoradiography using a CanoScan LiDE 110 film developer (Canon; Tokyo, Japan). The signal intensities of the protein bands were quantified by densitometry using ImageJ software.

2.3.10. Data analysis. The plasma concentration of ^{125}I-ApoA-I from 0-59 min post-injection was plotted as a function of time. To serve as a reference for comparison of ApoA-I plasma kinetics reported previously, data points were extracted from the study in which an IV bolus of Alexa Fluor™ 647-labeled recombinant ApoA-I (AF647-rApoA-I) was administered to plasma in mice (Stukas et al., 2014a). Based on the bi-exponential plasma concentration vs. time profile of AF647-rApoA-I reported in that study, plasma concentration values from 0-3 h corresponding to the initial phase were compared to those obtained for ^{125}I-ApoA-I from 0-59 min in the present study.

The residual plasma volume (V_p) and permeability-surface area (PS) product for radioiodinated ApoA-I in each brain region were determined using methods described previously (Poduslo and Curran, 1992). The V_p (µL/g) of each brain region was determined as follows:

$$V_p = \frac{q_p \times 10^3}{C_v \times W}$$

where q_p is the ^{131}I-ApoA-I activity (cpm) in the brain region, C_v is the concentration of ^{131}I-ApoA-I (cpm/mL) in the plasma at 60 min, and W is the weight (g) of the brain region.

Given the total ^{125}I-ApoA-I activity in each brain region (q_T) (cpm), the ^{125}I-ApoA-I activity in the extravascular space (q) (cpm/g) was determined as follows:

$$q = \frac{q_T}{W} - \frac{V_p C_a}{10^3}$$

where C_a is the concentration of ^{125}I-ApoA-I (cpm/mL) at t = 60 min, corrected for spillover between ^{125}I and ^{131}I channels.

The PS value (mL/g/s) for ^{125}I-ApoA-I at each brain region was determined as follows:

$$PS = \frac{q}{\int_0^t C_p dt}$$

where t is the observation time (s), q is the extravascular amount of ^{125}I-ApoA-I (cpm/g) in the brain region at time t, and $\int_0^t C_p dt$ is the ^{125}I-ApoA-I plasma area under the curve (AUC) for the time interval, 0-59 min. The plasma AUC (min x cpm/mL) of ^{125}I-ApoA-I was calculated using the logarithmic trapezoidal method. The overall PS value for ^{125}I-ApoA-I in rat brain was determined based on the total extravascular ^{125}I-ApoA-I activity in all six brain regions and was calculated in similar fashion. For comparison, the PS value for AF647-rApoA-I in mouse brain was determined using data extracted from the study by Stukas et al. (2014a) and was calculated by dividing the reported AF647-

rApoA-I amount in brain at 1 h (ng/mg) by the plasma AUC from 0-1 h (h x µg/mL) determined using the logarithmic trapezoidal method.

2.3.11. Statistical analysis. All statistical tests were conducted using GraphPad Prism (GraphPad software; La Jolla, CA). The significance of differences observed in the slopes of the plasma concentration vs. time curves for ^{125}I-ApoA-I and AF647-rApoA-I was evaluated by F-test. The significance of differences in the PS and V_p values determined for ^{125}I-ApoA-I in different brain regions was evaluated by one-way ANOVA followed by Bonferroni post-tests. The significance of differences in the median fluorescence uptake of cells treated with/without MβCD or nystatin was evaluated by one-way ANOVA followed by Bonferroni post-tests. The significance of differences in the mean fluorescence uptake of individual cells transfected with/without clathrin siRNA was evaluated by student's t-test. The significance of differences in clathrin heavy chain expression of cells transfected with/without clathrin siRNA was evaluated by student's *t*-test.

2.4. Results

2.4.1. Overview. In this study, ^{125}I-ApoA-I permeability at various brain regions was used to identify the distribution patterns indicative of transport across the BBB and/or the BCSFB. In addition, the mechanism of AF647-ApoA-I endocytosis in human cerebral microvascular endothelial cell (hCMEC/D3) monolayers was examined to support the distribution analysis.

2.4.2. Plasma pharmacokinetics of ^{125}I-ApoA-I. Following IV bolus injection, the plasma concentration of ^{125}I-ApoA-I in adult rats declined in a log-linear fashion over the first 60 min (Fig. 2.2). The plasma pharmacokinetic parameters of ^{125}I-ApoA-I were calculated by fitting the log-concentration vs. time profile to a mono-exponential equation. The rate constant for ^{125}I-ApoA-I decline in plasma was determined to be 0.0043 ± 0.0004 min^{-1} (n= 6). Notably, this rate was not significantly different from the initial rate of AF647-rApoA-I decline in the plasma of adult mice determined using the data reported by Stukas et al. (2014).

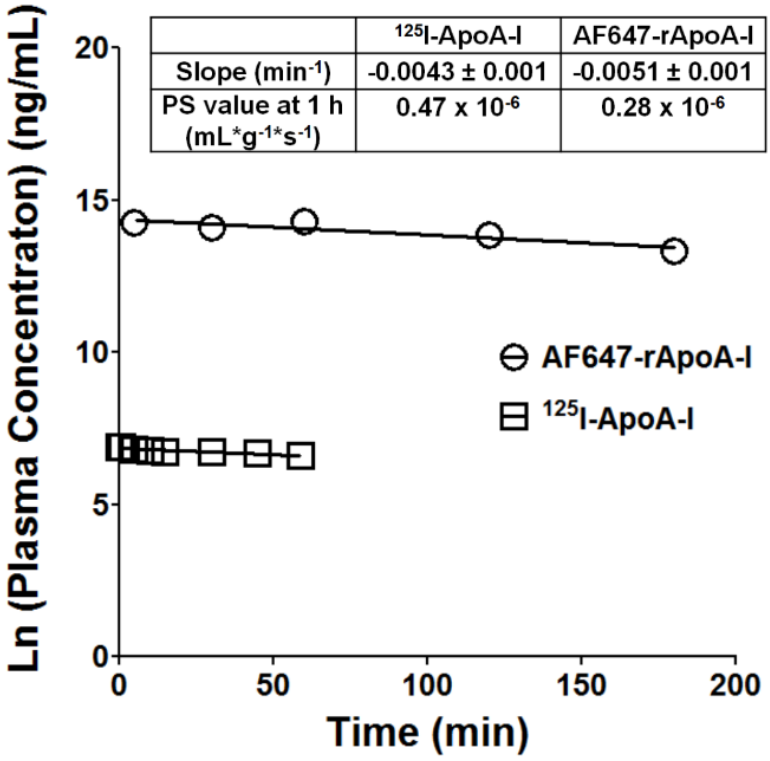

Figure 2.2. Comparison of plasma concentration vs. time profiles of ^{125}I-ApoA-I in rats (open squares) and Alexa Fluor™ 647-labeled recombinant ApoA-I (AF647-rApoA-I) in mice (open circles). Mouse data was extracted from a previous study by Stukas et al. (2014a) in which an IV bolus of AF647-rApoA-I (60 mg/kg) was injected via the tail vein (n= variable for each data point). Data points from the current study represent mean values (n=6 for rats). Based on the F-test, the slope values are not significantly different:

F(1,9)= 0.1544, P= 0.7035. Slope and PS values for ^{125}I-ApoA-I represent mean ± SD (n=6).

2.4.3. Brain permeability of ^{125}I-ApoA-I. Average permeability-surface area product (PS) and cerebrovascular volume (V_p) values for ^{125}I-ApoA-I in various brain regions such as cortex, caudate putamen, hippocampus, thalamus, brain stem, and cerebellum are shown in Table 2.1. The PS and V_p values of ^{125}I-ApoA-I in brain stem and cerebellum are significantly greater than those determined for other brain regions ($p < 0.05$). The periventricular brain regions, i.e. thalamus and hypothalamus, are anatomically adjacent to the choroid ventricles that form the BCSFB. Notably, the PS value of ^{125}I-ApoA-I in thalamus is not significantly different from that determined for cortex, caudate putamen, or hippocampus. The total PS value for ^{125}I-ApoA-I in all six brain regions was found to be 0.47 ± 0.11 (mL/g/s x 10^{-6}). This agrees with the PS value for AF647-rApoA-I in mouse brain (0.29 x 10^{-6} mL/g/s, Fig. 2.2 inset), determined using the data extracted from the study by Stukas et al. (2014).

Brain Region	PS (mL/g/s x 10^{-6})	V_p (µL/g)
Cortex	0.39 ± 0.08	6.93 ± 0.59
Caudate putamen	0.28 ± 0.07	6.49 ± 0.93
Hippocampus	0.28 ± 0.07	6.94 ± 0.84
Thalamus	0.36 ± 0.12	9.45 ± 1.27
Brain stem	0.69 ± 0.22	14.37 ± 2.50
Cerebellum	0.76 ± 0.21	17.18 ± 3.38

Table 2.1. Permeability-surface area (PS) product and cerebrovascular volume (V_p) of ^{125}I-ApoA-I in various regions of rat brain at 60 min. Data are mean ± SD (n=6). ^{131}I-ApoA-I was injected to serve as a measure of V_p. According to one-way ANOVA

followed by Bonferroni post tests, *PS* and V_p values for brain stem and cerebellum are significantly greater ($p < 0.05$) than that of other regions.

2.4.4. Transcytosis of AF647-ApoA-I across BBB cell monolayers. We conducted a battery of mechanistic assays to further verify ApoA-I trafficking at the BBB. The Z-stack composite confocal micrographs of polarized hCMEC/D3 endothelial cell monolayers incubated with AF647-ApoA-I on the luminal (blood) side demonstrated AF647-ApoA-I internalization (Fig. 2.3A). Upon closer examination, tracts of AF647-ApoA-I moving to the abluminal (brain) side of the endothelium were clearly evident (Fig. 2.3B). Moreover, following AF647-ApoA-I incubation on the luminal side, full-length ApoA-I was detected by western blot in both the cell lysate and abluminal solution, thus providing confirmation of its luminal-to-abluminal transcytosis (Fig. 2.3C-D).

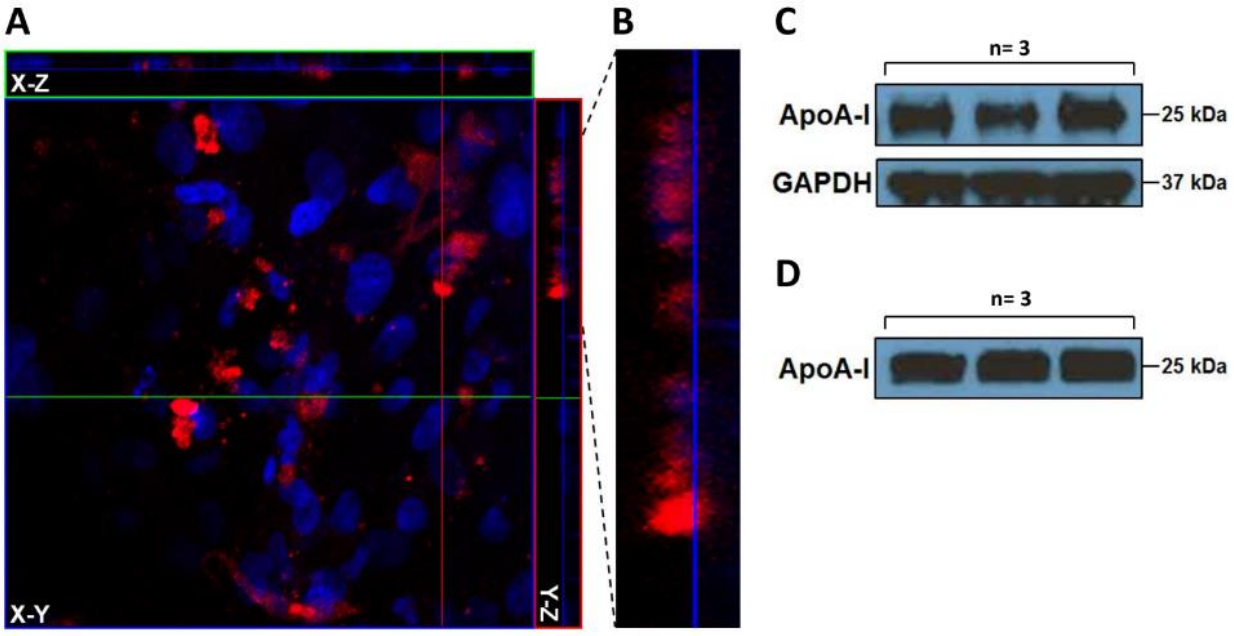

Figure 2.3. Transcytosis of AF647-ApoA-I across hCMEC/D3 monolayers cultured on 0.4 µm Transwell® filters. (A) The Z-stack composite image demonstrates internalization

of AF647-ApoA-I (0.4 μM) in polarized hCMEC/D3 monolayers after 1 h incubation on the luminal side. The image presented in X-Y (transversal), X-Z (vertical), and Y-Z (vertical) planes is a composite of 32 optical sections imaged with a 0.53 μm Z-step interval. Red= AF647-ApoA-I; blue= DAPI-stained nuclei. (B) Enlarged section of the Y-Z plane showing permeation of AF647-ApoA-I across the endothelium. (C) Western blot showing ApoA-I in hCMEC/D3 lysate after 1 h incubation on the luminal side. (D) Western blot showing ApoA-I on the abluminal side after 1 h incubation on the luminal side.

2.4.5. Mechanisms of AF647-ApoA-I endocytosis in BBB cell monolayers. Endocytosis is the predominant mechanism by which large proteins are internalized at the BBB endothelium (Xiao and Gan, 2013). Hence, we sought to investigate the mechanisms of AF647-ApoA-I endocytosis in hCMEC/D3 endothelial cells, using the approaches of small molecule inhibition and siRNA knockdown.

2.4.6. MβCD and nystatin reduce AF647-ApoA-I uptake in BBB cell monolayers. Uptake of AF647-ApoA-I by hCMEC/D3 monolayers with and without pretreatment with methyl-β-cyclodextrin (MβCD) or nystatin was investigated to evaluate the role of membrane cholesterol in AF647-ApoA-I endocytosis. MβCD is known to deplete membrane cholesterol, whereas nystatin is known to sequester membrane cholesterol. Both agents are widely used to investigate cholesterol-dependent endocytic pathways, often to study the involvement of lipid rafts (Zidovetzki and Levitan, 2007; Hussain et al., 2011). When evaluated by flow cytometry, AF647-ApoA-I uptake in hCMEC/D3 monolayers was significantly reduced following pretreatment with 10 mM MβCD or 50 μM nystatin ($p < 0.001$) (Fig. 2.4A-B). In addition, confocal micrographs of MβCD treated hCMEC/D3 cell monolayers demonstrated lower intracellular accumulation of AF647-ApoA-I and showed bright fluorescence on the plasma membrane (Fig. 2.4C).

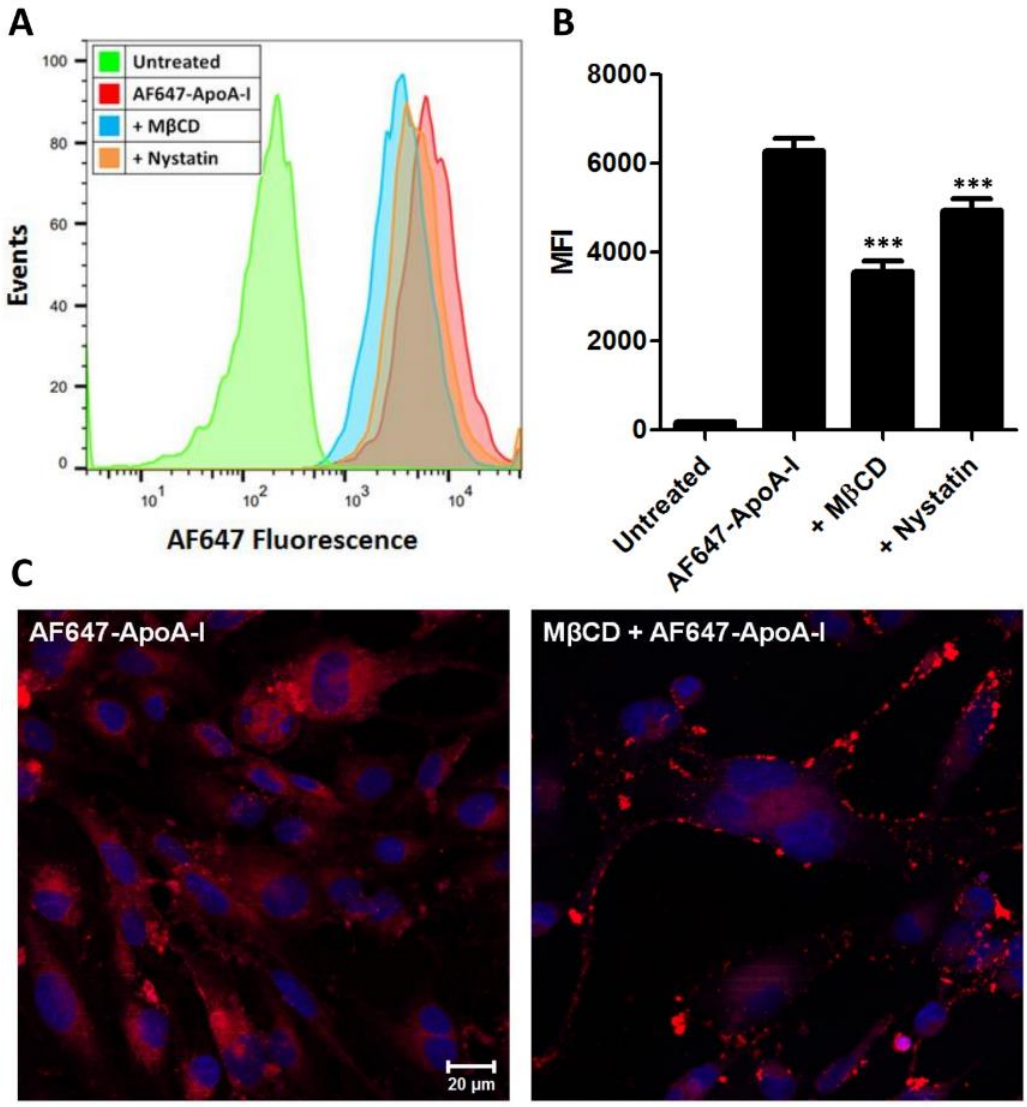

Figure 2.4. Disruption of membrane cholesterol with methyl-β-cyclodextrin (MβCD) or Nystatin reduces the uptake of Alexa Fluor™ 647-labeled ApoA-I (AF647-ApoA-I) in hCMEC/D3 monolayers. (A) Representative flow cytometry histograms showing a decrease in the fluorescence uptake of AF647-ApoA-I (0.4 µM) following 1 h pretreatment with MβCD (10 mM) or Nystatin (50 µM). (B) Evaluation by flow cytometry: fluorescence uptake of AF647-ApoA-I following pretreatment with MβCD or Nystatin represented as median fluorescence intensity (MFI) ± SD (n=3). One-way ANOVA followed by Bonferonni post tests showed a significant decrease in AF647-ApoA-I uptake in the MβCD or Nystatin pretreated cells compared to cells treated with AF647-ApoA-I alone (***$p < 0.001$). (C) Laser confocal micrographs of hCMEC/D3 monolayers pretreated with MβCD show reduced intracellular accumulation of AF647-ApoA-I (right) when compared to cells treated with AF647-ApoA-I alone (left). The images are

representative of 2 independent experiments. Red = AF647-ApoA-I; blue = DAPI-stained nuclei. Scale bar = 20 µm.

2.4.7. Clathrin knockdown has no effect on AF647-ApoA-I uptake in BBB cell monolayers. The siRNA knockdown of clathrin heavy chain is expected to reduce clathrin-mediated endocytosis of proteins. Transfection with siGLO red transfection indicator, a fluorescent oligonucleotide duplex, established the efficient transfection of siRNA in hCMEC/D3 monolayers (data not shown). Uptake of AF647-ApoA-I by clathrin siRNA transfected hCMEC/D3 monolayers was not notably altered (Fig. 2.5A-B). However, uptake of FITC-TRF was reduced in clathrin siRNA transfected monolayers, whereas the cells transfected with vehicle alone displayed punctate intracellular localization of FITC-TRF, possibly in the endosomes (Fig. 2.5A-B). TRF is predominantly internalized at clathrin-coated pits and may thereby serve as a marker to investigate clathrin-mediated endocytosis (Boucrot et al., 2006; McMahon and Boucrot, 2011; Mayle et al., 2012). Quantification of the confocal micrographs revealed that intracellular fluorescence of FITC-TRF decreased significantly, but no change in AF647-ApoA-I fluorescence was observed in siRNA transfected cells compared to cells transfected with vehicle alone ($p < 0.001$) (Fig. 2.5C). The decrease in expression of clathrin heavy chain following siRNA transfection was verified by western blots (Fig. 2.5D-E).

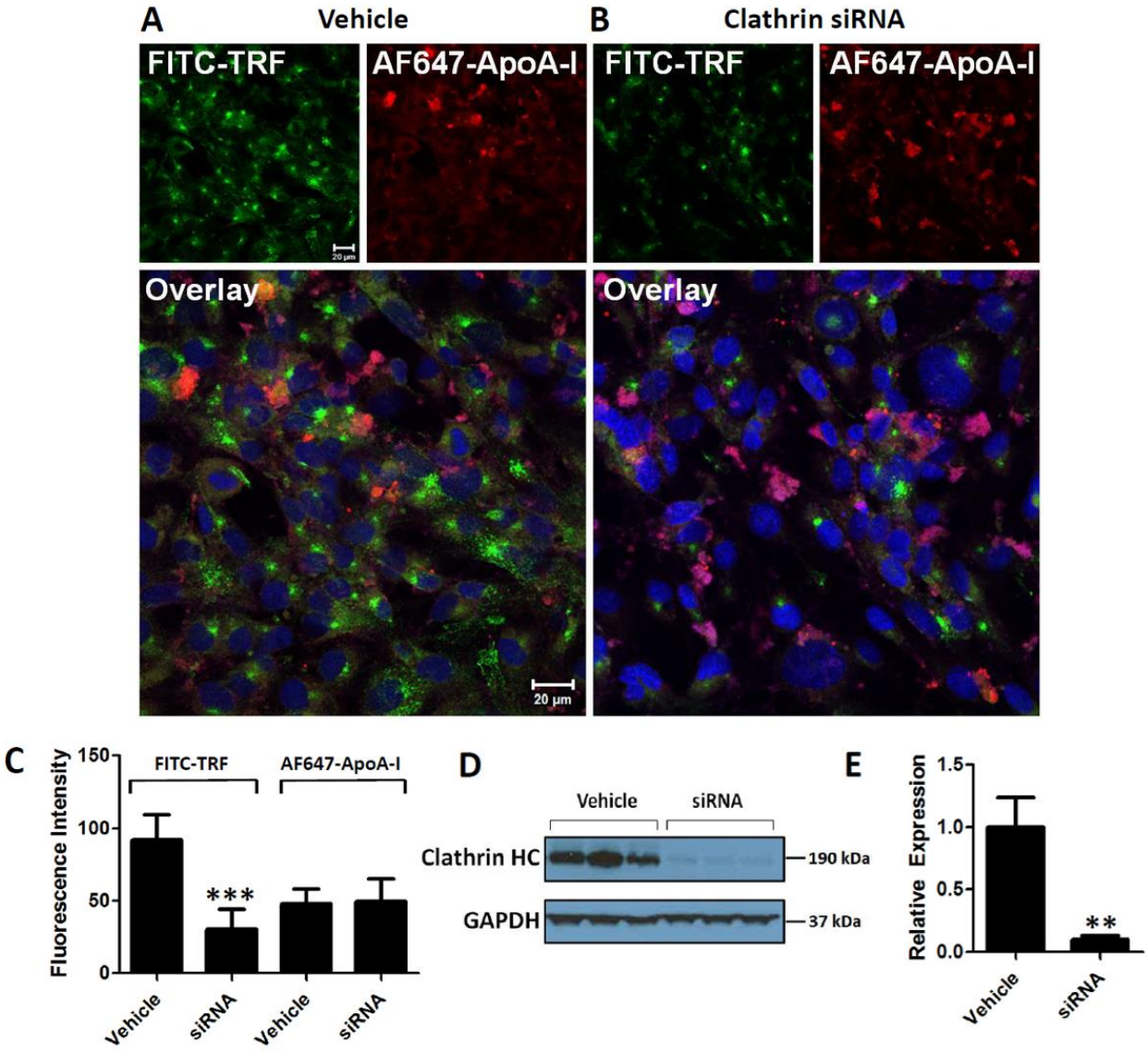

Figure 2.5. siRNA knockdown of clathrin heavy chain has little effect on AF647-ApoA-I uptake in hCMEC/D3 monolayers. (A) Laser confocal micrographs of hCMEC/D3 transfected with vehicle alone show punctate localization of fluorescein isothiocyanate-labeled transferrin (FITC-TRF), most likely in the endosomes. The images are representative of two independent experiments. (B) The hCMEC/D3 monolayers transfected with clathrin siRNA show greatly reduced uptake of FITC-TRF with little change in intracellular accumulation of AF647-ApoA-I (0.4 μM). All images were processed similarly and obtained using the same instrument settings. Green = FITC-TRF; red = AF647-ApoA-I; blue = DAPI-stained nuclei. Scale bar = 20 μm. (C) Intracellular fluorescence intensities from 25 cells were quantified using ImageJ software and presented as mean ± SD (n=4). Student's t-test showed a significant

decrease in FITC-TRF uptake with no change in AF647-ApoA-I uptake in the siRNA transfected cells compared to cells transfected with vehicle alone ($p < 0.001$). (D) western blot showing the decrease in expression of clathrin heavy chain (HC) in hCMEC/D3 following siRNA transfection. (E) Semiquantitative analysis by densitometry showing the decrease in clathrin HC expression in the siRNA transfected cells. Values are normalized to vehicle and presented as mean ± SD (n=3). Student's t-test showed a significant decrease in clathrin HC expression for the siRNA transfected cells (**$p < 0.01$).

2.5. Discussion and Conclusions

ApoA-I in the brain is expected to originate from the systemic circulation and therefore must undergo transport at the BSCFB and/or the BBB. Upon IV bolus injection, AF647-rApoA-I fluorescence signal primarily localized at the choroid plexus, which led investigators to conclude that BCSFB is the main portal for ApoA-I entry into brain from systemic circulation (Stukas et al., 2014a). Based solely on this observation, uptake of ApoA-I via the BBB endothelium, which is a major portal for protein delivery to brain (Brasnjevic et al., 2009), cannot be ruled out. Moreover, due to the emerging role of ApoA-I in reducing Aβ deposition in the cerebral vasculature (CAA), clarifying the interaction and transcytosis of ApoA-I at the BBB is important for understanding the cerebrovascular contributions to AD pathogenesis.

To this end, we determined the permeability-surface area (PS) product of ^{125}I-ApoA-I in various brain regions following a femoral vein IV bolus injection in wild-type rats. The PS value is known to reflect permeability and thereby can be used to assess the relative contributions of the BBB and BCSFB in ApoA-I transport, based on the permeability differences observed at different brain regions (Smith and Rapoport, 1986). The total PS value of ^{125}I-ApoA-I in entire rat brain coincided with the PS value of

AF647-rApoA-I in mice, determined from the data published by Stukas et al. (2014a). The lack of dependence on label and animal species may suggest broader applicability. Moreover, the plasma pharmacokinetics of ^{125}I-ApoA-I in the initial phase closely matched with that of AF647-rApoA-I. This agreement suggests that broader conclusions related to ApoA-I disposition in plasma and brain could be drawn by employing the data from both studies.

PS values of ^{125}I-ApoA-I were found to vary with the brain region. Notably, PS values in brain stem and cerebellum were significantly higher compared to other regions. While the physiological relevance of these differences is not immediately apparent, it is important to stress that the PS value in thalamus, which is anatomically adjacent to the ventricles, is not significantly higher compared to other brain regions. Inorganic ions such as ^{36}Cl are predominantly transported into brain via the BCSFB, and have been reported to display preferential accumulation in thalamus (Smith and Rapoport, 1986). The moderate PS observed for ^{125}I-ApoA-I in thalamus relative to other regions suggests that ApoA-I transport at the BCSFB accounts for only a portion of total ApoA-I brain delivery, and therefore contribution of the BBB cannot be ignored. Moreover, the PS values observed for all brain regions are consistent with substantial ^{125}I-ApoA-I transport across the entire diffuse network of cerebral microvessels that are lined by the BBB. As acknowledged by the authors in the previous study, their fluorescence-based approach may have lacked the sensitivity to capture the diffuse signal from AF647-rApoA-I in the cerebral vasculature. Use of ^{125}I-ApoA-I, which could be detected with greater sensitivity than AF647-rApoA-I, enabled detection of low levels

of ^{125}I-ApoA-I uptake at different brain regions, without requiring substantial processing of the brain tissue.

Protein delivery to brain is predominantly receptor mediated, as the barrier properties of the BBB endothelium and choroid epithelium greatly restrict diffusional and paracellular transport of macromolecules into the brain. Albumin and insulin are two endogenous proteins that are believed to exhibit receptor mediated endocytosis at the BBB via gp60 and insulin receptors, respectively. However, Poduslo et. al (2001) have shown that the PS value of ^{125}I-albumin in rat brain regions (0.7 to 1.3 mL/g/s x 10^{-6}) is very low compared to that of ^{125}I-insulin, which was determined to be between 14.0 and 20 mL/g/s x 10^{-6}. The PS values of ^{125}I-ApoA-I in various brain regions, determined by similar approach, were found to be between 0.28 and 0.76 mL/g/s x 10^{-6}, which are similar to that of ^{125}I-albumin.

Previous studies have shown that luminal-to-abluminal transport of ApoA-I/HDL is saturable in porcine brain capillary endothelial cell (pBCEC) monolayers (Balazs et al., 2004). The lower PS values of ^{125}I-ApoA-I could be due to receptor saturation by substantially higher ApoA-I plasma levels (~7 mg/dL) (Schonfeld et al., 1976). Despite low overall brain PS values, ApoA-I displays a very long plasma elimination half-life, which was reported to be 10.9 h in mice (Stukas et al., 2014a). For comparison, the half-life of insulin was found to be around 10 min in mice (Cresto et al., 1977). Although the PS values of ^{125}I-ApoA-I are ~30 fold lower than ^{125}I-insulin, the plasma residence time of ^{125}I-ApoA-I is ~60 fold longer than that of ^{125}I-insulin, which may make the overall brain uptake after a single dose injected in plasma similar for both proteins.

Using laser confocal microscopy, we showed that AF647-ApoA-I endocytosis in polarized hCMEC/D3 monolayers is cholesterol-dependent. In addition, the Z-stack composite image of the internalized AF647-ApoA-I displayed a typical transcytosis pattern comparable to several other proteins we have studied previously that have well-characterized transport mechanisms at the BBB (Agyare et al., 2013; Swaminathan et al., 2018a). By western blot, we also showed that intact ApoA-I is transcytosed across the endothelial cell monolayer to the abluminal side. Two previous studies have also demonstrated the luminal-to-abluminal transcytosis of ApoA-I or HDL across in-vitro BBB models (Balazs et al., 2004; Merino-Zamorano et al., 2016). A recent study has shown the involvement of scavenger receptor class B type 1 (SR-B1) in the internalization of HDL in brain microvascular endothelial cells, which was found to be independent of both caveolin and clathrin (Fung et al., 2017). The investigators found that the internalized HDL co-localized with SR-B1, and that SR-B1 knockdown significantly reduced HDL uptake. Given that ApoA-I is the major protein component of plasma HDL, these findings suggest that SR-B1 at the BBB is responsible for ApoA-I endocytosis on the luminal side. The investigators also observed a decrease in HDL uptake following treatment with nystatin, a known membrane cholesterol disrupter. Moreover, SR-B1 is well-established as the HDL receptor mediating uptake in liver to facilitate reverse cholesterol transport (Ganesan et al., 2016). These reports are consistent with the current findings that demonstrated reduction in AF647-ApoA1 uptake following nystatin or MβCD treatment. Based on the published reports and observations made in the present study, we speculate that ApoA-I endocytosis is mediated by SR-B1

localized in non-caveolae lipid raft microdomains present on the luminal surface of the BBB.

Given the observed accumulation of AF647-ApoA1 in BBB endothelial cell monolayers, some portion of peripherally derived ApoA-I/HDL may exert its protective effect on the cerebral vasculature by accumulating in the BBB endothelium itself. Previous studies conducted to evaluate the role of ApoA-I overexpression/deletion on brain amyloid accumulation have shown that ApoA-I reduces cerebrovascular amyloid deposition with modest impact on parenchymal amyloid burden. A recent study has demonstrated the ability of luminal ApoA-I to increase Aβ efflux across BBB endothelial cells from the abluminal side (Merino-Zamorano et al., 2016), suggesting that ApoA-I present in serum could influence brain clearance of Aβ in vivo. It is also possible that ApoA-I in the brain and plasma play differential roles in preserving cerebrovascular integrity and function.

In conclusion, the findings from this chapter indicate that ApoA-I with ^{125}I or AF647 label are taken up at the BBB endothelium. The internalized ApoA-I could be utilized for endothelial-specific actions, and/or may be transcytosed into brain parenchyma to elicit physiological functions. While this study does not refute the brain delivery of ApoA-I via the BCSFB, it provides evidence to support the role of BBB in delivering ApoA-I to brain parenchyma and stresses the need for further studies to resolve the mechanisms of cerebrovascular versus parenchymal actions of ApoA-I and its functional impact on the pathogenic processes of CAA and AD.

Chapter 3: Effects of normal aging on Aβ peptide and insulin trafficking at the BBB

3.1. Synopsis

Age is the most common risk factor for Alzheimer's disease (AD), a neurodegenerative disorder characterized by the pathological hallmarks of toxic Aβ plaques and hyperphosphorylated tau tangles. Moreover, sub-physiological brain insulin levels, which are likely due to impaired insulin transport from blood-to-brain, has emerged as one of the pathological manifestations of AD. The aim of this chapter is to identify age-related changes in the plasma disposition and BBB trafficking of Aβ peptides and insulin. Upon systemic injection of ^{125}I-Aβ40, ^{125}I-Aβ42, or ^{125}I-insulin, plasma pharmacokinetics and brain influx were assessed in wild-type (WT) or AD transgenic (APP/PS1) mice at various ages. Additionally, publicly available single-cell RNA-Seq data [GSE129788] was employed to investigate pathways regulating BBB transport in WT mice at various ages. Brain influx of ^{125}I-Aβ40, estimated as the permeability-surface area (PS) product, decreased with age, accompanied by an increase in plasma AUC. In contrast, the brain influx of ^{125}I-Aβ42 increased with age, accompanied by a decrease in plasma AUC. The age-dependent changes in ^{125}I-Aβ trafficking in WT mice were accelerated in APP/PS1 mice. As seen with ^{125}I-Aβ40, the brain influx of ^{125}I-insulin decreased with age in WT mice, accompanied by an increase in plasma AUC. This finding was further supported by dynamic single-photon emission computed tomography (SPECT/CT) imaging studies. RAGE and PI3K/AKT signaling pathways at the BBB, which are implicated in Aβ and insulin transcytosis, respectively, were upregulated with age in WT mice, indicating BBB insulin resistance. Thus, normal

aging differentially affects plasma pharmacokinetics and brain influx of Aβ isoforms and insulin in such a manner that augments AD risk.

3.2. Background

The blood-brain barrier (BBB) is responsible for maintaining dynamic equilibria between endogenous solute levels in the blood and the brain. The BBB endothelium serves dual functions, acting as both a gatekeeper to restrict the uptake of toxic substances circulating in the blood, and as a trafficking portal to mediate the highly selective delivery of essential nutrients to the brain. Additionally, the BBB plays a crucial role in clearing metabolic waste products from the brain. Disruptions to these spatially coordinated trafficking events have been implicated in the etiology of several neurodegenerative disorders, including sporadic Alzheimer's disease (AD). Progression of physiological age is widely recognized as the greatest risk factor for AD (Gao et al., 1998). While normal aging is associated with gradual loss of BBB function (Montagne et al., 2015) and appearance of neuropathological changes, these are accelerated in AD brain and trigger catastrophic neurocognitive changes (Popescu et al., 2009).

One major consequence of age-related BBB dysfunction in AD brain is the increased accumulation of amyloid-β (Aβ) peptides in the cerebral vasculature as amyloid deposits and in the brain parenchyma as senile plaques (Rodrigue et al., 2009). Of the two major Aβ isoforms that predominate in AD brain, Aβ40 is the major isoform present in cerebrovascular amyloid deposits, whereas Aβ42 is the major isoform present in parenchymal plaques. Notably, Aβ42 is more neurotoxic and amyloidogenic than Aβ40 (Qiu et al., 2015). Interestingly, Aβ40 is also suggested to be protective

against Aβ42-induced neurotoxicity (Kim et al., 2007; Murray et al., 2009). However, changes in how the BBB handles each Aβ isoform during aging and AD remain unclear. Brain Aβ deposition precedes cognitive decline and continues to increase substantially over the course of AD progression. It has been estimated that 20-30% of all cognitively normal older adults display significant Aβ deposition in the brain (Rodrigue et al., 2009). It is well established that decreased Aβ clearance from the brain promotes Aβ accumulation and plaque formation during aging and AD (Yoon and Jo, 2012). In contrast, very little is known about how alterations in Aβ handling by the periphery contribute to brain Aβ deposition in AD. Although the Aβ concentrations in plasma are typically ~6 fold lower than the concentrations in the brain interstitial fluid (ISF), the absolute amount of Aβ in plasma is estimated to be ~10 fold greater than the amount of soluble Aβ in the brain (Deane et al., 2004). In aged nonhuman primates, it was shown that systemically injected Aβ efficiently crossed the BBB and became incorporated into existing parenchymal plaques (Mackic et al., 2002). Further, increased brain Aβ deposition in aged rats was associated with increased BBB expression of the receptor for advanced glycation end products (RAGE), which handles Aβ influx to the brain (Silverberg et al., 2010b). Elevated serum Aβ levels are also known to increase the risk of AD in elderly patients (Okereke et al., 2009). Therefore, it is likely that systemic Aβ can directly, by trafficking Aβ into the brain, or indirectly, by reducing the ability of BBB to clear brain Aβ, contribute to the brain's Aβ load.

BBB dysfunction in aging and AD also appears as a decreased influx of essential nutrients to the brain (Sartorius et al., 2015). Glucose and insulin are produced almost exclusively in peripheral tissues and must be delivered to the brain across the BBB.

Decreased insulin levels in the cerebrospinal fluid (CSF) are associated with progression of cognitive decline in early stage AD patients (Gil-Bea et al., 2010). In another study, insulin concentrations and insulin receptor (IR) density in postmortem brain decreased with age in subjects with or without AD (Frolich et al., 1998). We and others have demonstrated that Aβ peptide exposure interferes with the neurobiological functions mediated by insulin and IR (Xie et al., 2002; Zhao et al., 2008; Swaminathan et al., 2018b; Gali et al., 2019). Further, we reported that insulin modulates Aβ peptide transport at the BBB in mice, as well as the membrane expression of Aβ receptors (RAGE, LRP-1) in a BBB cell culture model (Swaminathan et al., 2018a). Thus, insulin and Aβ effects on the BBB are strongly interconnected, and disruptions in this relationship are expected to promote BBB dysfunction in AD.

To investigate the contributions of aging to BBB dysfunction, we examined the plasma distribution and brain influx kinetics of ^{125}I radiolabeled Aβ40, Aβ42, and insulin in female wild-type (WT) and/or AD transgenic (APP/PS1) mice at various ages. Using single-cell RNA-Seq data previously published by Ximerakis et al. (2019), we further assessed the activity of various transport/signaling pathways in brain endothelial cells obtained from WT mice at different ages. Our findings reveal a switch in BBB trafficking with age, accompanied by disruptions to transport/signaling pathways at the BBB. These changes are expected to contribute to pathological alterations in Aβ and insulin levels in the brain that are intricately linked with neuropathological changes observed in AD patients.

3.3. Materials & Methods

3.3.1. Preparation of Aβ peptides. Aβ40 and Aβ42 peptides were custom synthesized on a fluorenylmethyloxycarbonyl (FMOC) column by the Mayo Clinic proteomics core facility (Rochester, MN). Solutions of soluble Aβ were prepared using the procedure developed by Klein et al. (Klein et al., 2004). Briefly, solid Aβ was dissolved in ice cold hexafluoro-2-propanol (HFIP) (MP Biomedicals, Santa Ana, CA) and then incubated at room temperature for 1 hour. Solvent was evaporated overnight, then further dried under vacuum, and the resultant Aβ films were stored at -20°C prior to use. Before labeling with ^{125}I, the Aβ films were dissolved in DMSO, diluted in Ham's F-12 media (Mediatech, Manassas, VA), and centrifuged at 18,000 rpm to remove any insoluble Aβ aggregates.

3.3.2. Radioiodination of Aβ peptides and insulin. Carrier-free Na^{125}I and Na^{131}I radionuclides were obtained from PerkinElmer Life and Analytical Sciences (Boston, MA). The following peptides/proteins were labeled with ^{125}I or ^{131}I using the chloramine-T procedure as described previously (Poduslo et al., 1994; Kandimalla et al., 2005): Aβ40, Aβ42, bovine serum albumin (BSA) (Sigma-Aldrich, St. Louis, MO), and human insulin (Sigma-Aldrich). Free radioactive iodine was separated from the radiolabeled peptide/protein by dialysis against 0.01 M phosphate-buffered saline (PBS) at pH 7.4 (Sigma-Aldrich). Purity of the radiolabeled peptides/proteins was assessed by trichloroacetic acid (TCA) precipitation. The preparation was deemed acceptable if the precipitable radioactivity counts were greater than 95% of the total counts.

3.3.3. Animals. All studies were carried out in accordance with the Guide for Care and Use of Laboratory animals outlined by the National Institutes of Health, and the protocols were approved by the Animal Care and Use Committee at Mayo Clinic (Rochester, MN). Wild type (C57BL/6J) and AD transgenic (APP/PS1) mice were purchased from The Jackson Laboratory (Bar Harbor, ME). The APP/PS1 line consists of C57BL/6J genetic background with transgenes added for amyloid precursor protein (APP695swe) and presenilin 1 (PS1-dE9). APP/PS1 mice exhibit Aβ overexpression, accelerated brain Aβ deposition, and cognitive decline. Mice were housed in a virus-free barrier facility with 12-hour light and dark cycles and were provided with pellet food and purified water ad libitum. All studies were performed using female mice.

3.3.4. Plasma pharmacokinetics and brain permeability of ^{125}I-Aβ42 and ^{125}I-Aβ40. These experiments were carried out as described in our earlier publications (Kandimalla et al., 2005; Agyare et al., 2013). The age groups were selected based on our previous findings which demonstrated that in APP/PS1 mice, brain Aβ plaques were undetectable at 12 weeks of age, with initiation of plaque formation at 24 weeks, and full-scale plaque burden at 52 weeks (Jack et al., 2005). Briefly, wild-type (WT) or APP/PS1 transgenic mice at various ages (8, 24, or 52 weeks) weighing 25-35 g were catheterized at the femoral vein and femoral artery while under general anesthesia (1.5 % isoflurane; 4 L/min oxygen). A single dose (100 µCi) of ^{125}I-Aβ40 or ^{125}I-Aβ42 in PBS (100 µL) was bolus injected into the femoral vein. Blood was sampled serially (20 µL) from the femoral artery at 0.25, 1, 3, 5, 10, and 15 minutes post-injection. Immediately after the 15-minute sampling event, ^{131}I-BSA (100 µCi) was bolus injected into the

femoral vein to serve as a measure of the residual plasma volume (V_p). One minute after the ^{131}I-BSA injection, a final blood sample was collected, and the animal was euthanized. Blood samples were diluted in PBS and centrifuged to separate the plasma. The plasma was subjected to TCA precipitation and then centrifuged. Total ^{125}I and ^{131}I activity counts in the pellet, corresponding to intact radiolabeled peptide/protein, were assayed using a two-channel gamma counter (Cobra II; PerkinElmer Life and Analytical Sciences, Boston, MA).

^{125}I-Aβ40 and ^{125}I-Aβ42 plasma concentration vs. time data were fit to the following bi-exponential equation using Phoenix WinNonlin® 6.4 (Certara, St. Louis, MO):

$$C(t) = Ae^{-\alpha t} + Be^{-\beta t}$$

where C(t) is concentration (μCi/mL) in plasma at time t (min), A and B are the intercepts of the distribution and elimination phases, respectively, and α and β are the distribution and elimination macro-rate constants (min^{-1}), respectively. The secondary plasma pharmacokinetic parameters are reported in Table 3.1.

At the end of the experiment, the brain was removed from the cranial cavity and dissected into anatomical regions (cortex, caudate putamen, hippocampus, thalamus, brain stem, and cerebellum). Individual brain regions were assayed for ^{125}I and ^{131}I activity using a two-channel gamma counter. Residual plasma volume (V_p) at each brain region (mL per gram tissue) was estimated using the equation:

$$V_p = \frac{q_p}{C_v W}$$

where q_p is the total ^{131}I-BSA activity in the brain region (µCi), C_v is the ^{131}I-BSA concentration in plasma (µCi/mL), and W is the weight of the brain region (g). Given the total ^{125}I-Aβ40 or ^{125}I-Aβ42 activity in the brain region (q_T; µCi), the amount that permeated into the brain extravascular space (q; µCi per gram tissue) was estimated using the equation:

$$q = \frac{q_T}{W} - V_p C_a$$

where C_a is the final ^{125}I-Aβ concentration in plasma (µCi/mL). The permeability-surface area (PS) product (mL/s per gram tissue) for ^{125}I-Aβ40 or ^{125}I-Aβ42 at each brain region was estimated using the equation:

$$PS = \frac{q}{60 \int_0^t C_p \, dt}$$

where $\int_0^t C_p \, dt$ is the area under the observed plasma concentration vs. time profile (AUC) from 0-15 minutes (min*µCi/mL) obtained using the linear-trapezoidal method. The PS product for the whole brain was estimated based on the sum of q in all six dissected brain regions. The % of the injected dose that permeated into the whole brain per gram tissue (% ID/g) was estimated using the equation:

$$\%\ ID/g = \frac{q}{Dose\ (100\ \mu Ci)}$$

3.3.5. Plasma pharmacokinetics and brain permeability of ^{125}I-insulin. These experiments were performed as described above for ^{125}I-Aβ. Briefly, WT mice at various ages (8, 24, or 52 weeks) were bolus injected with a single dose (100 µCi) of ^{125}I-insulin in PBS (100 µL) into the femoral vein. Blood was sampled serially (20 µL) from the femoral artery at 0.25, 1, 3, 5, 10, and 14 minutes post-injection. Immediately after the

14-minute sampling event, ^{131}I-BSA (100 µCi) was bolus injected into the femoral vein to serve as a measure of V_p. One minute after the ^{131}I-BSA injection, a final blood sample was collected, and the animal was euthanized. Plasma pharmacokinetics and brain uptake of ^{125}I-insulin were assessed as described above for ^{125}I-Aβ. The secondary plasma pharmacokinetic parameters for ^{125}I-insulin are reported in Table 3.2.

3.3.6. Dynamic SPECT/CT imaging of ^{125}I-insulin influx to the brain. WT mice at 12 or 104 weeks of age weighing 25-35 g were catheterized at the femoral vein and femoral artery while under general anesthesia (1.5 % isoflurane; 4 L/min oxygen). A single dose (500 µCi) of ^{125}I-Insulin diluted in PBS was bolus injected into the femoral vein. Immediately following which, the entire animal was placed inside the single-photon emission computed tomography (SPECT/CT) scanner (Gamma Medica, Northridge, CA), and the biodistribution of radioactive signal was imaged at 1 min intervals over the next 40 min, followed by a 5 min CT scan to locate regions of interest (ROIs). The brain influx of ^{125}I-insulin was assessed by Gjedde-Patlak graphical analysis (Patlak et al., 1983), which involved plotting:

$$\frac{X_b(t)}{C_p(t)} \text{ vs. } \frac{\int_0^t C_p\,dt}{C_p(t)}$$

where $X_b(t)$ is the measured amount (µCi) of radioactive signal in the brain ROI at time t (min), $C_p(t)$ is the plasma concentration (µCi/mL) at time t, and $\int_0^t C_p\,dt$ is the plasma AUC (min*µCi/mL) from 0-t. Both $C_p(t)$ and $\int_0^t C_p\,dt$ were predicted based on the primary plasma pharmacokinetic parameters obtained in a separate experiment. The slope

obtained after linear regression corresponds to the brain influx clearance, K_i (mL/min) of ^{125}I-insulin.

3.3.7. Transcriptomic analysis of brain endothelial cells from WT mice. A comprehensive, transcriptomic analysis of gene expression profiles of brain endothelial cells obtained from WT mice at 12 and 104 weeks of age was recently published by Ximerakis et al. (2019). In these studies, the transcriptomes of 50,212 single cells obtained from brains of young or aged mice were assessed by single-cell RNA-Seq. Following this, an established clustering method was used to group transcriptionally similar cells based on the expression of multiple cell-type-specific marker genes, such as those specific for brain endothelial cells (CD31, tight junction proteins, etc.).

Using the single-cell RNA-Seq data publicly available at http://shiny.baderlab.org/AgingMouseBrain/, we applied a non-parametric Gene Set Variation Analysis (GSVA) method (Hänzelmann et al., 2013) to assess the pathway-level activity in young and aged cohorts at an individual sample level. Curated gene sets defining specific pathways were obtained from MSigDB. The GSVA method condenses a gene-level expression matrix into pathway enrichment scores. The directionality of pathway scores was determined from the mean difference between the cohorts. Significance was assessed by unpaired, two-tailed *t*-tests. The analysis was performed using the GSVA package in R studio (R software; Boston, MA).

We also performed Gene Set Enrichment Analysis (GSEA) on brain endothelial cell expression data published by Ximerakis et al. (2019). Similar to GSVA, the GSEA method can also be used to assess differences in pathway-level activity when

comparing cohorts (Hänzelmann et al., 2013). The same pathways (gene sets) assessed by GSVA were assessed by GSEA. Pathway enrichment scores were calculated based on the list of genes ranked according to their differential expression. Significance was assessed by a permutation test, which determines the probability of obtaining an enrichment score that is as strong as or stronger than that observed under the permutation-generated null distribution. The analysis was performed using the fgsea package in R studio.

3.3.8. Statistical analysis. Statistical tests were performed using GraphPad Prism 8.4 (GraphPad software; La Jolla, CA). A *p* value of less than 0.05 was regarded as statistically significant. Two-way ANOVA followed by Bonferroni post-hoc tests were used to compare the plasma pharmacokinetic parameters or PS products of ^{125}I-Aβ40 and ^{125}I-Aβ42 at 8, 24, and 52 weeks of age in WT mice, as well as in APP/PS1 mice. One-way ANOVA followed by Bonferroni post-hoc tests were used to compare plasma pharmacokinetic parameters or PS products of ^{125}I-insulin in WT mice at 8, 24, and 52 weeks of age. Unpaired, two-tailed *t*-tests were used to compare the slopes obtained from Gjedde-Patlak plots for ^{125}I-insulin in WT mice at 12 and 104 weeks of age.

3.4. Results

3.4.1. Age-dependent changes in plasma pharmacokinetics of ^{125}I-Aβ40 and ^{125}I-Aβ42 in WT and APP/PS1 mice. Plasma pharmacokinetics of ^{125}I-Aβ40 and ^{125}I-Aβ42 were assessed in WT and APP/PS1 transgenic mice at 8, 24, and 52 weeks of age. Female mice were used for the studies, given that AD disproportionately affects women, and

that female APP/PS1 transgenic mice display higher brain Aβ levels and greater occurrence of histopathological hallmarks compared to their male littermates (Wang et al., 2003; Gali et al., 2019). Following a bolus injection into the femoral vein, both peptides exhibited bi-exponential decline in their plasma concentrations with time (Fig. 3.1), which is consistent with our earlier publications (Kandimalla et al., 2005; Swaminathan et al., 2018a). The plasma exposure to ^{125}I-Aβ40 in WT mice, estimated by the area under the concentration vs. time curve (AUC), was unaltered between 8 and 24 weeks, but increased by ~7 fold at 52 weeks; a concomitant decrease in plasma clearance was observed (Fig. 3.1A; Table 3.1). In contrast, the plasma AUC of ^{125}I-Aβ42 reduced by ~2 fold in WT mice around 24 or 52 weeks of age compared to 8 weeks; a concomitant increase in plasma clearance was observed (Fig. 3.1B; Table 3.1). Further, at 52 weeks, the plasma AUC of ^{125}I-Aβ40 in WT mice was ~12 fold higher than that of ^{125}I-Aβ42, whereas no significant differences were observed between the two peptides at 8 or 24 weeks (Table 3.1).

In APP/PS1 mice, the plasma AUC of ^{125}I-Aβ40 was not significantly altered across all three age groups, although an increasing trend was observed at 24 and 52 weeks compared to 8 weeks (Fig. 3.1C; Table 3.1). The plasma AUC of ^{125}I-Aβ42 was also not significantly different across all three age groups of APP/PS1 mice, but an increasing trend was observed at 24 weeks compared to 8 or 52 weeks (Fig. 3.1D; Table 3.1). In APP/PS1 mice, no significant differences were observed between the plasma AUC of ^{125}I-Aβ40 and ^{125}I-Aβ42 at any of the three age groups, although an increasing trend was observed for ^{125}I-Aβ40 compared to ^{125}I-Aβ42 at 52 weeks (Table 3.1). Interestingly, in both WT and APP/PS1 mice, the maximum observed plasma

concentration (C_{max}) was higher for ^{125}I-Aβ40 compared to ^{125}I-Aβ42 at all three age groups.

Wild-type						
	^{125}I-Aβ$_{40}$			^{125}I-Aβ$_{42}$		
Age (weeks)	C_{max} (μCi/mL)	AUC (μCi.min/mL)	Clearance (mL/min)	C_{max} (μCi/mL)	AUC (μCi.min/mL)	Clearance (mL/min)
8	23.2 ± 0.6	63.5 ± 6.5	1.6 ± 0.2	11.3 ± 0.5$^{###}$	78.9 ± 11.8	1.3 ± 0.2
24	16.4 ± 0.4	43.5 ± 3.1	2.3 ± 0.2	5.2 ± 0.3$^{###}$	40.1 ± 9.4	2.5 ± 0.3*
52	12.8 ± 0.1	373 ± 63***	0.26 ± 0.04**	6.0 ± 0.3$^{###}$	31.2 ± 3.5$^{####}$	3.2 ± 0.3***

APP/PS1						
	^{125}I-Aβ$_{40}$			^{125}I-Aβ$_{42}$		
Age (weeks)	C_{max} (μCi/mL)	AUC (μCi.min/mL)	Clearance (mL/min)	C_{max} (μCi/mL)	AUC (μCi.min/mL)	Clearance (mL/min)
8	17.7 ± 1.8	49.7 ± 12.4	2.1 ± 0.5	3.4 ± 0.3$^{###}$	27.6 ± 9.4	3.6 ± 1.2
24	12.5 ± 0.2	103.0 ± 34.5	1.0 ± 0.3	7.1 ± 0.2$^{##}$	72.2 ± 19.7	1.4 ± 0.3
52	13.7 ± 0.2	86.8 ± 22.8	1.2 ± 0.3	5.1 ± 1.0$^{###}$	30.9 ± 7.8	3.2 ± 0.8

Table 3.1. Plasma pharmacokinetics of ^{125}I-Aβ40 and ^{125}I-Aβ42 in WT and APP/PS1 transgenic mice at 8, 24, and 52 weeks. Data represent mean ± SE, n=3-5. Significance was assessed over age ($^{*}p < 0.05$, $^{**}p < 0.01$ and $^{***}p < 0.001$) and ^{125}I-Aβ40 vs. ^{125}I-Aβ42 ($^{\#\#}p < 0.01$, $^{\#\#\#}p < 0.001$, and $^{\#\#\#\#}p < 0.0001$; two-way ANOVA with Bonferroni post-tests).

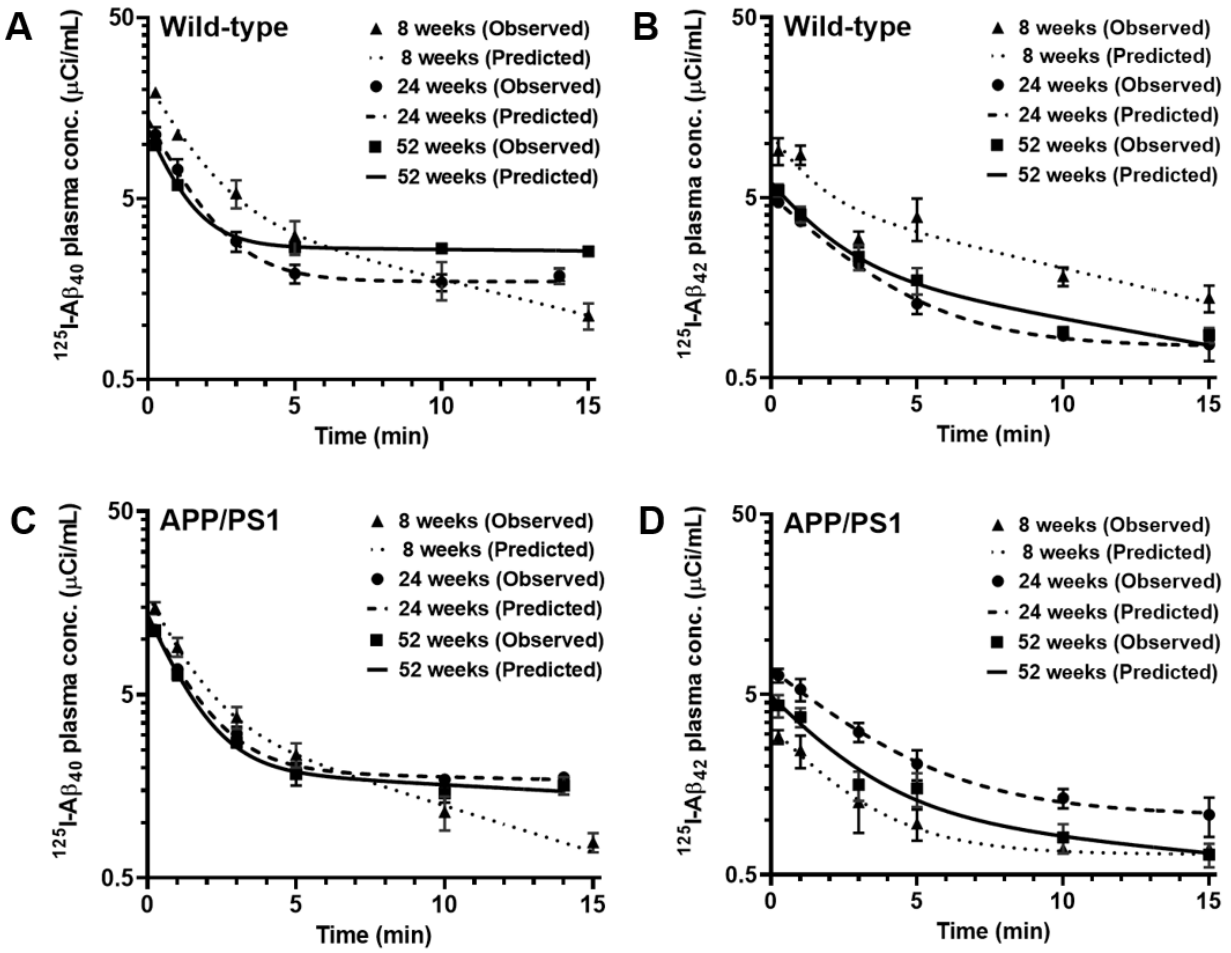

Figure 3.1. Plasma pharmacokinetics of ^{125}I-Aβ40 and ^{125}I-Aβ42 in WT and APP/PS1 mice at 8, 24, and 52 weeks. WT or APP/PS1 transgenic mice were bolus injected with 100 µCi of ^{125}I-Aβ40 (A, C) or ^{125}I-Aβ42 (B, D) into the femoral vein. Plasma was sampled periodically between 0-15 minutes, and radioactivity in the intact ^{125}I-Aβ fraction was measured. The plasma concentration vs. time data was fit to a bi-exponential equation. Shown are the observed values (mean ± SD, n=3-5) overlaid on the predicted curves.

3.4.2. Brain uptake of ^{125}I-Aβ40 decreases and that of ^{125}I-Aβ42 increases with age in WT mice, which is disrupted in APP/PS1 mice. Following a bolus injection of ^{125}I-Aβ40 or ^{125}I-Aβ42 into the femoral vein of WT or APP/PS1 transgenic mice at 8, 24, and 52 weeks of age, brain uptake was assessed as the permeability-surface area (PS)

product. In WT mice, the PS values of ^{125}I-Aβ40 in various brain regions were unaltered at 8 and 24 weeks, but decreased by ~4 fold at 52 weeks (Fig. 3.2B). In contrast, the PS values of ^{125}I-Aβ42 were unaltered at 8 and 24 weeks, but increased by ~1.5 fold at 52 weeks in the WT mice (Fig. 3.2C). In APP/PS1 mice, the PS values of ^{125}I-Aβ40 were unaltered at 8 and 24 weeks, but decreased by ~1.5 fold at 52 weeks (Fig. 3.2D). Interestingly, the PS values of ^{125}I-Aβ42 at various brain regions in APP/PS1 mice were unaltered at 8 and 52 weeks, but decreased by ~1.5 fold at 24 weeks (Fig. 3.2E).

When comparing age-matched WT and APP/PS1 mice, the PS products of ^{125}I-Aβ40 in the whole brain were ~1.5 fold lower in APP/PS1 mice compared to WT mice, at both 8 and 24 weeks. However, by 52 weeks, at which point the PS products of ^{125}I-Aβ40 had decreased substantially in WT mice, no differences were observed between WT and APP/PS1 mice (Fig. 3.2F). Interestingly, for ^{125}I-Aβ42, no significant differences between WT and APP/PS1 mice were observed in any of the age groups (Fig. 3.2F). When comparing Aβ40 vs. Aβ42 in WT mice, the PS products in the whole brain were ~1.5 fold higher for ^{125}I-Aβ40 compared to ^{125}I-Aβ42 at both 8 and 24 weeks; however, by 52 weeks, a dramatic shift was observed in the PS product of ^{125}I-Aβ42, which increased by ~4 fold compared to ^{125}I-Aβ40 (Fig. 3.2F). Conversely, in APP/PS1 mice, the PS products in the whole brain were similar for ^{125}I-Aβ40 compared to ^{125}I-Aβ42 at both 8 and 24 weeks; however, by 52 weeks, again a shift was observed in the PS product of ^{125}I-Aβ42, which increased by ~3 fold compared to ^{125}I-Aβ40 (Fig. 3.2F). Similar trends were observed in the overall brain accumulation, which was expressed as the % of the injected dose (ID) accumulated in the brain per gram of tissue (% ID/g) (Fig. 3.2G).

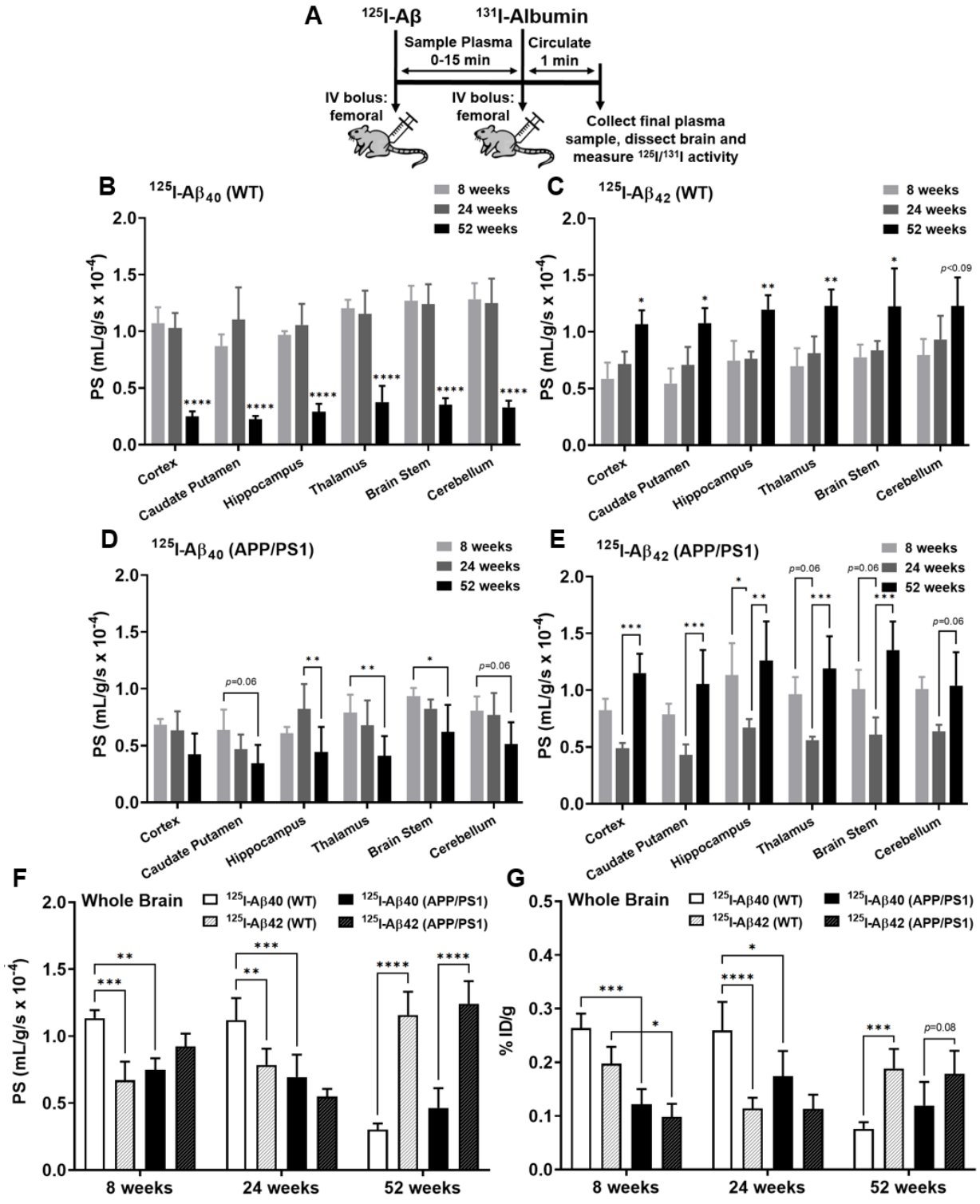

Figure 3.2. Brain uptake of ^{125}I-Aβ40 and ^{125}I-Aβ42 in WT and APP/PS1 mice at 8, 24, and 52 weeks. (A) Experiment scheme. WT or APP/PS1 transgenic mice were bolus

injected with 100 µCi of ^{125}I-Aβ40 or ^{125}I-Aβ42 into the femoral vein. At the end of the experiment, 100 µCi of ^{131}I-albumin was injected to serve as a marker of V_p. The brain regions were dissected and assayed for radioactivity. Shown are the PS value estimates for ^{125}I-Aβ40 (B, D) and ^{125}I-Aβ42 (C, E) uptake at various brain regions. (F) The PS values are shown for the whole brain. (G) The overall brain accumulation was assessed as % ID/g. Data represent mean ± SD, n=3-5. $^{*}p < 0.05$, $^{**}p < 0.01$, $^{***}p < 0.001$, and $^{****}p < 0.0001$; two-way ANOVA with Bonferroni post-tests).

3.4.3. Age-dependent changes in plasma pharmacokinetics of ^{125}I-insulin in WT mice.

The plasma pharmacokinetics of ^{125}I-Insulin were assessed in WT mice at 8, 24 and 52 weeks of age. Following a bolus injection into the femoral vein, a bi-exponential decline in ^{125}I-insulin plasma concentrations was observed with time (Fig. 3.3), which is consistent with earlier publications (Sato et al., 1990). The plasma AUC of ^{125}I-insulin increased by ~3 fold at 52 weeks compared to 8 or 24 weeks; a concomitant decrease in clearance was observed. The value of C_{max} was also increased at 52 weeks compared to 8 or 24 weeks (Table 3.2).

^{125}I-insulin			
Age (weeks)	**C_{max} (µCi/mL)**	**AUC (µCi.min/mL)**	**Clearance (mL/min)**
8	19.6 ± 0.2	83.7 ± 7.9	1.19 ± 0.11
24	23.5 ± 0.5****	170 ± 15	0.61 ± 0.06***
52	28.0 ± 0.4****	357 ± 68**	0.28 ± 0.05****

Table 3.2. Plasma pharmacokinetics of ^{125}I-insulin in WT mice at 8, 24 and 52 weeks. Data are mean ± SE, n=3-5. Significance was assessed over age ($^{**}p < 0.01$, $^{***}p < 0.001$, $^{****}p < 0.0001$; one-way ANOVA with Bonferroni post-tests).

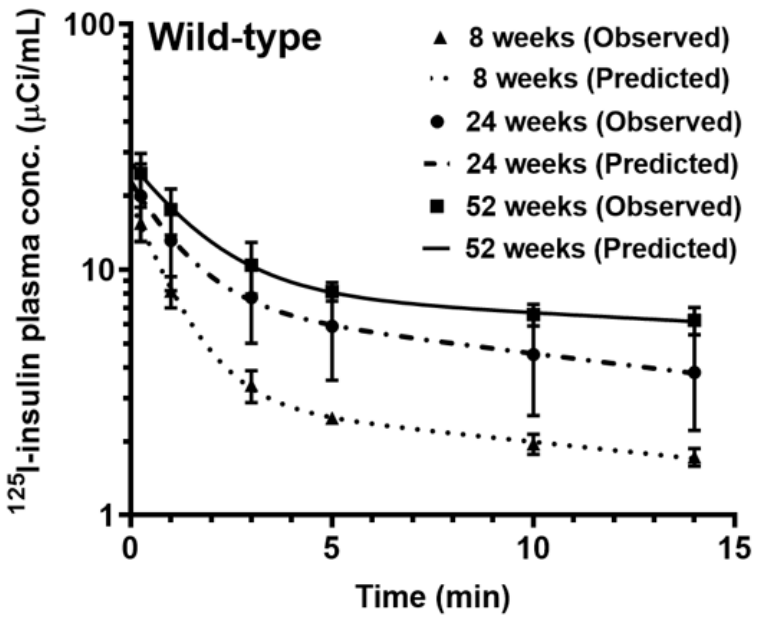

Figure 3.3. Plasma pharmacokinetics of ^{125}I-insulin in WT mice at 8, 24 and 52 weeks. Mice were bolus injected with 100 µCi of ^{125}I-insulin into the femoral vein. Plasma was sampled periodically between 0-14 minutes, and radioactivity in the intact ^{125}I-insulin fraction was measured. The plasma concentration vs. time data was fit to a bi-exponential equation. Shown are the observed values (mean ± SD, n=3-5) overlaid on the predicted curves.

3.4.4. Brain uptake of ^{125}I-insulin decreases with age in WT mice. Following a bolus injection of ^{125}I-insulin into the femoral vein of WT mice at 8, 24 and 52 weeks of age, brain influx was assessed as the PS product (Fig. 3.4A). The PS products of ^{125}I-insulin at various brain regions decreased by ~5 fold at 24 weeks compared to 8 weeks, but did not further decrease at 52 weeks (Fig. 3.4B). Similarly, the % ID/g of ^{125}I-insulin in the whole brain decreased by ~3 fold at 24 and 52 weeks compared to 8 weeks. To study the effects of advanced aging, brain influx of ^{125}I-insulin was further assessed in WT mice at 12 and 104 weeks of age by dynamic SPECT/CT imaging. After femoral injection, accumulation of ^{125}I-insulin in the brain was imaged from 0-40 minutes (Fig.

3.5A). Gjedde-Patlak plots were constructed to estimate the brain influx clearance (Patlak et al., 1983), which corresponds to the slope (K_i; mL/min) obtained after linear regression (Fig. 3.5B). The brain influx clearance of ^{125}I-insulin decreased by ~2 fold at 104 weeks compared to 12 weeks (Fig. 3.5 inset).

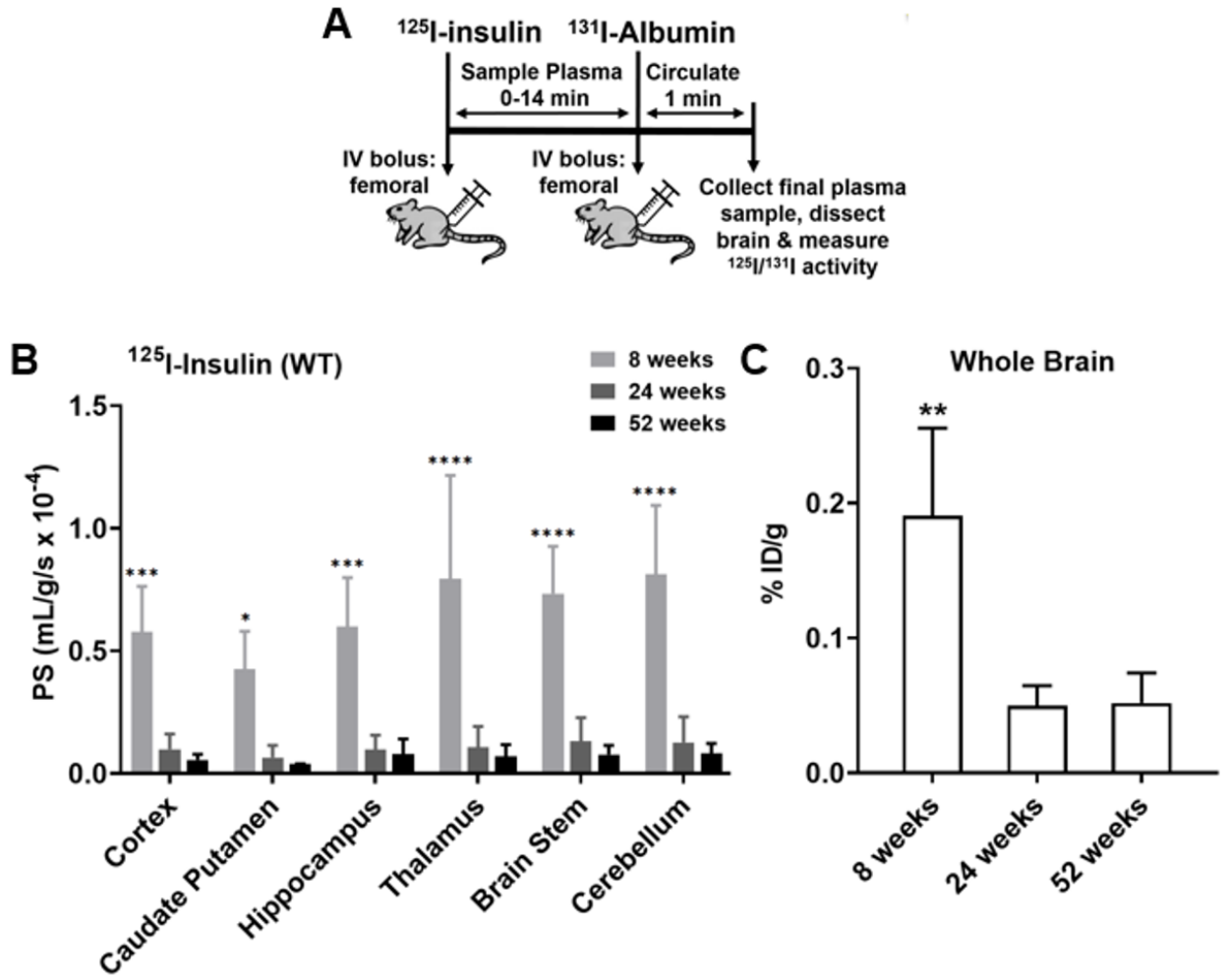

Figure 3.4. Brain uptake of ^{125}I-insulin in WT mice at 8, 24 and 52 weeks. (A) Experimental scheme. WT mice were bolus injected with 100 µCi of ^{125}I-insulin into the femoral vein. At the end of the experiment, 100 µCi of ^{131}I-albumin was injected to serve as a marker of V_p. The brain regions were dissected and assayed for radioactivity. (B) The PS value estimates for ^{125}I-insulin uptake in various brain regions are shown. Data represent mean ± SD, n=3-5. $^{*}p < 0.05$, $^{***}p < 0.001$, $^{****}p < 0.0001$; two-way ANOVA

with Bonferroni post-tests. (C) The overall brain accumulation was assessed as % ID/g. $^{**}p < 0.01$; one-way ANOVA with Bonferroni post-tests.

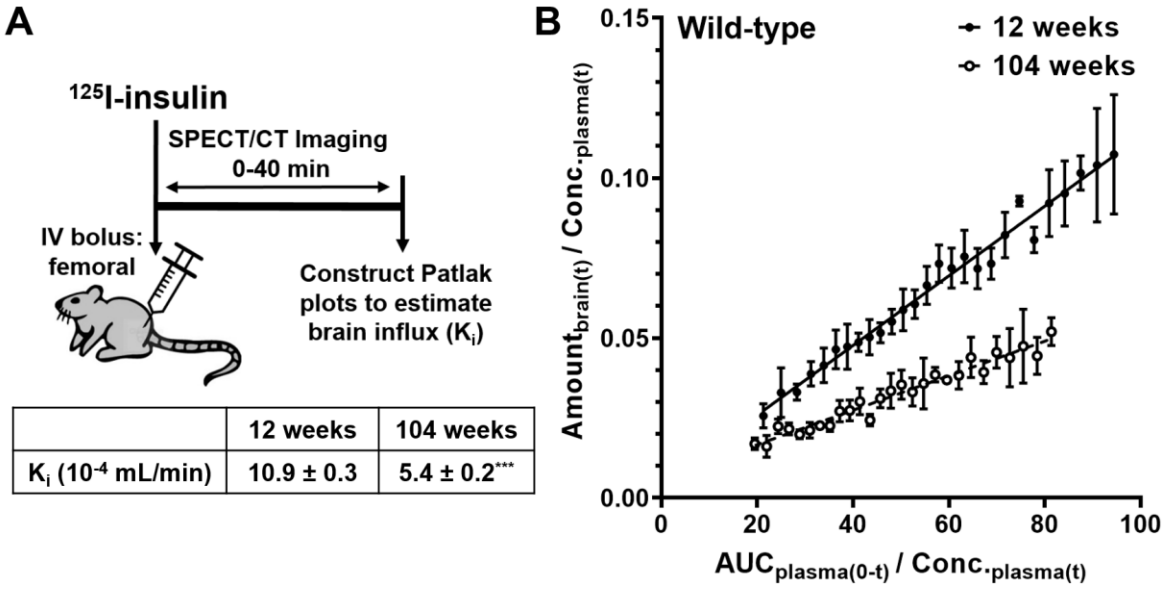

	12 weeks	104 weeks
K_i (10^{-4} mL/min)	10.9 ± 0.3	5.4 ± 0.2***

Figure 3.5. Dynamic SPECT/CT imaging of ^{125}I-insulin uptake to the brain. (A) Experimental scheme. WT mice were bolus injected with 500 µCi of ^{125}I-insulin into the femoral vein and the accumulation of ^{125}I-insulin in the brain was monitored between 0-40 minutes post-injection by dynamic SPECT/CT imaging. (B) The brain influx clearance (K_i) of ^{125}I-insulin was estimated by the slope obtained from Gjedde-Patlak graphical analysis. In the graph, $Amount_{brain(t)}$ is the measured radioactivity in the brain ROI (µCi) at each time point (data are mean ± SD, n=4), whereas $AUC_{plasma(0-t)}$ (min.µCi/mL) and $Conc._{plasma(t)}$ (µCi/mL) were predicted using the plasma pharmacokinetic parameters. The K_i predictions presented in the table are mean ± SE, n=4. $^{***}p < 0.001$; unpaired two-tailed *t*-test.

3.4.5. Age-dependent changes in transporter/signaling pathways at the BBB in WT mice. Using the publicly available single cell RNA-Seq data published by Ximerakis et al. (Ximerakis et al., 2019), we performed Gene Set Variation Analysis (GSVA) and also Gene Set Enrichment Analysis (GSEA) to assess the activity of various cellular pathways that are implicated in Aβ or insulin trafficking at the BBB. Pathways relating to

RAGE signaling, insulin/Akt signaling, and T2DM pathology were upregulated in brain endothelial cells obtained from WT mice at 104 weeks compared to 12 weeks (Table 3.3). In contrast, ABC transporter and tight junction networks were downregulated in the brain endothelial cells obtained at 104 weeks compared to 12 weeks (Table 3.3).

Pathway	GSVA		GSEA	
	Directionality	*p* value	Directionality	*p* value
KEGG_AGE RAGE Signaling Pathway	Up	0.088	Up	0.25
PID_Insulin Pathway		0.035		0.11
PID_PI3KCI AKT Pathway		1.5E-08		0.0043
KEGG_Type II Diabetes Mellitus		0.012		0.12
KEGG_ABC Transporters	Down	0.0058	Down	0.086
REACTOME_Tight Junction Interactions		2.9E-05		0.13

Table 3.3. Enrichment of various transporter/signaling pathways in brain endothelial cells from WT mice at 12 and 104 weeks. The GSVA and GSEA methods were used to compare the enrichment of various transporter/signaling pathways in brain endothelial cells obtained from WT mice at different ages, using the single-cell RNA-Seq data published by Ximerakis et al. (2019). The directionality indicates upregulation or downregulation of the pathway in the aged compared to young mice.

3.5. Discussion and Conclusions

BBB dysfunction is observed in the aging brain (Popescu et al., 2009) and is thought to be among the earliest changes driving AD pathogenesis (Nelson et al., 2016). The BBB dysfunction is customarily studied from the perspective of loss of tight junction integrity (Sweeney et al., 2018) and reduced cerebral blood flow (Tarumi and Zhang, 2018). However, age related changes in cellular and molecular mechanisms that drive these changes in BBB functions are only partially understood. Even less understood are age related changes in diverse BBB functions that coordinate the delivery of essential nutrients like glucose and insulin to the brain (Sartorius et al.,

2015), as well as the clearance of toxic metabolites like Aβ peptides from the brain (Silverberg et al., 2010a).

Our findings demonstrate that plasma pharmacokinetics of Aβ isoforms and insulin are differentially affected by aging in WT mice. The liver and kidneys are the major organs responsible for clearing Aβ from the periphery (Ghiso et al., 2004), but it remains poorly understood how systemic Aβ clearance is affected during normal aging and in AD. We showed that in WT mice, the plasma AUC of ^{125}I-Aβ40 increased with age, but that of ^{125}I-Aβ42 decreased. This demonstrates an age dependent switch in plasma pharmacokinetics of the two major Aβ isoforms. Consistent with these findings, the plasma AUC of Aβ40 was reported to increase with age in squirrel monkeys (Mackic et al., 1998). The observed age dependent changes in Aβ40 plasma pharmacokinetics in WT mice were evident at an even earlier age in APP/PS1 transgenic mice, likely due to accelerated AD pathology in these animals. Similarly, it was reported that Aβ40 plasma concentrations increased with age in healthy patients, but not in AD patients (Mehta et al., 2000). This is expected to promote a decrease in the Aβ42/Aβ40 ratio in plasma with age, which has been strongly linked to amyloid plaque deposition and AD risk in patients (Lui et al., 2010; Rembach et al., 2014). The increase in ^{125}I-Aβ40 plasma AUC with age predicts increased exposure of this isoform to the luminal surface of the BBB. Increased plasma Aβ40 levels are associated with cerebrovascular disease, which is prevalent in approximately 90% of all AD patients (Brenowitz et al., 2015).

The current study demonstrates that the plasma-to-brain influx of Aβ isoforms and insulin are progressively and differentially affected by aging in WT mice. Using the publicly available single-cell RNA-Seq data of BBB endothelial cells in WT mice

(Ximerakis et al., 2019), we identified age-dependent changes to various trafficking/signaling pathways implicated in Aβ and insulin delivery to the brain. Changes in Aβ trafficking are evident in AD transgenic mice at a much younger age, suggesting that age-related pathophysiological changes are accelerated in AD. Brain influx of ^{125}I-Aβ40 is lower in APP/PS1 mice than in WT mice at both 8 and 24 weeks of age; but no significant differences in ^{125}I-Aβ42 influx were observed between WT and APP/PS1 mice in these age groups. At 52 weeks, the differences between WT and APP/PS1 mice were entirely lost, with Aβ42 influx dominating over Aβ40 influx. Previously, we reported that in APP/PS1 mice, initiation of Aβ plaque formation occurs at 24 weeks of age, with full-scale plaque burden observed by 52 weeks (Jack et al., 2005). It was also reported that cognitive deficits first appear in APP/PS1 mice at 24 weeks, and become more severe by 52 weeks (Filali and Lalonde, 2009). Thus, we speculate the shift in the preferential brain influx of Aβ42 vs. Aβ40 observed at 52 weeks is associated with enhanced amyloid deposition and cognitive decline in the APP/PS1 mice.

Normal aging, AD, and T2DM have all been associated with hyperinsulinemia and insulin resistance, which manifests as increased insulin plasma levels and impaired insulin sensitivity in the brain (Young et al., 2006; Kullmann et al., 2016). We showed the plasma AUC of ^{125}I-insulin increased from 8 to 24 weeks, and then further increased at 52 weeks in WT mice. This could be due to impaired renal clearance of insulin, which was claimed to be a major driver of hyperinsulinemia (Kotronen et al., 2008), and/or decreased distribution from plasma to peripheral tissues and the brain. The PS products of ^{125}I-insulin in WT mice declined steeply from 8 to 24 weeks, then remained unchanged from 24 to 52 weeks. In contrast, the PS products of ^{125}I-Aβ40 and ^{125}I-Aβ42

remained unchanged from 8 to 24 weeks, then decreased and increased, respectively, at 52 weeks. In the AD brain, increased levels of toxic $A\beta_{42}$ peptides are paralleled by decreased levels of the essential growth factor insulin (Gil-Bea et al., 2010). It was also shown that WT mice demonstrate learning/memory deficits at 52 weeks compared to 24 weeks (Wong and Brown, 2007). Taken together, these findings suggest that age related pathological changes in insulin transport at the BBB precede the changes in Aβ transport at the BBB and the onset of cognitive decline in WT mice.

Brain uptake of insulin is extremely rapid relative to other serum proteins, indicating a highly specialized and efficient trafficking system for delivering insulin across the BBB (Poduslo et al., 1994). To capture the initial rate of insulin uptake, dynamic SPECT/CT imaging studies were performed to measure ^{125}I-insulin uptake to the brain after systemic injection in WT mice at 12 and 104 weeks. These age groups were selected based on a previous study that established age dependent changes in insulin sensitivity in WT mice (Reynolds et al., 2019). Based on Gjedde-Patlak graphical analysis, the ^{125}I-insulin brain influx clearance decreased at 104 weeks compared to 12 weeks. Thus, we showed that compared to young WT mice, insulin uptake to the brain was decreased in both middle aged (52 weeks) and advanced aged (104 weeks) mice. Furthermore, we recently showed that ^{125}I-insulin uptake to the brain is decreased in APP/PS1 mice compared to age matched WT mice (Swaminathan et al., 2018b). Together, these findings suggest that reduced insulin transport at the BBB during aging in WT mice may decrease further in APP/PS1 mice and reduce brain insulin levels.

Both insulin and Aβ peptides are known to exhibit saturable, receptor-mediated transcytosis at the BBB (Zlokovic et al., 1993; Rhea et al., 2018). Brain uptake of Aβ

peptides is thought to be primarily mediated by RAGE, expressed on the luminal surface of the BBB (Deane et al., 2004). Membrane RAGE is reported to localize in caveolae microdomains (Stitt et al., 2000), while IR is reported to localize in clathrin-coated pits (Carpentier, 1994). Although the role of IR at the BBB in insulin delivery to the brain is controversial (Gray et al., 2017; Rhea et al., 2018), insulin transcytosis across microvascular endothelial cells was reported to be clathrin dependent (Azizi et al., 2015). We previously showed that Aβ42 uptake in BBB endothelial cells is caveolae dependent, whereas Aβ40 uptake is clathrin dependent (Sharda et al., 2021). This suggests that in addition to RAGE, Aβ40 uptake at the BBB may be handled by other receptor(s) that involve clathrin-dependent endocytosis. In a recent study, aging in WT mice was shown to be associated with increased expression of caveolin-1 and decreased expression of clathrin heavy chain in the brain microvessels (Yang et al., 2020). Therefore, our current findings that aging in WT mice is associated with increased brain uptake of Aβ42 and decreased uptake of Aβ40 and insulin could be resulting from the age dependent switch from clathrin to caveolae mediated endocytosis at the BBB.

In addition to serving as an endocytosis receptor, RAGE also functions as a signaling receptor to trigger the activation of pro-inflammatory pathways, which have been implicated in Aβ uptake at the BBB (Chen et al., 2018). It was reported that RAGE expression at the BBB increased with age in rats (Silverberg et al., 2010b). By performing pathway level analyses (GSVA and GSEA) on publicly available single cell RNA-Seq data (Ximerakis et al., 2019), we found that the RAGE signaling pathway was upregulated in brain endothelial cells obtained from WT mice at 104 weeks compared to

12 weeks. In contrast, ABC transporter proteins, which were claimed to mediate Aβ efflux from the brain (Abuznait and Kaddoumi, 2012), as well as tight junction proteins were downregulated at 104 weeks. Thus, increased RAGE expression and signaling at the BBB likely contributed to the increased ^{125}I-Aβ42 uptake observed in the aged mice. However, these trends cannot explain the concomitant decrease in ^{125}I-Aβ40 uptake. We speculate that these differences are engendered by other unidentified luminal receptors reliant on clathrin dependent endocytosis that demonstrate higher selectivity for Aβ40 over Aβ42. During normal aging and AD progression, down regulation of such receptors could promote a decrease in the brain influx of Aβ40. The differential handling of Aβ40 vs. Aβ42 by cell surface receptors and intracellular mechanisms governing their disposition require further investigation.

Insulin signaling networks in the brain are disrupted during normal aging and AD, which triggers brain insulin resistance and contributes to cognitive decline (Akintola and van Heemst, 2015; Gabbouj et al., 2019). The PI3K-AKT signaling pathway is downstream of IR and has canonical functions in glucose metabolism. By performing GSVA and GSEA on the single cell RNA-Seq data (Ximerakis et al., 2019), we found that insulin signaling and PI3K-AKT pathways were upregulated at the BBB in WT mice at 104 weeks compared to 12 weeks. Previously, it was reported that sustained over-activation of PI3K-AKT signaling in the aging brain is associated with brain insulin resistance and Aβ pathology (O' Neill, 2013; Chen et al., 2019). Consistent with these findings, we observed upregulation of a set of proteins implicated in insulin resistance/T2DM in the 104 week-old mice. These age groups match with those used in the ^{125}I-insulin SPECT/CT imaging studies. Based on these reports and our current

findings, we speculate that in aged WT mice, insulin signaling disruptions at the BBB triggered by hyperinsulinemia and peripheral insulin resistance inhibit insulin transcytosis at the BBB, resulting in decreased insulin uptake to the brain.

Insulin signaling networks have also been implicated in the regulation of Aβ trafficking receptors at the BBB (Vandal et al., 2015). We previously reported that stimulation with insulin modulates the plasma membrane expression of LRP-1 in hCMEC/D3 cell monolayers (BBB cell model) (Swaminathan et al., 2018a), while others demonstrated similar findings in hepatocytes (Laatsch et al., 2009). Insulin is also suggested to modulate expression of other important Aβ receptors, specifically RAGE and P-glycoprotein, at the BBB (Liu and Liu, 2014; Sun et al., 2015; Swaminathan et al., 2018a). Moreover, we have previously shown that insulin differentially regulates the trafficking of Aβ isoforms at the BBB. Specifically, systemic insulin injection in WT mice decreased brain influx of ^{125}I-Aβ42, but increased brain influx of ^{125}I-Aβ40, with concomitant changes in their plasma pharmacokinetics (Swaminathan et al., 2018a). Therefore, we speculate that impaired insulin signaling in the BBB endothelium contributes to the Aβ trafficking perturbations observed in aged mice.

In summary, we demonstrated age dependent changes in the plasma disposition and brain influx of Aβ isoforms and insulin in mice. Brain influx of both ^{125}I-insulin and ^{125}I-Aβ40 decreased and ^{125}I-Aβ42 influx increased in WT mice with age. The increase in plasma AUC of ^{125}I-insulin with age is indicative of hyperinsulinemia, whereas the increase in ^{125}I-Aβ40 plasma AUC and decrease in ^{125}I-Aβ42 plasma AUC could reduce the Aβ42/Aβ40 ratio in plasma. Both changes are heavily implicated in AD risk. Thus, pathological changes during normal aging alter systemic clearance and BBB trafficking

of both insulin and Aβ peptides in a manner that could augment AD risk. Additionally, aging was associated with various transporter/signaling deficits in BBB endothelial cells, which is indicative of BBB dysfunction and insulin resistance. Further studies are needed to clarify the molecular mechanisms by which insulin and Aβ trafficking in the brain and periphery are impacted during normal aging and in AD.

Chapter 4: Effects of peripheral insulin resistance and Aβ peptide exposure on insulin transport and signaling at the BBB

4.1. Synopsis

Metabolic disorders such as type II diabetes mellitus (T2DM) have emerged as major risk factors for Alzheimer's disease (AD). Decreased brain insulin levels are associated with progression of cognitive decline in both T2DM and AD patients. Insulin in the brain is derived from systemic circulation via receptor-mediated transcytosis at the blood-brain barrier (BBB). At this time, the pathophysiological mechanisms that perturb insulin trafficking at the BBB in T2DM and AD remain poorly understood. We hypothesize that T2DM sequelae and exposure to toxic amyloid beta (Aβ) peptides, which predominate in AD brain, cooperate to disrupt BBB insulin signaling and thereby inhibit insulin delivery to the brain. Further, we propose that insulin signaling defects at the BBB contribute to elevated Aβ levels in AD brain. Here, we examined the separate and combined effects of T2DM and Aβ exposure on insulin trafficking and signaling at the BBB. Two different T2DM mouse models were investigated: wild-type (WT) mice maintained on a high-fat (HF) or regular chow (RC) diet, along with diabetic db/db mice

(leptin receptor deficient) and nondiabetic db/+ control mice. As an AD model, APP/PS1 transgenic mice, which overexpress Aβ peptides, were maintained on HF or RC diet. Dynamic SPECT/CT imaging studies were performed to assess the brain influx of ^{125}I-insulin after systemic injection in each group of mice. Plasma pharmacokinetics were assessed in a separate experiment. Patlak plots were constructed to estimate brain influx clearance, which was found to be lowest in APP/PS1-HF, followed by APP/PS1-RC and WT-HF compared to WT-RC mice. Similar trends were observed in total ^{125}I activity measured in brain dissected at the end of experiment. ^{125}I-insulin uptake into the brain was similarly reduced in db/db mice compared to db/+ mice. To examine effects of T2D and Aβ exposure on insulin signaling at the BBB, brain microvessels were harvested from the mice, and western blots were performed. Insulin receptor (IR-β) expression as well as AKT and GSK3β phosphorylation were lowest in APP/PS1-HF mice, followed by APP/PS1-RC and WT-HF compared to WT-RC mice. In summary, insulin uptake into the brain was lowest in mice that manifest both T2D and AD, followed by mice with T2D or AD alone, when compared to the healthy control. These deficiencies in insulin trafficking at the BBB were associated with reduced expression/activity of key insulin signaling kinases in isolated brain microvessels.

4.2. Background

Type 2 diabetes mellitus (T2DM) has emerged as a major risk factor for Alzheimer's disease (AD). Numerous studies have indicated that T2DM is associated with blood-brain barrier (BBB) dysfunction, as evidenced by increased brain uptake of tracer molecules, along with altered BBB expression of tight junction proteins (Starr et

al., 2003; Hawkins et al., 2007). Further, loss of BBB integrity was shown to precede the onset of cognitive decline and neurodegeneration in mice maintained on a high-fat diet (Takechi et al., 2017). According to Zlokovic's widely adopted two-hit vascular hypothesis, initial insults to the BBB and consequent barrier dysfunction eventually leads to the catastrophic neurocognitive changes observed in AD. The two histopathological hallmarks defining AD are the deposition of amyloid-beta (Aβ) peptides in both brain parenchyma and at the BBB, and formation of neurofibrillary tangles consisting of hyperphosphorylated tau protein.

Peripheral insulin resistance, which is a hallmark of T2DM, has been shown to interfere with the BBB transport of insulin. Insulin delivery to the brain from systemic circulation is crucial for normal brain functions, such as energy metabolism and learning/memory. In healthy human subjects, the severity of insulin resistance was shown to correlate with reduced insulin ratios in brain/plasma (Heni et al., 2014). Elevated plasma insulin levels, known as hyperinsulinemia, is highly prevalent among T2DM patients and represents a major risk factor for AD (Luchsinger et al., 2004). Furthermore, insulin levels in the brain are reduced in patients with mild-cognitive impairment or AD, when compared to age-matched non-demented controls (Gil-Bea et al., 2010). Thus, insulin levels in brain are reduced in patients with peripheral insulin resistance or AD. However, the combined effects of both pathologies on brain insulin levels have not been explored.

Insulin signaling is critical for neurobiological functions such as energy metabolism (Jauch-Chara et al., 2012), neuronal growth/division (Gu et al., 2014), and learning/memory (Dou et al., 2005). Insulin signaling is mediated by the insulin receptor

(IR) and insulin-like growth factor 1 receptor (IGF1R), which converge at several downstream signaling kinases. The two major signaling arms are the PI3K/Akt and MAPK/Erk pathways. These two pathways are canonically responsible for metabolic and mitogenic functions, respectively. Previously, it was shown that patients with either T2DM or AD both exhibit reduced expression/activity of several components of the insulin/PI3K/AKT signaling pathway in the frontal cortex (Liu et al., 2011). Moreover, patients with both T2DM and AD had the most severe deficits in brain insulin signaling, which also correlated with increased tau hyperphosphorylation (Liu et al., 2011). However, additional studies are required to elucidate the effects of T2DM and AD pathology on BBB insulin signaling pathways, and the deleterious effects this may have on BBB transport functions.

Here, we examined the plasma distribution and brain influx kinetics of ^{125}I radiolabeled insulin in various mouse models of T2DM and/or AD. Two different T2DM models were used: wild-type (WT) mice maintained on a high-fat (HF) or regular chow (RC) diet, along with diabetic db/db mice (leptin receptor deficient) and nondiabetic db/+ control mice. As an AD model, APP/PS1 transgenic mice, which overexpress Aβ peptides, were maintained on HF or RC diet. Further, brain microvessels were harvested from the mice, and western blots were performed to assess the expression/phosphorylation of key insulin signaling kinases. Our findings reveal that in the T2DM and/or AD mouse models, reductions in insulin uptake to the brain are associated with deficits in insulin signaling pathways at the BBB.

4.3. Materials & Methods

4.3.1. Animals. Diabetic db/db mice and nondiabetic db/+ control mice were obtained from the Jackson Laboratory (Bar Harbor, ME) and housed in the Mayo Clinic animal care facility. Mice were maintained in a temperature-controlled room (22-24 °C) with 12-h light/12-h dark cycles and were provided with food and water ad libitum. Female mice around four months of age were used for all studies. All procedures involving the use of animals were approved by the Mayo Institutional Animal Care and Use Committee and were performed in accordance with the Guide for the Care and Use of Laboratory Animals outlined by the National Institute of Health.

As a model of T2D, mice were placed on high-fat (HF) diet 4 months prior to the experiments. As a model of AD, APP/PS1 transgenic mice were used. The APP/PS1 line consists of C57BL/6J genetic background with transgenes added for amyloid precursor protein (APP_{swe}) and presenilin-1 ($PS1_{dE9}$), leading to Aβ overexpression and AD pathology. Studies were performed in 4 groups of mice: wild-type (WT) mice maintained on regular chow (RC) diet, WT mice maintained on HF diet, APP/PS1 mice on RC diet, and APP/PS1 mice on HF diet. All experiments were conducted at 10-12 months of age, with equal representation of both genders.

4.3.2. Radioiodination of insulin. Recombinant human insulin (Sigma-Aldrich, St. Louis, MO) was labeled with ^{125}I radionuclide (PerkinElmer Life and Analytical Sciences, Boston, MA) using the chloramine-T procedure as described previously (Poduslo et al., 2001). Following dialysis to remove unconjugated radionuclide, the purity of ^{125}I-labeled

insulin was determined by trichloroacetic acid (TCA) precipitation. Greater than 95% of total radioactivity counts were recovered upon TCA precipitation.

4.3.3. Plasma pharmacokinetics and brain permeability of ^{125}I-insulin after intravenous injection. These experiments were carried out as described in our previous publications (Kandimalla et al., 2005). Briefly, the mice were anesthetized (1.5% isoflurane with 4 L/min O_2) and catheterized at the femoral vein/artery. A single dose of ^{125}I-insulin (100 µCi in 200 µL of PBS) was administered by intravenous bolus injection to the femoral vein. Blood samples (20 µL) were collected from the femoral artery at 0.5, 1, 3, 5, 10, 15 and 30 min post-injection. The plasma was separated, and the protein fraction was isolated by TCA precipitation. The ^{125}I activity in the protein fraction was assayed using a gamma counter (Cobra II; Amersham Biosciences Inc., Piscataway, NJ). Immediately after the final blood sample was collected, the mouse was euthanized by transcardial perfusion with excess PBS to flush any remaining ^{125}I activity from the vasculature. The whole brain was removed and dissected into anatomical regions (cortex, caudate putamen, hippocampus, thalamus, brain stem and cerebellum). ^{125}I activity in the brain regions was assayed using the gamma counter.

^{125}I-insulin plasma concentration vs. time data was fit to a two-compartment pharmacokinetic model using Phoenix WinNonlin (Pharsight, Mountain View, CA):

$$C_p(t) = Ae^{-\alpha t} + Be^{-\beta t}$$

where $C_p(t)$ is the concentration (µCi/mL) at time t (min), $A + B$ is the concentration at $t = 0$, and α and β are the rate constants describing the distribution and elimination phases, respectively. The following secondary pharmacokinetic parameters were also

estimated: elimination half-life, $t_{1/2,\ \beta}$ (min); whole-body clearance, CL (mL/min); volume of the central compartment, V_c (mL); and area under the plasma concentration vs. time curve from time zero to infinity, $AUC_{0\text{-}inf}$ (min.µCi/mL).

Permeability-surface area (PS) products (mL/g/s) for ^{125}I-insulin uptake for various brain regions were calculated using the following equation:

$$PS = \frac{X_{brain}}{AUC_{plasma} \times W_{brain}}$$

where X_{brain} is the amount of ^{125}I activity (µCi) in the brain region, AUC_{plasma} is the area under the plasma concentration vs. time curve (µCi.min/mL) from 0-30 min estimated by the logarithmic trapezoidal method, and W_{brain} is the brain region weight (g). Accumulation of ^{125}I-insulin in the whole brain was expressed as:

$$\%\, ID/g = \frac{\left(\frac{X_{brain}}{Dose} \times 100\right)}{W_{brain}}$$

where $\%\, ID/g$ is the percent of the injected dose measured in the whole brain, normalized to the brain weight, X_{brain} is the amount of ^{125}I activity (µCi) measured in the brain, $Dose$ is the 100 or 500 µCi injected dose, and W_{brain} is the whole brain weight (g).

4.3.4. Dynamic SPECT/CT imaging of ^{125}I-insulin distribution to the brain after intravenous injection. Dynamic Single Photon Emission Computed Tomography/Computed Tomography (SPECT/CT) imaging studies were performed as described in our earlier publications (Swaminathan et al., 2017). Briefly, mice were anesthetized and catheterized as described above. A single dose of ^{125}I-insulin (500 µCi in PBS) was administered by intravenous bolus injection to the femoral vein. The mouse

was immediately transferred to a SPECT/CT scanner (Gamma Medica, Northridge, CA), and SPECT scans were taken at 1 min intervals over the next 40 min. This was followed by a 5 min CT scan to map the anatomical regions of interest (ROIs), including the brain. At the end of the imaging experiment, the mouse was transcardially perfused with excess PBS to flush any remaining ^{125}I activity from the vasculature, and a final SPECT scan was taken to measure ^{125}I-insulin brain accumulation.

The blood-to-brain influx clearance of ^{125}I-insulin was determined by Gjedde-Patlak graphical analysis (Patlak et al., 1983), which involves plotting:

$$\frac{X_{ROI}(t)}{C_p(t)} \text{ vs. } \frac{AUC_{p_0}^{\ t}}{C_p(t)}$$

where $X_{ROI}(t)$ is the amount of ^{125}I activity (µCi) in the brain ROI at time t (min), $C_p(t)$ is the concentration in plasma (µCi/mL) at time t (min), and $AUC_{p_0}^{\ t}$ is the area under the plasma concentration vs. time profile (µCi.min/mL) from time 0-t obtained by the logarithmic trapezoidal method. The slope obtained from regression of the linear portion of the curve estimates the brain influx clearance, K_i (mL/min). ^{125}I-insulin plasma concentrations at each imaging time point were predicted using the two-compartment pharmacokinetic parameters obtained in the preceding experiment.

4.3.5. Brain microvessel isolation. Brain microvessels were isolated from the different groups of mice as described previously (Gali et al., 2019). Briefly, the dissected brain hemispheres devoid of meninges were pooled together (n=3 per group), gently homogenized, subjected to digestion with dispase (0.1 g/100 mL, 1 h, 37 ^{o}C), and then centrifuged. The cell suspension was briefly digested with collagenase/dispase (3.5

mg/20 mL, 1 min, 37 ^{o}C) to detach the basement membrane, then centrifuged, and the suspension was filtered through a nylon mesh (180 µm). The resulting microcapillary fragments were purified by centrifugation in a Percoll density gradient. The brain capillary endothelial cells were collected from the interfacial layer.

4.3.6. Western blots. Western blots were performed as described in our previous publications (Gali et al., 2019). Brain microvessels were lysed in RIPA buffer containing protease and phosphatase inhibitors (Sigma-Aldrich, St. Louis). Total protein concentrations in the lysates were determined by bicinchoninic acid (BCA) assay (Pierce, Waltham, MA). Lysates (15 µg protein per lane) were loaded onto 4-12% Criterion XT precast gels and resolved by SDS-PAGE under reducing conditions (Bio-Rad Laboratories, Hercules, CA). Proteins were then electroblotted onto a 0.45 µm nitrocellulose membrane. Membranes were blocked with 5% non-fat dry milk protein (Bio-Rad Laboratories), then incubated overnight at 4 ^{o}C with primary antibodies (1:1000) against: insulin receptor β subunit (IR-β), protein kinase B (AKT), p-Akt (S473), glycogen synthase kinase-3β (GSK-3β), p-GSK-3β (S9), and GAPDH (Cell Signaling Technology, Danvers, MA). The next day, the blot was washed 4 times with TBST and incubated for 1.25 h with the appropriate anti-rabbit or anti-mouse horseradish peroxidase (HRP)-conjugated secondary antibody (1:5000, Cell Signaling Technology; Danvers, MA). After washing 4 times with TBST, the blot was incubated with SuperSignal™ West Dura Extended Duration Substrate (ThermoFisher Scientific; Waltham, MA) and then imaged by autoradiography using a CanoScan LiDE 110 film developer (Canon; Tokyo, Japan).

4.3.7. Statistical analysis. All statistical tests were performed using GraphPad Prism (GraphPad software; La Jolla, CA). A p value of ≤ 0.05 was considered statistically significant. Unpaired, two-tailed t-tests were used to compare the following in different groups of mice: % ID/g in the whole brain, and Patlak plot K_i estimates. Two-way ANOVA with Bonferroni's post-tests were used to compare the PS values in various brain regions of different groups of mice.

4.4. Results

4.4.1. Plasma pharmacokinetics of ^{125}I-insulin are unaltered in db/db mice. After a single bolus injection of ^{125}I-insulin into the femoral vein of db/+ or db/db mice, the tracer exhibited a bi-exponential decline in plasma concentrations with time (Fig. 4.4.1). This is consistent with our previous studies performed in wild-type mice (Zhou et al., 2022). No significant differences were observed in the two-compartment pharmacokinetic parameter estimates ($t_{1/2,\ \beta}$, CL, V_c and $AUC_{0\text{-}inf}$) obtained for ^{125}I-insulin in db/db mice compared to db/+ mice (Table 4.1).

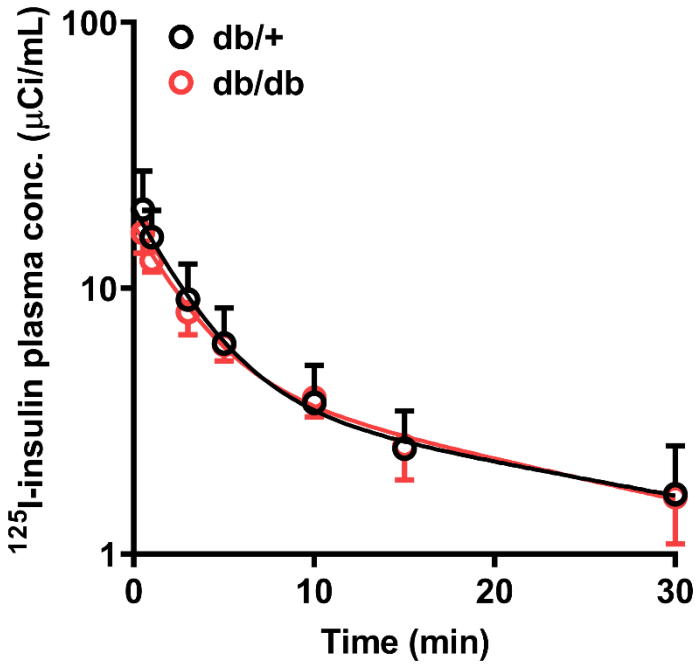

Figure 4.4.1. Plasma concentration vs. time profile of ^{125}I-insulin following a single bolus injection (100 µCi) into the femoral vein of db/+ or db/db mice. The observed values (circles; mean ± SD, n=3-4) are overlaid with the curve predicted from the two-compartment model parameters.

Parameter	db/+	db/db
$t_{1/2,\beta}$ (min)	24 ± 6	20 ± 5
CL (mL/min)	0.54 ± 0.05	0.59 ± 0.04
V_c (mL)	5.0 ± 0.5	5.8 ± 0.5
$AUC_{0\text{-inf}}$ (min.µCi/mL)	184 ± 17	167 ± 14

Table 4.1. Pharmacokinetic parameter estimates for ^{125}I-insulin in db/+ and db/db mice. The beta half-life ($t_{1/2,\beta}$), whole-body clearance (CL), volume of the central compartment (V_c), and area under the curve from time zero to infinity ($AUC_{0\text{-inf}}$) are shown. Parameter estimates are mean ± SE, n=3-4.

4.4.2. Plasma-to-brain distribution of ^{125}I-insulin is lowered in db/db mice. ^{125}I-insulin brain uptake at 30 minutes post-injection was assessed as the % of the injected dose that reached the brain per gram tissue (%ID/g). %ID/g in whole brain was ~2 fold lower in the db/db mice compared to the db/+ mice (Fig. 4.4.2A). In addition, permeability-surface area (PS) products were determined to assess the uptake of ^{125}I-insulin at specific brain regions upon intravenous administration. PS values for ^{125}I-insulin uptake to the hippocampus were ~2 fold lower in the db/db mice compared to db/+ mice (Fig. 4.4.2B).

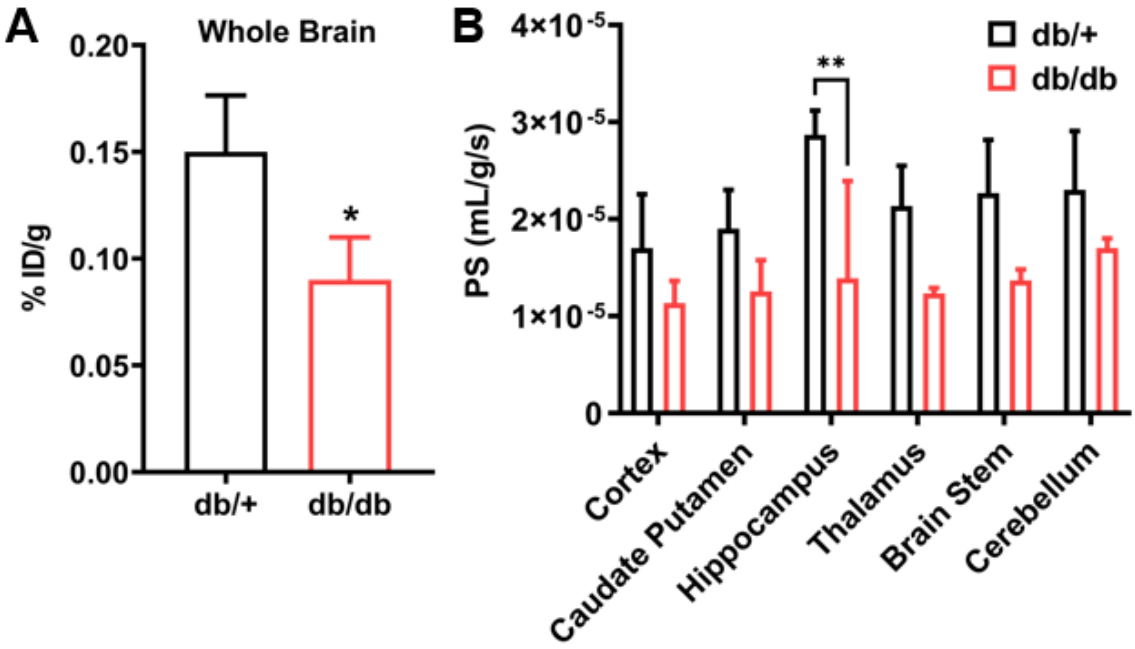

Figure 4.4.2. Blood-to-brain distribution of ^{125}I-insulin is lowered in db/db mice. (A) The brain accumulation of ^{125}I-insulin at 30 minutes post-injection was assessed as % of the injected dose measured in brain per gram tissue (%ID/g). Data are mean ± SD (n=3-4). *p<0.05; unpaired two-tailed t-test. (B) Permeability-surface area (PS) products for ^{125}I-insulin at various brain regions in db/db vs. db/+ mice. Data are mean ± SD (n=3-4). **p<0.01; two-way ANOVA with Bonferroni's post-tests.

Dynamic SPECT/CT imaging studies were performed to further examine brain uptake of ^{125}I-insulin upon intravenous administration in db/+ vs. db/db mice. Based on Patlak graphical analysis, the brain influx clearance (K_i) of ^{125}I-insulin was ~1.5 fold lower in db/db mice compared to db/+ mice (Fig. 4.4.3). The linear section of the Patlak plot corresponded to the imaging data between 5-30 min post-injection of ^{125}I-insulin.

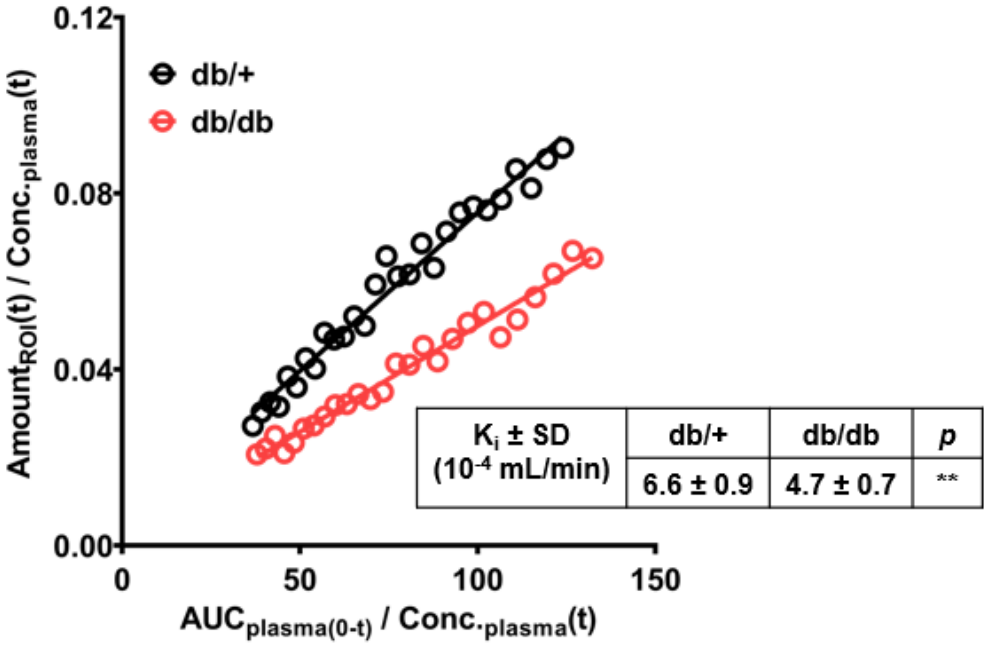

Figure 4.4.3. Dynamic SPECT/CT imaging of ^{125}I-insulin distribution to the brain after intravenous injection in db/db vs. db/+ mice. Representative Patlak plot of ^{125}I-insulin distribution to the brain, in which the brain influx clearance (K_i) is estimated from the slope. Inset table values are group mean ± SD (n=4-5). ***p*<0.01; unpaired two-tailed *t*-test

4.4.3. Plasma pharmacokinetics of ^{125}I-insulin in WT and APP/PS1 mice on regular-chow or high-fat diet. Plasma pharmacokinetic parameter estimates for ^{125}I-insulin in healthy control mice (WT-RC), mice with T2DM alone (WT-HF), mice with AD alone (APP/PS1-RC), and mice that manifest AD and T2DM (APP/PS1-HF) are provided in Table 4.2. ^{125}I-insulin plasma pharmacokinetics were not substantially altered when

comparing WT-RC, WT-HF and APP/PS1-RC mice (Fig. 4.4.4). However, a modest reduction was observed in plasma distribution volume and plasma exposure (AUC) of ^{125}I-insulin in the APP/PS1-HF mice compared to the other three groups of mice (Table 4.2).

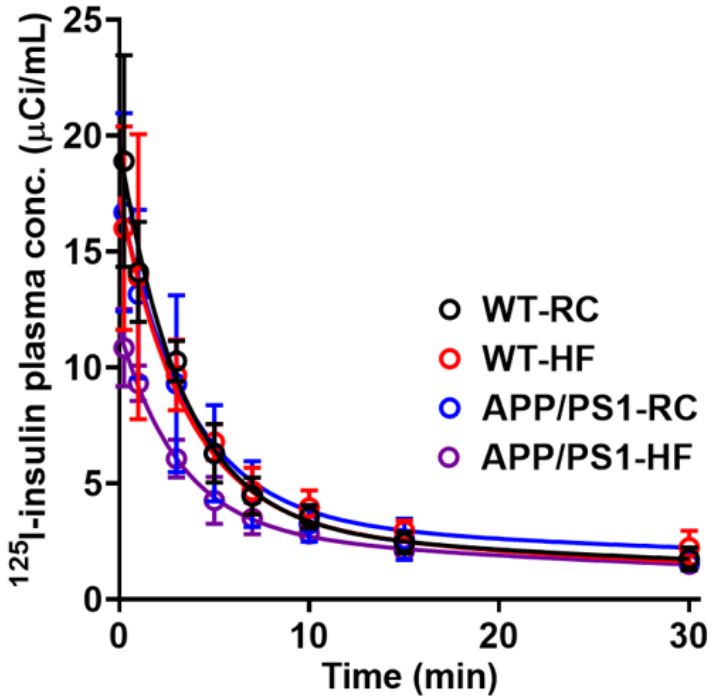

Figure 4.4.4. Plasma concentration vs. time profile of ^{125}I-insulin following a single bolus injection (100 μCi) into the femoral vein of WT or APP/PS1 mice maintained on regular-chow (RC) or high-fat (HF) diet. Observed values (circles; mean ± SD, n=4) are overlaid with the curve predicted from the two-compartment model parameters.

Parameter	Mean ± SE			
	WT-RC	WT-HF	APP/PS1-RC	APP/PS1-HF
CL (mL/min)	0.5 ± 0.1	0.3 ± 0.1	0.5 ± 0.2	0.6 ± 0.1
V_1 (mL)	5.1 ± 0.3	5.8 ± 0.2	5.8 ± 0.1	8.6 ± 0.1
V_{SS} (mL)	18.2 ± 4.3	20.4 ± 4.2	17.1 ± 7.6	23.5 ± 3.0
$t_{1/2,\beta}$ (min)	35.4 ± 14.1	49.4 ± 21.0	29.2 ± 22.4	30.7 ± 8.0
AUC_0^∞ (min x μCi/mL)	214 ± 39	292 ± 72	188 ± 68	158 ± 23

Table 4.2. Plasma pharmacokinetic parameter estimates for ^{125}I-insulin in WT or APP/PS1 mice maintained on regular-chow (RC) or high-fat (HF) diet. Values are mean ± SE (n=4).

4.4.4. Plasma-to-brain distribution of ^{125}I-insulin is lowest in APP/PS1 mice on high-fat diet, followed by APP/PS1 mice on regular-chow diet and WT mice on high-fat diet, when compared to the healthy controls. ^{125}I-insulin brain uptake at 30 minutes post-injection was assessed as % of the injected dose that reached the brain per gram tissue (%ID/g). %ID/g of ^{125}I-insulin in the whole brain was ~1.5 fold lower in APP/PS1-RC mice compared to WT-RC mice, and ~2 fold lower in APP/PS1-HF mice compared to WT-RC mice (Fig. 4.4.5).

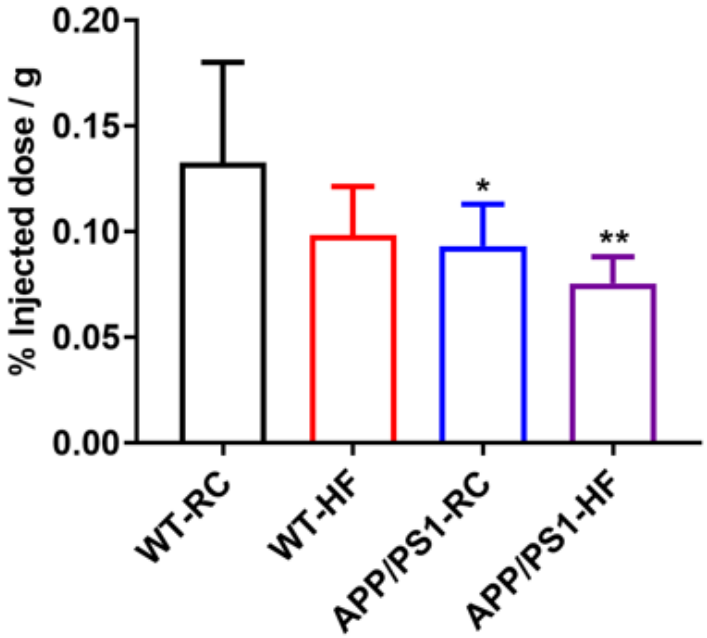

Figure 4.4.5. Blood-to-brain distribution of ^{125}I-insulin is lowest in APP/PS1-HF mice, which manifest both AD and T2DM. The brain accumulation of ^{125}I-insulin at 30 minutes post-injection was assessed as % of injected dose measured in whole brain per gram

tissue (%ID/g). Data are mean ± SD (n=4). *p<0.05, **p<0.01; one-way ANOVA with Bonferroni's post-tests.

Dynamic SPECT/CT imaging studies were performed to further assess brain distribution of ^{125}I-insulin upon intravenous administration in the WT and APP/PS1 mice maintained on a regular-chow (RC) or high-fat (HF) diet. Based on Patlak graphical analysis, brain influx clearance (K_i) of ^{125}I-insulin was found to be lowest in APP/PS1-HF mice that manifest both AD and T2DM, followed by APP/PS1-RC mice and WT-HF mice, when compared to healthy WT-RC control mice (Fig. 4.4.6).

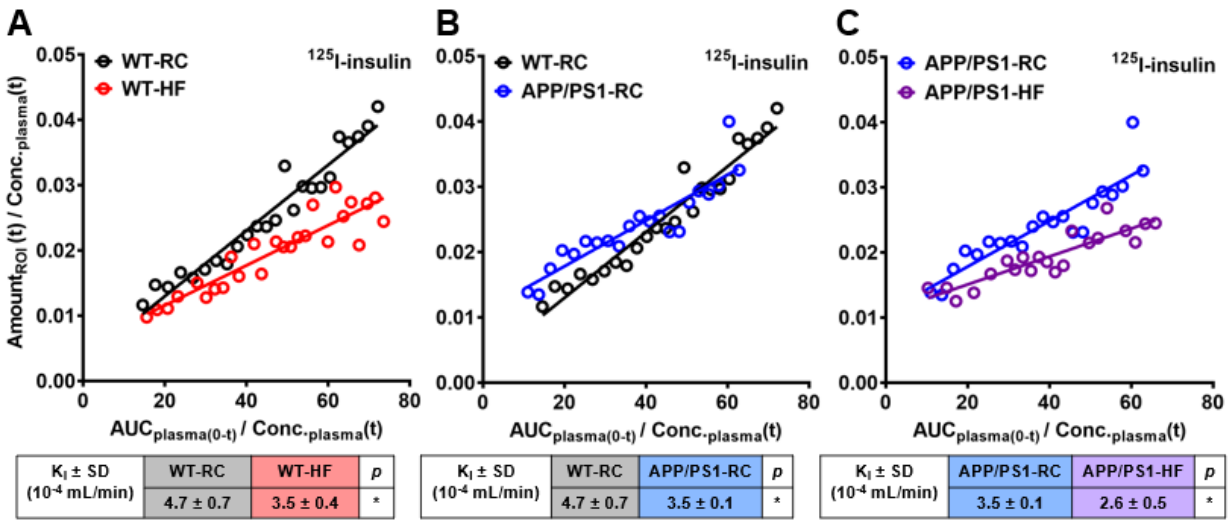

K_i ± SD (10^{-4} mL/min)	WT-RC	WT-HF	p
	4.7 ± 0.7	3.5 ± 0.4	*

K_i ± SD (10^{-4} mL/min)	WT-RC	APP/PS1-RC	p
	4.7 ± 0.7	3.5 ± 0.1	*

K_i ± SD (10^{-4} mL/min)	APP/PS1-RC	APP/PS1-HF	p
	3.5 ± 0.1	2.6 ± 0.5	*

Figure 4.4.6. Dynamic SPECT/CT imaging of ^{125}I-insulin distribution to brain after intravenous injection in WT or APP/PS1 mice maintained on a regular-chow (RC) or high-fat (HF) diet. Representative Patlak plots of ^{125}I-insulin distribution to the brain, in which brain influx clearance (K_i) is estimated from the slope. Inset table values are group mean ± SD (n=4). *p<0.05; unpaired two-tailed t-test.

4.4.5. Insulin signaling pathways in brain microvessels are most severely compromised in APP/PS1 mice on high-fat diet, followed by APP/PS1 mice on regular-chow diet and

WT mice on high-fat diet, when compared to the healthy controls. Brain microvessels were harvested from the four groups of mice, and western blots were performed to assess expression/activity of various insulin signaling kinases (Fig 4.4.7). Compared to the microvessels obtained from the healthy WT-RC mice, both the WT-HF and APP/PS1-RC mice showed reduced expression of IR-β and reduced phosphorylation of both AKT and GSK-3β. Moreover, the largest reductions were observed in the APP/PS1-HF mice that manifest both AD and T2DM (Fig. 4.4.7). In brain tissue lysate, minimal differences were observed in the expression/phosphorylation of the insulin signaling kinases. However, a substantial reduction in GSK-3β phosphorylation, which is involved in tau neurofibrillary tangle formation, was observed in the APP/PS1-HF mice compared to the other three groups (Fig. 4.4.7).

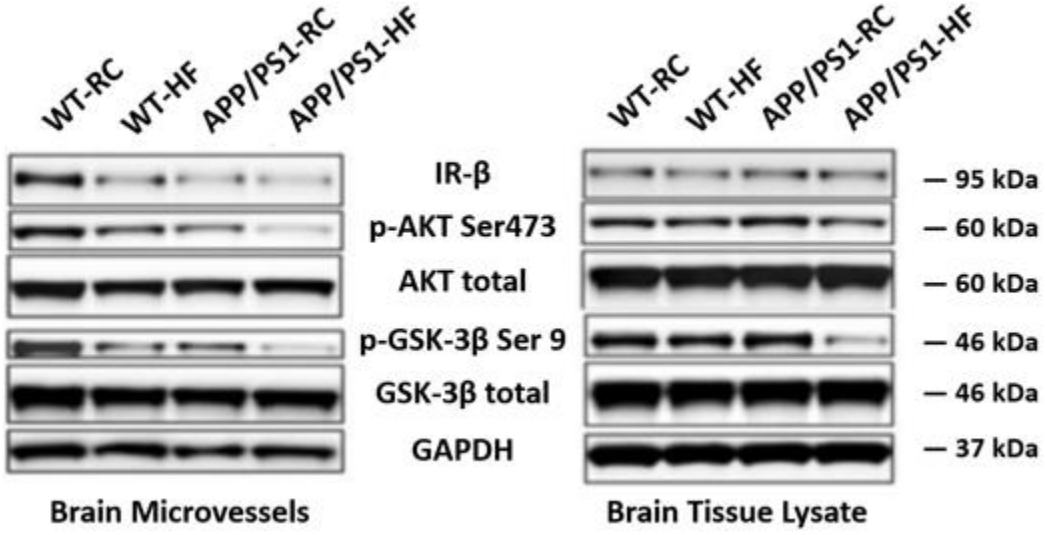

Figure 4.4.7. Western blots for various insulin signaling kinases performed on brain microvessels and brain tissue lysate harvested from the WT or APP/PS1 mice maintained on a regular-chow (RC) or high-fat (HF) diet. Representative blots are shown.

4.5. Discussion and Conclusions

Elevated plasma insulin levels, known as hyperinsulinemia, is highly prevalent among T2DM patients and represents a major risk factor for AD (Luchsinger et al., 2004). Elevated plasma levels could lead to overstimulation of IR expressed on the luminal side of BBB endothelial cells, resulting in negative feedback mechanisms that downregulate IR and trigger BBB insulin resistance. A recent study demonstrated that high-fat diet led to increased IR expression in tandem with decreased IR signaling in brain microvessels harvested from mice (Watson et al., 2022). Thus, T2DM and its associated pathologies are associated with various deleterious changes in BBB dysfunction, which have been linked to the etiology of AD.

Over the last 5 years, substantial controversy has arisen surrounding the molecular mechanisms and regulators of insulin transport at the BBB. Historically, the insulin receptor (IR) was believed to be responsible for mediating receptor-mediated transcytosis of insulin at the BBB (Rhea and Banks, 2021). This belief was largely based on earlier studies that demonstrated insulin binding to IR in isolated brain microvessels (Frank and Pardridge, 1981; Yu et al., 2006), and subsequent studies that showed insulin uptake/transport in BBB cells is blocked by a selective IR inhibitor, S961 (Meijer et al., 2016; Gray et al., 2017). However, it was more recently reported that insulin uptake to the brain is maintained in endothelial-specific IR knockout mice, as well as in wild-type mice upon treatment with S961 (Rhea et al., 2018). A separate group further demonstrated that insulin transport across an in vitro BBB cell model was not inhibited by S961 (Hersom et al., 2018). This led the authors to conclude that IR is not required for insulin transport at the BBB. An alternate explanation is that compensatory

mechanisms may still enable insulin transport at the BBB, such as via the IGF-1 receptor (Yu et al., 2006).

In peripheral tissues, it has been shown that insulin transport across the vascular endothelium is mediated by insulin binding to IR (Hachiya et al., 1988; Wang et al., 2006; Jaldin-Fincati et al., 2018). The insulin-IR complex is then internalized, allowing for subsequent transcytosis across the cell (Fagerholm et al., 2009). While it is possible that insulin transport across BBB endothelium follows a different mechanism than insulin transport across vascular endothelium that lines peripheral tissues, further studies are needed to clarify the role of IR in insulin transport at the BBB. Additionally, there are conflicting reports on the role of clathrin vs. caveolin in mediating insulin endocytosis in vascular endothelial cells (Wang et al., 2011; Azizi et al., 2015; Wang et al., 2015), which further highlights the need for additional mechanistic studies.

In summary, findings from this chapter indicate that insulin distribution from blood to brain is decreased in mouse models of T2DM or AD compared to healthy mice. This trend was observed in two different mouse models of T2DM/insulin resistance: db/db mice that are leptin receptor deficient and wild type mice maintained on a high fat diet. A similar trend was observed in APP/PS1 transgenic mice, which overexpress Aβ and develop AD. Moreover, insulin distribution to the brain was lowest in APP/PS1 transgenic mice maintained on high fat diet, which manifest both AD and T2DM pathologies. The reductions in insulin distribution to the brain were associated with reduced expression/activity of key insulin signaling kinases at the BBB, assessed by western blots performed on brain microvessels harvested from the mice. Together, these findings suggest that combining the two pathologies of T2DM and AD amplified

the deficits in insulin transport and signaling at the BBB that were observed for each pathology alone. These results could potentially help explain why AD patients with T2DM as a comorbidity tend to exhibit severe brain insulin resistance that may exacerbate progression of AD.

Chapter 5: Molecular mechanisms by which insulin resistance contributes to BBB dysfunction

5.1. Synopsis

The BBB is instrumental in clearing toxic metabolites such as Aβ peptides from the brain, and in delivering essential nutrients to the brain, such insulin. In Alzheimer's disease (AD) brain, increased Aβ levels are paralleled by decreased insulin levels, which are accompanied by insulin signaling deficits at the BBB. Thus, we investigated the impact of insulin-like growth factor and insulin receptor (IGF1R and IR) signaling on Aβ and insulin trafficking at the BBB. Following intravenous infusion of an IGF1R/IR kinase inhibitor (AG1024) in wild-type mice, BBB trafficking of ^{125}I radiolabeled Aβ peptides and insulin were assessed by dynamic SPECT/CT imaging. Brain efflux of ^{125}I-Aβ42 decreased upon AG1024 treatment. Additionally, brain influx of ^{125}I-insulin, ^{125}I-Aβ42, ^{125}I-Aβ40 and ^{125}I-albumin (BBB integrity marker) were decreased, increased, unchanged and unchanged, respectively, upon AG1024 treatment. Subsequent mechanistic studies were performed using an in vitro BBB cell model. Cell uptake of ^{125}I-insulin, ^{125}I-Aβ42 and ^{125}I-Aβ40 were decreased, increased and unchanged, respectively, upon AG1024 treatment. Further, AG1024 reduced phosphorylation of insulin signaling kinases (Akt and Erk) and membrane expression of Aβ and insulin

trafficking receptors (LRP-1, RAGE and IR-β). These findings reveal that insulin signaling differentially regulates BBB trafficking of Aβ peptides and insulin. Moreover, deficits in IGF1R and IR signaling, as observed in the brains of type II diabetes and AD patients, are expected to increase Aβ accumulation while decreasing insulin delivery to the brain, which has been linked to the progression of cognitive decline in AD.

5.2. Background

The BBB plays an essential role in maintaining the brain microenvironment by facilitating transport of endogenous solutes between the systemic circulation and brain interstitial fluid. The exquisite selectivity of the BBB endothelium is achieved by the presence of tight junctions and specialized receptors/transporters, along with their associated regulatory networks. These properties enable highly selective uptake of essential nutrients to the brain, while greatly restricting uptake of toxic metabolites circulating in blood. The BBB also functions as a clearance portal to remove metabolic waste products from the brain, such as amyloid beta (Aβ) peptides. Impairments in BBB transport functions are among the earliest neuropathological changes documented in patients with Alzheimer's disease (AD) (Zlokovic, 2011).

BBB dysfunction contributes to increased levels of toxic Aβ peptides in brain, which represents one of the primary neuropathological hallmarks of AD. Two major Aβ isoforms accumulate in AD brain: Aβ42, which is regarded as the most neurotoxic and amyloidogenic isoform (Qiu et al., 2015), and Aβ40, which is less neurotoxic and was shown to be protective against Aβ42 aggregation and toxicity (Kim et al., 2007; Murray et al., 2009). While Aβ42 is the major isoform present in parenchymal plaques, Aβ40 is

the major isoform present in cerebrovascular amyloid deposits and gives rise to cerebral amyloid angiopathy (CAA).

Aβ peptides are produced primarily in the brain and to a lesser extent in the periphery. Clearance of Aβ peptides from the brain is handled by receptor-mediated transcytosis at the BBB along with perivascular drainage. Although Aβ concentrations in plasma are ~6 fold lower than the soluble Aβ concentrations in the brain, the absolute amount of Aβ in plasma is estimated to be ~10 fold greater than the amount of soluble Aβ in the brain (Deane et al., 2004). It was also reported that upon systemic injection, Aβ peptides were rapidly incorporated into existing Aβ plaques in the brains of aged monkeys (Mackic et al., 2002). Moreover, elevated plasma Aβ levels are associated with increased AD risk in elderly patients (Okereke et al., 2009). Thus, systemic Aβ is proposed to contribute to brain Aβ load directly, by Aβ trafficking into the brain, and indirectly, by impairing the ability of the BBB to clear Aβ from the brain.

Transcytosis of Aβ at the BBB in the blood-to-brain direction is predominantly mediated by the receptor for advanced glycation end products (RAGE), and in the brain-to-blood direction by the low-density lipoprotein receptor related protein 1 (LRP1) (Deane et al., 2004). These bidirectional transcytotic processes maintain a dynamic equilibrium between the soluble Aβ pools in brain and plasma (Xin et al., 2018). We previously reported that intravenous bolus injection of insulin altered brain influx of Aβ peptides in mice, and that insulin treatment increased plasma membrane levels of RAGE and LRP-1 in BBB cells in vitro (Swaminathan et al., 2018a). These findings suggest that insulin signaling could be involved in the regulation of Aβ transcytosis at the BBB.

In AD brain, increased levels of toxic Aβ peptides are paralleled by decreased levels of the essential nutrient insulin, which is needed for neurotrophic functions. Insulin in the brain is derived from the systemic circulation via receptor-mediated transcytosis at the BBB (Woods et al., 2003). Decreased brain insulin levels are associated with the progression of cognitive decline in patients with either AD or type II diabetes mellitus (T2DM) (Gil-Bea et al., 2010; Heni et al., 2014). Brain insulin resistance is further aggravated in AD patients with T2DM (Liu et al., 2011), thus making T2DM a major risk factor for AD (Huang et al., 2014).

Insulin signaling pathways are critical for neurobiological functions such as energy metabolism (Jauch-Chara et al., 2012), neuronal growth/division (Gu et al., 2014), and learning/memory (Dou et al., 2005). Insulin signaling is mediated by the insulin receptor (IR) and insulin-like growth factor 1 receptor (IGF1R), which converge at several downstream signaling kinases. The two major signaling arms are the PI3K/Akt and MAPK/Erk pathways. Both T2DM and AD patients demonstrate reduced brain expression of IR and altered phosphorylation of kinases in the PI3K/Akt pathway (Liu et al., 2011). Expression of IGF1R is also reduced in AD patient brains (Freude et al., 2009). These signaling deficits engender brain insulin resistance and are thought to contribute to AD progression (Arnold et al., 2018). However, the functional role of insulin signaling at the BBB and its contribution to AD remain unclear (Rhea and Banks, 2019).

To investigate the role of cerebrovascular insulin signaling on BBB trafficking of key endogenous macromolecules, we assessed the brain efflux of ^{125}I radiolabeled Aβ42 in wild-type mice after systemic infusion of AG1024, an IGF1R/IR dual kinase inhibitor (Párrizas et al., 1997). Further, we examined the effects of AG1024 on blood-

to-brain influx of ^{125}I labeled insulin, Aβ42, Aβ40 and albumin in wild-type mice. The in vivo findings were supported by cell uptake, signaling and membrane expression studies performed using an in vitro BBB cell culture model. The findings indicate that downregulation of IR and IGF-1R kinase activity, which is observed under insulin resistance, reduces the brain efflux of Aβ42 and differentially modulates brain influx of Aβ peptides and insulin in a manner that is expected to exacerbate AD pathology.

5.3. Materials & Methods

5.3.1. Animals. B6SJLF1 mice were obtained from Jackson Laboratory (Bar Harbor, ME). Mice were housed in the Mayo Clinic animal facility and were provided with food and water ad libitum. Female mice around four months of age were used in all studies. All procedures involving the use of animals were approved by the Mayo Institutional Animal Care and Use Committee and were performed in accordance with the Guide for the Care and Use of Laboratory Animals provided by the National Institute of Health.

5.3.2. Radioiodination of insulin, Aβ peptides and albumin. Recombinant human insulin (Sigma-Aldrich, St. Louis, MO), synthetic Aβ40 or Aβ42 (AAPPtec, LLC; Louisville, KY), and bovine serum albumin (BSA; Sigma-Aldrich, St. Louis, MO) were labeled with ^{125}I radionuclide (PerkinElmer Life and Analytical Sciences, Boston, MA) using the chloramine-T procedure described previously (Poduslo et al., 1994; Kandimalla et al., 2005). Unconjugated ^{125}I was removed by dialysis. Purity of ^{125}I-labeled proteins was assessed by trichloroacetic acid (TCA) precipitation. Over 95% of the total radioactivity counts were precipitated with TCA.

5.3.3. Dynamic SPECT/CT imaging of ^{125}I-Aβ42 efflux after intracerebral injection.

These experiments were performed as described in our previous publications (Swaminathan et al., 2018a; Swaminathan et al., 2020)). Briefly, mice were anesthetized using 1.5% isoflurane with 4 L/min oxygen and the left internal carotid artery was catheterized. The AG1024 (30 µg; Selleck Chem, Houston, TX) or vehicle control (7% DMSO in 150 µL phosphate-buffered saline; PBS) was infused over 15 min into the left internal carotid artery. Following that, unlabeled insulin (100 µg in 50 µL PBS) was infused over 5 min into the left internal carotid artery. Fifteen minutes after the end of the infusion, a bolus of ^{125}I-Aβ42 (3 µCi in 1 µL PBS) was injected directly into the right hippocampus. The mouse was immediately placed inside a SPECT/CT scanner (Gamma Medica, Northridge, CA) and imaged at 5 min intervals over the course of 100 min, followed by a 5 min CT scan to map the anatomical regions of interest (ROIs). To correct for minor variations in the injected dose, the data was normalized to the ^{125}I-Aβ42 concentration (µCi/cc) in the brain ROI at the first time point. Normalized concentrations were plotted on the natural log scale against time. Given the mono-exponential decline in ^{125}I-Aβ42 brain concentrations with time, the slope obtained after linear regression corresponds to the brain efflux rate constant, k (min^{-1}).

5.3.4. Plasma pharmacokinetics and brain permeability of ^{125}I-insulin. These experiments were conducted as described in our previous publications (Kandimalla et al., 2005; Swaminathan et al., 2018a). Briefly, mice were anesthetized using 1.5% isoflurane with 4 L/min oxygen. The femoral vein, femoral artery, and left internal carotid artery were catheterized. The AG1024 (30 µg; Selleck Chem, Houston, TX) or vehicle

control (7% DMSO in 150 µL PBS) was infused over 15 min into the left internal carotid artery. Fifteen minutes after the end of the infusion, a bolus of ^{125}I-insulin (100 µCi) was injected into the femoral vein. Blood samples (20 µL) were collected from the femoral artery at 0.25, 1, 3, 5, 7, 10, 15, and 30 min post-insulin injection. After separating the plasma, the protein fraction was isolated by TCA precipitation, and then assayed for ^{125}I radioactivity in the gamma counter (Cobra II; Amersham Biosciences Inc., Piscataway, NJ). Immediately after obtaining the final sample, the mouse was euthanized by transcardial perfusion with excess PBS to flush any residual ^{125}I activity from the vasculature. The whole brain was dissected and assayed for ^{125}I activity using the gamma counter.

The ^{125}I-insulin plasma concentration vs. time profile was fitted to a two-compartment model using WinNonlin Phoenix (Pharsight, Mountain View, CA):

$$C_p(t) = Ae^{-\alpha t} + Be^{-\beta t}$$

Where $C_p(t)$ is the concentration (µCi/mL) at time t (min), $A + B$ is the concentration at time zero, and α and β are the rate constants.

The permeability-surface area (PS) product (mL/g/s) of ^{125}I-insulin was determined as described previously (Poduslo et al., 2001), using the following equation:

$$PS = \frac{X_{brain}}{AUC_{plasma} \times W_{brain}}$$

where X_{brain} is the amount of ^{125}I activity (µCi) in the whole brain, AUC_{plasma} is the area under the plasma concentration vs. time profile (µCi.min/mL) from 0-30 min obtained by the logarithmic trapezoidal method, and W_{brain} is the brain weight (g).

5.3.5. Dynamic SPECT/CT imaging of ^{125}I-insulin and ^{125}I-Aβ distribution to the brain.

These experiments were performed as described in our earlier publications (Swaminathan et al., 2018a). Briefly, mice were anesthetized, catheterized, and infused with AG1024 (30 µg) or vehicle control as described above. Fifteen minutes after the end of infusion, a bolus of ^{125}I-insulin (500 µCi) was injected into the femoral vein. The mouse was then immediately placed inside a SPECT/CT scanner and imaged at 1 min intervals over the course of 40 min, followed by a 5 min CT scan. For ^{125}I-Aβ studies, after infusion with AG1024 or vehicle, unlabeled insulin (100 µg in 50 µL PBS) was infused over 5 min into the left internal carotid artery. Fifteen minutes after the end of the insulin infusion, a bolus of ^{125}I-Aβ42 or ^{125}I-Aβ40 (500 µCi) was injected into the femoral vein, and the mouse was imaged as described above.

Blood-to-brain influx clearances of ^{125}I-insulin, ^{125}I-Aβ42, and ^{125}I-Aβ40 were determined by Gjedde-Patlak graphical analysis (Patlak et al., 1983), which involves plotting:

$$\frac{X_{ROI}(t)}{C_p(t)} \text{ vs. } \frac{AUC_{p_0}^{\ t}}{C_p(t)}$$

where $X_{ROI}(t)$ is the amount of ^{125}I activity (µCi) in the brain ROI at time t (min), $C_p(t)$ is concentration in plasma (µCi/mL) at time t (min), and $AUC_{p_0}^{\ t}$ is the area under the plasma concentration vs. time profile (µCi.min/mL) from time 0-t obtained by the logarithmic trapezoidal method. The slope obtained from regression of the linear portion of the curve corresponds to the brain influx clearance, K_i (mL/min). To construct plots for ^{125}I-insulin, plasma concentrations at each imaging time point were predicted using the two-compartment pharmacokinetic parameters modeled from the preceding experiment.

To construct plots for ^{125}I-Aβ42 and ^{125}I-Aβ40, concentrations measured in the heart ROI during the imaging experiment were used as a surrogate for the plasma concentrations. Use of heart imaging data as a surrogate for plasma pharmacokinetics is a well-established method (Bao et al., 2019), but was not suitable for the ^{125}I-insulin studies due to substantial accumulation of insulin in heart tissue.

5.3.6. Brain accumulation of ^{125}I-insulin and ^{125}I-Aβ. At the end of the SPECT/CT imaging experiment, the mice were euthanized by transcardial perfusion with excess PBS. Individual brain regions were dissected and assayed for ^{125}I activity using a gamma counter. The accumulation of ^{125}I-insulin, ^{125}I-Aβ42 or ^{125}I-Aβ40 in the cortex, caudate putamen, hippocampus, thalamus, brain stem or cerebellum was expressed as:

$$\%\,\mathrm{ID/g} = \frac{\left(\frac{\mathrm{X_{brain}}}{\mathrm{Dose}} \times 100\right)}{\mathrm{W_{brain}}}$$

where $\%\,\mathrm{ID/g}$ is the percent of the injected dose measured in the brain region per gram of tissue, $\mathrm{X_{brain}}$ is the amount of ^{125}I activity (μCi) in the brain region, Dose is the 500 μCi injected dose, and $\mathrm{W_{brain}}$ is the brain region weight (g).

5.3.7. Brain accumulation of ^{125}I-BSA. Mice were anesthetized, catheterized, and infused with AG1024 (30 μg) or vehicle control as described above. Following that, a mixture of ^{125}I-BSA (100 μCi) and unlabeled insulin (100 μg) in 50 μL of PBS was infused over 5 min into the left internal carotid artery. Fifteen minutes after the end of the infusion, the mice were euthanized by transcardial perfusion with excess PBS. Individual brain regions were dissected and assayed for ^{125}I activity in the gamma

counter. Accumulation of ^{125}I-BSA in various brain regions was assessed as the $\%\,ID/g$ as described above.

5.3.8. Cell culture. The immortalized human cerebral microvascular endothelial cell line (hCMEC/D3) was kindly obtained as a gift from P-O Couraud (Institut Cochin, France). Cells were cultured as described previously (Weksler et al., 2013; Zhou et al., 2019). Briefly, cells were seeded at 25,000 cells per cm^2 in 75 cm^2 flasks or 6-well plates coated with rat tail collagen (Sigma-Aldrich). Cells were cultured in endothelial cell basal media (Sigma-Aldrich) with the following additives: 1% v/v penicillin-streptomycin (Sigma-Aldrich), 1.4 mM hydrocortisone (Sigma-Aldrich), 5 mg/ml ascorbic acid (Sigma-Aldrich), 1% v/v chemically defined lipid concentrate (ThermoFisher Scientific, Waltham, MA), 10 mM HEPES (Sigma-Aldrich), 1 ng/ml recombinant human fibroblast growth factor-basic (PeproTech, Rocky Hill, NJ), and 5% v/v fetal bovine serum (Atlanta Biologicals, Flowery Branch, GA). Media was changed every 2 days until the cells reached confluence (~4 days total). The day before the experiments, the media was replaced with the same media containing 1% v/v fetal bovine serum. Cells from passages 32-34 were used for the experiments.

5.3.9. Cell uptake of insulin and Aβ peptides after AG1024 treatment. Cell uptake of fluorescently-labeled insulin in human cerebral microvascular endothelial cell (hCMEC/D3) monolayers was assessed by flow cytometry as described in our previous publications (Swaminathan et al., 2020). Briefly, hCMEC/D3 monolayers cultured on 6-well plates were treated with or without AG1024 (100 µM) in DMEM for 30 min at 37 ^{o}C. Alexa Fluor 647-labeled insulin (Nanocs, New York, NY) was then spiked into the media

(final conc. = 200 nM), and the cells were incubated for another 30 min at 37 ^{o}C. Following which, the cells were washed 3x with ice-cold PBS, trypsinized, and then fixed in 4% paraformaldehyde. The fluorescence uptake was measured by flow cytometry (BD Biosciences, San Jose, CA).

For Aβ cell uptake studies, the hCMEC/D3 monolayers cultured on 12-well plates were treated with or without AG1024 (100 µM) in DMEM for 10 min at 37 ^{o}C. Unlabeled insulin was then spiked into the medium (final conc. = 100 nM), and the cells were incubated for another 20 min at 37 ^{o}C. Then ^{125}I-Aβ42 or ^{125}I-Aβ40 was spiked into the medium (final conc. = 5 µCi/mL), and the cells were incubated for another 60 min at 37 ^{o}C. Following that, the cells were washed three times with ice-cold PBS and lysed in RIPA buffer. The ^{125}I activity in the cell lysate was measured using a gamma counter.

5.3.10. Western blot. Western blots were performed as described in our previous publications (Swaminathan et al., 2018a; Gali et al., 2019). Briefly, hCMEC/D3 monolayers cultured on 6-well plates were treated with or without AG1024 (100 µM) in DMEM for 10 min at 37 ^{o}C. Unlabeled insulin was spiked into the medium (final conc. = 100 nM), and the cells were incubated for another 20 min at 37 ^{o}C. Following that, the cells were washed three times with PBS and lysed in RIPA buffer containing protease and phosphatase inhibitors (Sigma-Aldrich, St. Louis). Total protein concentrations in the lysates were determined by bicinchoninic acid (BCA) assay (Pierce, Waltham, MA). The lysates (15 µg protein per lane) were loaded onto 4-12% Criterion XT precast gels and resolved by SDS-PAGE under reducing conditions (Bio-Rad Laboratories, Hercules, CA). The proteins were then electroblotted onto a 0.45 µm nitrocellulose

membrane. Membranes were blocked with 5% non-fat dry milk protein (Bio-Rad Laboratories), then incubated overnight at 4 ^{o}C with primary antibodies (1:1000) against: Akt, p-Akt (S473), Erk, p-Erk(T42/Y44), and Vinculin (Cell Signaling Technology, Danvers, MA), followed by incubation with infrared dye conjugated secondary antibody (1:2000) for 1 h at room temperature (LI-COR, Lincoln, NE). Immuno-reactive bands were then imaged (Odyssey CLx; LI-COR, Lincoln, NE) and the band intensities were quantified by densitometry (Image Studio Lite). Vinculin was used as the loading control.

5.3.11. Subcellular fractionation. The hCMEC/D3 monolayers cultured on T-75 flasks were treated with or without AG1024 (100 µM) in DMEM for 10 min at 37 ^{o}C. Unlabeled insulin was spiked into the medium (final conc. = 100 nM), and the cells were incubated for another 20 min at 37 ^{o}C. Following that, the cells were washed with PBS, collected using a cell scraper, and centrifuged to pellet the cells. The pellet was resuspended in lysis buffer (5 mM Tris-HCL, 2 mM EDTA, pH 7.4, with protease and phosphatase inhibitors), followed by 15 strokes with a handheld homogenizer. Lysate was centrifuged at 15,000 x g for 15 min at 4 ^{o}C to pellet the cell debris. The supernatant was then centrifuged at 100,000 x g for 60 min at 4 ^{o}C to pellet the membrane components. The pellet was rinsed with lysis buffer and centrifuged twice at 100,000 x g for 15 min at 4 ^{o}C to eliminate cytoplasmic remnants. The membrane pellet was resuspended in lysis buffer, incubated on ice for 30 min, and then sonicated for 5 min. Total protein concentrations in the membrane fraction were determined by BCA assay. Western blots were performed as described above using primary antibodies (1:1000) against: LRP-1,

RAGE, IR-β (Cell Signaling Technology, Danvers, MA), and Calnexin (Santa Cruz Biotechnology, Dallas, TX). Calnexin was used as the loading control.

5.3.12. *Cell uptake of insulin and Aβ peptides after treatment with various insulin signaling inhibitors.* The cell uptake of AF647-insulin, ^{125}I-Aβ42 and ^{125}I-Aβ40 were assessed in hCMEC/D3 monolayers cultured on 12 well plates after treatment with the following insulin signaling inhibitors: trametinib (MEK inhibitor), MK2206 (AKT inhibitor), rapamycin (mTOR inhibitor), or genistein (EGFR inhibitor). For AF647-insulin studies, cells were treated with or without trametinib (1 μM), MK2206 (1 μM), trametinib+MK2206 (1 μM+1 μM), or rapamycin (100 nM) in D3 culture media supplemented with 1% FBS, for 24 hours at 37 ºC. After that, AF647-insulin was spiked into the media (6.25 nM final conc.), then continued incubating at 37 ºC for 30 min. Cells were washed and prepared for flow cytometry as described in section 5.3.9. AF647 fluorescence uptake was measured.

For Aβ cell uptake studies, hCMEC/D3 monolayers were treated with or without trametinib (1 μM), MK2206 (12.5 μM), genistein (10 μM), or rapamycin (1 μM) in DMEM for 10 min at 37 ºC. Unlabeled insulin was then spiked into the media (100 nM final conc.), and the cells were incubated for another 20 min at 37 ºC. Then ^{125}I-Aβ42 or ^{125}I-Aβ40 was spiked into the medium (5 μCi/mL final conc.), and the cells were incubated for another 60 min at 37 ºC. Cells were washed and prepared for gamma counting as described in section 5.3.9. ^{125}I activity in the cell lysate was measured.

5.3.13. *Cell uptake of insulin after treatment with S961 or Aβ peptides.* The hCMEC/D3 monolayers cultured on 12 well plates were treated for 30 min at 37 ºC with or without

varied concentrations (1 nM to 10 µM) of the following agents in DMEM: S961, a specific insulin receptor antagonist, Aβ42 or Aβ40. Following that, AF647-insulin was spiked into the media (final conc. of 3.12 or 12.5 nM), then continued incubating at 37 ^{o}C for 30 min. Cells were washed and prepared for flow cytometry as described in section 5.3.9. The AF647-insulin fluorescence uptake was measured.

The half maximal inhibitory concentration (IC_{50}) of S961, Aβ42 or Aβ40 in reducing the cell uptake of 3.12 nM AF647-insulin was determined using the following equation:

$$Y = \text{Bottom} + \frac{\text{Top} - \text{Bottom}}{1 + \left(\frac{X}{IC_{50}}\right)^{n}}$$

Where Y is the extent of AF647-insulin uptake measured in the presence of inhibitor, normalized to the AF647-insulin alone control and expressed as a percentage (%), Top is the maximal AF647-insulin uptake and was fixed to a value of 100%, Bottom is the % of AF647-insulin uptake achieved under maximal inhibition, X is the inhibitor concentration (nM), and IC_{50} is the inhibitor concentration (nM) required for half-maximal inhibition of AF647-insulin uptake.

To confirm that the results were not influenced by the chosen insulin label, similar studies were performed using ^{125}I-insulin. The hCMEC/D3 monolayers cultured on 12 well plates were treated with unlabeled insulin (1 µM), S961 (200 nM) or Aβ40 (12.5 µg/mL) for 30 min at 37 or 4 ^{o}C. Following that, ^{125}I-insulin was spiked into the media (final conc. of 0.08 µCi/mL= 3.1 nM), then continued incubating for 30 min at 37 or 4 ^{o}C. Cells were washed and prepared for gamma counting as described in section 5.3.9. ^{125}I activity in the cell lysate was measured.

5.3.14. Statistical analysis. All statistical tests were performed using GraphPad Prism (GraphPad software; La Jolla, CA). A p value of ≤ 0.05 was considered statistically significant. Unpaired two-tailed t-tests were used to compare the brain efflux rate constants (k), PS products, and brain influx clearances (K_i) of the radiolabeled peptides/proteins in mice treated with or without AG1024. Two-way ANOVA with Bonferroni's post-tests were used to compare the accumulation of radiolabeled peptides/proteins in various brain regions (% ID/g) of mice treated with or without AG1024. Unpaired two-tailed t-tests were used to compare the uptake of AF647-insulin in cells treated with or without AG1024. One-way ANOVA with Bonferroni's post-tests were used to compare the uptake of radiolabeled Aβ peptides as well as the protein expression or phosphorylation in cells treated with or without AG1024 and/or insulin.

5.4. Results

5.4.1. AG1024 decreases the brain efflux of ^{125}I-Aβ42. Dynamic SPECT/CT imaging was performed to examine the effects of AG1024 on brain efflux of intracerebrally injected ^{125}I-Aβ42 in wild-type mice stimulated with insulin (Fig. 5.1A). A mono-exponential decline in ^{125}I-Aβ42 concentrations in the brain ROI was observed with time (Fig. 5.1B), which is consistent with our previous publications (Swaminathan et al., 2018a). This data was used to estimate the rate constant (k) that describes the brain efflux of ^{125}I-Aβ42. The brain efflux rate constant was ~4 fold lower (p < 0.01, two-tailed t-test) in mice infused with AG1024 compared to mice infused with the saline control (Fig. 5.1 inset).

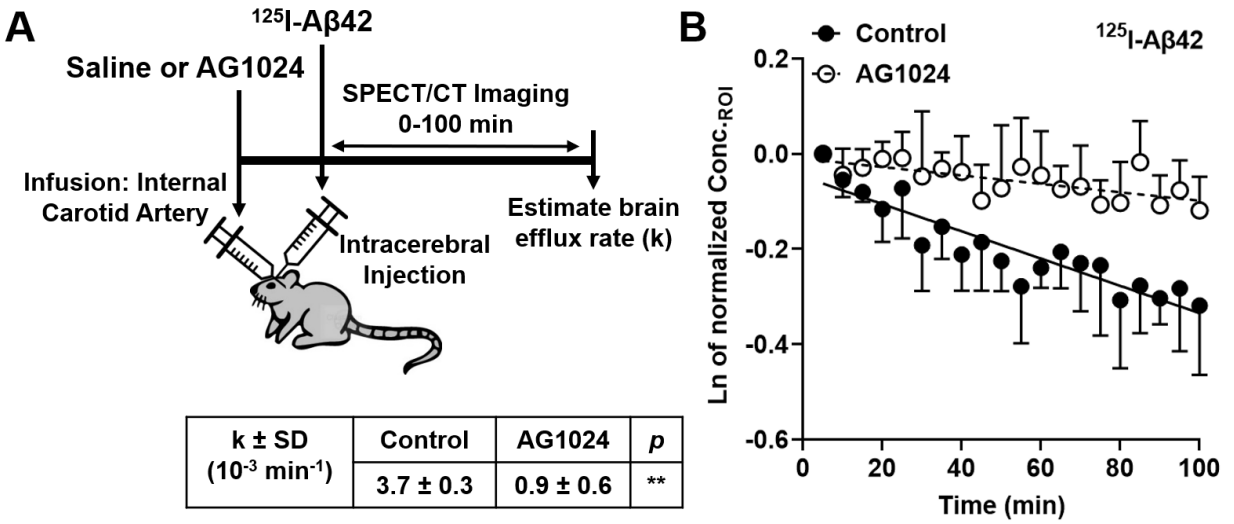

k ± SD (10^{-3} min^{-1})	Control	AG1024	*p*
	3.7 ± 0.3	0.9 ± 0.6	**

Figure 5.1. Brain efflux of intracerebrally injected ^{125}I-Aβ42 is decreased in mice infused with AG1024. (A) Experimental scheme. Mice were infused with AG1024 (30 µg) or saline control followed by insulin (100 µg) via the internal carotid artery. Following that, ^{125}I-Aβ42 (3 µCi) was injected directly into the right hippocampus. Tracer depletion from the brain was monitored by dynamic SPECT/CT imaging from 0-100 min. (B) Decline in ^{125}I-Aβ42 brain concentrations with time for mice infused with AG1024 or saline control. The slope obtained after linear regression of the natural log transformed data corresponds to the brain efflux rate constant (k). Data are mean ± SD (n=3). **p<0.01; unpaired two-tailed t-test.

5.4.2. AG1024 decreases the brain uptake of ^{125}I-insulin. After systemic injection, ^{125}I-insulin displayed a bi-exponential disposition in plasma (Fig. 5.2A-B), which is consistent with previous publications (Sato et al., 1990). The plasma pharmacokinetics of ^{125}I-insulin were unaltered in mice infused with AG1024 (Fig. 5.2B). However, a ~3 fold decrease ($p < 0.05$, two-tailed *t*-test) in the PS values for ^{125}I-insulin uptake at the BBB was observed in the AG1024-infused mice compared to the saline-infused mice (Fig. 5.2C).

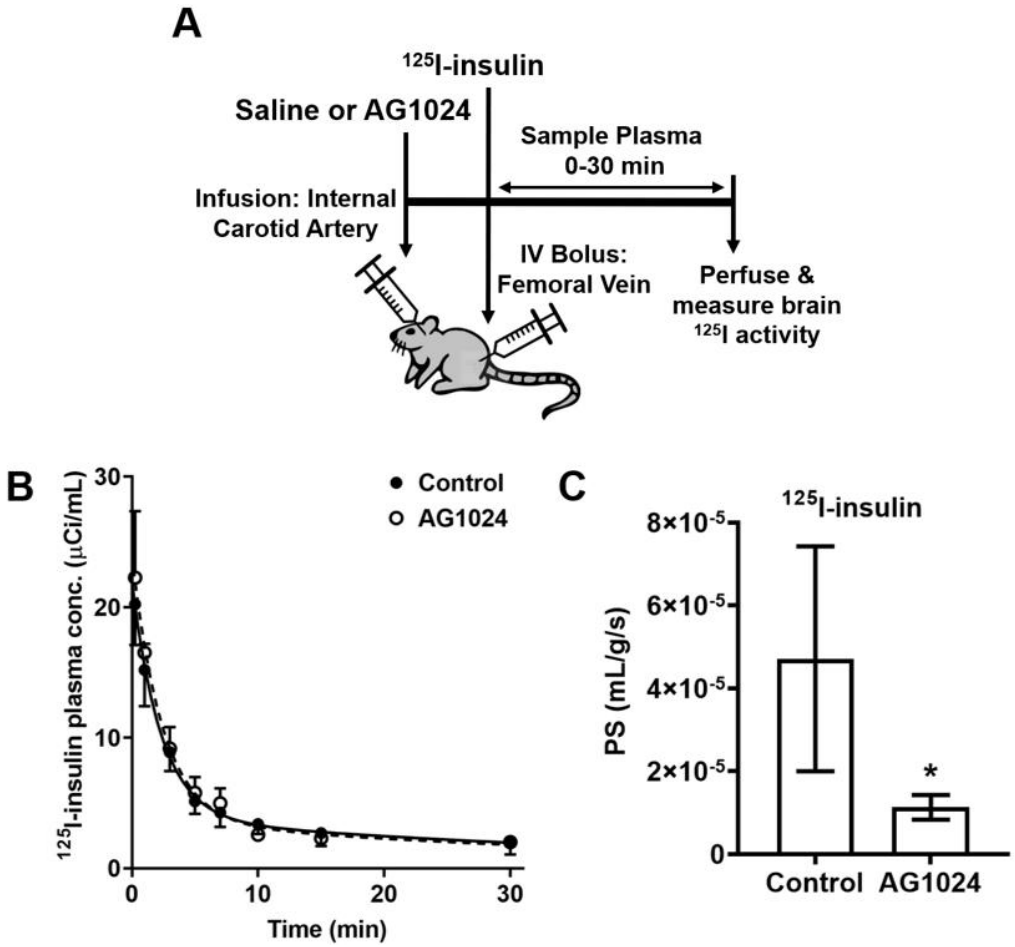

Figure 5.2. Brain permeability to ^{125}I-insulin is decreased in mice infused with AG1024. (A) Experimental scheme. Mice were infused with AG1024 (30 µg) or saline control via the internal carotid artery. Following that, ^{125}I-insulin (100 µCi) was bolus injected into the femoral vein. Plasma was sampled periodically from the femoral artery from 0-30 min. After the final sampling event, mice were transcardially perfused with PBS. ^{125}I activity in the plasma samples and dissected brain was assayed. (B) Plasma concentration vs. time profile of ^{125}I-insulin in mice infused with AG1024 or saline control. Shown are observed values (mean ± SD, n=4) overlaid with the predicted curves. (C) The permeability-surface area (PS) products for ^{125}I-insulin uptake into the whole brain were estimated in mice infused with AG1024 or saline control. Data are mean ± SD (n=4). *p<0.05; unpaired two-tailed t-test.

Dynamic SPECT/CT imaging studies were conducted to further examine the effects of AG1024 on the blood-to-brain distribution of ^{125}I-insulin (Fig. 5.3A). Based on

Gjedde-Patlak graphical analysis, the brain influx clearance (K_i) of ^{125}I-insulin was ~2 fold lower ($p < 0.05$, two-tailed *t*-test) in the AG1024-infused mice compared to the saline-infused mice (Fig. 5.3B). This is consistent with the decrease in PS values, both of which indicate that AG1024 reduces the rate of ^{125}I-insulin uptake at the BBB. The accumulation (% ID/g) of ^{125}I-insulin in various brain regions dissected at the end of the imaging experiment was also reduced in the AG1024-infused mice (Fig. 5.4A), specifically in the caudate putamen, hippocampus and thalamus ($p < 0.05$, two-way ANOVA with Bonferroni post-tests).

5.4.3. AG1024 increases the brain uptake of ^{125}I-Aβ42 but has no effect on ^{125}I-Aβ40.

Using similar methods as described for ^{125}I-insulin, dynamic SPECT/CT imaging studies were conducted to examine the effects of AG1024 on the blood-to-brain distribution of ^{125}I-Aβ42 and ^{125}I-Aβ40 in mice stimulated with insulin. Based on Gjedde-Patlak graphical analysis, the brain influx clearance of ^{125}I-Aβ42 was ~2 fold higher ($p < 0.05$, two-tailed *t*-test) in the AG1024-infused mice compared to the saline-infused mice (Fig. 5.3C). Interestingly, the brain influx clearance of ^{125}I-Aβ40 was unaltered in mice infused with AG1024 (Fig. 5.3D). Consistent with these trends, accumulation (% ID/g) of ^{125}I-Aβ42 in various brain regions dissected at the end of the imaging experiment increased in mice infused with AG1024, specifically in the cortex, hippocampus and thalamus (Fig. 5.4B). The ^{125}I-Aβ40 accumulation in various brain regions was not significantly altered, except in the thalamus (Fig. 5.4C; $p < 0.05$, two-way ANOVA with Bonferroni post-tests).

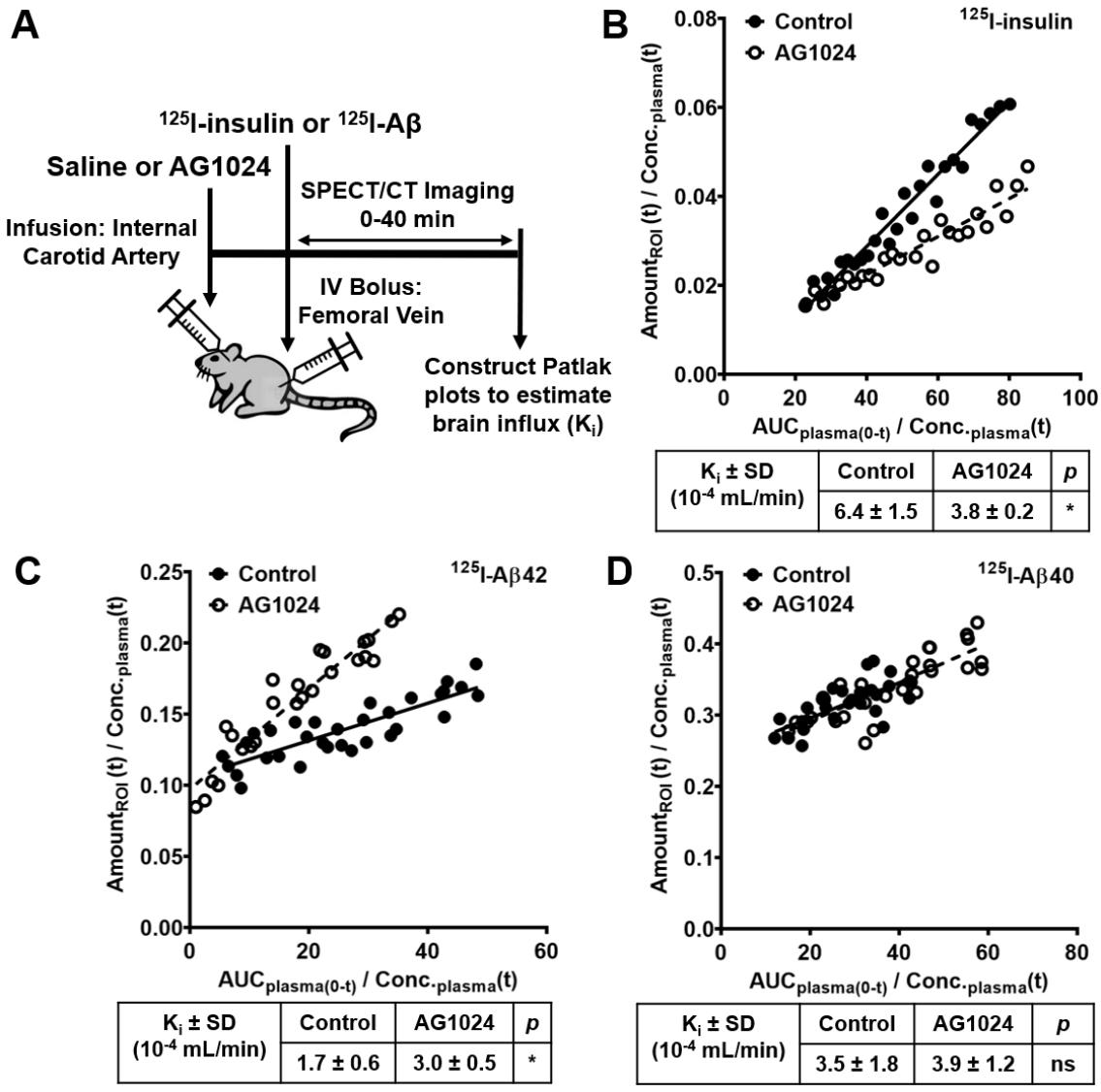

Figure 5.3. Differential effects of AG1024 on the brain influx clearance of ^{125}I-insulin, ^{125}I-Aβ42, and ^{125}I-Aβ40 in mice. Experimental scheme. Mice were infused with AG1024 (30 µg) or saline control via the internal carotid artery. Following which, ^{125}I-insulin, ^{125}I-Aβ42, or ^{125}I-Aβ40 (500 µCi) was bolus injected into the femoral vein. Tracer accumulation in the brain was monitored by dynamic SPECT/CT imaging from 0-40 min. For the ^{125}I-Aβ studies, unlabeled insulin was administered immediately following infusion with AG1024 or saline control. (B-D) The brain influx clearance (K_i) of ^{125}I-insulin, ^{125}I-Aβ42, and ^{125}I-Aβ40 was estimated by the slope obtained from Gjedde-Patlak graphical analysis. Representative graphs are shown. Inset table values are mean ± SD (n=4). *p<0.05; unpaired two-tailed t-test.

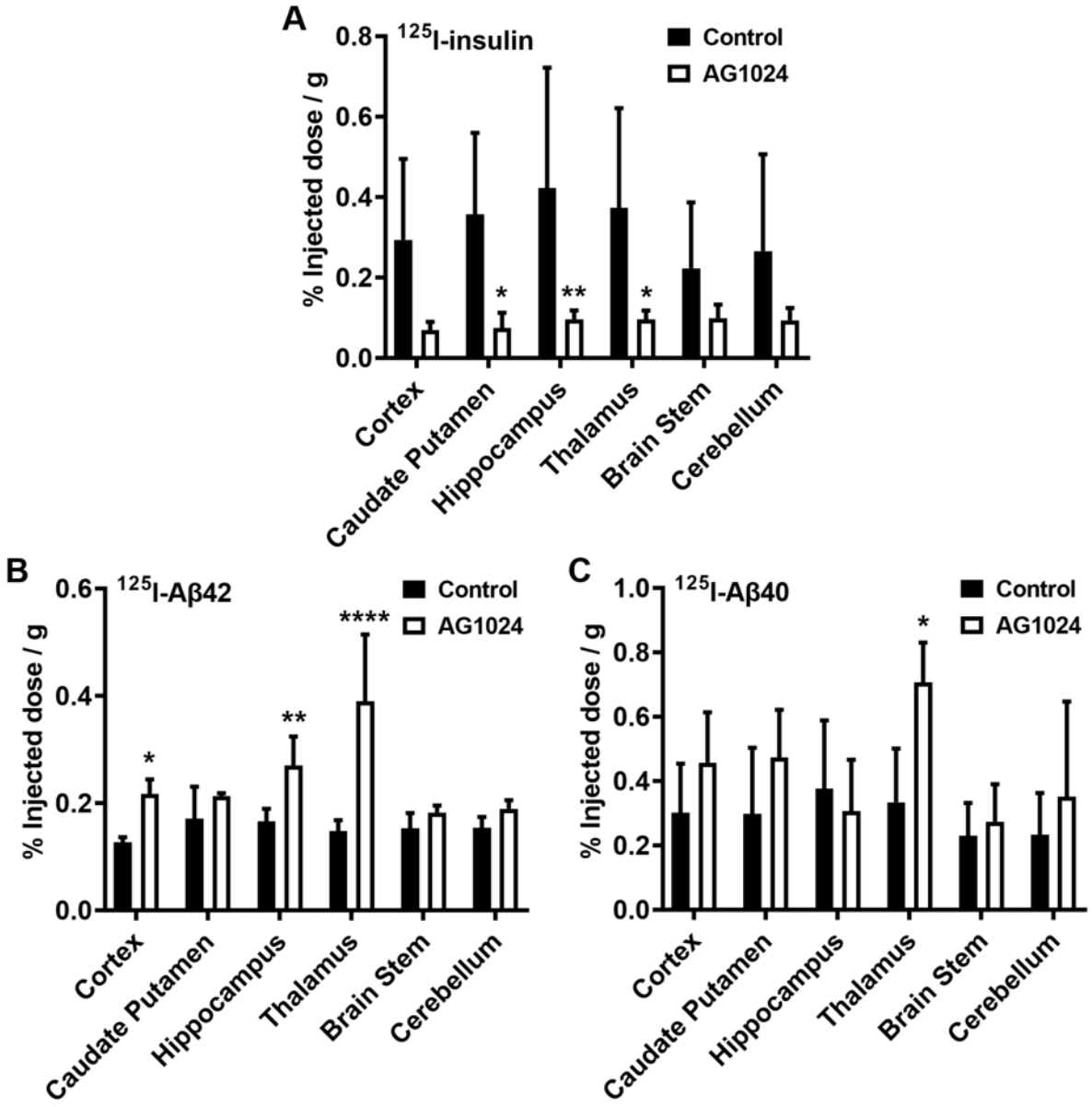

Figure 5.4. Differential effects of AG1024 on the brain accumulation of ^{125}I-insulin, ^{125}I-Aβ42, and ^{125}I-Aβ40 in mice. Brain accumulation of ^{125}I-insulin (A), ^{125}I-Aβ42 (B), and ^{125}I-Aβ40 (C) after femoral injection in mice infused with AG1024 (30 µg) or saline control is presented as the % of the injected dose measured in each brain region per gram of tissue. Data are mean ± SD (n=4). *p<0.05, **p<0.01, ****p<0.0001; two-way ANOVA with Bonferroni's post-tests.

5.4.4. AG1024 has no effect on the brain uptake of ^{125}I-BSA. Brain uptake studies were additionally performed using ^{125}I-BSA, which was included as a marker for BBB

breakdown. Under healthy conditions with an intact BBB, brain uptake of albumin is expected to be extremely low (Goldim et al., 2019). Accumulation of ^{125}I-BSA in various brain regions (% ID/g) was not significantly altered in the AG1024-infused mice compared to the saline-infused mice (Fig. 5.5). This suggests that AG1024 treatment did not lead to nonspecific changes in BBB integrity.

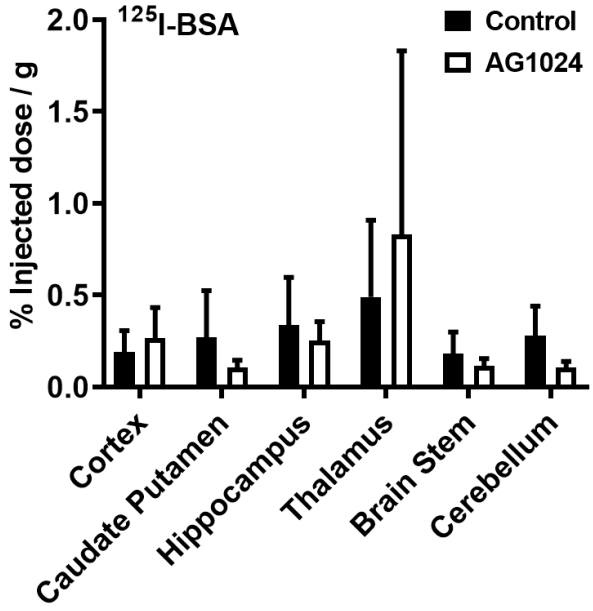

Figure 5.5. Brain accumulation of ^{125}I-BSA is unaltered in mice infused with AG1024. The brain accumulation of ^{125}I-BSA after internal carotid injection in mice infused with AG1024 (30 µg) or saline control is presented as the % of injected dose measured in each brain region per gram of tissue. Data are mean ± SD (n=4).

5.4.5. AG1024 differentially modulates insulin and Aβ uptake in polarized BBB endothelial cell monolayers. Further studies were performed to assess the effects of AG1024 on the endothelial cell uptake of insulin, Aβ42, and Aβ40 in hCMEC/D3 monolayers, which represents a widely used in vitro BBB model. Upon treatment with AG1024, the cell uptake of AF647-insulin decreased (Fig. 5.6A-B). In contrast, the cell

uptake of ^{125}I-Aβ42 increased (Fig. 5.6C), while that of ^{125}I-Aβ40 was unchanged (Fig. 5.6D) in the AG1024 treated cells. Interestingly, the AG1024-dependent increase in ^{125}I-Aβ42 uptake was only observed in the presence of insulin. These trends are consistent with the observed effects of AG1024 on the brain uptake of insulin, Aβ42 and Aβ40 in mice.

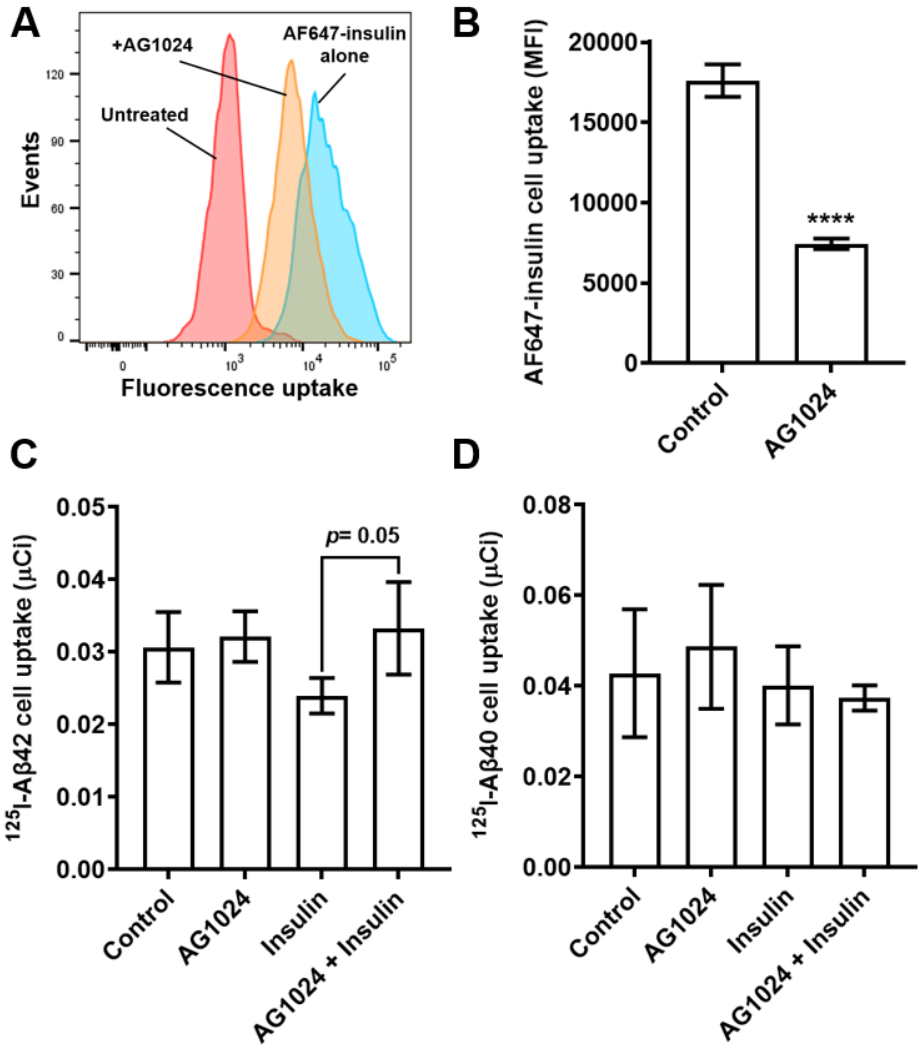

Figure 5.6. Differential effects of AG1024 on the uptake of insulin, Aβ42, and Aβ40 in polarized BBB endothelial cell monolayers. (A-B) Cell uptake of Alexa Fluor 647-labeled insulin (AF647-insulin) was assessed in hCMEC/D3 monolayers following 30 min treatment with or without AG1024 (100 µM). Fluorescence uptake was measured by flow cytometry. Shown are representative histograms and bar charts of the group mean

± SD (n=3). ****p<0.0001; unpaired two-tailed t-test. (C-D) Cell uptake of ^{125}I-Aβ42 and ^{125}I-Aβ40 was assessed in hCMEC/D3 monolayers following 30 min treatment with or without AG1024 (100 μM) and stimulation with insulin (100 nM). ^{125}I uptake was measured using a gamma counter. Data are mean ± SD (n=4). p=0.05; one-way ANOVA with Bonferroni post-tests).

5.4.6. AG1024 inhibits insulin signaling pathways in BBB cell monolayers. Western blots were conducted to examine the effects of AG1024 on the activity of insulin signaling kinases in hCMEC/D3 monolayers. Upon treatment with AG1024, a decrease in phosphorylation of both Akt (S473) and Erk (T42/Y44) was observed (Fig. 5.7). Thus, AG1024 inhibited both the PI3K/Akt and MAPK/Erk arms of the insulin signaling pathway in the BBB cell monolayers. This effect was observed with or without prior stimulation with insulin (Fig. 5.7).

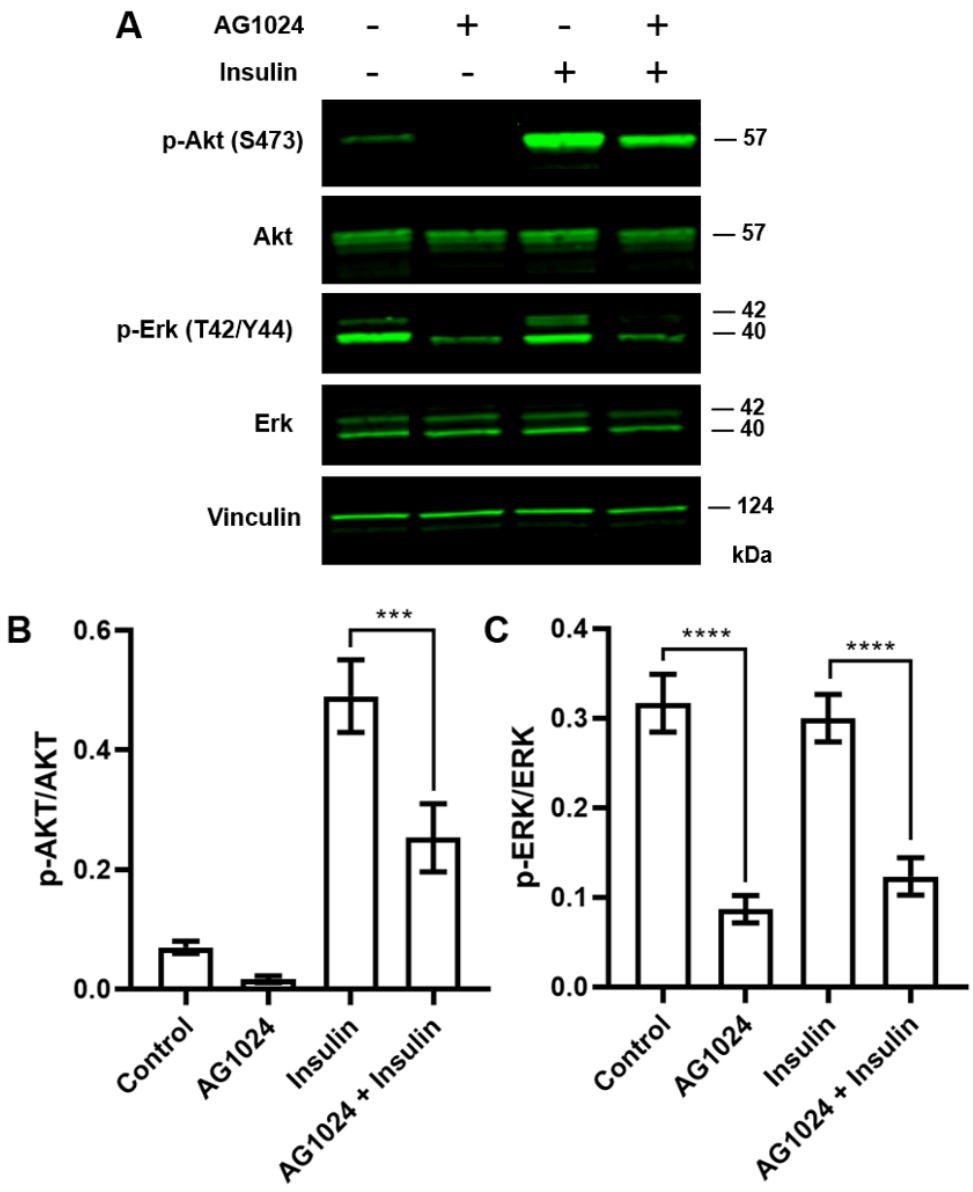

Figure 5.7. AG0124 inhibits insulin signaling pathways in polarized BBB endothelial cell monolayers. Western blots were performed to assess the expression and phosphorylation of the insulin signaling kinases Akt and Erk in hCMEC/D3 monolayers following 30 min treatment with or without AG1024 (100 µM) and stimulation with insulin (100 nM). Treatment with AG1024 decreased the phosphorylation of Akt (S473) and Erk (T42/Y44), indicating inhibition of both insulin signaling arms. Vinculin was used as a loading control. Shown are representative immunoblots (A) and bar charts of the group mean ± SD (n=3) of the quantification for p-Akt/Akt (B) and p-Erk/Erk (C). ***p<0.001, ****p<0.0001; one-way ANOVA with Bonferroni post-tests).

5.4.7. AG1024 alters the membrane expression of insulin and Aβ trafficking receptors in BBB cell monolayers. Subcellular fractionation of hCMEC/D3 cells followed by western blot was performed to investigate the effects of AG1024 on membrane expression levels of receptors implicated in insulin and Aβ peptide trafficking at the BBB (Fig. 5.8). Treatment with AG1024 alone had no effect on membrane expression of Aβ trafficking receptors (LRP-1 and RAGE). In contrast, treatment with insulin alone increased membrane expression of both LRP-1 and RAGE, which is consistent with our previous findings (Swaminathan et al., 2018a). However, upon treatment with AG1024 and insulin together, membrane expression of LRP-1 and RAGE decreased to the baseline levels that were observed in the untreated cells (Fig. 5.8).

Interestingly, membrane expression of the insulin trafficking receptor IR-β increased in cells treated with either AG1024 alone or insulin alone. However, upon treatment with AG1024 and insulin together, membrane expression of IR-β decreased to the baseline levels that were observed in the untreated cells (Fig. 5.8).

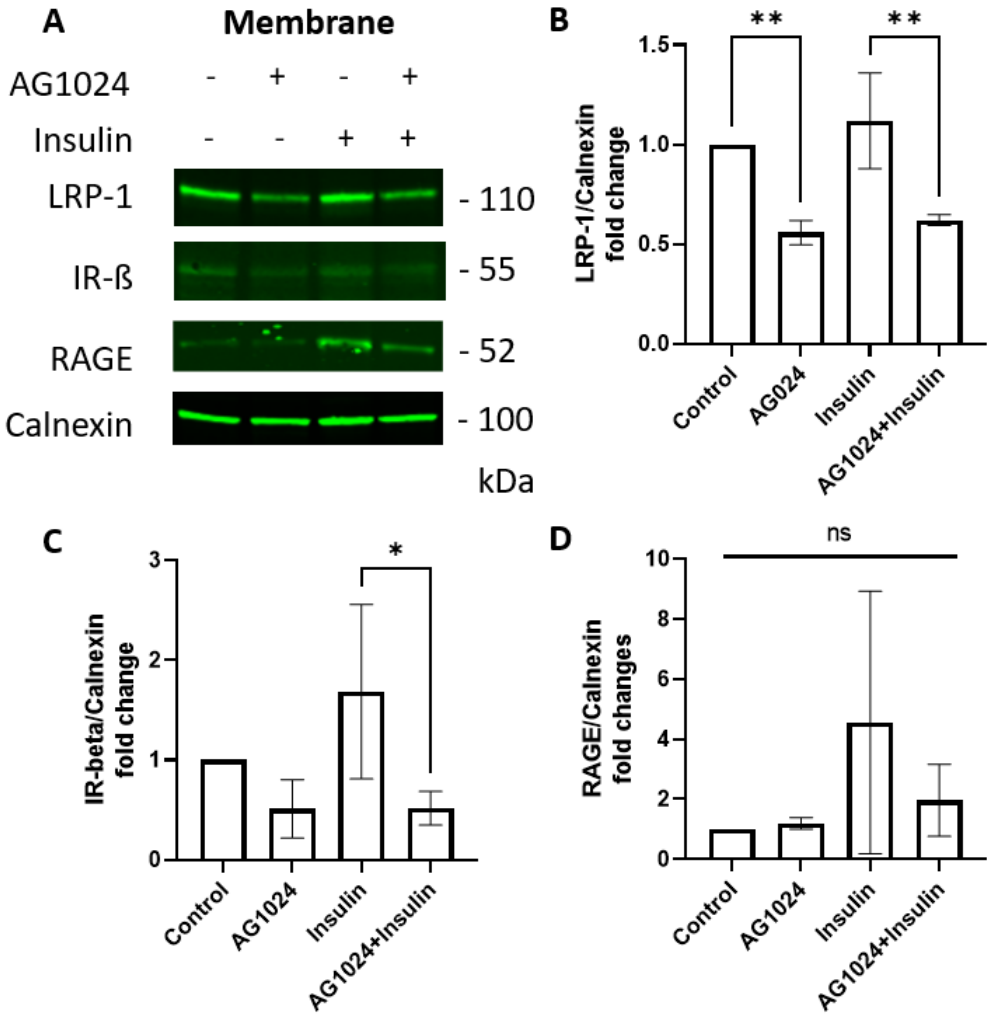

Figure 5.8. AG1024 decreases the membrane expression of Aβ and insulin trafficking receptors in polarized BBB endothelial cell monolayers. Subcellular fractionation followed by western blot was performed to assess the membrane expression of Aβ and insulin transport receptors (LRP-1, RAGE and IR-β) in hCMEC/D3 monolayers following 30 min treatment with or without AG1024 (100 µM) and stimulation with insulin (100 nM). Compared to the cells treated with insulin alone, treatment with AG1024 and insulin decreased the membrane expression of LRP-1 and IR-β, with no significant effect on RAGE. Calnexin was used as a loading control. Shown are representative immunoblots (A) and bar charts of the group mean ± SD (n=3) of the quantification for LRP-1/Calnexin (B), IR-β/Calnexin (C), and RAGE/Calnexin (D). *p<0.05, **p<0.01; one-way ANOVA with Bonferroni post-tests).

5.4.8. Insulin uptake in BBB cell monolayers is increased upon inhibition of the MEK signaling arm, but not the AKT signaling arm. Further studies were performed using a panel of insulin signaling inhibitors to delineate the individual roles of the PI3K/AKT and MAPK/ERK signaling arms, which are downstream of IR, in modulating insulin and Aβ peptide uptake at the BBB. Interestingly, the cell uptake of AF647-insulin increased in the presence of the MEK inhibitor trametinib, either alone or in combination with the AKT inhibitor MK2206 (Fig. 5.9A&C). In contrast, treatment with MK2206 alone or the mTOR inhibitor rapamycin had no effect on AF647-insulin uptake (Fig. 5.9B&D).

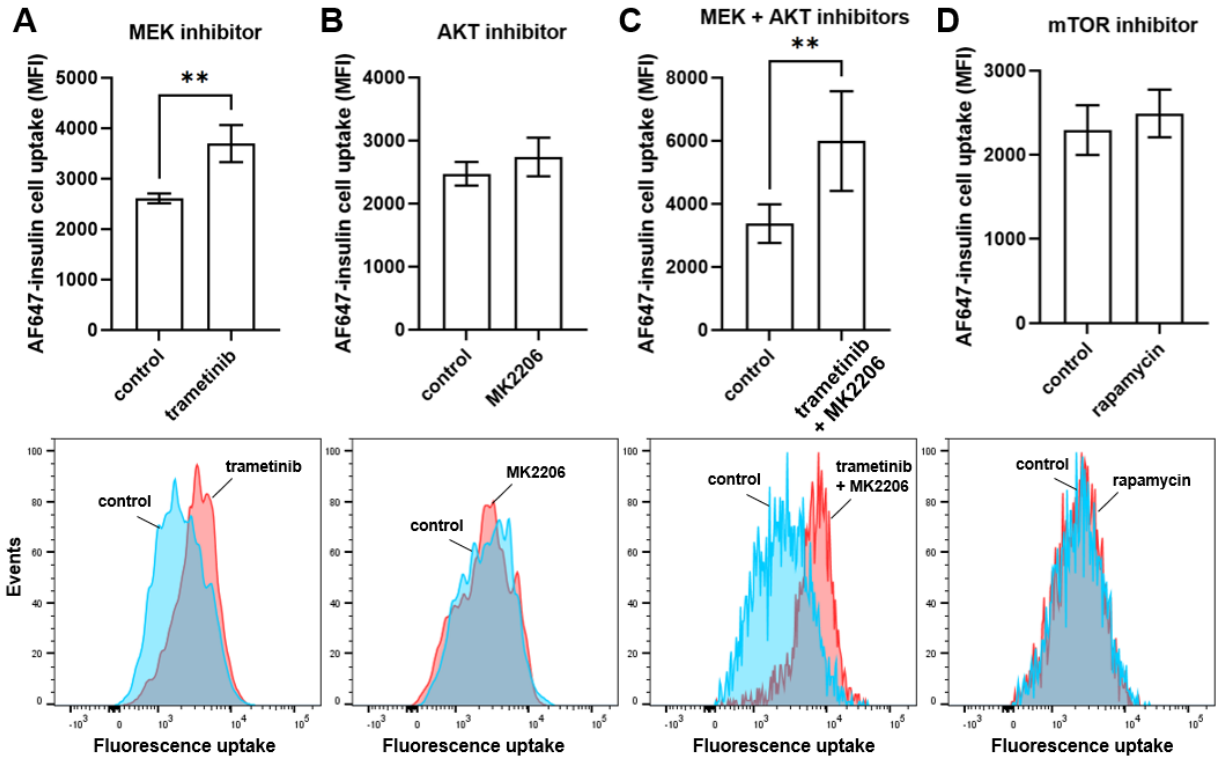

Figure 5.9. Insulin uptake in BBB cell monolayers is increased by the MEK inhibitor trametinib, but not by the AKT inhibitor MK2206 or the mTOR inhibitor rapamycin. Cell uptake of AF647-insulin (6.25 nM) was assessed in hCMEC/D3 monolayers after 24 hour treatment with either: (A) 1 µM trametinib; (B) 1 µM MK2206; (C) 1 µM trametinib + 1 µM MK2206; (D) 100 nM rapamycin. Fluorescence uptake was measured by flow cytometry. Shown are representative histograms and bar charts of the group mean ± SD (n=3). ***p*<0.01; unpaired two-tailed *t*-test.

5.4.9. Differential effects of MEK and AKT inhibitors on Aβ42 and Aβ40 uptake in BBB cell monolayers. Upon treatment with the MEK inhibitor trametinib, the cell uptake of ^{125}I-Aβ42 increased (Fig. 5.10A), while ^{125}I-Aβ40 uptake was unchanged (Fig. 5.10E). This trend is consistent with the observed effects of AG1024 in modulating ^{125}I-Aβ42 and ^{125}I-Aβ40 uptake in hCMEC/D3 monolayers (Fig. 5.6C-D). Upon treatment with the AKT inhibitor MK2206, cell uptake of ^{125}I-Aβ42 was unaltered (Fig. 5.10B), while ^{125}I-Aβ40 uptake was increased (Fig. 5.10F). Treatment with either the EGFR inhibitor genistein or the mTOR inhibitor rapamycin had no effect on ^{125}I-Aβ42 or ^{125}I-Aβ40 uptake in the hCMEC/D3 monolayers (Fig. 5.10C-D&G-H).

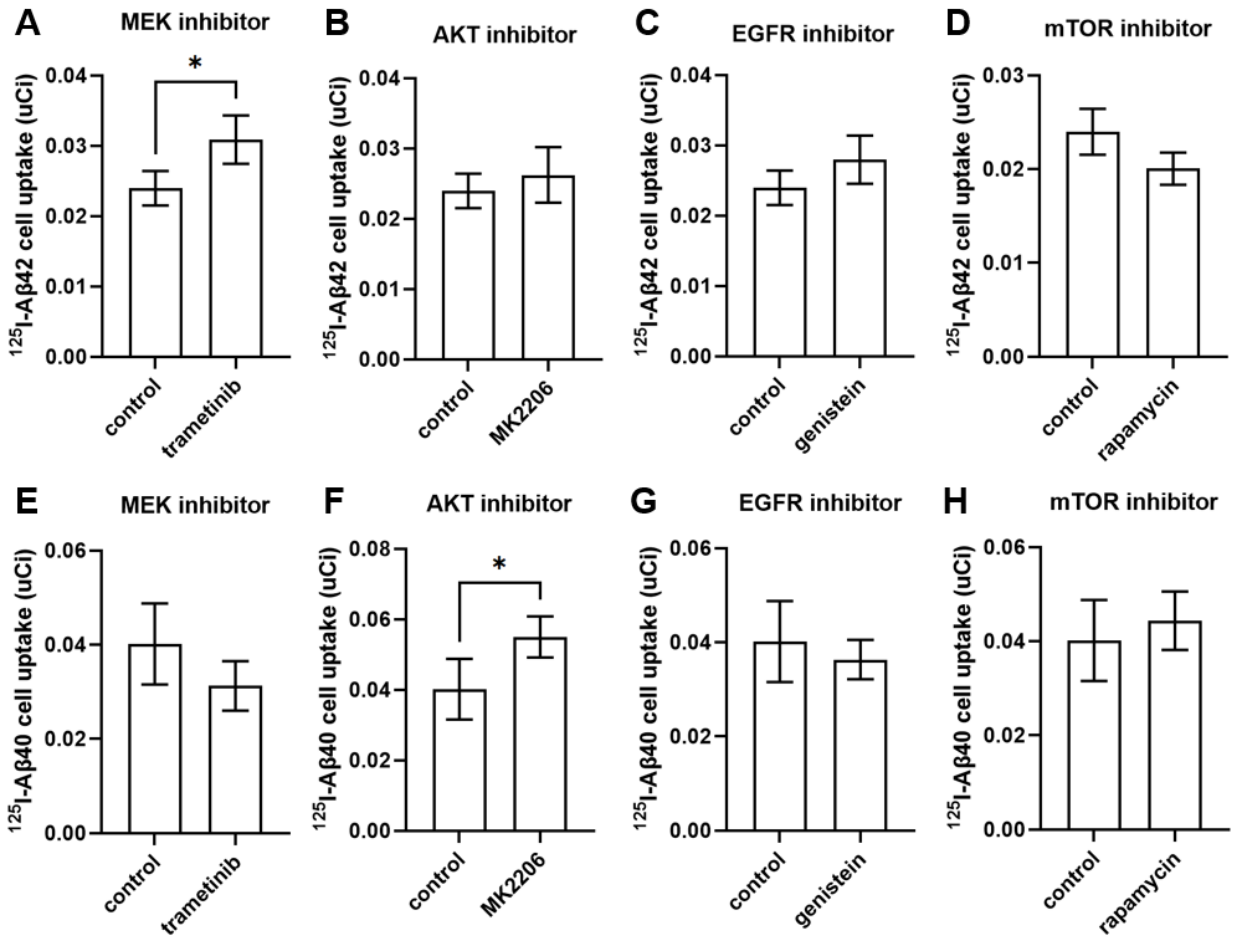

Figure 5.10. Differential effects of MEK and AKT inhibitors on Aβ42 and Aβ40 uptake in BBB cell monolayers. Cell uptake of ^{125}I-Aβ42 (A-D) and ^{125}I-Aβ40 (E-H) were assessed in hCMEC/D3 monolayers after treatment with various signaling inhibitors and stimulation with insulin. Cells were treated for 30 min with either 1 µM trametinib, 12.5 µM MK2206, 10 µM genistein, or 1 µM rapamycin, followed by a 60 min co-incubation with ^{125}I-Aβ (5 µCi/mL). ^{125}I-Aβ cell uptake was measured by gamma counting. Data are mean ± SD (n=3). **p*<0.05; unpaired two-tailed *t*-test.

5.4.10. Insulin uptake in BBB cell monolayers is reduced upon exposure to a selective IR inhibitor or Aβ peptides. Further studies were performed using S961, a selective IR antagonist that competes for insulin binding to IR and inhibits IR signal transduction (Sharma and Kumar, 2018). A concentration-dependent decrease in AF647-insulin uptake in hCMEC/D3 monolayers was observed upon treatment with increasing concentrations of S961 (Fig. 5.11A). This is consistent with the observed decrease in AF647-insulin uptake upon treatment with the IGF1R/IR kinase inhibitor AG1024 (Fig. 5.6A-B). In similar fashion, a concentration-dependent decrease in AF647-insulin uptake in hCMEC/D3 monolayers was observed upon treatment with increasing concentrations of Aβ42 or Aβ40 (Fig. 5.11B-C).

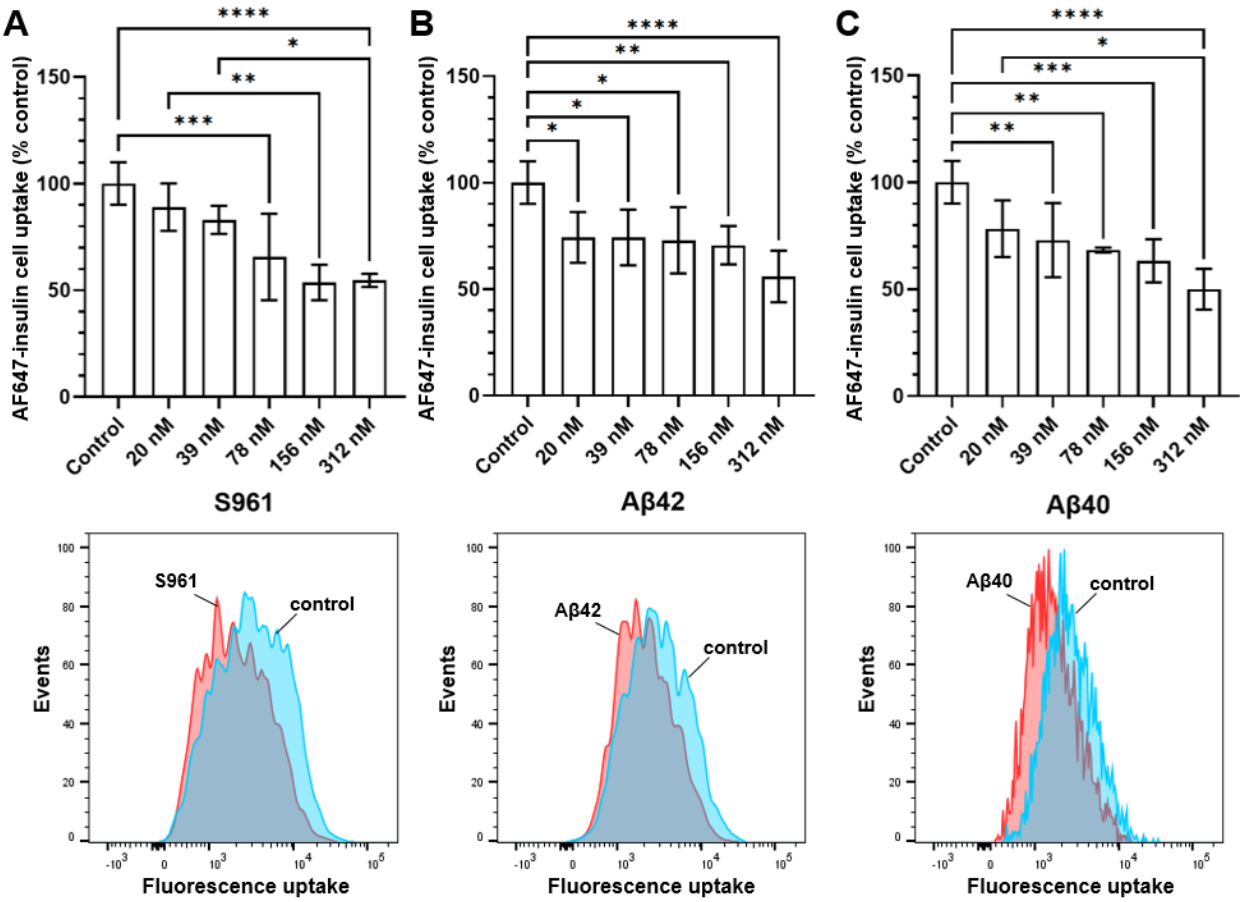

Figure 5.11. Concentration-dependent effects of S961 (A), Aβ42 (B) and Aβ40 (C) on AF647-insulin uptake in BBB cell monolayers. hCMEC/D3 monolayers were treated with varied concentrations (20-312 nM) of S961, Aβ42 or Aβ40 for 30 min, followed by a 30 min co-incubation with AF647-insulin (3.1 nM). AF647-insulin cell uptake was measured by flow cytometry. Representative histograms are shown. Data are mean ± SD (n=4). **p*<0.05; ***p*<0.01; ****p*<0.001; *****p*<0.0001; unpaired two-tailed *t*-test.

To further characterize the inhibitory effects on insulin uptake, the half-maximal inhibitory concentration (IC_{50}) of S961, Aβ42 or Aβ40 in reducing the uptake of AF647-insulin (12.5 nM) in hCMEC/D3 monolayers was determined. The IC_{50} of S961, Aβ42 and Aβ40 were estimated to be 370, 610 and 810 nM, respectively (Fig. 5.12).

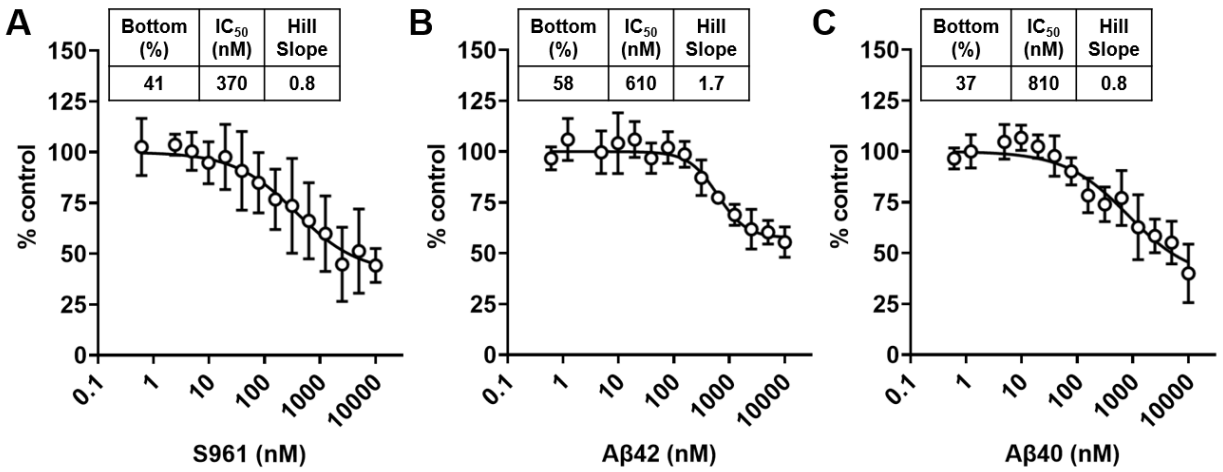

Figure 5.12. IC_{50} curves of S961, Aβ42 and Aβ40 in reducing the uptake of AF647-insulin in BBB cell monolayers. The hCMEC/D3 monolayers were treated with varied concentrations (1 nM-10 uM) of S961 (A), Aβ42 (B) or Aβ40 (C) for 30 min, followed by a 30 min co-incubation with AF647-insulin (12.5 nM). AF647-insulin cell uptake was measured by flow cytometry. MFI values in presence of inhibitor were normalized to the AF647-insulin alone control. Data was fit to an IC_{50} equation with variable slope. Data are mean ± SD (n=4).

To confirm the observed trends on insulin uptake are independent of the AF647 label, similar studies were performed using ^{125}I-insulin. The binding of ^{125}I-insulin to hCMEC/D3 monolayers was reduced in the presence of excess unlabeled insulin (Fig. 5.13A), which is consistent with a saturable, receptor-mediated uptake process. Uptake of ^{125}I-insulin was also reduced by pretreatment with S961 or Aβ40 peptides (Fig. 5.13B), which is consistent with the findings obtained using AF647-insulin.

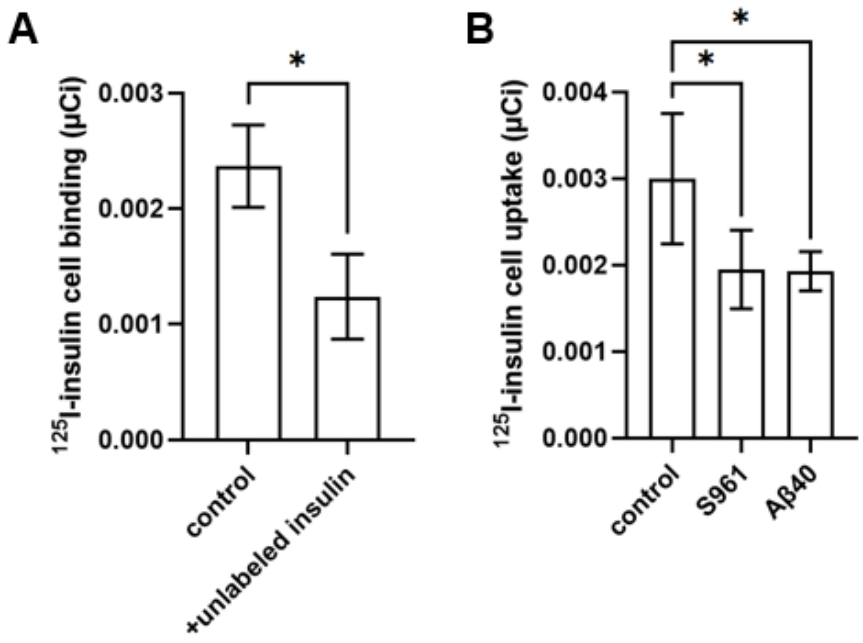

Figure 5.13. Binding/uptake of ^{125}I-insulin in BBB cell monolayers is reduced in the presence of excess unlabeled insulin, S961 or Aβ40 peptides. (A) The hCMEC/D3 monolayers were treated with excess unlabeled insulin (1 µM) at 4 deg, followed by co-incubation with ^{125}I-insulin (3.1 nM). (B) hCMEC/D3 monolayers were treated with S961 (200 nM) or Aβ40 (12.5 ug/mL), followed by co-incubation with ^{125}I-insulin (3.1 nM). ^{125}I-insulin cell uptake was measured by gamma counting. Data are mean ± SD (n=3). *p<0.05; unpaired two-tailed t-test.

5.5. Discussion and Conclusions

Exposure to toxic Aβ peptides was reported to inhibit insulin signaling in a pattern similar to AG1024, a dual IGF1R/IR kinase inhibitor that decreased phosphorylation of the insulin signaling kinases Akt and Erk in neurons (Townsend et al., 2007). Previously, we reported that Aβ exposure inhibits both insulin signaling and insulin transcytosis at the BBB in mice (Swaminathan et al., 2018b; Gali et al., 2019). Thus, we hypothesized that insulin signaling pathways are implicated in the mechanisms by which Aβ peptides inhibit insulin transcytosis at the BBB. To test this hypothesis, we showed that ^{125}I-insulin uptake to the brain from the systemic circulation decreased in healthy

mice upon treatment with AG1024. Insulin uptake was notably decreased in the hippocampus, where IR is densely expressed and modulates learning/memory processes (Grillo et al., 2015). In vitro studies performed using a BBB cell model showed that AG1024 inhibited the phosphorylation of Akt and Erk, decreased the membrane expression of IR-β, and decreased the cell uptake of insulin. Thus, IR and/or IGF1R signaling were shown to regulate insulin transcytosis at the BBB, likely by modulating IR translocation between membrane and cytosolic compartments.

Previously, it was reported that insulin signaling is required for insulin endocytosis in aortic endothelial cells (Wang et al., 2008), but not in BBB endothelial cells (Gray et al., 2017). In these prior studies, the BBB cells were treated with either PI3K/Akt or MAPK/Erk inhibitors (Wortmannin, Genistein, or PD98059). The current findings suggest the possibility of compensatory mechanisms by the unaltered signaling arm, which could still facilitate insulin transcytosis at the BBB. We speculate that both the PI3K/Akt and MAPK/Erk signaling arms must be inhibited, which is observed upon Aβ peptide or AG1024 exposure, to inhibit insulin transcytosis at the BBB and reduce its delivery to the brain.

Insulin signaling was also proposed to regulate Aβ transcytosis at the BBB (Vandal et al., 2015). Feeding AD transgenic (3xTg) mice with a high fat diet, which triggers peripheral insulin resistance, was shown to increase soluble brain Aβ levels. Subsequent injection of insulin decreased brain Aβ levels, suggesting they were driven by insulin signaling deficits (Vandal et al., 2014). The current work provides mechanistic support to this claim, in which AG1024 treatment in healthy mice decreased the brain efflux of ^{125}I-Aβ42 following intracerebral injection. This effect could potentially be

explained by decreased membrane expression of LRP-1, which handles Aβ trafficking in the brain-to-blood direction, that was observed in BBB cells treated with AG1024.

Insulin signaling deficits could further exacerbate brain Aβ accumulation by increasing Aβ42 uptake to the brain from systemic circulation, as observed in mice treated with AG1024. Aβ42 uptake was notably increased in the cortex and hippocampus, which are the brain regions most severely compromised in AD. The opposite effects of AG1024 on Aβ42 trafficking in the brain-to-blood vs. blood-to-brain directions are likely driven by differences in the BBB receptors and regulatory networks governing Aβ trafficking in each direction. However, an unexpected decrease in membrane expression of RAGE, which handles Aβ trafficking in the blood-to-brain direction, was observed in BBB cells treated with AG1024. This discrepancy is potentially explained by unidentified effects of AG1024 in facilitating vesicular sorting or exocytosis of Aβ42 in the blood-to-brain direction, which could offset the decreased membrane RAGE levels and lead to increased Aβ42 uptake to the brain. Potential differences in receptor affinities, vesicular sorting, and exocytosis of Aβ42 vs. Aβ40 at the BBB could also explain the selective effects of AG1024 on the Aβ42 isoform. Previously, we reported that insulin treatment had opposite effects on Aβ42 vs. Aβ40 trafficking at the BBB in mice and increased the membrane expression of RAGE and LRP-1 in BBB cells in vitro (Swaminathan et al., 2018a). However, the underlying mechanisms by which insulin signaling differentially regulates BBB trafficking of Aβ42 vs. Aβ40 isoforms have not been elucidated.

It was previously reported that insulin decreased the binding of amyloid-derived diffusible ligands (ADDLs) to neurons, while AG1024 prevented the insulin-induced

effect (De Felice et al., 2009; Zhou and Klein, 2012). Given that ADDLs predominantly consistent of Aβ42, these reports are consistent with the current finding that insulin decreased the BBB cell uptake of Aβ42, which was prevented by AG1024. This suggests that under normal physiological conditions, insulin is protective against Aβ42 accumulation at the BBB and in neurons. However, under conditions of insulin resistance in which insulin signaling is inhibited, insulin loses this protective function, which may contribute to the development of AD. Additionally, it was reported that insulin treatment inhibited, while AG1024 treatment promoted, the aggregation of ADDLs in neuronal media (Zhao et al., 2009). As such, AG1024 effects on Aβ42 trafficking at the BBB are potentially influenced by effects on Aβ42 oligomerization and aggregation, which could alter the interactions with membrane receptors.

Insulin signaling deficits may also contribute to AD by promoting loss of BBB tight junction integrity, which is reported in T2DM patients and rodent models (Prasad et al., 2014; Yoo et al., 2016; Takechi et al., 2017). Insulin treatment was shown to increase the transendothelial electrical resistance (TEER) of BBB cell monolayers, which was prevented by AG1024 (Ito et al., 2017). Under conditions of an intact BBB, brain uptake of the serum protein albumin is very minimal (Goldim et al., 2019). Here, we showed that ^{125}I-BSA accumulation in various brain regions was not significantly altered in mice treated with AG1024. This suggests that AG1024, at the dose tested, did not promote a nonspecific loss of BBB integrity. Thus, the observed changes in BBB trafficking upon AG1024 treatment are likely driven by specific effects on insulin and Aβ transcytosis machinery. The selective effects of AG1024 on Aβ42 vs. Aβ40 trafficking further indicate the trends were not driven by nonspecific changes in BBB integrity.

In summary, systemic administration of a dual IGF1R/IR kinase inhibitor in healthy mice: decreased brain efflux of Aβ42, increased brain influx of Aβ42, and decreased brain influx of insulin. The in vivo results were supported by cell uptake, signaling, and membrane expression studies performed using a BBB cell culture model. These findings provide a functional validation of the role of IR and/or IGF1R signaling in regulating Aβ peptide and insulin transcytosis at the BBB. Moreover, under conditions of insulin resistance (i.e. T2DM), insulin signaling deficits at the BBB are expected to contribute to increased brain Aβ42 levels and decreased brain insulin levels, which have both been linked to the progression of cognitive decline in AD patients (Näslund et al., 2000; Gil-Bea et al., 2010). Further studies are needed to resolve the independent contributions of IR, IGF1R, and the downstream signaling kinases (PI3K/Akt and MAPK/Erk pathways) in regulating Aβ peptide and insulin transcytosis at the BBB.

Chapter 6: HDL mimetic peptide 4F efficiently crosses the BBB and modulates Aβ peptide trafficking at the BBB

6.1. Synopsis

Treatments to elevate high-density lipoprotein (HDL) levels in plasma have decreased cerebrovascular Aβ deposition and mitigated cognitive decline in Alzheimer's disease (AD) transgenic mice. Since the major protein component of HDL particles, apolipoprotein A-I (ApoA-I), has very low permeability at the blood-brain barrier (BBB), we investigated 4F, an 18 amino acid ApoA-I/HDL mimetic peptide, as a therapeutic alternative. Specifically, we examined BBB permeability of 4F and its effects on ^{125}I-Aβ trafficking from brain-to-blood and from blood-to-brain. After systemic injection in mice,

BBB permeability of ^{125}I-4F, estimated as the permeability-surface area (PS) product, ranged between 2 and 5 x 10^{-6} ml/g/s in various brain regions. The PS products of ^{125}I-4F were ~1000 fold higher compared to those determined for ^{125}I-ApoA-I. Moreover, systemic infusion with 4F increased brain efflux of intracerebrally injected ^{125}I-Aβ42. Conversely, 4F infusion decreased brain influx of systemically injected ^{125}I-Aβ42. Interestingly, 4F did not significantly alter brain influx of ^{125}I-Aβ40. To corroborate the in vivo findings, we evaluated the effects of 4F on ^{125}I-Aβ42 transcytosis across polarized human BBB endothelial cell (hCMEC/D3) monolayers. Treatment with 4F increased abluminal-to-luminal flux and decreased luminal-to-abluminal flux of ^{125}I-Aβ42 across the hCMEC/D3 monolayers. Additionally, 4F decreased endothelial accumulation of fluorescein-labeled Aβ42 in the hCMEC/D3 monolayers. These findings provide a mechanistic interpretation for the reductions brain Aβ burden reported in AD mice after oral 4F administration, representing a novel strategy for treating AD and cerebral amyloid angiopathy.

6.2. Background

Toxic Aβ peptides generated in the brain accumulate as senile plaques in brain parenchyma, constituting one of the pathological hallmarks of Alzheimer's disease (AD). In around half of individuals over 60 years of age and in 95% of AD patients, Aβ also accumulates in the cerebral vasculature, which culminates in cerebral amyloid angiopathy (CAA) (Herzig et al., 2006; Charidimou et al., 2012; Yamada and Naiki, 2012). CAA triggers cerebrovascular inflammation and represents the major cause of intracerebral hemorrhages, which lead to rapid decline in cognitive and neurological

functions in older subjects with and without AD pathology (Viswanathan and Greenberg, 2011; Charidimou et al., 2012). The two major Aβ isoforms associated with CAA and AD are Aβ40 and Aβ42, respectively, which differ by the presence of two additional amino acids on the C terminus. Aβ40 is considered to be the more vasculotropic isoform, whereas Aβ42 is considered to be more neurotoxic and amyloidogenic (Qi and Ma, 2017). The blood-brain barrier (BBB) maintains a dynamic equilibrium between brain and plasma Aβ pools. Along with perivascular drainage, the BBB participates in Aβ clearance from the brain. Disruption of these spatially coordinated Aβ clearance portals is believed to cause anomalous Aβ accumulation in brain parenchyma and in the cerebral vasculature (Michaud et al., 2013a; Michaud et al., 2013b). Use of pharmacological agents to remodel Aβ trafficking mechanisms at the BBB and promote Aβ clearance from the brain could therefore improve vascular health and mitigate cognitive decline in CAA and AD.

It is well established that high-density lipoprotein (HDL) particles in plasma help to mitigate the formation of atherosclerotic plaques, thereby providing protection from cardiovascular disease (CVD) (Assmann and Gotto, 2004). Emerging evidence also suggests that HDL is important for cerebrovascular and neurobiological functions (Hottman et al., 2014; Button et al., 2019). The major protein constituent of HDL particles in the periphery, apolipoprotein A-I (ApoA-I), was shown to mitigate age related cognitive decline in AD transgenic mice by us (Lewis et al., 2010) and others (Lefterov et al., 2010). These two studies established that ApoA-I overexpression reduces cerebrovascular Aβ deposition (CAA) and attenuates Aβ-associated neuroinflammation (Lewis et al., 2010), whereas ApoA-I deletion exacerbates CAA in AD transgenic mice

(Lefterov et al., 2010). Intriguingly, genetic manipulation of ApoA-I expression did not alter parenchymal Aβ deposition (Fagan et al., 2004; Lefterov et al., 2010; Lewis et al., 2010). Recently, we reported that radioiodinated ApoA-I displays very low brain permeability in Sprague-Dawley rats after systemic injection (Zhou et al., 2019). Since ApoA-I is almost exclusively expressed in the periphery, the absence of effects on parenchymal Aβ deposition could potentially be attributed to the low brain permeability of ApoA-I.

Despite the well-documented cardio- and neuro-vasoprotective effects of ApoA-I, therapeutic applications are limited by its poor oral bioavailability, high manufacturing costs, and low brain permeability. To address these limitations, small peptides that mimic ApoA-I/HDL function have been developed (Navab et al., 2010). The most notable of these HDL mimetics is the 18 amino acid peptide “4F”, which contains 4 phenylalanine (F) residues (Ac-DWFKAFYDKVAEKFKEAF-NH_2) and was designed to mimic the amphipathic alpha helix motif present in ApoA-I, which is important for its biological activity (Anantharamaiah et al., 2007). Oral administration of 4F was shown to reduce atherosclerotic lesions and plaque inflammation in a diabetes mouse model (Morgantini et al., 2010). Treatment with 4F was also shown to decrease cerebrovascular inflammation and improve cognitive function in a mouse model of atherosclerosis (Buga et al., 2006). Moreover, oral administration of 4F together with a statin drug reduced Aβ deposition in the brain parenchyma, ameliorated Aβ-associated neuroinflammation, and improved cognitive function in an AD transgenic mouse model (Handattu et al., 2009).

These literature reports suggest that 4F could potentially be employed as a therapeutic agent to mitigate sporadic CAA and AD related neurovascular pathologies. However, the brain penetrance of 4F has not been established, and the mechanisms by which 4F influences parenchymal and cerebrovascular Aβ deposition are poorly understood. Here, we assessed the permeability of radioiodinated 4F vs. ApoA-I at various brain regions after systemic injection in mice. Additionally, we examined the effects of 4F on both the brain efflux and brain influx of radioiodinated Aβ peptides. The in vivo findings were further supported by complementary studies conducted in BBB cell monolayers.

6.3. Materials & Methods

6.3.1. Animals. Wild-type mice (B6SJLF1/J) were bred in-house at the Mayo clinic animal facilities. Animals were raised with food and water ad-libitum with 12 hour / 12 hour light and dark cycles. Animal studies were carried out in accordance with the guide for the care and use of laboratory animals provided by the National Institutes of Health. All protocols were approved by the Mayo Clinic Institutional Animal Care and Use Committee. All studies were conducted using female mice between 8-12 months of age, weighing approximately 30 grams.

6.3.2. Radioiodination of 4F, ApoA-I and Aβ peptides. The following peptides/proteins were labeled with ^{125}I (PerkinElmer Life and Analytical Sciences; Boston, MA) using the chloramine-T reaction as described previously (Poduslo et al., 2001; Jaruszewski et al., 2014): D-4F peptide (American Peptide Company (now Bachem), Sunnyvale, CA),

human serum-derived ApoA-I (EMD Millipore, Burlington, MA), and Aβ42 and Aβ40 peptides (custom synthesized by AAPPTec, Louisville, KY or Mayo Clinic proteomics core facility). Unconjugated ^{125}I was removed by dialysis overnight in phosphate-buffered saline (PBS), and purity of the radiolabeled proteins was determined by trichloroacetic acid (TCA) precipitation as described previously (Kandimalla et al., 2007).

6.3.3. Brain influx of ^{125}I-4F vs. ^{125}I-ApoA-I after systemic injection. These assays were conducted as described in our previous publications (Swaminathan et al., 2018a). Briefly, mice were anesthetized under a mixture of isoflurane (1.5%) and oxygen (4 L/min), and then catheterized at the femoral vein and artery (n=4). A bolus of ^{125}I-4F (100 µCi; 11 nmol) or ^{125}I-ApoA-I (100 µCi; 0.88 nmol) was injected into the femoral vein, and then 20 µL blood samples were collected from the femoral artery at 0.25, 1, 3, 5, 10 and 15 minutes using heparinized capillary tubes. Blood samples were diluted with saline and centrifuged to separate plasma. ^{125}I-4F or ^{125}I-ApoA-I in plasma were precipitated using TCA and centrifuged to collect the pellet. Total ^{125}I radioactivity counts in the pellet, corresponding to intact peptide/protein, were measured using a gamma counter (Cobra II; Amersham Biosciences, Piscataway, NJ). Immediately following the final sampling event, the mice were euthanized by transcardial perfusion with excess PBS to flush remaining radioactivity from the vasculature. Individual brain regions (cortex, caudate putamen, hippocampus, thalamus, brain stem, cerebellum) were dissected and assayed for ^{125}I radioactivity using a gamma counter.

Influx of ^{125}I-4F and ^{125}I-ApoA-I at each brain region was assessed as the permeability-surface area (PS) product. The PS product (mL/g/s) at each brain region was determined using the equation:

$$PS = \frac{q(t)}{\int_0^t C_p dt}$$

where q(t) is the extravascular amount of ^{125}I-4F or ^{125}I-ApoA-I in the brain region per gram of tissue (μCi/g) at the end of the experiment, and $\int_0^t C_p dt$ is the area under the plasma concentration vs. time profile (min x μCi/mL) from 0-15 minutes, calculated using the linear-trapezoidal method.

6.3.4. Impact of 4F on the brain-to-blood efflux of ^{125}I-Aβ42. Mice were anesthetized as described above, and the left internal carotid artery was catheterized. Immediately following that, mice were mounted on a stereotaxic apparatus. Skin above the skull was cut open and sutures were exposed. As per the accurate stereotaxic coordinates, a small hole was drilled into the skull directly above the hippocampus. Animals were infused over 60 minutes with or without 2 mg (0.9 μmol) of 4F peptide dissolved in 200 μL of saline (n=3 each group) via the left internal carotid artery, which supplies blood directly to the left hemisphere and thereby allows for greater 4F exposure to the BBB. At the end of the infusion, the mice were injected with ^{125}I-Aβ42 (0.7 μCi) dissolved in PBS (1 μL), directly into the right hippocampus. After 40 minutes post-Aβ injection, the animals were transcardially perfused with excess PBS. Brain hemispheres were dissected and assayed for ^{125}I radioactivity using a gamma counter. Measured brain

radioactivity per gram of tissue was normalized to the radioactivity measured at the site of injection using the following equation:

$$\text{Brain} - \text{to} - \text{Blood Efflux} = \frac{\text{Radioactivity per gram of brain tissue } \left(\frac{\mu\text{Ci}}{\text{g}}\right)}{\text{Radioactivity at the injection site } (\frac{\mu\text{Ci}}{\text{g}})}$$

6.3.5. Impact of 4F on the blood-to-brain influx of ^{125}I-Aβ42 and ^{125}I-Aβ40. These assays were conducted as described in our previous publications (Swaminathan et al., 2017; Swaminathan et al., 2018a). Briefly, mice were anesthetized, and the femoral vein, femoral artery, and left internal carotid artery were catheterized. Animals were then infused with saline (200 µL) with or without 2 mg (0.9 µmol) of 4F peptide via the left internal carotid artery over a period of 60 minutes. Following that, the animals were bolus injected with 100 µCi of ^{125}I-Aβ42 or ^{125}I-Aβ40 into the femoral vein (n=3 each group). Blood samples of 20 µL were collected from the femoral artery at 0.25, 1, 3, 5, 10 and 15 minutes post-Aβ injection. After separating the plasma, the intact ^{125}I-Aβ42 or ^{125}I-Aβ40 in plasma was precipitated using TCA and then centrifuged. Total ^{125}I radioactivity counts in the pellet were measured using a gamma counter. Immediately following the final sampling event, the animals were transcardially perfused with PBS, the brain regions were dissected, and ^{125}I radioactivity was measured using a gamma counter. PS products for ^{125}I-Aβ42 and ^{125}I-Aβ40 at the hippocampus and the left hemisphere were determined as described above for ^{125}I-4F.

6.3.6. Impact of 4F on ^{125}I-Aβ42 and ^{125}I-Aβ40 plasma pharmacokinetics. ^{125}I-Aβ42 and ^{125}I-Aβ40 plasma concentration vs. time data from 0-15 minutes were evaluated by non-compartmental analysis (NCA) using Phoenix WinNonlin® (Certara). Parameters of

interest included the area under the concentration vs. time profile from 0-15 minutes (AUC_{0-t}; min x µCi/mL) and terminal clearance (CL; mL/min).

6.3.7. Cell culture. The immortalized human cerebral microvascular endothelial cell line (hCMEC/D3) was generously provided by Perrie-Oliver Couraud, Institut Cochin, France (Weksler et al., 2013). The cells were grown at 37°C under 5% CO_2 atmosphere on rat tail collagen (Corning, Corning, NY) coated cell culture grade flasks (Corning) using EBM-2 endothelial basal media (Lonza, Walkersville, MD) supplemented with 5% fetal bovine serum (FBS) (Atlanta biologicals, Flowery Branch, GA), penicillin–streptomycin (1%) (Corning), 1.4 µM hydrocortisone (Sigma-Aldrich, St Louis, MO), ascorbic acid (5 µg/ml, Sigma-Aldrich, St Louis, MO), chemically defined lipid concentrate (1%) (Life Technologies, Grand Island, NY), 10 mM HEPES and 1 ng/mL basic fibroblast growth factor (bFGF) (Peprotech, Rocky Hill, NJ). Cells in passages 27-35 were used in the experiments.

6.3.8. Impact of 4F on the abluminal-to-luminal vs. luminal-to-abluminal flux of radioiodinated Aβ across BBB cell monolayers. These experiments were performed as described in our previous publications (Agyare et al., 2013). Briefly, hCMEC/D3 cells were cultured on 12 mm Transwell® inserts with 0.4 µm pores (Corning) until a continuous monolayer was formed. Monolayer integrity was verified by measuring the transendothelial electrical resistance (TEER). Experiments were conducted when TEER values ranged between 80 and 120 Ω/cm^2. The evening before the experiment, the growth media containing 5% FBS and 10 mM HEPES was replaced with growth media containing 1% FBS and 20 mM HEPES. To investigate abluminal-to-luminal (A-L)

transport, cells were pretreated with or without 4F (10 µg/mL) on the abluminal side for 60 minutes at 37 ^{o}C (n=4 each group). Without removing 4F, ^{125}I-Aβ42 (10 µCi/mL) was then spiked into the abluminal media. The luminal media was then sampled (20 µL) at 10, 20, 30, 45, 60, and 90 minutes post-Aβ addition, and the ^{125}I radioactivity was measured using a gamma counter. Similar studies were conducted to investigate luminal-to-abluminal (L-A) transport, with 4F pre-incubation and ^{125}I-Aβ42 addition occurring on the luminal side, followed by sampling from the abluminal side. The cumulative amount of radioactivity reaching the contralateral side was plotted against time. The slope obtained after linear regression of the linear region of the curve, in which unidirectional transfer is assumed, was divided by the surface area of the Transwell® insert (1.12 cm^2) to calculate ^{125}I-Aβ42 flux across the monolayer.

6.3.9. Impact of 4F on the accumulation of fluorescein-labeled Aβ42 and Aβ40 in BBB cell monolayers. Flow cytometry studies: hCMEC/D3 cells were cultured on 6 well plates (Corning) until a continuous monolayer was formed. The evening before the experiment, the growth media containing 5% FBS was replaced with growth media containing 1% FBS. Cells were pretreated with or without 4F (10 µg/mL) for 60 minutes at 37 ^{o}C (n=3 each group). Following that, fluorescein-labeled Aβ42 (F-Aβ42) or F-Aβ40 (synthesized by the Mayo Clinic proteomics core facility) was spiked into the media (12.5 µg/mL) and then further incubated for 60 minutes. Cells were washed three times with ice-cold PBS, trypsinized, and then resuspended in PBS followed by 1:1 dilution with 4% paraformaldehyde (PFA) on ice. Cellular uptake of the fluorescence signal was measured using a LSR-II Fortessa flow cytometry equipped with a 20 mW (488 nm)

laser (BD Biosciences, San Jose, CA). Data analysis was performed using FlowJo software (TreeStar Inc., San Carlos, CA).

Confocal microscopy studies: hCMEC/D3 cells were cultured on 35 mm coverslip bottom dishes (MatTek, Ashland, MA) until a continuous monolayer was formed. The evening before the experiment, the growth media containing 5% FBS was replaced with growth media containing 1% FBS. Cells were pretreated with or without 4F (10 µg/mL) for 60 minutes at 37 ^{o}C (n=3 each group). Following that, F-Aβ42 was spiked into the media (12.5 µg/mL) and then further incubated for 60 minutes. Cells were washed three times with ice-cold PBS, fixed in 4 % PFA for 60 minutes on ice, and then mounted with ProLong Diamond mounting media containing 4',6-diamidino-2-phenylindole (DAPI) (Invitrogen). Cell monolayers were imaged using a Zeiss LSM 780 laser confocal microscope using a C-Apochromat 40x/1.2W objective.

6.3.10. Statistical analysis. All statistical tests were conducted using GraphPad Prism (GraphPad software; La Jolla, CA). A p value of < 0.05 was considered statistically significant. One-way ANOVA with Tukey's post-tests were used to compare the ^{125}I-4F vs. ^{125}I-ApoA-I distribution in various brain regions. Unpaired, two-tailed t-tests were used to compare the ^{125}I-Aβ distribution in the brain or plasma in mice, the ^{125}I-Aβ flux in vitro, and the F-Aβ uptake in vitro, in groups with vs. without 4F treatment.

6.4. Results

6.4.1. Brain influx of ^{125}I-4F is substantially higher than ^{125}I-ApoA-I. Following femoral injection, the permeability of ^{125}I-4F and ^{125}I-ApoA-I at each brain region was

determined as the PS product, which was obtained by dividing the total radioactivity per gram tissue by the plasma $AUC_{0\text{-}t}$ (Fig. 6.1A). The ^{125}I-4F permeability at various brain regions ranged from 2 to 5 x 10^{-6} ml/g/s, which was ~1000 fold greater ($p < 0.0001$, one-way ANOVA with Tukey's post-tests) compared to the ^{125}I-ApoA-I permeability, which ranged from 2 to 12 x 10^{-9} ml/g/s at various brain regions (Fig. 6.1B).

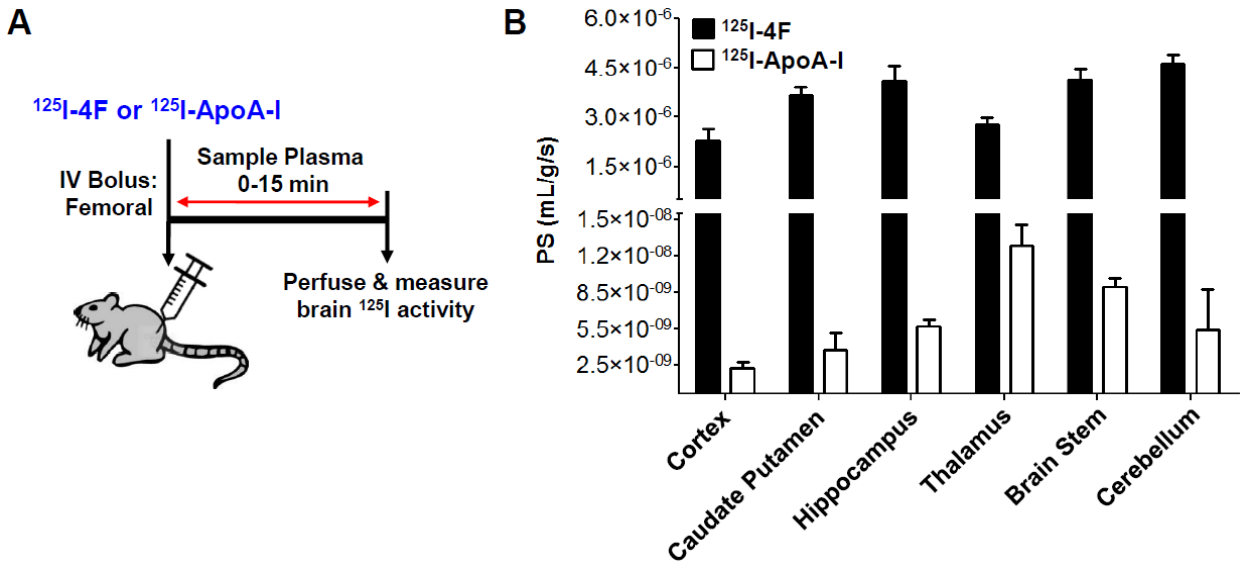

Figure 6.1. Brain influx of ^{125}I-4F is substantially higher than ^{125}I-ApoA-I. (A) Experimental scheme. B6SJLF1/J mice were bolus injected with 100 µCi of ^{125}I-4F or ^{125}I-ApoA-I via the femoral vein. Blood was sampled periodically from the femoral artery from 0-15 minutes. Plasma was separated, intact protein was precipitated with TCA, and radioactivity was measured. After the final sampling event, mice were transcardially perfused with excess PBS, brain regions were dissected, and the radioactivity was measured. (B) The ^{125}I-4F vs. ^{125}I-ApoA-I permeability-surface area (PS) product estimates are shown for various brain regions. Data represent mean ± SD (n=4). ***$p < 0.0001$; one-way ANOVA.

6.4.2. 4F promotes the brain efflux of ^{125}I-Aβ42. Following infusion with saline or 4F (2 mg) via the internal carotid artery, ^{125}I-Aβ42 (0.7 µCi) was stereotaxically injected into the right hippocampus. After forty minutes, ^{125}I radioactivity retained in the brain was

measured and normalized to radioactivity at the site of injection (Fig. 6.2). In mice infused with 4F, retention of ^{125}I-Aβ42 in whole brain (1.7 ± 0.2, mean ± SD, n=3) was decreased by ~2 fold ($p < 0.05$, two-tailed *t*-test) compared to mice infused with saline control (4.0 ± 1.2, mean ± SD, n=3). Similar trends were observed for the right hemisphere, in which the ^{125}I-Aβ42 retention was decreased ($p < 0.05$, two-tailed *t*-test) in the 4F infused mice (1.6 ± 0.2) compared to the saline control (2.9 ± 0.6). The observed decrease in brain retention is reflective of increased brain efflux.

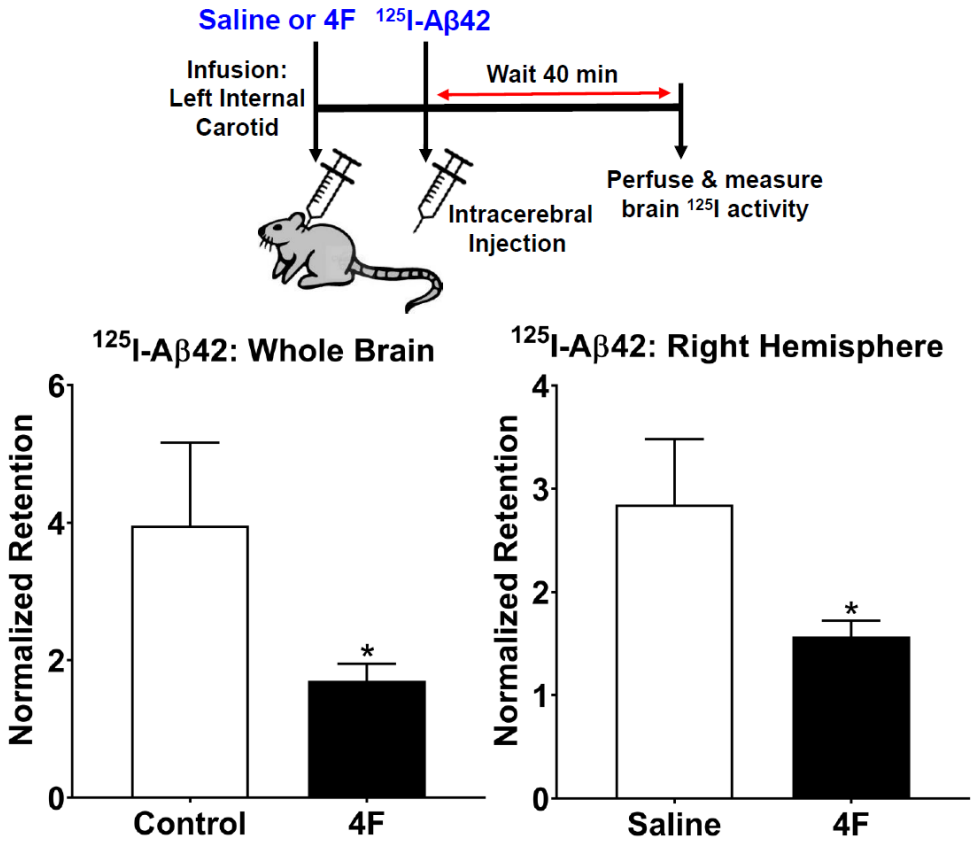

Figure 6.2. 4F promotes brain efflux of ^{125}I-Aβ42. Mice were infused with saline or 4F (2 mg) via the left internal carotid artery over a period of 60 minutes. At the end of infusion, ^{125}I-Aβ42 (0.7 μCi) was stereotaxically injected into the right hippocampus. After 40 minutes, the mice were transcardially perfused with excess PBS, and radioactivity retained in the whole brain and right hemisphere was measured. The bar charts indicate

the radioactivity in whole brain or right hemisphere relative to the radioactivity at the injection site. Data represent mean ± SD (n=3). *$p < 0.05$; unpaired two-tailed *t*-test.

6.4.3. 4F inhibits the brain influx of ^{125}I-Aβ42 but not ^{125}I-Aβ40. Influx of ^{125}I-Aβ42 and ^{125}I-Aβ40 into the brain after femoral injection was assessed as the PS product, determined using the methods described above for ^{125}I-4F. In mice infused with 4F, influx of ^{125}I-Aβ42 into the hippocampus (0.34 ± 0.09 x 10^{-4} mL/g/s, mean ± SD, n=3) decreased by ~4 fold ($p < 0.0001$, two-tailed *t*-test) compared to mice infused with saline control (1.3 ± 0.2 mL/g/s * 10^{-4}, mean ± SD, n=3) (Fig. 6.3A). The hippocampus is the brain region most severely compromised in Alzheimer's disease (Smith, 2002). Aβ influx into the individual brain hemispheres was also evaluated. In mice infused with 4F, influx of ^{125}I-Aβ42 into the left hemisphere (0.54 ± 0.16 x 10^{-4} mL/g/s) decreased by ~2 fold ($p < 0.05$, two-tailed *t*-test) compared to mice infused with saline control (1.1 ± 0.3 x 10^{-4} mL/g/s) (Fig. 6.3B). In contrast, a non-significant increase (p=0.13, two-tailed *t*-test) in ^{125}I-Aβ40 influx into the left hemisphere was observed in the 4F infused mice (1.4 ± 0.8 x 10^{-4} mL/g/s, mean ± SD, n=3) when compared to saline infused mice (0.70 ± 0.54 x 10^{-4} mL/g/s, mean ± SD, n=3) (Fig. 6.3C).

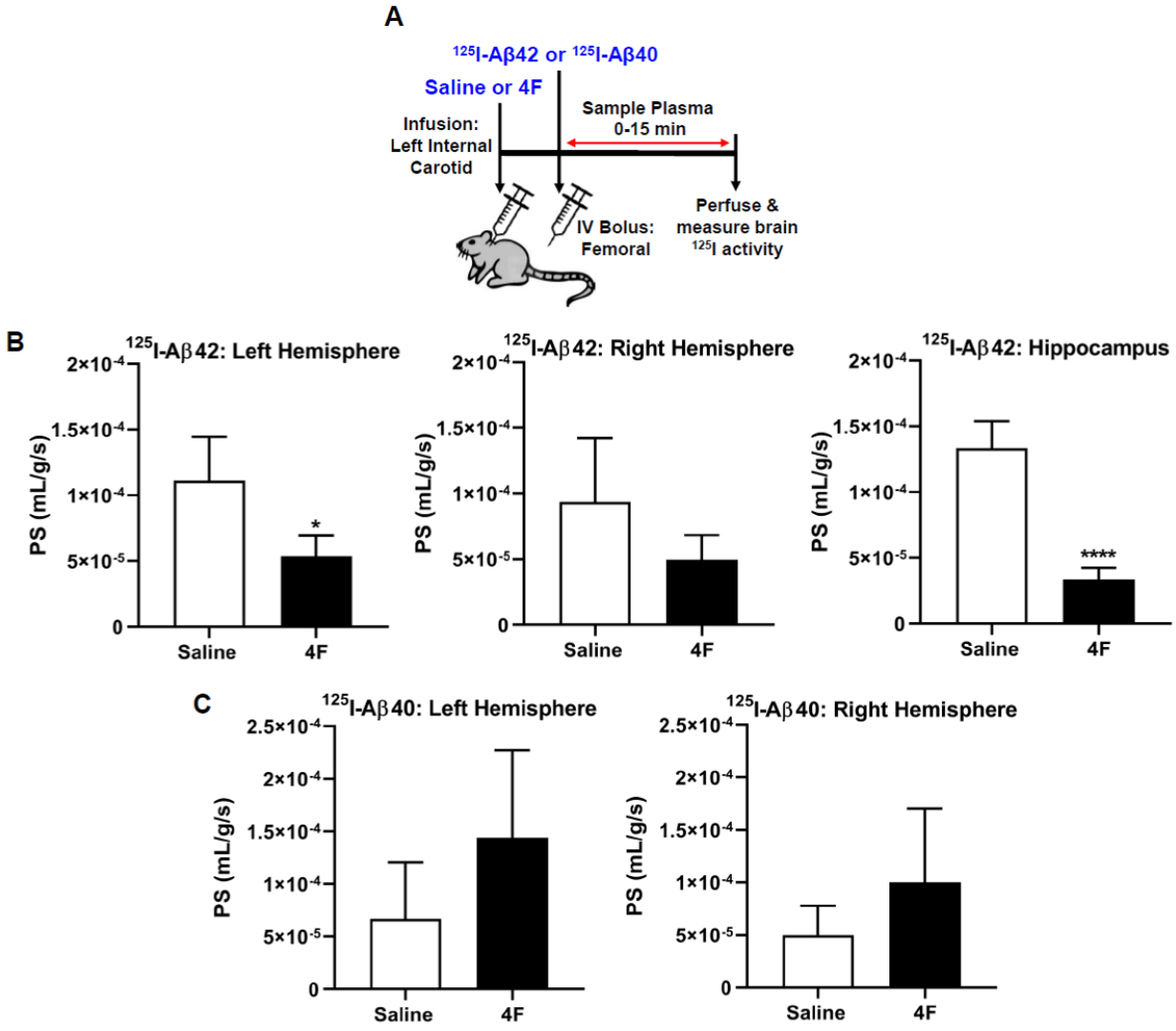

Figure 6.3. 4F inhibits the brain influx of ^{125}I-Aβ42 but not ^{125}I-Aβ40. (A) Experimental scheme. Mice were infused with saline or 4F (2 mg) via the left internal carotid artery over a period of 60 minutes. Following which, 100 µCi of ^{125}I- Aβ42 or ^{125}I-Aβ40 was bolus injected via the femoral vein. Blood was sampled periodically from the femoral artery from 0-15 minutes. Post-perfusion, the brain regions were harvested and the radioactivity was measured. (B) Permeability-surface area (PS) product estimates for ^{125}I-Aβ42 in the left/right hemispheres and hippocampus are shown. Data represent mean ± SD (n=3). *p < 0.05; unpaired two-tailed t-test. (C) The PS product estimates for ^{125}I-Aβ40 in the left/right hemispheres are shown. Data represent mean ± SD (n=3).

6.4.4. Impact of 4F on ^{125}I-Aβ42 and ^{125}I-Aβ40 plasma pharmacokinetics. The ^{125}I-Aβ42 and ^{125}I-Aβ40 plasma concentration vs. time data between 0-15 minutes after femoral injection were evaluated by noncompartmental analysis (Fig. 6.4). The AUC_{0-t} and terminal clearance of ^{125}I-Aβ42 in saline infused mice were estimated as 25.3 ± 18.4 min x µCi/mL and 4.1 ± 2.3 mL/min (mean ± SD, n=3), respectively. These parameters were not significantly altered in the 4F infused mice and were found to be 39.5 ± 27.6 min x µCi/mL (mean ± SD, n=3) and (2.9 ± 1.6 mL/min), respectively. For ^{125}I-Aβ40, the AUC_{0-t} and terminal clearance in saline infused mice were estimated as 53.3 ± 11.7 min x µCi/mL and 1.6 ± 0.3 mL/min (mean ± SD, n=3), respectively. These parameters were unaltered in the 4F infused mice and were estimated as 49.3 ± 16.2 min x µCi/mL and 1.5 ± 0.5 mL/min (mean ± SD, n=3), respectively.

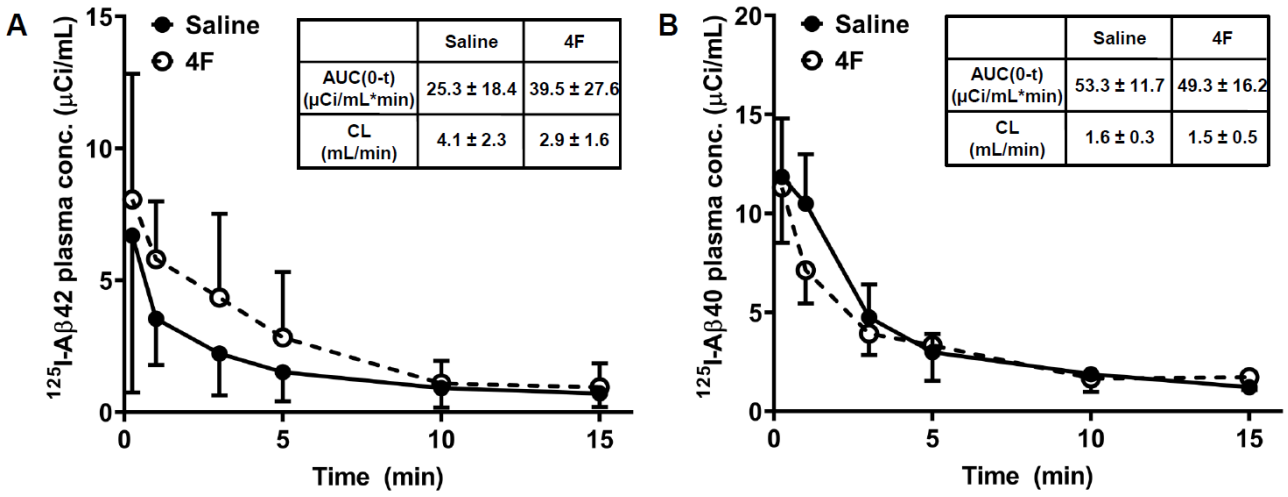

Figure 6.4. Impact of 4F on ^{125}I-Aβ42 and ^{125}I-Aβ40 plasma pharmacokinetics. Mice were infused with saline or 4F (2 mg) via the left internal carotid artery over a period of 60 minutes. Following that, 100 µCi of ^{125}I-Aβ42 or ^{125}I-Aβ40 was bolus injected via the femoral vein. Blood was sampled periodically from the femoral artery between 0-15 minutes. Plasma was separated, intact protein was precipitated with TCA, and radioactivity was measured. Plasma concentration vs. time profiles for ^{125}I-Aβ42 (A) and ^{125}I-Aβ40 (B) were evaluated by noncompartmental analysis. Inset tables show

estimates for the area under the concentration vs. time curve from 0-15 minutes (AUC_{0-t}) and the terminal clearance (CL). Data represent mean ± SD (n=3).

6.4.5. 4F promotes the abluminal-to-luminal flux and inhibits the luminal-to-abluminal flux of ^{125}I-Aβ42 across BBB cell monolayers. To corroborate the in vivo findings, further studies were conducted to examine transport of ^{125}I-Aβ42 across hCMEC/D3 monolayers cultured on Transwell® filters, a widely used in vitro BBB model (Weksler et al., 2013). ^{125}I-Aβ42 transport was investigated in both directions. To study abluminal-to-luminal (A-L) transport (i.e. from brain to blood), cells were treated with 4F and then ^{125}I-Aβ42 was added together on the abluminal side, followed by periodic sampling of the luminal side (Fig. 6.5A). The slope of the linear portion of the cumulative radioactivity vs. time plot estimates the ^{125}I-Aβ42 flux in the A-L direction. A-L flux was increased by ~2 fold ($p < 0.05$, two-tailed *t*-test) in the 4F treated cells ($4.9 \pm 0.4 \times 10^{-4}$ µCi/min, mean ± SD, n=4) as compared to the untreated control ($2.8 \pm 0.3 \times 10^{-4}$ µCi/min, mean ± SD, n=4). To study luminal-to-abluminal (L-A) transport, (i.e. from blood to brain), cells were treated with 4F and then ^{125}I-Aβ42 was added together on the luminal side, followed by periodic sampling of the abluminal side (Fig. 6.5B). The ^{125}I-Aβ42 flux in the L-A direction was decreased by ~2 fold ($p < 0.05$, two-tailed *t*-test) in the 4F treated cells ($2.2 \pm 0.2 \times 10^{-4}$ µCi/min, mean ± SD, n=4) compared to the untreated control ($4.9 \pm 0.9 \times 10^{-4}$ µCi/min, mean ± SD, n=4).

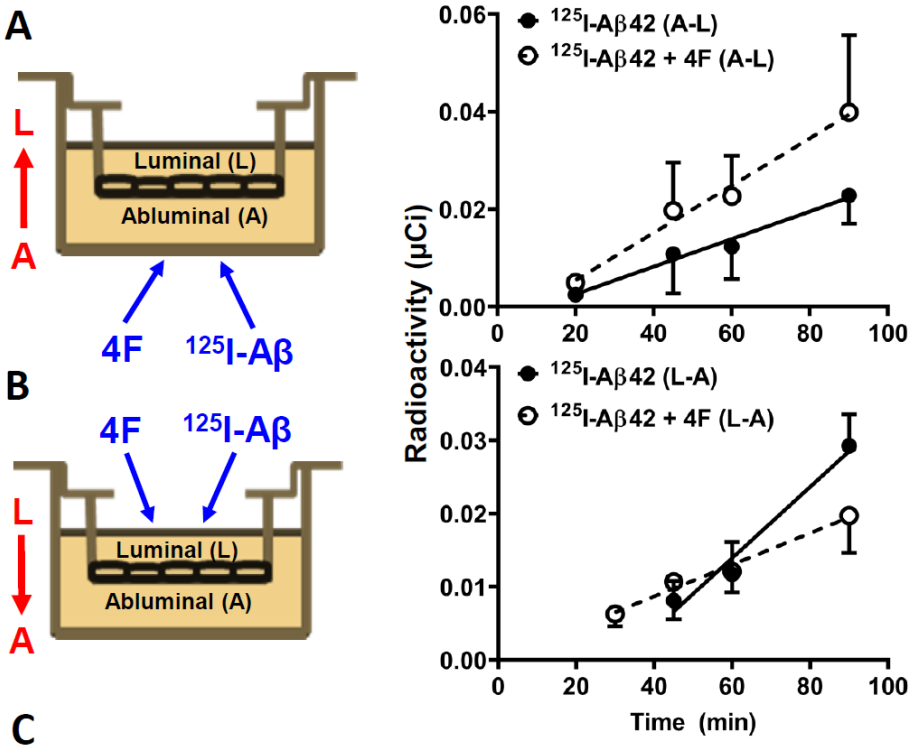

C

	^{125}I-Aβ42	^{125}I-Aβ42 + 4F	Signif.
(A-L) Flux (µCi/min/cm^2 x 10^{-4})	2.5 ± 0.3	4.3 ± 0.4	*
(L-A) Flux (µCi/min/cm^2 x 10^{-4})	4.3 ± 0.8	1.9 ± 0.2	*

Figure 6.5. 4F promotes the abluminal-to-luminal flux and inhibits the luminal-to-abluminal flux of ^{125}I-Aβ42 across BBB cell monolayers. Polarized hCMEC/D3 monolayers cultured on Transwell® filters were treated with 4F (10 µg/mL) and ^{125}I radiolabeled Aβ42 (10 µCi/mL) together on the abluminal side to investigate A-L flux (A), or on the luminal side to investigate L-A flux (B). Receiver medium was periodically sampled from the contralateral side, and radioactivity was measured. Cumulative radioactivity was plotted against time, and the linear region was fit to a linear regression model. Data represent mean ± SD (n=4). (C) Flux was obtained by dividing the linear regression slope by the surface area (1.12 cm^2) of the insert. Data represent mean ± SE (n=4). *$p < 0.05$; unpaired two-tailed t-test.

6.4.6. 4F inhibits the accumulation of fluorescein-labeled Aβ42 in BBB cell monolayers.

The effects of 4F on the uptake of fluorescein-labeled Aβ (F-Aβ) in hCMEC/D3 monolayers was further investigated. Treatment with 4F decreased cellular uptake of F-

Aβ42 by ~1.4 fold ($p < 0.05$, two-tailed *t*-test) when assessed by flow cytometry (Fig. 6.6A). In contrast, no significant differences were observed in cell uptake of F-Aβ40 following treatment with 4F (Fig. 6.6B). Further, confocal micrographs depicted lower intracellular accumulation of F-Aβ42 in cells treated with 4F (Fig. 6.6C).

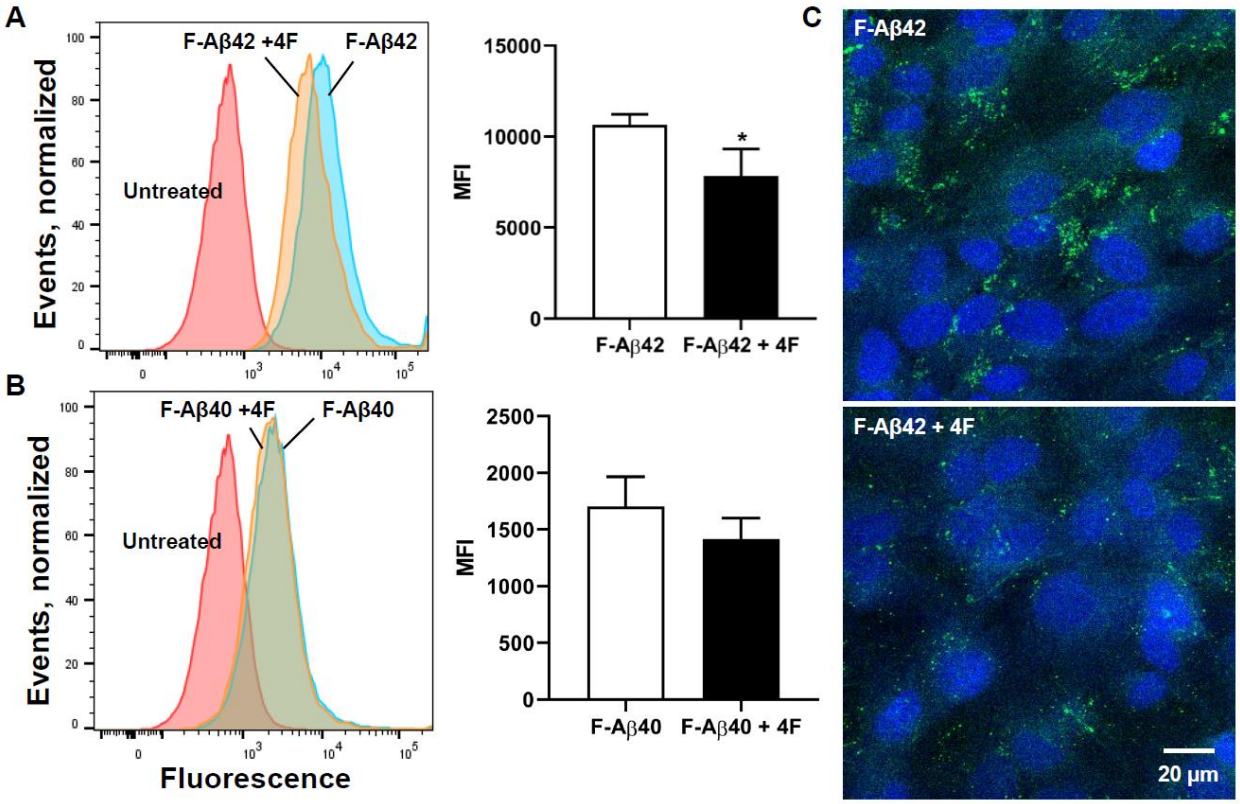

Figure 6.6. 4F inhibits accumulation of fluorescein-labeled Aβ42 in BBB cell monolayers. hCMEC/D3 monolayers were treated for 60 minutes with 10 µg/mL 4F peptide, followed by another 60 minutes with 12.5 µg/mL of fluorescein-labeled Aβ42 (F-Aβ42) (A) or F-Aβ40 (B). Fluorescence uptake was assessed by flow cytometry. Shown are representative histograms and bar charts of group mean ± SD (n=3). *$p < 0.05$; unpaired two-tailed *t*-test. (C) Confocal micrographs are shown depicting F-Aβ42 internalization in hCMEC/D3 monolayers cultured on coverslip dishes following 4F treatment as described above (representative images, n=3). Green = F-Aβ42; blue = DAPI-stained nuclei.

6.5. Discussion and Conclusions

It is well-established that plasma ApoA-I levels are strong predictors of cardiovascular risk. Given that metabolic disorders, CVD and AD are closely linked, it is construed that decreased serum ApoA-I levels contribute toward cerebrovascular dysfunction in AD. This claim is strongly supported by published reports that have demonstrated inverse correlations between plasma ApoA-I levels and AD risk in elderly patients (Saczynski et al., 2007; Ma et al., 2015; Slot et al., 2017). We previously showed that CAA, the most prevalent cerebrovascular pathology in AD, and cognitive decline could be mitigated by increasing ApoA-I levels in the plasma of AD transgenic mice (Lewis et al., 2010). However, the mechanisms by which ApoA-I promotes cerebrovascular Aβ clearance and thereby protects from CAA and related neurovascular pathologies are poorly understood.

Our previous studies have shown that increased Aβ uptake on the luminal side and/or decreased Aβ efflux from the abluminal side could trigger Aβ buildup in the cerebral vasculature (Agyare et al., 2013), which is expected to further impede Aβ clearance from the brain. Hence, it is likely that ApoA-I reduces cerebrovascular Aβ deposition by modulating Aβ trafficking machinery at the BBB. Interestingly, ApoA-I on the luminal side was shown to increase Aβ efflux in the abluminal-to-luminal direction across cerebrovascular endothelial cell monolayers (Merino-Zamorano et al., 2016). However, it remains unclear if it is ApoA-I in the plasma, in the brain, or both that drive cerebrovascular Aβ clearance.

Decreased ApoA-I levels in the brain and cerebrospinal fluid are associated with neurological diseases like schizophrenia (Huang et al., 2008). ApoA-I is mostly

produced in the periphery, with little to no production in the brain (Elliott et al., 2010). Thus, the ApoA-I present in brain is thought to be delivered from systemic circulation via trafficking at the BBB endothelium and/or the blood-cerebrospinal fluid barrier epithelium. ApoA-I is a large protein and its permeability across these barriers is extremely low (Stukas et al., 2014a; Zhou et al., 2019). Hence, it is important to consider ApoA-I mimetic peptides, like 4F, as therapeutic alternatives. Further, the 18 amino acid 4F peptide is more amenable to pharmaceutical development compared to the full-length ApoA-I protein. As a small, amphipathic peptide that interacts with the plasma membrane (Datta et al., 2001), 4F is expected to cross the BBB efficiently. To confirm this in vivo, the PS product, a widely used parameter to assess brain uptake of macromolecules, was determined after systemic injection of ^{125}I-4F or ^{125}I-ApoA-I in mice. PS values of ^{125}I-4F at various brain regions were ~1000 fold greater than those determined for ^{125}I-ApoA-I, and were commensurate to those of proteins like transferrin and insulin, which are efficiently delivered across the BBB (Poduslo et al., 1994). In contrast, PS values of ^{125}I-ApoA-I were similar to those of proteins that demonstrate very low BBB permeability, such as Immunoglobulin G and albumin (Poduslo et al., 1994). Efficient brain penetrance of 4F provides a plausible mechanistic interpretation of the robust 4F effects on neuropathology in AD mice. Given that PS values are representative only of influx, the impact of 4F brain efflux on the overall brain delivery remains to be clarified.

Further, we investigated the ability of 4F to modulate Aβ trafficking from brain-to-blood and from blood-to-brain. To assess 4F effect on ^{125}I-Aβ42 clearance from brain-to-blood, the ^{125}I-Aβ42 radioactivity retained in the brain following intracerebral injection

was assessed in mice infused with 4F via the internal carotid artery, which supplies blood directly to the brain. This experimental modality allowed us to specifically investigate 4F effects on ^{125}I-Aβ42 transport at the BBB. Brain retention of ^{125}I-Aβ42 was substantially decreased in 4F treated mice, which could be attributed to increased ^{125}I-Aβ42 brain efflux. It was also observed that after femoral injection, brain influx of ^{125}I-Aβ42, assessed as the PS product, was substantially decreased in 4F treated mice. Together, these findings indicate that 4F reduces brain accumulation of ^{125}I-Aβ42 by increasing its brain-to-blood efflux and by decreasing its blood-to-brain influx. Intriguingly, 4F exhibited distinct effects in modulating brain influx of ^{125}I-Aβ40 as compared to ^{125}I-Aβ42; a non-significant increase in ^{125}I-Aβ40 brain influx was observed in the 4F treated mice. Importantly, Aβ42 is more neurotoxic and amyloidogenic than Aβ40, and parenchymal amyloid plaques in AD brain are seeded by Aβ42 aggregates (Miller et al., 1993). Additionally, Aβ40 is reported to inhibit Aβ42 oligomerization, fibrillogenesis, and toxicity (Jan et al., 2008; Murray et al., 2009). In AD patients, the accelerated amyloid accumulation in the cerebral vasculature and brain parenchyma is thought to be mostly due to impaired Aβ42 clearance from brain-to-blood (Sagare et al., 2012). By helping to restore Aβ42 clearance at the BBB, 4F could thereby reduce both cerebrovascular and parenchymal amyloid burden in AD brain.

No significant differences were observed in the ^{125}I-Aβ42 plasma pharmacokinetics in 4F treated mice, although a visual trend of increased AUC with a concomitant decrease in terminal clearance was observed. The apparent decrease in plasma clearance of ^{125}I-Aβ42 in the presence of 4F could be due to altered Aβ42 clearance mechanisms in kidneys and liver, which are the major organs responsible for

systemic Aβ clearance (Ghiso et al., 2004). Since the plasma disposition of Aβ and its trafficking at the BBB are thought to be handled by LDL receptor-related protein 1 (LRP1) and scavenger receptor class B type 1 (SR-B1) (Martins et al., 2009; Thanopoulou et al., 2010), both of which are highly expressed in the vascular endothelium, we speculate that 4F modulates Aβ disposition by interacting with these receptors. It was previously shown that HDL transcytosis at the BBB is mediated by SR-B1 (Fung et al., 2017). Furthermore, ATP-binding cassette transporter A1 (ABCA1), expressed on the abluminal surface of the BBB endothelium, was shown to mediate brain efflux of Aβ42 (Elali and Rivest, 2013). As a major lipid transporter, ABCA1 interacts with HDL/ApoA-I and other apolipoproteins that mediate lipid efflux and reverse cholesterol transport. Studies have shown that ABCA1 overexpression mitigates, whereas ABCA1 deletion exacerbates brain Aβ deposition in AD mice (Wahrle et al., 2005; Wahrle et al., 2008). We recently showed that 4F interacts with ABCA1 to mediate cholesterol/lipid efflux (Chernick et al., 2018). Thus, the altered brain influx of ^{125}I-Aβ42 upon 4F treatment could potentially be mediated by effects on ABCA1 at the BBB.

Since only female mice were used in this study, further studies are needed to examine potential gender differences in 4F efficacy. In various AD transgenic mouse models, such as 3xTg-AD (Carroll et al., 2010; Gali et al., 2019), APP/PS1, and Tg2576 mice (Callahan et al., 2001), female mice were reported to exhibit higher Aβ levels and greater occurrence of histopathological hallmarks compared to their male littermates. Moreover, gender differences were also apparent in the efficacy of experimental AD therapies that mitigate Aβ pathology (Long et al., 2016; Dodiya et al., 2019). In this

study, experiments were conducted solely on female mice, so that follow up studies can be pursued in female APP/PS1 mice, which are reported to manifest higher Aβ levels compared to male mice. APP/PS1 mice will serve as a more stringent model to test the efficacy and mechanistic action of 4F.

Further, we investigated ^{125}I-Aβ42 transcytosis in both directions across BBB cell monolayers cultured on Transwell® filters. Treatment with 4F was shown to increase the abluminal-to-luminal flux of ^{125}I-Aβ42, which is consistent with the increased brain efflux of ^{125}I-Aβ42 observed in 4F treated mice. We further showed that 4F decreased luminal-to-abluminal flux of ^{125}I-Aβ42, which is consistent with decreased brain influx of ^{125}I-Aβ42 observed in 4F treated mice. Together, these findings indicate that 4F differentially modulates ^{125}I-Aβ42 trafficking at the BBB in the luminal-to-abluminal (blood-to-brain) versus abluminal-to-luminal (brain-to-blood) directions.

To investigate the effects of 4F on cerebrovascular accumulation of Aβ, which predominates in both CAA and AD, cellular uptake of fluorescein-labeled Aβ in BBB cell monolayers was assessed upon 4F treatment. The F-Aβ42 cell uptake measured by flow cytometry was decreased in 4F treated cells, whereas the F-Aβ40 uptake was not significantly altered. Using laser confocal microscopy, we also demonstrated lower intracellular accumulation of F-Aβ42 in 4F treated cells. Although Aβ40 is the predominant isoform present in the cerebrovascular amyloid deposits, Aβ42 was shown to seed formation of these deposits (Roher et al., 1993; McGowan et al., 2005). Thus, 4F could be effective in reducing cerebrovascular Aβ deposition in CAA and AD.

In summary, brain permeability of ^{125}I-4F, assessed as the PS product, was found to be ~1000 fold greater than that of ^{125}I-ApoA-I, and was comparable to proteins

like transferrin and insulin which rapidly permeate across the BBB. Moreover, systemic infusion of 4F was shown to modulate BBB trafficking of ^{125}I-Aβ42 by increasing its brain-to-blood efflux and by decreasing its blood-to-brain influx. These findings clarify the effects of 4F on specific Aβ isoforms and provide a mechanistic interpretation of the decreased brain Aβ deposition reported in AD transgenic mice following chronic oral dosing of 4F (Handattu et al., 2009). However, it remains unclear whether 4F elicits these beneficial effects by acting on the luminal side, or by acting within the brain parenchyma after crossing the BBB. Further studies are needed to clarify molecular mechanisms by which 4F alleviates Aβ associated neuropathologies in CAA and AD. Although clinical efficacy of 4F was demonstrated in CVD patients (Bloedon et al., 2008; Dunbar et al., 2017), the efficacy of 4F in treating AD patients remains to be carefully elucidated, especially from the perspective of challenges encountered in the clinical translation of anti-Aβ therapeutics. Nevertheless, as an ApoA-I/HDL mimetic peptide, 4F also possesses anti-oxidative and inflammatory properties, and thus presents a novel therapeutic approach to enhance cerebrovascular function as well as to mitigate brain Aβ accumulation in CAA and AD.

Chapter 7: Systemic effects of an anti-Aβ monoclonal antibody on Aβ peptide trafficking at the BBB

7.1. Synopsis

Over the last 20 years, tremendous efforts have been made to develop therapeutic monoclonal antibodies targeting various Aβ species, intended to clear Aβ

peptides from the brain and mitigate cognitive decline in AD patients. The “sink hypothesis” purports that plasma exposure to these antibodies sequesters the plasma Aβ pool, creating a “sink” that promotes brain Aβ clearance. However, this hypothesis has yet to be experimentally validated by focused pharmacokinetic studies using Aβ peptide tracers. Here, we investigated the effects of IgG4.1, an established immunoglobulin G (IgG) antibody against fibrillar human Aβ42, on the plasma pharmacokinetics and BBB trafficking of Aβ peptides in wild-type mice. Upon intravenous administration of IgG4.1, plasma clearance of ^{125}I radiolabeled Aβ40 and Aβ42 peptides declined by 9-fold and 4-fold, respectively. This was accompanied by a modest decrease in ^{125}I-Aβ40 and ^{125}I-Aβ42 accumulation in various brain regions, alongside a 2-3-fold decrease in the PS values for ^{125}I-Aβ42 uptake at various brain regions. Dynamic SPECT/CT imaging was performed to further investigate the effects of IgG4.1 on ^{125}I-Aβ42 uptake and binding at the BBB. Based on Gjedde-Patlak graphical analysis, a 3-fold decrease in blood-to-brain influx clearance of ^{125}I-Aβ42 was observed in the IgG4.1 treated mice. Logan graphical analysis was performed to assess the initial binding of ^{125}I-Aβ42 to the BBB endothelium. Upon treatment with IgG4.1, a 2-fold decrease in the initial distribution volume occupied by ^{125}I-Aβ42 in the brain vasculature was observed. These findings indicate that plasma exposure to an anti-Aβ IgG substantially reduces Aβ peptide clearance from plasma and distribution to the brain. However, further studies are needed to delineate the systemic effects of anti-Aβ monoclonal antibodies on Aβ peptide clearance from brain to plasma. Such insights could have important ramifications toward the design of future Aβ immunotherapies for the treatment of AD.

7.2. Background

The passive immunotherapy approach using immunoglobulin G (IgG) antibodies engineered to bind and clear Aβ peptides from the brains of AD patients remains an attractive yet controversial area in AD drug development. This is largely due to the mixed success of several high-profile phase 3 clinical trials for various anti-Aβ monoclonal antibodies (mAbs) being developed by various pharmaceutical companies (Tolar et al., 2020). Aducanumab, the first Aβ immunotherapy to receive FDA approval in 2021, has been fraught with controversy regarding its efficacy in mitigating cognitive decline, and is broadly considered a commercial failure (Alexander et al., 2021). Furthermore, the serious side effect of cerebral microhemorrhages, referred to as amyloid-related imaging abnormalities (ARIA), is common for this class of drugs (Filippi et al., 2022; Foley and Wilcock, 2022). Similar molecules such as lecanemab and donanemab were shown to moderately reduce cognitive decline in early AD patients, although similar challenges were faced due to ARIA risk (Shi et al., 2022; van Dyck et al., 2023).

Conventional mAbs comprised of a full-length IgG backbone demonstrate extremely low permeability across the blood-brain barrier (BBB) after systemic administration (Poduslo et al., 1994). It is estimated that only 0.1% of a mAb dose given intravenously enters the brain (Bard et al., 2012). As such, the “sink hypothesis” has been proposed as a potential mechanism to explain the ability of systemically administered anti-Aβ mAbs to reduce brain Aβ burden in AD patients and mouse models (Zhang and Lee, 2011; Liu et al., 2015). This hypothesis proposes that anti-Aβ mAbs in plasma bind to and sequester circulating soluble Aβ species, resulting in a shift

in the dynamic equilibrium between the Aβ pools in plasma and brain interstitial fluid. These two pools undergo reversible exchange via bidirectional receptor-mediated transcytosis processes at the BBB (Deane et al., 2004). By sequestering plasma Aβ, the mAb is believed to act as a sink that drives brain Aβ efflux to the plasma, where it may then be cleared by the kidneys and liver (Ghiso et al., 2004).

In support of the sink hypothesis, solanezumab and ponezumab, which target Aβ but do not bind to insoluble aggregates in the brain, were shown to decrease brain Aβ burden in AD patients (Doody et al., 2014; Salloway et al., 2014). Notably, cerebral microhemorrhages associated with ARIA have been rarely observed for anti-Aβ mAbs that do not bind to Aβ aggregates in the brain, such as solanezumab (Carlson et al., 2011). This is potentially due to Fc effector functions that trigger inflammation directly at the sites of antibody binding to Aβ plaques/deposits in the brain (Mader et al., 2017). These observations suggest that peripheral action of anti-Aβ mAbs may have an improved safety profile over central action as a treatment for AD. In AD transgenic mice, systemic administration of an anti-Aβ mAb led to a rapid increase in endogenous plasma Aβ levels, which correlated with a decrease in brain Aβ burden (DeMattos et al., 2002). While this study and similar findings in the clinic have been broadly interpreted as evidence of the sink effect (Liu et al., 2015), the antibody effects on plasma Aβ could also be explained by antibody binding to Aβ in plasma, which is expected to alter the Aβ plasma pharmacokinetics.

To clarify the systemic effects of anti-Aβ mAbs on Aβ peptide distribution between plasma and brain, we investigated the effects of IgG4.1 on the plasma pharmacokinetics and BBB trafficking of ^{125}I radiolabeled Aβ peptides in wild-type mice.

IgG4.1 is an established IgG antibody against fibrillar human Aβ42, which we have characterized previously (Poduslo et al., 2007; Ramakrishnan et al., 2009). Upon a single intravenous injection of IgG4.1, the plasma pharmacokinetics of intravenously injected ^{125}I-Aβ42 and ^{125}I-Aβ40 were evaluated. Plasma-to-brain distribution and initial BBB binding of ^{125}I-Aβ42 were assessed based on the permeability-surface area (PS) products at various brain regions, and by dynamic SPECT/CT imaging studies of ^{125}I-Aβ42 distribution to the brain followed by Patlak and Logan graphical analyses. The current findings indicate that plasma exposure to IgG4.1 leads to a substantial reduction in ^{125}I-Aβ clearance from plasma and distribution to the brain.

7.3. Materials & Methods

7.3.1. Animals. B6SJLF1 mice were obtained from Jackson Laboratory (Bar Harbor, ME). Mice were housed in the Mayo Clinic animal facility and were provided with food and water ad libitum. An equal number of male and female mice around four to eight months of age were used in all studies. All procedures involving the use of animals were approved by the Mayo Institutional Animal Care and Use Committee and were performed in accordance with the Guide for the Care and Use of Laboratory Animals provided by the National Institute of Health.

7.3.2. Radioiodination of Aβ peptides. Human Aβ40 and Aβ42 peptides (AAPPtec, LLC; Louisville, KY) were labeled with ^{125}I radionuclide (PerkinElmer Life and Analytical Sciences, Boston, MA) using the chloramine-T procedure described previously (Poduslo et al., 1994; Kandimalla et al., 2005). Unconjugated ^{125}I was removed by dialysis. The

purity of ^{125}I-labeled proteins was assessed by trichloroacetic acid (TCA) precipitation. Over 95% of the total radioactivity counts were precipitated with TCA.

7.3.3. Plasma pharmacokinetics and brain accumulation of ^{125}I-Aβ40 and ^{125}I-Aβ42.

These experiments were carried out as described in our previous publications (Kandimalla et al., 2005). Briefly, male and female B6SJLF1 mice (n=4 per treatment) were anesthetized (1.5% isoflurane with 4 L/min O_2) and catheterized at the femoral vein/artery. A single dose of IgG4.1 (1 mg in 200 µL of PBS) or the vehicle alone was administered by intravenous bolus injection to the femoral vein. After 30 minutes, a single dose of ^{125}I-Aβ40 or ^{125}I-Aβ42 (100 µCi in 200 µL of PBS) was administered by intravenous bolus injection to the femoral vein. Blood samples (20 µL) were collected from the femoral artery at 0.5, 1, 3, 5, 10, 15, 30, 45 and 60 minutes post-Aβ injection. The plasma was separated, and the protein fraction was isolated by TCA precipitation. The ^{125}I activity in the protein fraction was assayed using a gamma counter (Cobra II; Amersham Biosciences Inc., Piscataway, NJ). Immediately after the final blood sample was collected, the mouse was euthanized by transcardial perfusion with excess PBS to flush any remaining ^{125}I activity from the vasculature. The whole brain was removed and dissected into anatomical regions (cortex, caudate putamen, hippocampus, thalamus, brain stem and cerebellum). ^{125}I activity in the brain regions was assayed using a gamma counter.

^{125}I-Aβ40 and ^{125}I-Aβ42 plasma concentration vs. time data were fit to a two-compartment pharmacokinetic model using Phoenix WinNonlin (Pharsight, Mountain View, CA):

$$C_p(t) = Ae^{-\alpha t} + Be^{-\beta t}$$

where $C_p(t)$ is the concentration (µCi/mL) at time t (min), $A + B$ is the concentration at $t = 0$, and α and β are the rate constants describing the distribution and elimination phases, respectively. The following secondary pharmacokinetic parameters were also estimated: whole-body clearance, CL (mL/min); volume of the central compartment, V_1 (mL); steady-state volume, V_{SS} (mL); terminal half-life, $t_{1/2,\beta}$ (min); and the area under the plasma concentration vs. time curve from time zero to infinity, $AUC_{0\text{-}inf}$ (min.µCi/mL).

The accumulation of ^{125}I-Aβ42 or ^{125}I-Aβ40 in the cortex, caudate putamen, hippocampus, thalamus, brain stem or cerebellum was expressed as:

$$\%\,\mathrm{ID/g} = \frac{\left(\frac{X_{brain}}{Dose} \times 100\right)}{W_{brain}}$$

where $\%\,\mathrm{ID/g}$ is the percent of the injected dose measured in the brain region per gram of tissue, X_{brain} is the amount of ^{125}I activity (µCi) in the brain region, $Dose$ is the 100 µCi injected dose, and W_{brain} is the brain region weight (g).

7.3.4. Dynamic SPECT/CT imaging of ^{125}I-Aβ42 distribution after intravenous injection.

Mice (n=4 per treatment) were anesthetized (1.5% isoflurane with 4 L/min O_2) and catheterized at the femoral vein/artery. A single dose of IgG4.1 (1 mg in 200 µL of PBS) or vehicle alone was administered by intravenous bolus injection to the femoral vein. After 30 minutes, a single dose of ^{125}I-Aβ40 or ^{125}I-Aβ42 (500 µCi in 200 µL of PBS) was administered by intravenous bolus injection to the femoral vein. Immediately following that, the entire animal was placed inside a single-photon emission computed tomography (SPECT/CT) scanner (Gamma Medica, Northridge, CA), and the

biodistribution of radioactive signal was imaged at 1 min intervals over the next 15 min, followed by a CT scan to locate regions of interest (ROIs), including the brain. Immediately following that, the mouse was euthanized by transcardial perfusion with excess PBS to flush any remaining ^{125}I activity from the vasculature. The whole brain was removed and dissected into anatomical regions (cortex, caudate putamen, hippocampus, thalamus, brain stem and cerebellum). ^{125}I activity in the brain regions was assayed using the gamma counter.

7.3.5. Permeability of ^{125}I-Aβ42 into various brain regions. The permeability-surface area (PS) product (mL/g/s) of ^{125}I-Aβ42 at different brain regions was determined as described previously (Poduslo et al., 2001), using the following equation:

$$\mathrm{PS} = \frac{\mathrm{X_{brain}}}{\mathrm{AUC_{plasma}} \times \mathrm{W_{brain}}}$$

Where $\mathrm{X_{brain}}$ is the amount of ^{125}I activity (µCi) measured in each brain region at 15 min post-injection, $\mathrm{AUC_{plasma}}$ is the predicted area under the plasma concentration vs. time profile (µCi.min/mL) from 0-15 min, estimated from the biexponential model parameters, and $\mathrm{W_{brain}}$ is the brain region weight (g).

7.3.6. Graphical analysis of dynamic imaging data to assess ^{125}I-Aβ42 distribution to the brain and initial binding at the BBB. Two related graphical analysis techniques, developed by Patlak et al. (Patlak et al., 1983) and Logan et al. (Logan et al., 1990), were used to assess blood-to-brain influx clearance and initial BBB binding of ^{125}I-Aβ42 in mice treated with or without IgG4.1.

Patlak plots were constructed to estimate the brain influx clearance of ^{125}I-Aβ42, which involved plotting:

$$\frac{X_{ROI}(t)}{C_p(t)} \; vs. \frac{AUC_{p_0}^{\;t}}{C_p(t)}$$

Where $X_{ROI}(t)$ is the amount of ^{125}I activity (µCi) in the brain ROI at time t (min), $C_p(t)$ is the concentration (µCi/mL) in plasma at time t (min), and $AUC_{p_0}^{\;t}$ is the area under the plasma concentration vs. time curve (µCi.min/mL) from time 0-t estimated by the logarithmic trapezoidal method. The ^{125}I-Aβ42 plasma concentrations at each imaging timepoint were predicted using the two compartment pharmacokinetic parameters. Regression was performed on the linear section of the Patlak plot, which corresponded to the data between 5-15 min post-injection. The slope estimates the plasma-to-brain influx clearance, K_i (mL/min), of ^{125}I-Aβ42.

Logan plots were constructed to estimate the initial distribution volume of ^{125}I-Aβ42 in the brain ROI. This involved plotting:

$$\frac{AUC_{ROI_0}^{\;t}}{C_{ROI}(t)} \; vs. \frac{AUC_{p_0}^{\;t}}{C_{ROI}(t)}$$

Where $AUC_{ROI_0}^{\;t}$ is the area under the brain ROI concentration vs. time curve (µCi.min/mL) from time 0-t estimated by the logarithmic trapezoidal method, $C_{ROI}(t)$ is the concentration (µCi/mL) in the ROI at time t, and $AUC_{p_0}^{\;t}$ is the area under the plasma concentration vs. time curve (µCi.min/mL) from time 0-t estimated by the logarithmic trapezoidal method. Given that ROI concentrations are measured in units of µCi/cc, the values were converted to µCi/mL based on the convention of 1 cc=1 mL. The ^{125}I-Aβ42 plasma concentrations at each imaging timepoint were predicted using the two-compartment pharmacokinetic parameters. The slope obtained from regression of the linear section of the Logan plot estimates the initial distribution volume, V_d, occupied by

^{125}I-Aβ42 in the brain ROI. V_d estimated by the Logan plot slope is expressed as a unitless ratio (mL/mL) (Logan et al., 1990).

7.3.7. Statistical analysis. All statistical tests were performed using GraphPad Prism (GraphPad software; La Jolla, CA). A *p* value of ≤ 0.05 was considered statistically significant. Two-way ANOVA with Bonferroni's post-tests were used to compare the %ID/g or PS values in different brain regions of mice treated with vs. without IgG4.1. Unpaired, two-tailed *t*-tests were used to compare the K_i or V_d estimates, obtained from the Patlak and Logan plot slopes, in mice treated with vs. without IgG4.1.

7.4. Results

7.4.1. IgG4.1 reduces the plasma clearance of ^{125}I-Aβ40 and ^{125}I-Aβ42. Upon femoral injection of ^{125}I-Aβ40 or ^{125}I-Aβ42, both peptides exhibited a biexponential decline in their plasma concentrations with time (Fig. 7.1). This is consistent with our earlier publications (Kandimalla et al., 2005; Swaminathan et al., 2017). The two-compartment model-derived pharmacokinetic parameters for ^{125}I-Aβ40 or ^{125}I-Aβ42 in mice injected with either 1 mg of IgG4.1 or the vehicle alone, administered to the femoral vein 30 min prior to ^{125}I-Aβ injection, are provided in Table 7.1. Upon systemic IgG4.1 treatment, a ~9-fold decrease was observed in the plasma clearance of ^{125}I-Aβ40 (Fig. 7.1A), while a ~4-fold decrease was observed in the plasma clearance of ^{125}I-Aβ42 (Fig. 7.1B). A ~3-4-fold decrease in the steady-state distribution volume in plasma (V_{ss}) of both peptides was observed in the mice treated with IgG4.1 (Table 7.1).

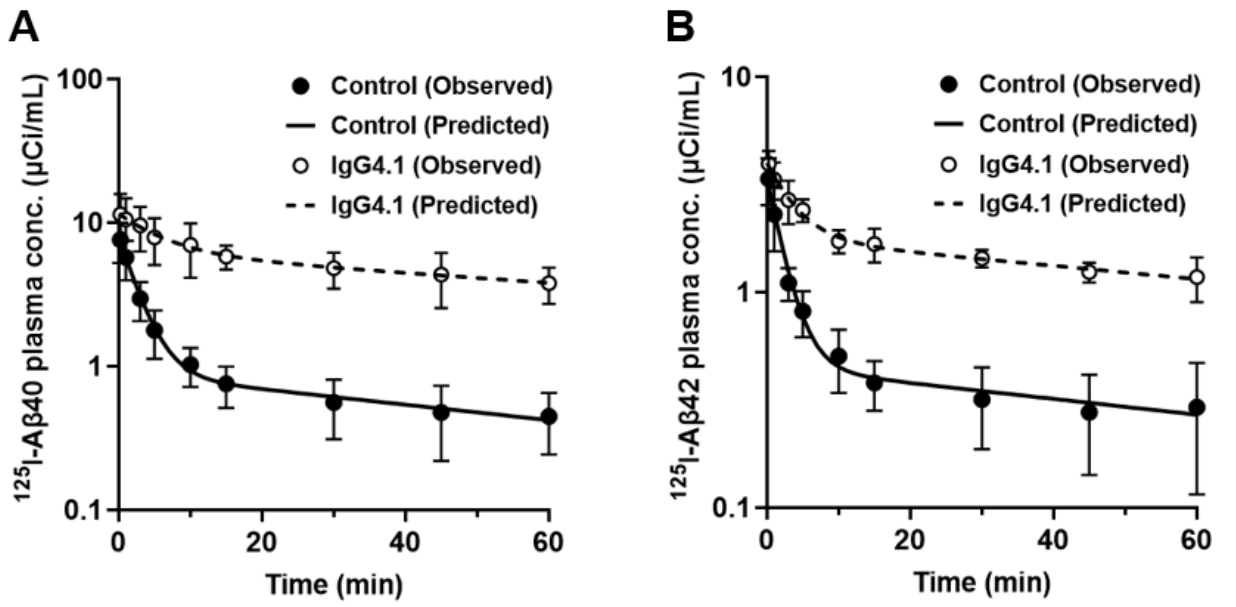

Figure 7.1. Systemic IgG4.1 treatment reduces the plasma clearance of ^{125}I-Aβ40 and ^{125}I-Aβ42 peptides. Plasma concentration vs. time profiles of ^{125}I-Aβ40 (A) or ^{125}I-Aβ42 (B) in mice treated with 1 mg of IgG4.1 or the vehicle control. The observed values (circles) are overlaid with the predicted curve obtained from the two-compartment modeled-derived parameters. Data points are mean ± SD (n=4).

Parameter	^{125}I-Aβ40		^{125}I-Aβ42	
	Control	IgG4.1	Control	IgG4.1
CL (mL/min)	1.11 ± 0.10	0.12 ± 0.02	1.67 ± 0.39	0.39 ± 0.05
V_1 (mL)	12.4 ± 0.8	8.6 ± 0.2	29.1 ± 2.9	25.1 ± 0.9
V_{ss} (mL)	72.0 ± 7.9	15.0 ± 1.0	175 ± 27	53.0 ± 3.0
$t_{1/2,\beta}$ (min)	56.0 ± 10.3	87.2 ± 17.4	81.8 ± 29.1	96.8 ± 18.6
AUC_0^∞ (min x μCi/mL)	90.1 ± 8.2	805 ± 106	59.8 ± 13.9	255 ± 35

Table 7.1. Plasma pharmacokinetic parameters of ^{125}I-Aβ40 and ^{125}I-Aβ42 in mice treated with IgG4.1. Estimates are mean ± SE.

7.4.2. IgG4.1 has minimal effect on ^{125}I-Aβ40 and ^{125}I-Aβ42 accumulation in various brain regions. Upon femoral injection of ^{125}I-Aβ40 or ^{125}I-Aβ42, brain accumulation after 60 minutes was assessed as the percent of the injected dose measured in each

dissected brain region per gram of tissue (%ID/g). This included the cortex, caudate putamen, hippocampus, thalamus, brain stem, cerebellum, and olfactory bulb. Interestingly, the %ID/g of ^{125}I-Aβ40 and ^{125}I-Aβ42 in most brain regions was not significantly altered in the mice treated with IgG4.1 (Fig. 7.2). However, a modest trend of reduced uptake was observed for both peptides.

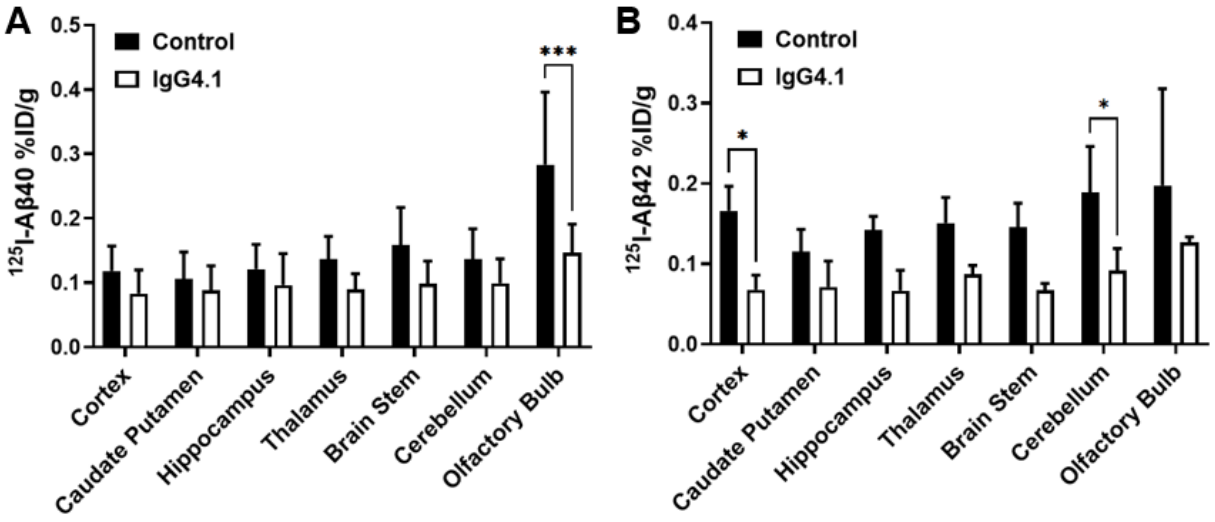

Figure 7.2. Systemic IgG4.1 treatment has minimal effect on the blood-to-brain accumulation of ^{125}I-Aβ40 and ^{125}I-Aβ42 peptides. Accumulation of ^{125}I-Aβ40 (A) or ^{125}I-Aβ42 (B) in various brain regions was assessed as the %ID/g after a 60-minute circulation in mice treated with 1 mg of IgG4.1 or the vehicle control. Data are mean ± SD (n=4). *p < 0.05, ***p < 0.001; two-way ANOVA with Bonferroni's post-tests.

7.4.3. IgG4.1 substantially reduces ^{125}I-Aβ42 permeability into various brain regions.

Permeability-surface area (PS) products for ^{125}I-Aβ42 uptake at different brain regions were estimated by dividing the ^{125}I activity measured in each brain region 15 minutes after intravenous injection by the area under the plasma concentration vs. time curve (AUC) from 0-15 minutes. Upon intravenous administration of IgG4.1, a ~3-4 fold decrease was observed in the PS values for ^{125}I-Aβ42 uptake in each dissected brain

region. This included the cortex, caudate putamen, hippocampus, thalamus, brain stem, cerebellum, and olfactory bulb (Fig. 7.3).

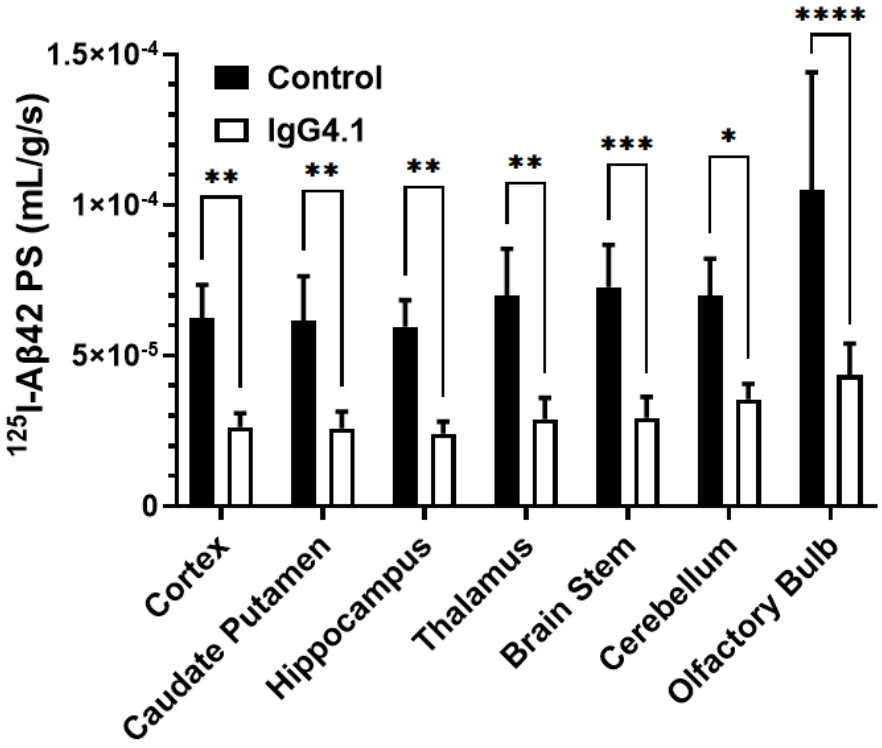

Figure 7.3. Systemic IgG4.1 treatment reduces the permeability of ^{125}I-Aβ42 into various brain regions after intravenous injection. The permeability-surface area (PS) products for ^{125}I-Aβ42 distribution to various brain regions upon intravenous injection was assessed in mice treated with 1 mg of IgG4.1 or the vehicle control. Data are mean ± SD (n=4). *p < 0.05, **p < 0.01, ***p < 0.001, ****p < 0.0001; two-way ANOVA with Bonferroni's post-tests.

7.4.4. IgG4.1 reduces the brain influx clearance of ^{125}I-Aβ42. Dynamic SPECT/CT imaging studies were performed to assess the effects of systemic IgG4.1 treatment on ^{125}I-Aβ42 distribution to various regions of interest (ROIs) over time, including the brain, following an intravenous injection of ^{125}I-Aβ42. A multiple-time-regression analysis method, originally developed by Patlak et al. (1983), was used to estimate the blood-to-

brain influx clearance of ^{125}I-Aβ42. In the Patlak plots, the ^{125}I-Aβ42 plasma concentrations at each SPECT imaging time point were simulated using the two-compartment model derived pharmacokinetic parameters for ^{125}I-Aβ42 in mice treated with or without IgG4.1 obtained in the preceding experiment (Fig. 7.4). Based on the Patlak plot slopes obtained from linear regression, a ~3-fold decrease was observed in the blood-to-brain influx clearance (K_i; mL/min) of ^{125}I-Aβ42 in the mice treated with IgG4.1 (Fig. 7.4). This is consistent with decreased permeability of ^{125}I-Aβ42 into various brain regions observed upon IgG4.1 treatment (Fig. 7.3).

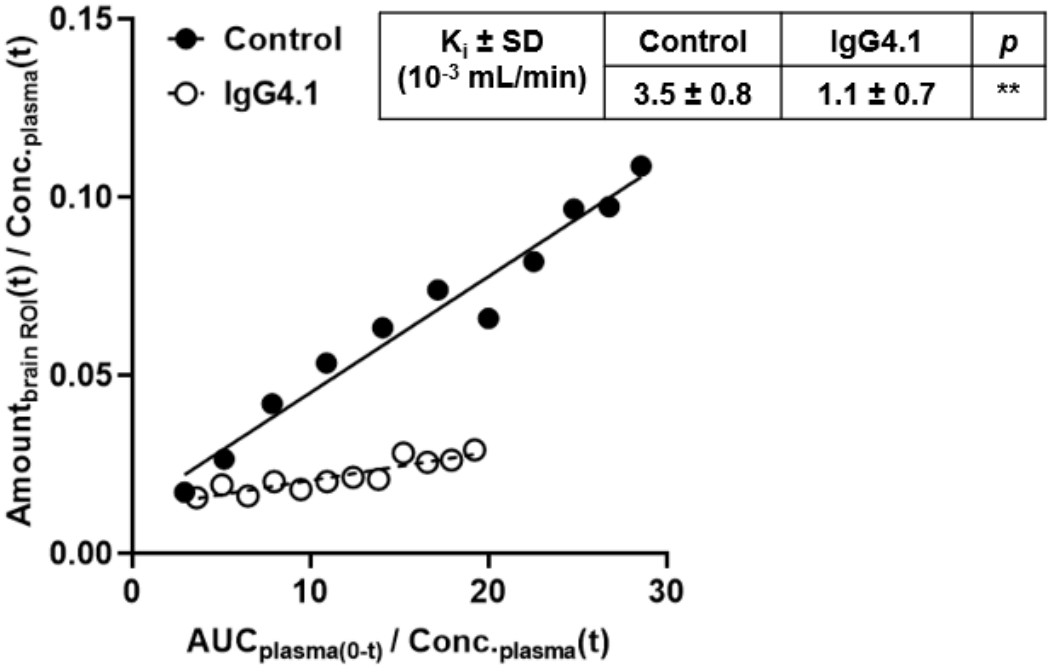

K_i ± SD (10^{-3} mL/min)	Control	IgG4.1	*p*
	3.5 ± 0.8	1.1 ± 0.7	**

Figure 7.4. Systemic IgG4.1 treatment reduces the brain influx clearance of ^{125}I-Aβ42 after intravenous injection. Dynamic SPECT/CT imaging was performed to monitor ^{125}I-Aβ42 distribution to the brain ROI over time after intravenous injection in mice treated with 1 mg of IgG4.1 or the vehicle alone. Brain influx clearance (K_i) of ^{125}I-Aβ42 was estimated by the slope obtained from Gjedde-Patlak graphical analysis. Representative plots are shown for the mice treated with IgG4.1 or vehicle alone. Inset table values are group mean ± SD (n=4). ***p*<0.01; unpaired two-tailed *t*-test.

7.4.5. IgG4.1 reduces the initial binding of ^{125}I-Aβ42 to the brain vasculature. Another multiple-time-regression graphical analysis method, originally developed by Logan et al. (1990) to assess reversible tracer distribution kinetics, was performed using the dynamic SPECT/CT imaging and plasma pharmacokinetic data of ^{125}I-Aβ42 in mice treated with or without IgG4.1. In the Logan plots, the ^{125}I-Aβ42 plasma concentrations at each SPECT imaging time point were simulated using the two-compartment model derived pharmacokinetic parameters for ^{125}I-Aβ42 obtained in the preceding experiment (Fig. 7.5). Based on the Logan plot slopes obtained from linear regression, a ~2-fold decrease was observed in the initial distribution volume (V_d) of ^{125}I-Aβ42 in the brain ROI upon treatment with IgG4.1 (Fig. 7.5).

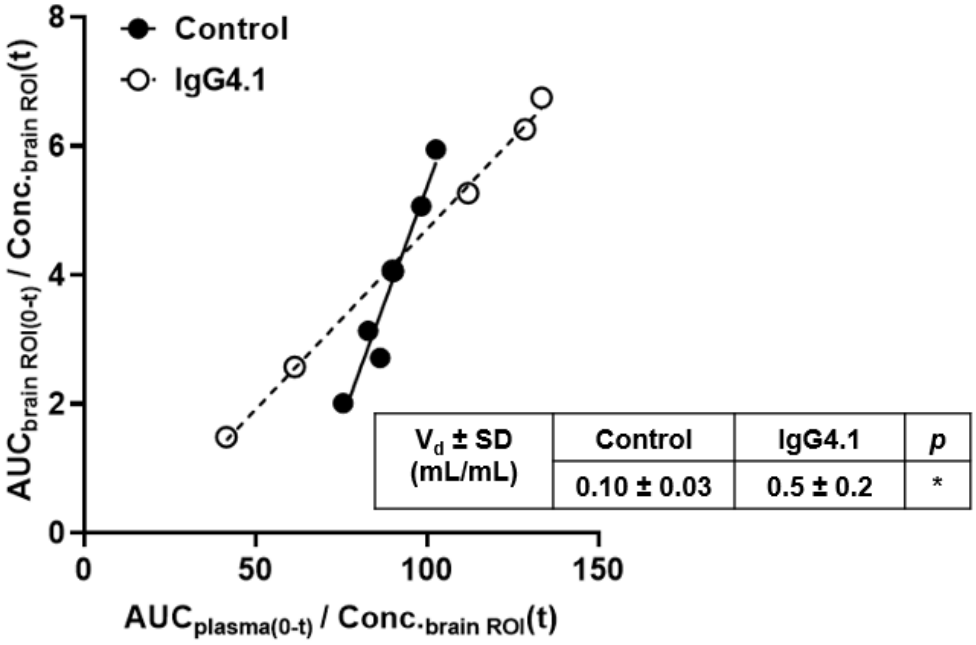

Figure 7.5. Systemic IgG4.1 treatment reduces the initial BBB binding of ^{125}I-Aβ42 after intravenous injection. Dynamic SPECT/CT imaging was performed to monitor ^{125}I-Aβ42 distribution to the brain ROI over time after intravenous injection in mice treated with 1 mg of IgG4.1 or the vehicle alone. The initial distribution volume (V_d) of ^{125}I-Aβ42 in the brain ROI was estimated by the slope obtained from Logan graphical analysis.

Representative plots are shown for the mice treated with IgG4.1 or vehicle alone. Inset table values are group mean ± SD (n=4). *p<0.05; unpaired two-tailed t-test.

7.5. Discussion and Conclusions

IgG4.1 is a mouse monoclonal antibody with epitope specificity for amino acid residues 2-10 of Aβ40 and Aβ42 peptides. Previously, we showed IgG4.1 binds with low affinity to monomeric Aβ40, but with high affinity to fibrillar Aβ40 (Ramakrishnan et al., 2009). In addition, we previously assessed the brain permeability of ^{125}I radiolabeled IgG4.1 and a fragment antigen binding (Fab) derivative of IgG4.1 after systemic injection in wild type mice (Poduslo et al., 2007). The PS values at various brain regions were ~10 fold higher for ^{125}I-Fab derivative compared to ^{125}I-IgG4.1 parental antibody. The low brain permeability of ^{125}I-IgG4.1, which ranged from ~0.1-0.2*10^{-6} mL/g/s at various brain regions, is comparable to that of other large proteins such as albumin (Poduslo et al., 2001). In contrast, the brain permeability of small peptides such as Aβ can be ~10-1000 fold higher (Poduslo et al., 2001).

In the present study, PS values of ^{125}I-Aβ42 at various brain regions ranged from ~2-3*10^{-5} mL/g/s in IgG4.1 pretreated mice, compared to ~6-10*10^{-5} mL/g/s in control mice. Thus, systemic IgG4.1 injection led to a ~2-3 fold decline in ^{125}I-Aβ42 brain permeability in wild type mice. This indicates that compared to free Aβ, the IgG-Aβ immune complex has reduced transport across the BBB. Interestingly, we previously showed the brain permeability of a different IgG-Aβ immune complex was ~2 fold higher compared to that of the free antibody, PC2 (Poduslo and Curran, 2001). This suggests that IgG binding to plasma Aβ, which itself has high brain permeability owing to

receptor-mediated transcytosis at the BBB, could help facilitate IgG transport at the BBB and increase its delivery to the brain.

The current findings indicate systemic IgG4.1 treatment in wild type mice reduced the plasma clearance of ^{125}I-Aβ40 by ~9 fold, and that of ^{125}I-Aβ42 by ~4 fold. This is likely due to immune complex formation impeding the mechanisms of peripheral Aβ elimination. Plasma Aβ is believed to be cleared predominantly via renal filtration (Tian et al., 2021), with a minor contribution from hepatic metabolism (Tian et al., 2021; Cheng et al., 2023). The IgG-Aβ immune complex is too large to undergo renal filtration and could potentially have lower uptake in hepatocytes compared to free Aβ, which could explain the reduced ^{125}I-Aβ plasma clearance in IgG4.1 pre-injected mice.

It was estimated that roughly 50% of Aβ produced in the brain is cleared by transport into the periphery, followed by elimination via kidneys/liver (Tian et al., 2021). Thus, it is critical to consider IgG effects on peripheral Aβ clearance when interpreting the effects of anti-Aβ immunotherapies on brain and plasma Aβ levels in AD patients and AD transgenic mouse models. For example, it was reported that in AD transgenic mice, peripheral administration of anti-Aβ IgG led to a decrease in brain Aβ burden, which coincided with a rise in plasma Aβ levels (DeMattos et al., 2002). The investigators attributed the rise in plasma Aβ levels solely to the IgG effects on promoting brain Aβ efflux. However, the current findings suggest the rise in plasma Aβ levels after systemic IgG administration could largely be explained by IgG effects on sequestering plasma Aβ and impeding its renal clearance.

The peripheral sink effect driven by systemic exposure to Aβ immunotherapies could be a “double edged sword”, since it may help to promote brain Aβ efflux, but it

also increases Aβ exposure in plasma due to the prolonged half-life of the IgG-Aβ immune complex. Increased plasma Aβ exposure could provide more opportunities for Aβ transcytosis across the BBB in the luminal to abluminal direction, i.e., from blood to brain. This could explain why systemic IgG4.1 administration had minimal impact on the overall brain accumulation (%ID/g) of injected ^{125}I-Aβ peptides, despite the substantial reduction observed in ^{125}I-Aβ brain permeability (PS values).

Solanezumab, which recognizes soluble Aβ species but does not bind to insoluble Aβ aggregates in the brain, is believed to promote brain Aβ removal predominantly via the sink effect (Siemers et al., 2010). The serious side effect of cerebral microhemorrhages related to amyloid related imaging abnormalities (ARIA), which has been commonly observed for this class of drugs, has been rarely observed for solanezumab (Carlson et al., 2011). Other Aβ immunotherapies designed to directly interact with sites of Aβ deposition in the brain could potentially trigger immune effector functions, contributing to neuroinflammation and ARIA risk (Mader et al., 2017). This suggests that peripheral action of anti-Aβ mAbs may have an improved safety profile over central action for clearing brain Aβ. However, it remains unclear whether the peripheral sink effect can clear enough brain Aβ to elicit meaningful changes in AD clinical outcomes, i.e., a reduction in the rate of cognitive decline. Results from several phase 3 clinical trials confirmed the excellent safety profile of solanezumab, but consistently showed the drug did not lead to a significant improvement in cognitive function compared to placebo (Doody et al., 2014). Thus, achieving an acceptable balance between efficacy and safety remains a challenge for this class of drugs.

In summary, these results provide the first experimental validation of the ability of peripherally administered anti-Aβ mAbs to reduce the plasma clearance and brain influx of Aβ peptides in mice. Given these findings, the increase in plasma Aβ levels reported upon peripheral administration of anti-Aβ mAbs in AD patients and transgenic mouse models could largely be explained by the antibody effects on Aβ plasma pharmacokinetics, and should not be solely attributed to the peripheral sink effect that promotes Aβ efflux from brain to plasma (DeMattos et al., 2002; Liu et al., 2015). Further studies are needed to clarify the effects of systemic antibody exposure on Aβ transport in the brain to blood direction, and whether the peripheral sink effect is sufficient to result in a meaningful reduction in brain Aβ burden, or whether antibody action directly in the brain is required to drive positive clinical outcomes.

Bibliography

Abuznait AH and Kaddoumi A (2012) Role of ABC Transporters in the Pathogenesis of Alzheimer's Disease. *ACS Chemical Neuroscience* **3**:820-831.

Adelborg K, Horváth-Puhó E, Ording A, Pedersen L, Sørensen HT and Henderson VW (2017) Heart failure and risk of dementia: a Danish nationwide population-based cohort study. *Eur J Heart Fail* **19**:253-260.

Agyare EK, Leonard SR, Curran GL, Yu CC, Lowe VJ, Paravastu AK, Poduslo JF and Kandimalla KK (2013) Traffic jam at the blood-brain barrier promotes greater accumulation of Alzheimer's disease amyloid-beta proteins in the cerebral vasculature. *Mol Pharm* **10**:1557-1565.

Akintola AA and van Heemst D (2015) Insulin, aging, and the brain: mechanisms and implications. *Front Endocrinol (Lausanne)* **6**:13.

Alexander GC, Emerson S and Kesselheim AS (2021) Evaluation of Aducanumab for Alzheimer Disease: Scientific Evidence and Regulatory Review Involving Efficacy, Safety, and Futility. *JAMA* **325**:1717-1718.

Anantharamaiah GM, Mishra VK, Garber DW, Datta G, Handattu SP, Palgunachari MN, Chaddha M, Navab M, Reddy ST, Segrest JP and Fogelman AM (2007) Structural requirements for antioxidative and anti-inflammatory properties of apolipoprotein A-I mimetic peptides. *Journal of lipid research* **48**:1915-1923.

Arnold SE, Arvanitakis Z, Macauley-Rambach SL, Koenig AM, Wang H-Y, Ahima RS, Craft S, Gandy S, Buettner C, Stoeckel LE, Holtzman DM and Nathan DM (2018) Brain insulin resistance in type 2 diabetes and Alzheimer disease: concepts and conundrums. *Nature Reviews Neurology* **14**:168-181.

Assmann G and Gotto AM, Jr. (2004) HDL cholesterol and protective factors in atherosclerosis. *Circulation* **109**:Iii8-14.

Azizi PM, Zyla RE, Guan S, Wang C, Liu J, Bolz S-S, Heit B, Klip A and Lee WL (2015) Clathrin-dependent entry and vesicle-mediated exocytosis define insulin transcytosis across microvascular endothelial cells. *Molecular Biology of the Cell* **26**:740-750.

Balazs Z, Panzenboeck U, Hammer A, Sovic A, Quehenberger O, Malle E and Sattler W (2004) Uptake and transport of high-density lipoprotein (HDL) and HDL-associated alpha-tocopherol by an in vitro blood-brain barrier model. *Journal of neurochemistry* **89**:939-950.

Bao B, Vasquez KO, Ho G, Zhang J, Delaney J, Rajopadhye M and Peterson JD (2019) Blood Pharmacokinetics Imaging by Noninvasive Heart Fluorescence Tomography and Application to Kidney Glomerular Filtration Rate Assessment. *J Pharmacol Exp Ther* **370**:288-298.

Bard F, Fox M, Friedrich S, Seubert P, Schenk D, Kinney GG and Yednock T (2012) Sustained levels of antibodies against Aβ in amyloid-rich regions of the CNS following intravenous dosing in human APP transgenic mice. *Exp Neurol* **238**:38-43.

Benedict C, Hallschmid M, Hatke A, Schultes B, Fehm HL, Born J and Kern W (2004) Intranasal insulin improves memory in humans. *Psychoneuroendocrinology* **29**:1326-1334.

Benedict C, Kern W, Schultes B, Born J and Hallschmid M (2008) Differential sensitivity of men and women to anorexigenic and memory-improving effects of intranasal insulin. *J Clin Endocrinol Metab* **93**:1339-1344.

Bloedon LT, Dunbar R, Duffy D, Pinell-Salles P, Norris R, DeGroot BJ, Movva R, Navab M, Fogelman AM and Rader DJ (2008) Safety, pharmacokinetics, and pharmacodynamics of oral apoA-I mimetic peptide D-4F in high-risk cardiovascular patients. *J Lipid Res* **49**:1344-1352.

Boucrot E, Saffarian S, Massol R, Kirchhausen T and Ehrlich M (2006) Role of lipids and actin in the formation of clathrin-coated pits. *Exp Cell Res* **312**:4036-4048.

Brasnjevic I, Steinbusch HW, Schmitz C and Martinez-Martinez P (2009) Delivery of peptide and protein drugs over the blood-brain barrier. *Progress in neurobiology* **87**:212-251.

Brenowitz WD, Nelson PT, Besser LM, Heller KB and Kukull WA (2015) Cerebral amyloid angiopathy and its co-occurrence with Alzheimer's disease and other cerebrovascular neuropathologic changes. *Neurobiol Aging* **36**:2702-2708.

Buga GM, Frank JS, Mottino GA, Hendizadeh M, Hakhamian A, Tillisch JH, Reddy ST, Navab M, Anantharamaiah GM, Ignarro LJ and Fogelman AM (2006) D-4F decreases brain arteriole inflammation and improves cognitive performance in LDL receptor-null mice on a Western diet. *J Lipid Res* **47**:2148-2160.

Button EB, Robert J, Caffrey TM, Fan J, Zhao W and Wellington CL (2019) HDL from an Alzheimer's disease perspective. *Current opinion in lipidology* **30**:224-234.

Callahan MJ, Lipinski WJ, Bian F, Durham RA, Pack A and Walker LC (2001) Augmented senile plaque load in aged female beta-amyloid precursor protein-transgenic mice. *Am J Pathol* **158**:1173-1177.

Carlson C, Estergard W, Oh J, Suhy J, Jack CR, Jr., Siemers E and Barakos J (2011) Prevalence of asymptomatic vasogenic edema in pretreatment Alzheimer's disease study cohorts from phase 3 trials of semagacestat and solanezumab. *Alzheimers Dement* **7**:396-401.

Carpentier JL (1994) Insulin receptor internalization: molecular mechanisms and physiopathological implications. *Diabetologia* **37 Suppl 2**:S117-124.

Carroll JC, Rosario ER, Kreimer S, Villamagna A, Gentzschein E, Stanczyk FZ and Pike CJ (2010) Sex differences in β-amyloid accumulation in 3xTg-AD mice: role of neonatal sex steroid hormone exposure. *Brain Res* **1366**:233-245.

Charidimou A, Gang Q and Werring DJ (2012) Sporadic cerebral amyloid angiopathy revisited: recent insights into pathophysiology and clinical spectrum. *Journal of neurology, neurosurgery, and psychiatry* **83**:124-137.

Chen F, Dong RR, Zhong KL, Ghosh A, Tang SS, Long Y, Hu M, Miao MX, Liao JM, Sun HB, Kong LY and Hong H (2016) Antidiabetic drugs restore abnormal transport of amyloid-β across the blood-brain barrier and memory impairment in db/db mice. *Neuropharmacology* **101**:123-136.

Chen F, Ghosh A, Hu M, Long Y, Sun H, Kong L, Hong H and Tang S (2018) RAGE-NF-κB-PPARγ Signaling is Involved in AGEs-Induced Upregulation of Amyloid-β Influx Transport in an In Vitro BBB Model. *Neurotoxicity Research* **33**:284-299.

Chen YR, Li YH, Hsieh TC, Wang CM, Cheng KC, Wang L, Lin TY, Cheung CHA, Wu CL and Chiang H (2019) Aging-induced Akt activation involves in aging-related pathologies and Aβ-induced toxicity. *Aging Cell* **18**:e12989.

Cheng Y, He CY, Tian DY, Chen SH, Ren JR, Sun HL, Xu MY, Tan CR, Fan DY, Jian JM, Sun PY, Zeng GH, Shen YY, Shi AY, Jin WS, Bu XL, Liu HM, Xu YM, Wang J and Wang YJ (2023) Physiological β-amyloid clearance by the liver and its therapeutic potential for Alzheimer's disease. *Acta Neuropathol* **145**:717-731.

Chernick D, Ortiz-Valle S, Jeong A, Swaminathan SK, Kandimalla KK, Rebeck GW and Li L (2018) High-density lipoprotein mimetic peptide 4F mitigates amyloid-beta-induced inhibition of apolipoprotein E secretion and lipidation in primary astrocytes and microglia. *J Neurochem* **147**:647-662.

Craft S, Asthana S, Newcomer JW, Wilkinson CW, Matos IT, Baker LD, Cherrier M, Lofgreen C, Latendresse S, Petrova A, Plymate S, Raskind M, Grimwood K and Veith RC (1999) Enhancement of memory in Alzheimer disease with insulin and somatostatin, but not glucose. *Arch Gen Psychiatry* **56**:1135-1140.

Craft S, Raman R, Chow TW, Rafii MS, Sun CK, Rissman RA, Donohue MC, Brewer JB, Jenkins C, Harless K, Gessert D and Aisen PS (2020) Safety, Efficacy, and Feasibility of Intranasal Insulin for the Treatment of Mild Cognitive Impairment and Alzheimer Disease Dementia: A Randomized Clinical Trial. *JAMA Neurol*.

Cresto JC, Lavine RL, Buchly ML, Penhos JC, Bhathena SJ and Recant L (1977) Half life of injected 125I-insulin in control and ob/ob mice. *Acta physiologica latino americana* **27**:7-15.

Datta G, Chaddha M, Hama S, Navab M, Fogelman AM, Garber DW, Mishra VK, Epand RM, Epand RF, Lund-Katz S, Phillips MC, Segrest JP and Anantharamaiah GM (2001) Effects of increasing hydrophobicity on the physical-chemical and biological properties of a class A amphipathic helical peptide. *J Lipid Res* **42**:1096-1104.

De Felice FG, Vieira MN, Bomfim TR, Decker H, Velasco PT, Lambert MP, Viola KL, Zhao WQ, Ferreira ST and Klein WL (2009) Protection of synapses against Alzheimer's-linked toxins: insulin signaling prevents the pathogenic binding of Abeta oligomers. *Proc Natl Acad Sci U S A* **106**:1971-1976.

de la Torre JC (2002) Vascular basis of Alzheimer's pathogenesis. *Ann N Y Acad Sci* **977**:196-215.

Deane R, Wu Z and Zlokovic BV (2004) RAGE (yin) versus LRP (yang) balance regulates alzheimer amyloid beta-peptide clearance through transport across the blood-brain barrier. *Stroke* **35**:2628-2631.

DeMattos RB, Bales KR, Cummins DJ, Paul SM and Holtzman DM (2002) Brain to plasma amyloid-beta efflux: a measure of brain amyloid burden in a mouse model of Alzheimer's disease. *Science* **295**:2264-2267.

Do TM, Dodacki A, Alata W, Calon F, Nicolic S, Scherrmann J-M, Farinotti R and Bourasset F (2016) Age-Dependent Regulation of the Blood-Brain Barrier Influx/Efflux Equilibrium of Amyloid-β Peptide in a Mouse Model of Alzheimer's Disease (3xTg-AD). *Journal of Alzheimer's Disease* **49**:287-300.

Dodiya HB, Kuntz T, Shaik SM, Baufeld C, Leibowitz J, Zhang X, Gottel N, Zhang X, Butovsky O, Gilbert JA and Sisodia SS (2019) Sex-specific effects of microbiome perturbations on cerebral Aβ amyloidosis and microglia phenotypes. *Journal of Experimental Medicine* **216**:1542-1560.

Doody RS, Thomas RG, Farlow M, Iwatsubo T, Vellas B, Joffe S, Kieburtz K, Raman R, Sun X, Aisen PS, Siemers E, Liu-Seifert H and Mohs R (2014) Phase 3 trials of solanezumab for mild-to-moderate Alzheimer's disease. *N Engl J Med* **370**:311-321.

Dou JT, Chen M, Dufour F, Alkon DL and Zhao WQ (2005) Insulin receptor signaling in long-term memory consolidation following spatial learning. *Learn Mem* **12**:646-655.

Dunbar RL, Movva R, Bloedon LT, Duffy D, Norris RB, Navab M, Fogelman AM and Rader DJ (2017) Oral Apolipoprotein A-I Mimetic D-4F Lowers HDL-Inflammatory Index in High-Risk Patients: A First-in-Human Multiple-Dose, Randomized Controlled Trial. *Clin Transl Sci* **10**:455-469.

Elali A and Rivest S (2013) The role of ABCB1 and ABCA1 in beta-amyloid clearance at the neurovascular unit in Alzheimer's disease. *Frontiers in Physiology* **4**:45.

Elhaik Goldman S, Goez D, Last D, Naor S, Liraz Zaltsman S, Sharvit-Ginon I, Atrakchi-Baranes D, Shemesh C, Twitto-Greenberg R, Tsach S, Lotan R, Leikin-Frenkel A, Shish A, Mardor Y, Schnaider Beeri M and Cooper I (2018) High-fat diet protects the blood–brain barrier in an Alzheimer's disease mouse model. *Aging Cell* **17**:e12818.

Elliott DA, Weickert CS and Garner B (2010) Apolipoproteins in the brain: implications for neurological and psychiatric disorders. *Clin Lipidol* **51**:555-573.

Fagan AM, Christopher E, Taylor JW, Parsadanian M, Spinner M, Watson M, Fryer JD, Wahrle S, Bales KR, Paul SM and Holtzman DM (2004) ApoAI deficiency results in marked reductions in plasma cholesterol but no alterations in amyloid-beta pathology in a mouse model of Alzheimer's disease-like cerebral amyloidosis. *Am J Pathol* **165**:1413-1422.

Fagerholm S, Ortegren U, Karlsson M, Ruishalme I and Strålfors P (2009) Rapid insulin-dependent endocytosis of the insulin receptor by caveolae in primary adipocytes. *PLoS One* **4**:e5985.

Filali M and Lalonde R (2009) Age-related cognitive decline and nesting behavior in an APPswe/PS1 bigenic model of Alzheimer's disease. *Brain Research* **1292**:93-99.

Filippi M, Cecchetti G, Spinelli EG, Vezzulli P, Falini A and Agosta F (2022) Amyloid-Related Imaging Abnormalities and β-Amyloid–Targeting Antibodies: A Systematic Review. *JAMA Neurology* **79**:291-304.

Foley KE and Wilcock DM (2022) Vascular Considerations for Amyloid Immunotherapy. *Current Neurology and Neuroscience Reports* **22**:709-719.

Frank HJ and Pardridge WM (1981) A direct in vitro demonstration of insulin binding to isolated brain microvessels. *Diabetes* **30**:757-761.

Freude S, Schilbach K and Schubert M (2009) The role of IGF-1 receptor and insulin receptor signaling for the pathogenesis of Alzheimer's disease: from model organisms to human disease. *Curr Alzheimer Res* **6**:213-223.

Frolich L, Blum-Degen D, Bernstein HG, Engelsberger S, Humrich J, Laufer S, Muschner D, Thalheimer A, Turk A, Hoyer S, Zochling R, Boissl KW, Jellinger K and Riederer P (1998) Brain insulin and insulin receptors in aging and sporadic Alzheimer's disease. *J Neural Transm (Vienna)* **105**:423-438.

Fung KY, Wang C, Nyegaard S, Heit B, Fairn GD and Lee WL (2017) SR-BI Mediated Transcytosis of HDL in Brain Microvascular Endothelial Cells Is Independent of Caveolin, Clathrin, and PDZK1. *Frontiers in Physiology* **8**.

Gabbouj S, Ryhänen S, Marttinen M, Wittrahm R, Takalo M, Kemppainen S, Martiskainen H, Tanila H, Haapasalo A, Hiltunen M and Natunen T (2019) Altered Insulin Signaling in Alzheimer's Disease Brain - Special Emphasis on PI3K-Akt Pathway. *Front Neurosci* **13**:629.

Gali CC, Fanaee-Danesh E, Zandl-Lang M, Albrecher NM, Tam-Amersdorfer C, Stracke A, Sachdev V, Reichmann F, Sun Y, Avdili A, Reiter M, Kratky D, Holzer P, Lass A, Kandimalla KK and Panzenboeck U (2019) Amyloid-beta impairs insulin signaling by accelerating autophagy-lysosomal degradation of LRP-1 and IR-β in blood-brain barrier endothelial cells in vitro and in 3XTg-AD mice. *Mol Cell Neurosci* **99**:103390.

Ganesan LP, Mates JM, Cheplowitz AM, Avila CL, Zimmerer JM, Yao Z, Maiseyeu A, Rajaram MVS, Robinson JM and Anderson CL (2016) Scavenger receptor B1, the HDL receptor, is expressed abundantly in liver sinusoidal endothelial cells. *Scientific Reports* **6**:20646.

Gao S, Hendrie HC, Hall KS and Hui S (1998) The Relationships Between Age, Sex, and the Incidence of Dementia and Alzheimer Disease: A Meta-analysis. *Archives of General Psychiatry* **55**:809-815.

Ghiso J, Shayo M, Calero M, Ng D, Tomidokoro Y, Gandy S, Rostagno A and Frangione B (2004) Systemic catabolism of Alzheimer's Abeta40 and Abeta42. *J Biol Chem* **279**:45897-45908.

Gil-Bea FJ, Solas M, Solomon A, Mugueta C, Winblad B, Kivipelto M, Ramirez MJ and Cedazo-Minguez A (2010) Insulin levels are decreased in the cerebrospinal fluid of women with prodomal Alzheimer's disease. *J Alzheimers Dis* **22**:405-413.

Goldim MPS, Della Giustina A and Petronilho F (2019) Using Evans Blue Dye to Determine Blood-Brain Barrier Integrity in Rodents. *Curr Protoc Immunol* **126**:e83.

Gray SM, Aylor KW and Barrett EJ (2017) Unravelling the regulation of insulin transport across the brain endothelial cell. *Diabetologia* **60**:1512-1521.

Grillo CA, Piroli GG, Lawrence RC, Wrighten SA, Green AJ, Wilson SP, Sakai RR, Kelly SJ, Wilson MA, Mott DD and Reagan LP (2015) Hippocampal Insulin Resistance Impairs Spatial Learning and Synaptic Plasticity. *Diabetes* **64**:3927-3936.

Gu T, Zhao T and Hewes RS (2014) Insulin signaling regulates neurite growth during metamorphic neuronal remodeling. *Biology Open* **3**:81-93.

Hachiya HL, Halban PA and King GL (1988) Intracellular pathways of insulin transport across vascular endothelial cells. *American Journal of Physiology-Cell Physiology* **255**:C459-C464.

Hallschmid M (2021) Intranasal Insulin for Alzheimer’s Disease. *CNS Drugs* **35**:21-37.

Handattu SP, Garber DW, Monroe CE, van Groen T, Kadish I, Nayyar G, Cao D, Palgunachari MN, Li L and Anantharamaiah GM (2009) Oral apolipoprotein A-I mimetic peptide improves cognitive function and reduces amyloid burden in a mouse model of Alzheimer's disease. *Neurobiol Dis* **34**:525-534.

Hawkins BT, Lundeen TF, Norwood KM, Brooks HL and Egleton RD (2007) Increased blood–brain barrier permeability and altered tight junctions in experimental diabetes in the rat: contribution of hyperglycaemia and matrix metalloproteinases. *Diabetologia* **50**:202-211.

Heni M, Schopfer P, Peter A, Sartorius T, Fritsche A, Synofzik M, Haring HU, Maetzler W and Hennige AM (2014) Evidence for altered transport of insulin across the blood-brain barrier in insulin-resistant humans. *Acta Diabetol* **51**:679-681.

Hersom M, Helms HC, Schmalz C, Pedersen TÅ, Buckley ST and Brodin B (2018) The insulin receptor is expressed and functional in cultured blood-brain barrier endothelial cells but does not mediate insulin entry from blood to brain. *American Journal of Physiology-Endocrinology and Metabolism* **315**:E531-E542.

Herzig MC, Van Nostrand WE and Jucker M (2006) Mechanism of cerebral beta-amyloid angiopathy: murine and cellular models. *Brain Pathol* **16**:40-54.

Hom S, Egleton RD, Huber JD and Davis TP (2001) Effect of reduced flow on blood-brain barrier transport systems. *Brain Res* **890**:38-48.

Hottman DA, Chernick D, Cheng S, Wang Z and Li L (2014) HDL and cognition in neurodegenerative disorders. *Neurobiol Dis* **72 Pt A**:22-36.

Huang CC, Chung CM, Leu HB, Lin LY, Chiu CC, Hsu CY, Chiang CH, Huang PH, Chen TJ, Lin SJ, Chen JW and Chan WL (2014) Diabetes mellitus and the risk of Alzheimer's disease: a nationwide population-based study. *PLoS One* **9**:e87095.

Huang JT, Wang L, Prabakaran S, Wengenroth M, Lockstone HE, Koethe D, Gerth CW, Gross S, Schreiber D, Lilley K, Wayland M, Oxley D, Leweke FM and Bahn S (2008) Independent protein-profiling studies show a decrease in apolipoprotein A1 levels in schizophrenia CSF, brain and peripheral tissues. *Molecular psychiatry* **13**:1118-1128.

Hussain KM, Leong KL, Ng MM and Chu JJ (2011) The essential role of clathrin-mediated endocytosis in the infectious entry of human enterovirus 71. *J Biol Chem* **286**:309-321.

Hänzelmann S, Castelo R and Guinney J (2013) GSVA: gene set variation analysis for microarray and RNA-seq data. *BMC Bioinformatics* **14**:7.

Iadecola C and Davisson RL (2008) Hypertension and cerebrovascular dysfunction. *Cell Metab* **7**:476-484.

Ito S, Yanai M, Yamaguchi S, Couraud PO and Ohtsuki S (2017) Regulation of Tight-Junction Integrity by Insulin in an In Vitro Model of Human Blood-Brain Barrier. *J Pharm Sci* **106**:2599-2605.

Jack CR, Jr., Wengenack TM, Reyes DA, Garwood M, Curran GL, Borowski BJ, Lin J, Preboske GM, Holasek SS, Adriany G and Poduslo JF (2005) In vivo magnetic resonance microimaging of individual amyloid plaques in Alzheimer's transgenic mice. *J Neurosci* **25**:10041-10048.

Jaldin-Fincati JR, Pereira RVS, Bilan PJ and Klip A (2018) Insulin uptake and action in microvascular endothelial cells of lymphatic and blood origin. *Am J Physiol Endocrinol Metab* **315**:E204-e217.

Jan A, Gokce O, Luthi-Carter R and Lashuel HA (2008) The ratio of monomeric to aggregated forms of Abeta40 and Abeta42 is an important determinant of amyloid-beta aggregation, fibrillogenesis, and toxicity. *The Journal of Biological Chemistry* **283**:28176-28189.

Jaruszewski KM, Curran GL, Swaminathan SK, Rosenberg JT, Grant SC, Ramakrishnan S, Lowe VJ, Poduslo JF and Kandimalla KK (2014) Multimodal nanoprobes to target cerebrovascular amyloid in Alzheimer's disease brain. *Biomaterials* **35**:1967-1976.

Jauch-Chara K, Friedrich A, Rezmer M, Melchert UH, H GS-E, Hallschmid M and Oltmanns KM (2012) Intranasal insulin suppresses food intake via enhancement of brain energy levels in humans. *Diabetes* **61**:2261-2268.

Julien C, Tremblay C, Phivilay A, Berthiaume L, Emond V, Julien P and Calon F (2010) High-fat diet aggravates amyloid-beta and tau pathologies in the 3xTg-AD mouse model. *Neurobiol Aging* **31**:1516-1531.

Kandimalla KK, Curran GL, Holasek SS, Gilles EJ, Wengenack TM and Poduslo JF (2005) Pharmacokinetic analysis of the blood-brain barrier transport of 125I-amyloid beta protein 40 in wild-type and Alzheimer's disease transgenic mice (APP,PS1) and its implications for amyloid plaque formation. *J Pharmacol Exp Ther* **313**:1370-1378.

Kandimalla KK, Wengenack TM, Curran GL, Gilles EJ and Poduslo JF (2007) Pharmacokinetics and amyloid plaque targeting ability of a novel peptide-based magnetic resonance contrast agent in wild-type and Alzheimer's disease transgenic mice. *J Pharmacol Exp Ther* **322**:541-549.

Kandimalla R, Thirumala V and Reddy PH (2017) Is Alzheimer's disease a Type 3 Diabetes? A critical appraisal. *Biochim Biophys Acta Mol Basis Dis* **1863**:1078-1089.

Kim J, Onstead L, Randle S, Price R, Smithson L, Zwizinski C, Dickson DW, Golde T and McGowan E (2007) Abeta40 inhibits amyloid deposition in vivo. *J Neurosci* **27**:627-633.

Klein WL, Stine WB, Jr. and Teplow DB (2004) Small assemblies of unmodified amyloid beta-protein are the proximate neurotoxin in Alzheimer's disease. *Neurobiol Aging* **25**:569-580.

Koch M, Furtado JD, Falk K, Leypoldt F, Mukamal KJ and Jensen MK (2017) Apolipoproteins and their subspecies in human cerebrospinal fluid and plasma. *Alzheimers Dement (Amst)* **6**:182-187.

Kondo T, Hafezi-Moghadam A, Thomas K, Wagner DD and Kahn CR (2004) Mice lacking insulin or insulin-like growth factor 1 receptors in vascular endothelial cells maintain normal blood-brain barrier. *Biochem Biophys Res Commun* **317**:315-320.

Kotronen A, Juurinen L, Tiikkainen M, Vehkavaara S and Yki-Jarvinen H (2008) Increased liver fat, impaired insulin clearance, and hepatic and adipose tissue insulin resistance in type 2 diabetes. *Gastroenterology* **135**:122-130.

Kullmann S, Heni M, Hallschmid M, Fritsche A, Preissl H and Häring H-U (2016) Brain Insulin Resistance at the Crossroads of Metabolic and Cognitive Disorders in Humans. *Physiological Reviews* **96**:1169-1209.

Laatsch A, Merkel M, Talmud PJ, Grewal T, Beisiegel U and Heeren J (2009) Insulin stimulates hepatic low density lipoprotein receptor-related protein 1 (LRP1) to increase postprandial lipoprotein clearance. *Atherosclerosis* **204**:105-111.

Lefterov I, Fitz NF, Cronican AA, Fogg A, Lefterov P, Kodali R, Wetzel R and Koldamova R (2010) Apolipoprotein A-I deficiency increases cerebral amyloid angiopathy and cognitive deficits in APP/PS1DeltaE9 mice. *The Journal of Biological Chemistry* **285**:36945-36957.

Leszek J, Mikhaylenko EV, Belousov DM, Koutsouraki E, Szczechowiak K, Kobusiak-Prokopowicz M, Mysiak A, Diniz BS, Somasundaram SG, Kirkland CE and Aliev G (2021) The Links between Cardiovascular Diseases and Alzheimer's Disease. *Curr Neuropharmacol* **19**:152-169.

Lewis TL, Cao D, Lu H, Mans RA, Su YR, Jungbauer L, Linton MF, Fazio S, LaDu MJ and Li L (2010) Overexpression of human apolipoprotein A-I preserves cognitive function and attenuates neuroinflammation and cerebral amyloid angiopathy in a mouse model of Alzheimer disease. *J Biol Chem* **285**:36958-36968.

Liu L and Liu X (2014) Alterations in function and expression of ABC transporters at blood-brain barrier under diabetes and the clinical significances. *Frontiers in Pharmacology* **5**.

Liu Y, Liu F, Grundke-Iqbal I, Iqbal K and Gong CX (2011) Deficient brain insulin signalling pathway in Alzheimer's disease and diabetes. *J Pathol* **225**:54-62.

Liu Y-H, Wang Y-R, Xiang Y, Zhou H-D, Giunta B, Mañucat-Tan NB, Tan J, Zhou X-F and Wang Y-J (2015) Clearance of Amyloid-Beta in Alzheimer's Disease: Shifting the Action Site from Center to Periphery. *Molecular Neurobiology* **51**:1-7.

Logan J, Fowler JS, Volkow ND, Wolf AP, Dewey SL, Schlyer DJ, MacGregor RR, Hitzemann R, Bendriem B, Gatley SJ and Christman DR (1990) Graphical Analysis of Reversible Radioligand Binding from Time—Activity Measurements Applied to [N-11C-Methyl]-(−)-Cocaine PET Studies in Human Subjects. *Journal of Cerebral Blood Flow & Metabolism* **10**:740-747.

Long Z, Zeng Q, Wang K, Sharma A and He G (2016) Gender difference in valproic acid-induced neuroprotective effects on APP/PS1 double transgenic mice modeling Alzheimer's disease. *Acta Biochim Biophys Sin (Shanghai)* **48**:930-938.

Luchsinger JA, Tang MX, Shea S and Mayeux R (2004) Hyperinsulinemia and risk of Alzheimer disease. *Neurology* **63**:1187-1192.

Lui JK, Laws SM, Li QX, Villemagne VL, Ames D, Brown B, Bush AI, De Ruyck K, Dromey J, Ellis KA, Faux NG, Foster J, Fowler C, Gupta V, Hudson P, Laughton K, Masters CL, Pertile K, Rembach A, Rimajova M, Rodrigues M, Rowe CC, Rumble R, Szoeke C, Taddei K, Taddei T, Trounson B, Ward V, Martins RN and Group AR (2010) Plasma amyloid-beta as a biomarker in Alzheimer's disease: the AIBL study of aging. *J Alzheimers Dis* **20**:1233-1242.

Ma C, Li J, Bao Z, Ruan Q and Yu Z (2015) Serum Levels of ApoA1 and ApoA2 Are Associated with Cognitive Status in Older Men. *Biomed Res Int* **2015**:481621.

Mackic JB, Bading J, Ghiso J, Walker L, Wisniewski T, Frangione B and Zlokovic BV (2002) Circulating amyloid-beta peptide crosses the blood-brain barrier in aged monkeys and contributes to Alzheimer's disease lesions. *Vascul Pharmacol* **38**:303-313.

Mackic JB, Weiss MH, Miao W, Kirkman E, Ghiso J, Calero M, Bading J, Frangione B and Zlokovic BV (1998) Cerebrovascular accumulation and increased blood-brain barrier permeability to circulating Alzheimer's amyloid beta peptide in aged squirrel monkey with cerebral amyloid angiopathy. *J Neurochem* **70**:210-215.

Mader S, Brimberg L and Diamond B (2017) The Role of Brain-Reactive Autoantibodies in Brain Pathology and Cognitive Impairment. *Front Immunol* **8**:1101.

Martins IJ, Berger T, Sharman MJ, Verdile G, Fuller SJ and Martins RN (2009) Cholesterol metabolism and transport in the pathogenesis of Alzheimer's disease. *Journal of neurochemistry* **111**:1275-1308.

Mayle KM, Le AM and Kamei DT (2012) The intracellular trafficking pathway of transferrin. *Biochim Biophys Acta* **1820**:264-281.

McGowan E, Pickford F, Kim J, Onstead L, Eriksen J, Yu C, Skipper L, Murphy MP, Beard J, Das P, Jansen K, DeLucia M, Lin WL, Dolios G, Wang R, Eckman CB, Dickson DW, Hutton M, Hardy J and Golde T (2005) Abeta42 is essential for parenchymal and vascular amyloid deposition in mice. *Neuron* **47**:191-199.

McMahon HT and Boucrot E (2011) Molecular mechanism and physiological functions of clathrin-mediated endocytosis. *Nat Rev Mol Cell Biol* **12**:517-533.

Mehta PD, Pirttila T, Mehta SP, Sersen EA, Aisen PS and Wisniewski HM (2000) Plasma and cerebrospinal fluid levels of amyloid beta proteins 1-40 and 1-42 in Alzheimer disease. *Arch Neurol* **57**:100-105.

Meijer RI, Gray SM, Aylor KW and Barrett EJ (2016) Pathways for insulin access to the brain: the role of the microvascular endothelial cell. *Am J Physiol Heart Circ Physiol* **311**:H1132-h1138.

Merino-Zamorano C, Fernandez-de Retana S, Montanola A, Batlle A, Saint-Pol J, Mysiorek C, Gosselet F, Montaner J and Hernandez-Guillamon M (2016) Modulation of Amyloid-

beta1-40 Transport by ApoA1 and ApoJ Across an in vitro Model of the Blood-Brain Barrier. *Journal of Alzheimer's disease : JAD* **53**:677-691.

Michaud JP, Bellavance MA, Prefontaine P and Rivest S (2013a) Real-time in vivo imaging reveals the ability of monocytes to clear vascular amyloid beta. *Cell Rep* **5**:646-653.

Michaud JP, Halle M, Lampron A, Theriault P, Prefontaine P, Filali M, Tribout-Jover P, Lanteigne AM, Jodoin R, Cluff C, Brichard V, Palmantier R, Pilorget A, Larocque D and Rivest S (2013b) Toll-like receptor 4 stimulation with the detoxified ligand monophosphoryl lipid A improves Alzheimer's disease-related pathology. *Proc Natl Acad Sci U S A* **110**:1941-1946.

Miller DL, Papayannopoulos IA, Styles J, Bobin SA, Lin YY, Biemann K and Iqbal K (1993) Peptide compositions of the cerebrovascular and senile plaque core amyloid deposits of Alzheimer's disease. *Archives of biochemistry and biophysics* **301**:41-52.

Montagne A, Barnes SR, Sweeney MD, Halliday MR, Sagare AP, Zhao Z, Toga AW, Jacobs RE, Liu CY, Amezcua L, Harrington MG, Chui HC, Law M and Zlokovic BV (2015) Blood-brain barrier breakdown in the aging human hippocampus. *Neuron* **85**:296-302.

Morgantini C, Imaizumi S, Grijalva V, Navab M, Fogelman AM and Reddy ST (2010) Apolipoprotein A-I mimetic peptides prevent atherosclerosis development and reduce plaque inflammation in a murine model of diabetes. *Diabetes* **59**:3223-3228.

Murray MM, Bernstein SL, Nyugen V, Condron MM, Teplow DB and Bowers MT (2009) Amyloid beta protein: Abeta40 inhibits Abeta42 oligomerization. *J Am Chem Soc* **131**:6316-6317.

Navab M, Shechter I, Anantharamaiah GM, Reddy ST, Van Lenten BJ and Fogelman AM (2010) Structure and function of HDL mimetics. *Arteriosclerosis, thrombosis, and vascular biology* **30**:164-168.

Nelson AR, Sweeney MD, Sagare AP and Zlokovic BV (2016) Neurovascular dysfunction and neurodegeneration in dementia and Alzheimer's disease. *Biochim Biophys Acta* **1862**:887-900.

Näslund J, Haroutunian V, Mohs R, Davis KL, Davies P, Greengard P and Buxbaum JD (2000) Correlation between elevated levels of amyloid beta-peptide in the brain and cognitive decline. *Jama* **283**:1571-1577.

O' Neill C (2013) PI3-kinase/Akt/mTOR signaling: Impaired on/off switches in aging, cognitive decline and Alzheimer's disease. *Experimental Gerontology* **48**:647-653.

Okereke OI, Xia W, Selkoe DJ and Grodstein F (2009) Ten-year change in plasma amyloid beta levels and late-life cognitive decline. *Arch Neurol* **66**:1247-1253.

Patlak CS, Blasberg RG and Fenstermacher JD (1983) Graphical evaluation of blood-to-brain transfer constants from multiple-time uptake data. *J Cereb Blood Flow Metab* **3**:1-7.

Párrizas M, Gazit A, Levitzki A, Wertheimer E and LeRoith D (1997) Specific Inhibition of Insulin-Like Growth Factor-1 and Insulin Receptor Tyrosine Kinase Activity and Biological Function by Tyrphostins. *Endocrinology* **138**:1427-1433.

Poduslo JF and Curran GL (1992) Increased permeability across the blood-nerve barrier of albumin glycated in vitro and in vivo from patients with diabetic polyneuropathy. *Proc Natl Acad Sci U S A* **89**:2218-2222.

Poduslo JF and Curran GL (2001) Amyloid beta peptide as a vaccine for Alzheimer's disease involves receptor-mediated transport at the blood-brain barrier. *Neuroreport* **12**:3197-3200.

Poduslo JF, Curran GL and Berg CT (1994) Macromolecular permeability across the blood-nerve and blood-brain barriers. *Proc Natl Acad Sci U S A* **91**:5705-5709.

Poduslo JF, Curran GL, Wengenack TM, Malester B and Duff K (2001) Permeability of proteins at the blood-brain barrier in the normal adult mouse and double transgenic mouse model of Alzheimer's disease. *Neurobiol Dis* **8**:555-567.

Poduslo JF, Ramakrishnan M, Holasek SS, Ramirez-Alvarado M, Kandimalla KK, Gilles EJ, Curran GL and Wengenack TM (2007) In vivo targeting of antibody fragments to the nervous system for Alzheimer's disease immunotherapy and molecular imaging of amyloid plaques. *Journal of Neurochemistry* **102**:420-433.

Popescu BO, Toescu EC, Popescu LM, Bajenaru O, Muresanu DF, Schultzberg M and Bogdanovic N (2009) Blood-brain barrier alterations in ageing and dementia. *J Neurol Sci* **283**:99-106.

Prasad S, Sajja RK, Naik P and Cucullo L (2014) Diabetes Mellitus and Blood-Brain Barrier Dysfunction: An Overview. *J Pharmacovigil* **2**:125.

Qi XM and Ma JF (2017) The role of amyloid beta clearance in cerebral amyloid angiopathy: more potential therapeutic targets. *Transl Neurodegener* **6**:22.

Qiu T, Liu Q, Chen YX, Zhao YF and Li YM (2015) Abeta42 and Abeta40: similarities and differences. *J Pept Sci* **21**:522-529.

Ramakrishnan M, Kandimalla KK, Wengenack TM, Howell KG and Poduslo JF (2009) Surface plasmon resonance binding kinetics of Alzheimer's disease amyloid beta peptide-capturing and plaque-binding monoclonal antibodies. *Biochemistry* **48**:10405-10415.

Reger MA, Watson GS, Frey WH, 2nd, Baker LD, Cholerton B, Keeling ML, Belongia DA, Fishel MA, Plymate SR, Schellenberg GD, Cherrier MM and Craft S (2006) Effects of intranasal insulin on cognition in memory-impaired older adults: modulation by APOE genotype. *Neurobiol Aging* **27**:451-458.

Rembach A, Faux NG, Watt AD, Pertile KK, Rumble RL, Trounson BO, Fowler CJ, Roberts BR, Perez KA, Li QX, Laws SM, Taddei K, Rainey-Smith S, Robertson JS, Vandijck M, Vanderstichele H, Barnham KJ, Ellis KA, Szoeke C, Macaulay L, Rowe CC, Villemagne VL, Ames D, Martins RN, Bush AI and Masters CL (2014) Changes in plasma amyloid beta in a longitudinal study of aging and Alzheimer's disease. *Alzheimers Dement* **10**:53-61.

Reynolds TH, Dalton A, Calzini L, Tuluca A, Hoyte D and Ives SJ (2019) The impact of age and sex on body composition and glucose sensitivity in C57BL/6J mice. *Physiol Rep* **7**:e13995.

Rhea EM and Banks WA (2019) Role of the Blood-Brain Barrier in Central Nervous System Insulin Resistance. *Front Neurosci* **13**:521.

Rhea EM and Banks WA (2021) A historical perspective on the interactions of insulin at the blood-brain barrier. *J Neuroendocrinol* **33**:e12929.

Rhea EM, Rask-Madsen C and Banks WA (2018) Insulin transport across the blood-brain barrier can occur independently of the insulin receptor. *J Physiol* **596**:4753-4765.

Rodrigue KM, Kennedy KM and Park DC (2009) Beta-amyloid deposition and the aging brain. *Neuropsychol Rev* **19**:436-450.

Roheim PS, Carey M, Forte T and Vega GL (1979) Apolipoproteins in human cerebrospinal fluid. *Proc Natl Acad Sci U S A* **76**:4646-4649.

Roher AE, Lowenson JD, Clarke S, Woods AS, Cotter RJ, Gowing E and Ball MJ (1993) beta-Amyloid-(1-42) is a major component of cerebrovascular amyloid deposits: implications for the pathology of Alzheimer disease. *Proc Natl Acad Sci U S A* **90**:10836-10840.

Saczynski JS, White L, Peila RL, Rodriguez BL and Launer LJ (2007) The relation between apolipoprotein A-I and dementia: the Honolulu-Asia aging study. *Am J Epidemiol* **165**:985-992.

Sagare AP, Bell RD and Zlokovic BV (2012) Neurovascular dysfunction and faulty amyloid beta-peptide clearance in Alzheimer disease. *Cold Spring Harbor perspectives in medicine* **2**.

Salloway S, Sperling R, Fox NC, Blennow K, Klunk W, Raskind M, Sabbagh M, Honig LS, Porsteinsson AP, Ferris S, Reichert M, Ketter N, Nejadnik B, Guenzler V, Miloslavsky M,

Wang D, Lu Y, Lull J, Tudor IC, Liu E, Grundman M, Yuen E, Black R and Brashear HR (2014) Two phase 3 trials of bapineuzumab in mild-to-moderate Alzheimer's disease. *N Engl J Med* **370**:322-333.

Sartorius T, Peter A, Heni M, Maetzler W, Fritsche A, Haring HU and Hennige AM (2015) The brain response to peripheral insulin declines with age: a contribution of the blood-brain barrier? *PLoS One* **10**:e0126804.

Sato H, Tsuji A, Hirai K-I and Kang YS (1990) Application of HPLC in Disposition Study of A14-¹²⁵I-Labeled Insulin in Mice. *Diabetes* **39**:563-569.

Schonfeld G, Frick MS and Bailey AP (1976) Measurement of apolipoprotein A-I in rat high density lipoprotein and in rat plasma by radioimmunoassay. *Journal of lipid research* **17**:25-29.

Sharma P and Kumar S (2018) S961, a biosynthetic insulin receptor antagonist, downregulates insulin receptor expression & suppresses the growth of breast cancer cells. *Indian J Med Res* **147**:545-551.

Shi M, Chu F, Zhu F and Zhu J (2022) Impact of Anti-amyloid-β Monoclonal Antibodies on the Pathology and Clinical Profile of Alzheimer's Disease: A Focus on Aducanumab and Lecanemab. *Front Aging Neurosci* **14**:870517.

Siemers ER, Friedrich S, Dean RA, Gonzales CR, Farlow MR, Paul SM and Demattos RB (2010) Safety and changes in plasma and cerebrospinal fluid amyloid beta after a single administration of an amyloid beta monoclonal antibody in subjects with Alzheimer disease. *Clin Neuropharmacol* **33**:67-73.

Silverberg GD, Messier AA, Miller MC, Machan JT, Majmudar SS, Stopa EG, Donahue JE and Johanson CE (2010a) Amyloid efflux transporter expression at the blood-brain barrier declines in normal aging. *J Neuropathol Exp Neurol* **69**:1034-1043.

Silverberg GD, Miller MC, Messier AA, Majmudar S, Machan JT, Donahue JE, Stopa EG and Johanson CE (2010b) Amyloid deposition and influx transporter expression at the blood-brain barrier increase in normal aging. *J Neuropathol Exp Neurol* **69**:98-108.

Slot RE, Van Harten AC, Kester MI, Jongbloed W, Bouwman FH, Teunissen CE, Scheltens P, Veerhuis R and van der Flier WM (2017) Apolipoprotein A1 in Cerebrospinal Fluid and Plasma and Progression to Alzheimer's Disease in Non-Demented Elderly. *Journal of Alzheimer's disease : JAD* **56**:687-697.

Smith AD (2002) Imaging the progression of Alzheimer pathology through the brain. *Proceedings of the National Academy of Sciences* **99**:4135-4137.

Smith QR and Rapoport SI (1986) Cerebrovascular permeability coefficients to sodium, potassium, and chloride. *Journal of neurochemistry* **46**:1732-1742.

Starr JM, Wardlaw J, Ferguson K, MacLullich A, Deary IJ and Marshall I (2003) Increased blood-brain barrier permeability in type II diabetes demonstrated by gadolinium magnetic resonance imaging. *J Neurol Neurosurg Psychiatry* **74**:70-76.

Stitt AW, Burke GA, Chen F, McMullen CBT and Vlassara H (2000) Advanced glycation end product receptor interactions on microvascular cells occur within caveolin-rich membrane domains. *The FASEB Journal* **14**:2390-2392.

Strazielle N and Ghersi-Egea JF (2013) Physiology of blood-brain interfaces in relation to brain disposition of small compounds and macromolecules. *Mol Pharm* **10**:1473-1491.

Stukas S, Robert J, Lee M, Kulic I, Carr M, Tourigny K, Fan J, Namjoshi D, Lemke K, DeValle N, Chan J, Wilson T, Wilkinson A, Chapanian R, Kizhakkedathu JN, Cirrito JR, Oda MN and Wellington CL (2014a) Intravenously injected human apolipoprotein A-I rapidly enters the central nervous system via the choroid plexus. *J Am Heart Assoc* **3**:e001156.

Stukas S, Robert J and Wellington CL (2014b) High-density lipoproteins and cerebrovascular integrity in Alzheimer's disease. *Cell Metab* **19**:574-591.

Sun YN, Liu LB, Xue YX and Wang P (2015) Effects of insulin combined with idebenone on blood-brain barrier permeability in diabetic rats. *J Neurosci Res* **93**:666-677.

Swaminathan SK, Ahlschwede KM, Sarma V, Curran GL, Omtri RS, Decklever T, Lowe VJ, Poduslo JF and Kandimalla KK (2017) Insulin differentially affects the distribution kinetics of amyloid beta 40 and 42 in plasma and brain. *Journal of cerebral blood flow and metabolism : official journal of the International Society of Cerebral Blood Flow and Metabolism*:271678x17709709.

Swaminathan SK, Ahlschwede KM, Sarma V, Curran GL, Omtri RS, Decklever T, Lowe VJ, Poduslo JF and Kandimalla KK (2018a) Insulin differentially affects the distribution kinetics of amyloid beta 40 and 42 in plasma and brain. *J Cereb Blood Flow Metab* **38**:904-918.

Swaminathan SK, Min H-K, Sarma VV, Ahlschwede KM, Bruinsma TJ, Curran GL, Decklever T, Lowe VJ and Kandimalla KK (2018b) P1-197: AMYLOID BETA EFFECTS ON INSULIN PERMEABILITY FROM PLASMA TO BRAIN MEASURED BY I-125 INSULIN SPECT IN APP/PS1 MICE. *Alzheimer's & Dementia* **14**:P354-P354.

Swaminathan SK, Zhou AL, Ahlschwede KM, Curran GL, Lowe VJ, Li L and Kandimalla KK (2020) High-Density Lipoprotein Mimetic Peptide 4F Efficiently Crosses the Blood-Brain Barrier and Modulates Amyloid-β Distribution between Brain and Plasma. *J Pharmacol Exp Ther* **375**:308-316.

Sweeney MD, Sagare AP and Zlokovic BV (2018) Blood-brain barrier breakdown in Alzheimer disease and other neurodegenerative disorders. *Nat Rev Neurol* **14**:133-150.

Takechi R, Lam V, Brook E, Giles C, Fimognari N, Mooranian A, Al-Salami H, Coulson SH, Nesbit M and Mamo JCL (2017) Blood-Brain Barrier Dysfunction Precedes Cognitive Decline and Neurodegeneration in Diabetic Insulin Resistant Mouse Model: An Implication for Causal Link. *Frontiers in Aging Neuroscience* **9**.

Tan S, Ng Y and James David E (2011) Next-generation Akt inhibitors provide greater specificity: effects on glucose metabolism in adipocytes. *Biochemical Journal* **435**:539-544.

Tarumi T and Zhang R (2018) Cerebral blood flow in normal aging adults: cardiovascular determinants, clinical implications, and aerobic fitness. *J Neurochem* **144**:595-608.

Thanopoulou K, Fragkouli A, Stylianopoulou F and Georgopoulos S (2010) Scavenger receptor class B type I (SR-BI) regulates perivascular macrophages and modifies amyloid pathology in an Alzheimer mouse model. *Proceedings of the National Academy of Sciences of the United States of America* **107**:20816-20821.

Tian DY, Cheng Y, Zhuang ZQ, He CY, Pan QG, Tang MZ, Hu XL, Shen YY, Wang YR, Chen SH, Sun HL, Sun PY, Yu ZY, Fan DY, Bu XL, Tan CR, Zeng GH, Wang J, Zhao HW and Wang YJ (2021) Physiological clearance of amyloid-beta by the kidney and its therapeutic potential for Alzheimer's disease. *Mol Psychiatry* **26**:6074-6082.

Tolar M, Abushakra S, Hey JA, Porsteinsson A and Sabbagh M (2020) Aducanumab, gantenerumab, BAN2401, and ALZ-801—the first wave of amyloid-targeting drugs for Alzheimer's disease with potential for near term approval. *Alzheimer's Research & Therapy* **12**:95.

Torrandell-Haro G, Branigan GL, Vitali F, Geifman N, Zissimopoulos JM and Brinton RD (2020) Statin therapy and risk of Alzheimer's and age-related neurodegenerative diseases. *Alzheimers Dement (N Y)* **6**:e12108.

Townsend M, Mehta T and Selkoe DJ (2007) Soluble Abeta inhibits specific signal transduction cascades common to the insulin receptor pathway. *J Biol Chem* **282**:33305-33312.

van Dyck CH, Swanson CJ, Aisen P, Bateman RJ, Chen C, Gee M, Kanekiyo M, Li D, Reyderman L, Cohen S, Froelich L, Katayama S, Sabbagh M, Vellas B, Watson D,

Dhadda S, Irizarry M, Kramer LD and Iwatsubo T (2023) Lecanemab in Early Alzheimer's Disease. *N Engl J Med* **388**:9-21.
Vandal M, Bourassa P and Calon F (2015) Can insulin signaling pathways be targeted to transport Aβ out of the brain? *Frontiers in Aging Neuroscience* **7**.
Vandal M, White PJ, Tremblay C, St-Amour I, Chevrier G, Emond V, Lefrançois D, Virgili J, Planel E, Giguere Y, Marette A and Calon F (2014) Insulin Reverses the High-Fat Diet–Induced Increase in Brain Aβ and Improves Memory in an Animal Model of Alzheimer Disease. *Diabetes* **63**:4291-4301.
Viswanathan A and Greenberg SM (2011) Cerebral amyloid angiopathy in the elderly. *Annals of neurology* **70**:871-880.
Wahrle SE, Jiang H, Parsadanian M, Hartman RE, Bales KR, Paul SM and Holtzman DM (2005) Deletion of Abca1 increases Abeta deposition in the PDAPP transgenic mouse model of Alzheimer disease. *The Journal of Biological Chemistry* **280**:43236-43242.
Wahrle SE, Jiang H, Parsadanian M, Kim J, Li A, Knoten A, Jain S, Hirsch-Reinshagen V, Wellington CL, Bales KR, Paul SM and Holtzman DM (2008) Overexpression of ABCA1 reduces amyloid deposition in the PDAPP mouse model of Alzheimer disease. *The Journal of clinical investigation* **118**:671-682.
Wang H, Liu Z, Li G and Barrett EJ (2006) The vascular endothelial cell mediates insulin transport into skeletal muscle. *Am J Physiol Endocrinol Metab* **291**:E323-332.
Wang H, Wang AX, Aylor K and Barrett EJ (2015) Caveolin-1 phosphorylation regulates vascular endothelial insulin uptake and is impaired by insulin resistance in rats. *Diabetologia* **58**:1344-1353.
Wang H, Wang AX and Barrett EJ (2011) Caveolin-1 is required for vascular endothelial insulin uptake. *Am J Physiol Endocrinol Metab* **300**:E134-144.
Wang H, Wang AX, Liu Z and Barrett EJ (2008) Insulin signaling stimulates insulin transport by bovine aortic endothelial cells. *Diabetes* **57**:540-547.
Wang J, Tanila H, Puoliväli J, Kadish I and Groen Tv (2003) Gender differences in the amount and deposition of amyloidβ in APPswe and PS1 double transgenic mice. *Neurobiology of Disease* **14**:318-327.
Watson LS, Wilken-Resman B, Williams A, DiLucia S, Sanchez G, McLeod TL and Sims-Robinson C (2022) Hyperinsulinemia alters insulin receptor presentation and internalization in brain microvascular endothelial cells. *Diabetes and Vascular Disease Research* **19**:14791641221118626.
Wauson EM, Guerra ML, Barylko B, Albanesi JP and Cobb MH (2013) Off-target effects of MEK inhibitors. *Biochemistry* **52**:5164-5166.
Weksler B, Romero IA and Couraud PO (2013) The hCMEC/D3 cell line as a model of the human blood brain barrier. *Fluids and barriers of the CNS* **10**:16.
Weller RO, Preston SD, Subash M and Carare RO (2009) Cerebral amyloid angiopathy in the aetiology and immunotherapy of Alzheimer disease. *Alzheimers Res Ther* **1**:6.
Wong AA and Brown RE (2007) Age-related changes in visual acuity, learning and memory in C57BL/6J and DBA/2J mice. *Neurobiol Aging* **28**:1577-1593.
Woods SC, Seeley RJ, Baskin DG and Schwartz MW (2003) Insulin and the blood-brain barrier. *Curr Pharm Des* **9**:795-800.
Xiao G and Gan LS (2013) Receptor-mediated endocytosis and brain delivery of therapeutic biologics. *Int J Cell Biol* **2013**:703545.
Xie L, Helmerhorst E, Taddei K, Plewright B, Van Bronswijk W and Martins R (2002) Alzheimer's beta-amyloid peptides compete for insulin binding to the insulin receptor. *J Neurosci* **22**:Rc221.

Ximerakis M, Lipnick SL, Innes BT, Simmons SK, Adiconis X, Dionne D, Mayweather BA, Nguyen L, Niziolek Z, Ozek C, Butty VL, Isserlin R, Buchanan SM, Levine SS, Regev A, Bader GD, Levin JZ and Rubin LL (2019) Single-cell transcriptomic profiling of the aging mouse brain. *Nat Neurosci* **22**:1696-1708.

Xin SH, Tan L, Cao X, Yu JT and Tan L (2018) Clearance of Amyloid Beta and Tau in Alzheimer's Disease: from Mechanisms to Therapy. *Neurotox Res* **34**:733-748.

Yamada M and Naiki H (2012) Cerebral amyloid angiopathy. *Prog Mol Biol Transl Sci* **107**:41-78.

Yang AC, Stevens MY, Chen MB, Lee DP, Stähli D, Gate D, Contrepois K, Chen W, Iram T, Zhang L, Vest RT, Chaney A, Lehallier B, Olsson N, du Bois H, Hsieh R, Cropper HC, Berdnik D, Li L, Wang EY, Traber GM, Bertozzi CR, Luo J, Snyder MP, Elias JE, Quake SR, James ML and Wyss-Coray T (2020) Physiological blood-brain transport is impaired with age by a shift in transcytosis. *Nature* **583**:425-430.

Yoo DY, Yim HS, Jung HY, Nam SM, Kim JW, Choi JH, Seong JK, Yoon YS, Kim DW and Hwang IK (2016) Chronic type 2 diabetes reduces the integrity of the blood-brain barrier by reducing tight junction proteins in the hippocampus. *J Vet Med Sci* **78**:957-962.

Yoon SS and Jo SA (2012) Mechanisms of Amyloid-β Peptide Clearance: Potential Therapeutic Targets for Alzheimer's Disease. *Biomol Ther (Seoul)* **20**:245-255.

Young SE, Mainous AG, 3rd and Carnemolla M (2006) Hyperinsulinemia and cognitive decline in a middle-aged cohort. *Diabetes Care* **29**:2688-2693.

Yu Y, Kastin AJ and Pan W (2006) Reciprocal interactions of insulin and insulin-like growth factor I in receptor-mediated transport across the blood-brain barrier. *Endocrinology* **147**:2611-2615.

Zhang Y and Lee DHS (2011) Sink Hypothesis and Therapeutic Strategies for Attenuating Aβ Levels. *The Neuroscientist* **17**:163-173.

Zhao WQ, De Felice FG, Fernandez S, Chen H, Lambert MP, Quon MJ, Krafft GA and Klein WL (2008) Amyloid beta oligomers induce impairment of neuronal insulin receptors. *Faseb j* **22**:246-260.

Zhao WQ, Lacor PN, Chen H, Lambert MP, Quon MJ, Krafft GA and Klein WL (2009) Insulin receptor dysfunction impairs cellular clearance of neurotoxic oligomeric a{beta}. *J Biol Chem* **284**:18742-18753.

Zhou AL, Sharda N, Sarma VV, Ahlschwede KM, Curran GL, Tang X, Poduslo JF, Kalari KR, Lowe VJ and Kandimalla KK (2022) Age-Dependent Changes in the Plasma and Brain Pharmacokinetics of Amyloid-β Peptides and Insulin. *J Alzheimers Dis* **85**:1031-1044.

Zhou AL, Swaminathan SK, Curran GL, Poduslo JF, Lowe VJ, Li L and Kandimalla KK (2019) Apolipoprotein A-I Crosses the Blood-Brain Barrier through Clathrin-Independent and Cholesterol-Mediated Endocytosis. *J Pharmacol Exp Ther* **369**:481-488.

Zhou Y and Klein WL (2012) Aβ Oligomers-Induced Toxicity is Attenuated in Cells Cultured with NbActiv4™ Medium. *Neurotoxicity Research* **22**:335-344.

Zidovetzki R and Levitan I (2007) Use of cyclodextrins to manipulate plasma membrane cholesterol content: evidence, misconceptions and control strategies. *Biochim Biophys Acta* **1768**:1311-1324.

Zlokovic BV (2011) Neurovascular pathways to neurodegeneration in Alzheimer's disease and other disorders. *Nat Rev Neurosci* **12**:723-738.

Zlokovic BV, Ghiso J, Mackic JB, McComb JG, Weiss MH and Frangione B (1993) Blood-brain barrier transport of circulating Alzheimer's amyloid beta. *Biochem Biophys Res Commun* **197**:1034-1040.